EFFECT OF HUMPBACK WHALE-INSPIRED TUBERCLES ON VERTICAL AXIS WIND TURBINE BLADE

Thesis

Submitted in partial fulfillment of the requirements for the degree of

DOCTOR OF PHILOSOPHY

by

JEENA JOSEPH

DEPARTMENT OF MECHANICAL ENGINEERING
NATIONAL INSTITUTE OF TECHNOLOGY KARNATAKA
SURATHKAL, MANGALURU - 575025, INDIA

December, 2022

DECLARATION

(by the Ph.D. Research Scholar)

I hereby *declare* that the Research Thesis entitled **"Effect of Humpback whale-inspired tubercles on vertical axis wind turbine blade",** which is being submitted to the National Institute of Technology Karnataka, Surathkal in partial fulfilment of the requirements for the award of the Degree of Philosophy in Mechanical Engineering is *a bonafide report of the research work carried out by me*. The material contained in this Research Thesis has not been submitted to any University or Institution for the award of any degree.

Ms. Jeena Joseph
Register No. 165063 ME16F05
Department of Mechanical Engineering

Place : Surathkal
Date : 26 December, 2022

CERTIFICATE

This is to *certify* that the Research Thesis entitled **"Effect of Humpback whale-inspired tubercles on vertical axis wind turbine blade"**, submitted by **Ms. Jeena Joseph** (Register Number **165063 ME16F05**) as a record of the research work carried out by *her is accepted as the Research Thesis submission* in partial fulfilment of the requirements for the award of degree of Doctor of Philosophy.

राष्ट्रीय प्रौद्योगिकी संस्थान, कर्नाटक
यांत्रिकी अभियांत्रिकी विभाग
Dept. of Mechanical Engineering
National Institute of Technology Karnataka

Dr. A. Sathyabhama
Research Guide
Date: 29/12/2022

Dr. Ravikiran Kadoli
Chairman - DRPC
Dept. of Mechanical Engg.
Date: 29.12.2022

This thesis is dedicated

to my kids

Aryan & Ameya

ACKNOWLEDGEMENTS

I take this opportunity to express my gratitude to all the people who have made it possible for me to complete this long journey.

No words can express my gratitude to my mentor **Dr. A. Sathyabhama** for her constant encouragement, enormous help, and constructive criticism throughout my research work. A large part of this work would not have been possible without her thoughtful interventions in acquiring financial aid. The generous guidance and suggestions from the Research Progress Assessment Committee members, **Dr. Arun M.** and **Dr. H. Ramesh**, has helped me to improve at each step. I am very thankful to **Dr. K.V Gangadharan, Dr. Narendranath S., Dr. Srikantha S. Rao**, **Dr. S.M Kulkarni** and **Dr. Ravikiran Kadoli**, who acted as Head of the Department of Mechanical Engineering during the research tenure, for facilitating the research.

I also wish to express my appreciation to my colleagues **Dr.Sreejith B.K**, **Mr.Jaypal Reddy, Mr.Ram Prasad** and **Mr. Ganesh Kolapkar** for their support throughout these years for providing necessary aids and for their co-operation throughout the period of research work.

I cannot thank enough the staff at Open Circuit Wind Tunnel at Indian Institute of Science, Bangalore, for the technical support provided. I am deeply indebted to **Mr. Surendrenath V**, the principal research scientist at OCWT, for accommodating me in a very busy wind tunnel. His valuable advice and long experience in experimental aerodynamics shaped this research. I am thankful to **Mr. Seshadri, Mr. Suhas, Mr. Anurag, Mr. Brinny, and Mr. Kumar** for their innumerable help in conducting experiments.

Last but not the least, I would like to acknowledge the struggles and support of my family and friends. I am forever thankful to my husband **Mr. Jayakrishnan R**, whose unwavering support and kind words kept me going and to my little kids **Aryan** and **Ameya** for being so understanding. I am grateful to my beloved friends **Dr. Padmaraj N.H** and **Dr. Thara Reshma I.V** for all the general guidance and, most of all, for providing me the comfortable space of their home to work.

(JEENA JOSEPH)

ABSTRACT

Vertical axis wind turbines (VAWT) are gaining popularity for their potential to be used in urban and off-grid areas and in offshore wind farms. A study on the flow control potential of Humpback whale flipper-inspired tubercles on VAWT blade is the key focus of this thesis. This work studies the aerodynamic effect of leading-edge tubercles (LET) on certain flow phenomena such as Laminar Separation Bubble (LSB), stall, and hysteresis of the VAWT blade. The effect of tubercle shape and geometrical parameters on the steady-state and unsteady-state aerodynamic characteristics has also been studied.

Initially, a comparative study on unswept and various swept blades is conducted in order to detect the extent of performance enhancement brought about by incorporating LET on both types of blade. The aerodynamic characteristics of NACA 0021 swept and unswept blades have been studied and compared with their tubercle counterparts of tubercle amplitude and wavelength 6% and 21% of the airfoil chord, respectively. Tubercles along the flow direction have been incorporated on blades swept or inclined at 10°, 20°, and 30° and compared to the respective baselines and to unswept blades, in terms of static aerodynamic forces at a Reynolds number of 1×10^5. It was seen that tubercles are more beneficial on unswept and blades of low sweep than on blades of high sweep angle, in attaining a smooth stall.

Further, a detailed study of the effect of LET on the unswept blade has been done by analyzing the static force and surface pressure at varied Reynolds numbers ranging from 2.5×10^5 to 6×10^5. The LSB begins to appear on the suction surface of unmodified blade at an angle of attack (AOA) of 6°, which extends between 24% and 35% of the blade chord. With the increase in AOA, the LSB moves forward towards the blade's leading edge and decreases in size. However, due to the influence of tubercles, LSB is not present on the tubercle blade. Stall occurs earlier in the tubercle blade as compared to the baseline blade. The baseline blade exhibits an abrupt and deep stall that occurs in a single step, whereas the tubercle model has a soft gradual stall that occurs

in multiple stages for all Reynolds numbers studied. Surface pressure measurements for static models further reveal the mechanism of the stall. Stall initially originates at the midsection of the blade, which progresses towards the tips of the baseline blade. However, with the introduction of tubercles, the stall progression towards the tips is inhibited on the tubercle blade. The baseline blade also exhibits static hysteresis for lift, drag, and moment coefficient curves, and its extent increases with an increase in Reynolds number. However, for the tubercle model, hysteresis was completely absent.

The effect of tubercle shape and geometrical parameters on steady-state aerodynamics has been studied at a Reynolds number of 5×10^5 using blades incorporated with sinusoidal and triangular LET of varying amplitude to wavelength ratio (A/W). The static forces on four blades with sinusoidal LET of A/W 0.25, 0.5, 0.75 and 1, and two blades of triangular LET of A/W 0.5 and 1, are analyzed and compared to that of a baseline. For blades of sinusoidal and triangular LET, the lift coefficient is lower than that of the baseline in the pre-stall region and decreases with an increase in A/W. The drag and pitching moment increases with increase in A/W. However the tubercle blades are better performing in the post-stall region, where they have higher lift than the baseline. The tubercle blades have a stall earlier than the baseline. However, the tubercle blades have a better stall characteristic than baseline in terms of smooth stall. The stall gets smoother with increase in A/W of tubercles. The steady-state aerodynamic characteristics of sinusoidal and triangular blades of corresponding A/W are closely identical to one another.

Finally, considering the actual blade movement on VAWT, the effect of the LET on dynamic blades is studied. The effect of tubercles on unsteady flow has been studied by pitch-oscillating the above-mentioned blades with sinusoidal and triangular LET at various frequencies and obtaining the forces acting. The baseline blade has the maximum lift coefficient, $C_{L_{max}}$ but exhibits deep stall. Large hysteresis loops are seen in the stall region for the baseline blade. The triangular and sinusoidal LET help mitigate the intensity of stall and hysteresis of the blade. The tubercle blades (sinusoidal and triangular LET) with the least tubercle amplitude have the highest $C_{L_{max}}$ after baseline. The blades of the highest tubercle amplitude has the most desirable stall and hysteresis characteristics. The size of the hysteresis loop decreases with an increase in tubercle amplitude. Blades with triangular LET perform similar to the sinusoidal leading edge except for having a higher coefficient of normal force.

KEYWORDS: **VAWT, Leading-edge tubercles, hystersis, dynamic stall**

TABLE OF CONTENTS

LIST OF FIGURES

LIST OF TABLES

NOTATION

Roman Symbols

Symbol	Description	Unit
A	Amplitude of tubercle	$[m]$
A	Axial force along chord line	$[N]$
A_b	Planform area of blade	$[m^2]$
A_f	Planar area of whale flipper	$[m^2]$
c	Mean chord	$[m]$
C_L	Coefficient of lift	-
C_M	Coefficient of moment	-
C_N	Coefficient of normal force	-
C_P	Coefficient of pressure	-
C_D	Coefficient of drag	-
$C_{L_{max}}$	Coefficient of maximum lift	-
$C_{L_{p.s}}$	Coefficient of lift post stall	-
C_L	Coefficient of lift	-
$C_{M.b}$	Coefficient of moment in body axis coordinate system	-
$C_{N_{max}}$	Maximum coefficient of normal force	-
D	Drag force	$[N]$
L	Lift	$[N]$
L/D	Lift to drag ratio	-
L/D_{max}	Maximum lift to drag ratio	-
l_{LSB}	Extent of LSB	-
M	Moment	$[Nm]$
m_v	Virtual mass of whale	$[kg]$
N	Force normal to chord line	$[N]$
P	Static pressure at chord wise location	$[Pa]$
P_∞	Free stream static pressure	$[Pa]$
R	Point of reattachment	-

R	Radius of VAWT	$[m]$
R	Resultant force on airfoil	$[N]$
R_t	Turning radius of Humpback whale	$[m]$
Re	Reynolds number	-
Re_c	Chord based Reynolds number	-
S	Point of separation	-
s	Span of blade	$[m]$
T	Point of transition	-
U_I	Induced wind velocity	$[m/s]$
U_∞	Free stream velocity	$[m/s]$
U_{rel}	Wind speed relative to turbine blade	$[m/s]$
V_∞	Tunnel velocity	$[m/s]$
V_W	Wind velocity	$[m/s]$
W	Wavelength of tubercle	$[m]$
x	Chordwise/streamwise location	$[m]$
x/c	Normalized chordwise location	-
x/c_R	Chordwise location of reattachment	-
x/c_S	Chordwise location of separation	-
y	Spanwise location	$[m]$
y/s	Normalized spanwise location	-
k	Reduced frequency	-

Greek Symbols

Symbol	Description	Unit
α	Angle of attack (AOA)	$[^\circ]$
$\alpha_{d.stall}$	AOA at dynamic stall	$[^\circ]$
$\alpha_{h.l}$	Extent of hysteresis loop	$[^\circ]$
α_{rec}	AOA at stall recovery	$[^\circ]$
α_{stall}	AOA at stall	$[^\circ]$
β	Yaw angle	$[^\circ]$
γ	Angle between tubercle and flow	$[^\circ]$
λ	Sweep angle of blade	$[^\circ]$
τ	Shear stress	$[Pa]$
ε	Percentage error	-

η	Blade speed ratio	-
κ	Reduced frequency	-
ω	Angular velocity of blade	[rad/s]
ϕ	Bank angle during whale turning	[$^\circ$]
ρ	Density of air	[kg/m^3]
$\rho_{s.w}$	Density of sea water	[kg/m^3]
θ	Azimuth angle	[$^\circ$]

ABBREVIATIONS

AOA	Angle of Attack
ADC	Analog to Digital Converter
APC	Archives and Publications Cell
CAD	Computer Aided Design
CFD	Computational Fluid Dynamics
CNC	Computer Numerical Control
DSV	Dynamic Stall Vortices
FRP	Fibre Reinforced Plastic
HAWT	Horizontal Axis Wind turbine
LEE	Leading Edge Extension
LET	Leading Edge Tubercle
LSB	Laminar Separation Bubble
MAV	Micro Aerial Vehicle
NACA	National Advisory Committee for Aeronautics
OCWT	Open Circuit Wind Tunnel
PIV	Particle Image Velocimetry
STOL	Short Take-Off-and-landing
TSR	Tip Speed Ratio
UAV	Unmanned Air Vehicle
VAWT	Vertical Axis Wind Turbine

CHAPTER 1

INTRODUCTION

This chapter gives an introduction to Vertical Axis Wind Turbine (VAWT) and various flow problems encountered by its blades. Some flow control methods are also discussed in this chapter to give the reader an understanding of the potential of Humpback whale-inspired leading-edge tubercles (LET) in flow manipulation. Subsequently, an introduction to biomimicry and its role in solving many engineering problems, emphasizing flow control by tubercles on the Humpback whale flipper is presented. The final discussion on the potential of tubercles gives insight into the wide range of applications of LET as flow control elements on devices of day-to-day usage.

1.1 Vertical Axis Wind Turbine

There has been a resurgence in the research on VAWT, after realizing its potential in offshore (Paulsen *et al.*, 2014) and urban application (Islam *et al.*, 2013; Tummala *et al.*, 2016) as a versatile approach to wind energy extraction. Decades of less intensive research on VAWT has left its performance inferior to its horizontal axis counterparts (Rezaeiha *et al.*, 2017). However, the recent researches have helped in better understanding the flow complexities and problems encountered by VAWTs and devising solutions to mitigate the flow deteriorating effects. The VAWT is gaining popularity due to the many advantages it has over the Horizontal Axis Wind Turbine (HAWT).

The VAWT has an omni-directional nature of rotor, enabling it to pick up winds in any direction. Unlike so, the HAWT has to be placed in specific locations facing the wind flow. Special yaw mechanism components are required on HAWT to change the rotor orientation with respect to the direction of wind. Due to this operational difference, VAWT can be used in wide range of weather conditions including turbulent and gusty wind conditions. The VAWT does not need additional mechanical components for pitch, yaw, or rotational speed control, making it cheaper to manufacture. Lesser components would also lessen the wear and tear, increasing the operational life and reducing the cost of maintenance. Maintenance workers do not have to climb as high to reach parts of the turbine because the major components, such as the generators, are

built closer to the ground. The VAWT is more environment-friendly, as it operates with lower noise emission and are less fatal to birds.

The most important factor contributing to the popularity of VAWT is that it can be used in urban and off-grid areas. The design of VAWT is highly scalable and be placed closer to one another, which allows for a more significant number of turbines on a wind farm. Although VAWTs produce less energy per tower, they have the potential to generate as much as ten times more power than HAWT over a comparative area of land when placed in arrays (Craig *et al.*, 2017). Due to these reasons, VAWT is being considered an off-shore alternative to HAWT. However, a significant problem encountered by VAWT in its operation is dynamic stall (Noll and Ham, 1982; Laneville and Vittecoq, 1986), which shall be discussed in detail in section 1.2.4. Dynamic stall causes two significant issues on VAWT - the loss of lift and increased drag, resulting in a tremendous reduction of power production. Dynamic stall causes substantial variation in loads acting on the turbine leading to structural failure of the turbine.

1.2 Problems Associated with Flow Separation

Small length scales and working velocities of VAWT often result in a low chord-based Reynolds number, Re_c, usually less than 5×10^5. Flow in the Reynolds number range between 10^4 and 10^6 is called low Reynolds number (Re) flow, and its application also includes insects, birds, human-powered aircraft, Unmanned Aerial vehicles (UAV), Micro-Aerial vehicles (MAV), etc. (Lissaman, 1983). The aerodynamics at low Re is critical in designing small domestic wind turbines with rotor diameters less than 7m, wind turbines for research purposes, laboratory-scale rotors, Vertical Axis Wind Turbine (VAWT), etc. Many of the aerodynamic problems are particularly related to the management of boundary layer and comes into the picture, especially at low Re (Mueller and Batill, 1982). When it comes to the boundary layer of an airfoil, the main regions of interest are the region of separation near the leading edge and the trailing edge and the region where laminar to turbulent transition takes place (Mueller and Batill, 1982). Reynolds number, turbulence level or environment disturbances, and pressure gradient heavily influence the phenomenon of separation and transition (Mueller, 1985), which in turn play a crucial role in the development of boundary layer and thus overall airfoil performance (Mueller and Batill, 1982). The boundary layer separation on aerodynamic surfaces like an airfoil and turbine blades causes phenomena like stall, hysteresis, laminar separation bubble (LSB), etc., which can adversely affect its aero-

dynamic performance. Some problems associated with the boundary layer separation are discussed in the following sections.

1.2.1 Laminar Separation Bubble

The boundary layer flow at low Reynolds number is initially laminar and is susceptible to separation with a mild adverse pressure gradient. Due to the adverse pressure gradient, the laminar boundary layer separates, becomes transitional, and later turbulent. Under certain flow conditions, the separated flow reattaches to the surface and form a bubble region called the "LSB". The LSB usually occurs at the leading edge of airfoils of gas turbine blades and on MAV wings at low Re (Diwan and Ramesh, 2007). The presence of LSB could modify the effective shape of the airfoil, consequently affecting the aerodynamic performance, mainly in an adverse manner.

Figure 1.1 depicts the structure of LSB and the pressure distribution on a surface where LSB is present. The LSB is characterized by the formation of a pressure plateau between the point of separation to the point of transition, which is the laminar portion. Beyond the transition point, rapid pressure recovery occurs till the point of reattachment, which is the turbulent region. (Tani, 1964; Gaster, 1967). The LSB could modify the thickness and curvature of the airfoil and consequently have an adverse effect on aerodynamic performance like an increase in pressure drag, decrease in the lift, generation of aerodynamic noise, etc. The LSB formation depends on various factors like Re, angle of attack (AOA), the shape of the airfoil, etc.

1.2.2 Stall

The stall is a phenomenon that occurs beyond a critical AOA when the lift of an aerodynamic surface suddenly drops and drag increases rapidly, as a consequence of flow separation. For an airfoil, wing or any aerodynamic surface to be effective, air must completely bend around the leading edge. Figure 1.2 shows the flow over the cross-section of a stalling wing. At very small AOA (Figure 1.2a), the boundary layer vortices stay close to the wing until washed downstream. The wing produces significant lift and little drag. When the AOA increases (Figure 1.2b), the boundary layer vortices do not stay attached to the leading edge but separate from the wing surface. The incoming flow does not bend completely around the leading edge at this state. Thus, the wing is stalled, and there is a significant drag. Much of the lift is still present as the separated vortices

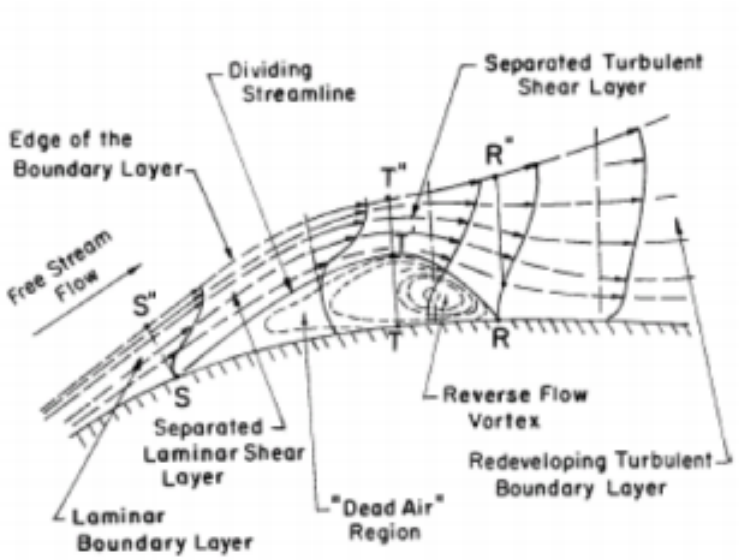

(a)

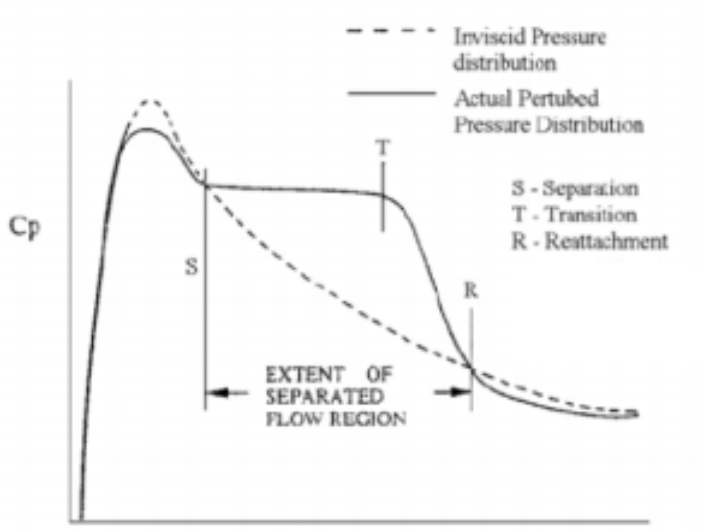

(b)

Figure 1.1: (a) Schematic of the LSB (b) pressure distribution on the suction surface where LSB is present (Gaster, 1967)

are still above the wing. The lift drops with higher AOA when the separated vortices are blown down the trailing edge (Figure 1.2c). For an aircraft, stall can occur during landing or take off when flight speed is low. At low speeds, the aerodynamic forces are small, and enough lift to carry the weight of the aircraft can only be attained by increasing the AOA, making it prone to stall. The stall has been a hazard from the early days of aviation. Otto Lilienthal crashed and perished due to a stall in 1896. Wilbur Wright experienced stall in 1901 while flying his second glider, convincing the Wright

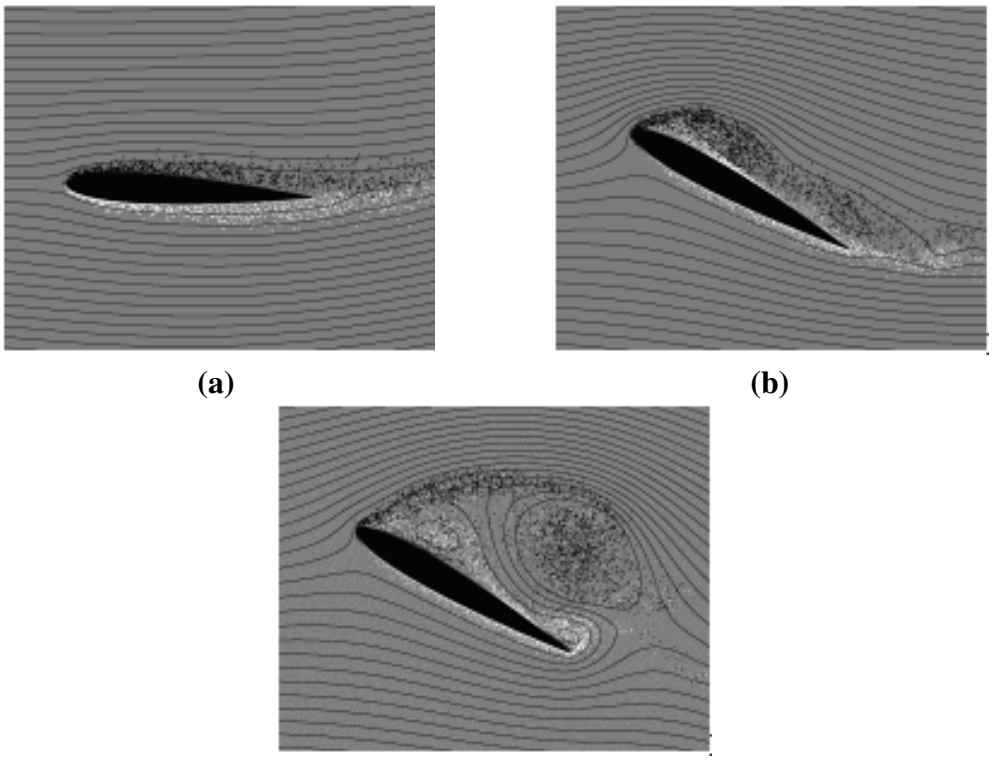

Figure 1.2: Stages of stall on a wing (Shih *et al.*, 1992)

brothers to design their aircraft in a canard configuration to facilitate easy stall recovery (Stoop and De Kroes, 2012). The stall is not only seen on aircraft, but also on fans, compressors (Bianchi *et al.*, 2013), and other aerodynamic surfaces. Several methods are used to control stall, including active devices like synthetic jets and actuators and passive ones like vortex generators and fences.

1.2.3 Hysteresis

Another consequence of flow separation and transition is the hysteresis (Mueller, 1985), which is usually seen around the stall region. In aerodynamics, hysteresis refers to the characteristic of an airfoil/ wing to respond to or be dependent on its history of change in AOA. The aerodynamic coefficients thus have more than one value for corresponding AOA based on if the wing/airfoil was moving up or down. The phenomenon of hysteresis is commonly seen in thick, round-nosed, cambered, and low Re airfoils (Mueller, 1985; Selig *et al.*, 1996) near their stall angles. The type of hysteresis loop depends on whether separation or transition happens first. When the AOA increases and laminar separation occurs first without reattachment, a counterclockwise hysteresis loop is

made. On the other hand, if the transition occurs first, either caused by a separation bubble or some other means, a clockwise hysteresis loop is created. Hysteresis was initially observed on a flat plate in the 1930s (Hoerner, 1965) and on a thick airfoil in the 1940s (Schmitz, 1967). Later, it was not studied extensively until the past decade, when there was the advent of MAV (Shyy *et al.*, 2007). In the same way, hysteresis could be significant in other low Re applications like wind turbines, UAVs, sailplanes, man-powered aircraft, etc. Aerodynamic hysteresis in the stall region is observed for airfoil, wing, and aircraft in the static and dynamic state (Ericsson and Reding, 1971; Ekaterinaris and Platzer, 1998). Though hysteresis in a dynamic state has been studied extensively (McCroskey, 1982), very less emphasis is obtained for static hysteresis. Some discussion on static hysteresis can be seen in the literature for low Re airfoil (Timmer, 2008; Williams *et al.*, 2017; Mizoguchi *et al.*, 2014).

In a study on aerodynamic characteristics of airfoils- Lissaman 7769 and Miley M06-13-128, at a Re of 3×10^5 (Pohlen and Mueller, 1984; Mueller, 1985), clockwise and anticlockwise hysteresis of lift curve was found, respectively. Smoke visualization on these airfoils (Mueller, 1985) also suggested that the laminar boundary layer separation and transition have a major influence on hysteresis. The actual performance of an airfoil and whether hysteresis occurs or not is sensitive to many factors, including airfoil shape, turbulence intensity in the wind tunnel, Reynolds number, acoustic turbulence, mechanical vibration, and surface roughness. Hysteresis usually occurs around the stall region and can be of great practical importance as it affects recovery from the stall. Hysteresis can be a predominant problem on VAWT blades due to the constantly changing direction of the blade, causing the effective angle to increase and decrease periodically.

1.2.4 Dynamic Stall

A significant consequence of flow separation on the rotating wind turbine blade is the dynamic stall . Dynamic stall is an unsteady phenomenon that occurs due to the rapid movement of an airfoil due to its operation beyond the critical stall angle. When the turbine blade rotates about the vertical shaft, the wind velocity, U_∞, and the linear velocity of blade, $R\omega$, give rise to an induced velocity relative to the blades, U_{rel}, as shown in Figure 1.3. The AOA of turbine blade, which is the angle between the chord line of the airfoil and relative velocity is a function of the tip speed ratio (TSR) and azimuth angle. The geometric AOA, α, at a particular azimuth angle, θ, for any given TSR, η, is given by equation 1.1.

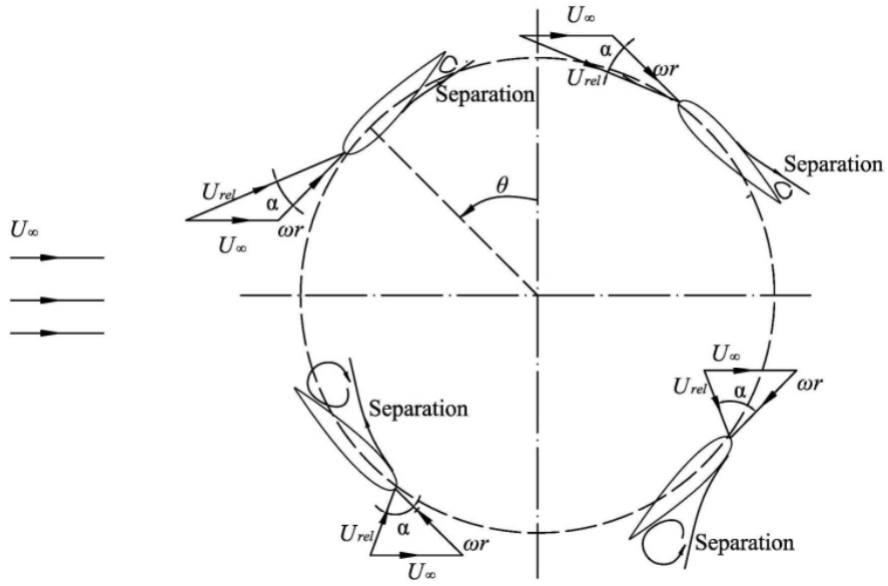

Figure 1.3: Velocity vector diagrams and flow separation zones on VAWT airfoil at different quadrants (Zhong *et al.*, 2019)

$$\alpha = tan^{-1}\left[\frac{sin\theta}{\eta + cos\theta}\right] \tag{1.1}$$

Figure 1.4 depicts the relation between azimuth angle and AOA for NACA 0018 airfoil at various TSR. From equation 1.1 and Figure 1.4, it can be seen that at low TSR ($\eta = 1 - 3$), the AOA of the blade exceeds the static stall angle, which ranges from 9° to 15° for the typical symmetric airfoils (Sheldahl and Klimas, 1981), resulting in significant dynamic stall. Dynamic stall is characterized by the formation and shedding of vortex from the airfoil surface under varying high AOAs. The phenomena of dynamic stall is complex for VAWT because flow separation happens on both sides of the airfoil (refer Figure 1.3). Dynamic stall can induce large unsteady aerodynamic loads and flow losses (Leishman, 1990). Therefore, to minimize blade AOA and onset of stall, a VAWT typically operates at a high TSR of 4 to 7, even though it causes high mechanical vibrations and turbine noise. The VAWT also has a higher rotational kinetic energy at high TSR, decreasing its operational safety.

The formation and development of dynamic stall vortex (DSV) is believed to affect the dynamic stall process. Many studies by Carr et.al (Carr *et al.*, 1977; Carr and McAlister, 1983; Carr, 1988; Chandrasekhara *et al.*, 1994) has greatly contributed to understanding DSV and dynamic stall. Before the onset of dynamic stall, a thin area of reversed flow is formed at the trailing edge. The reversed flow area gradually moves to the leading edge under the influence of adverse pressure gradient, during which the flow remains

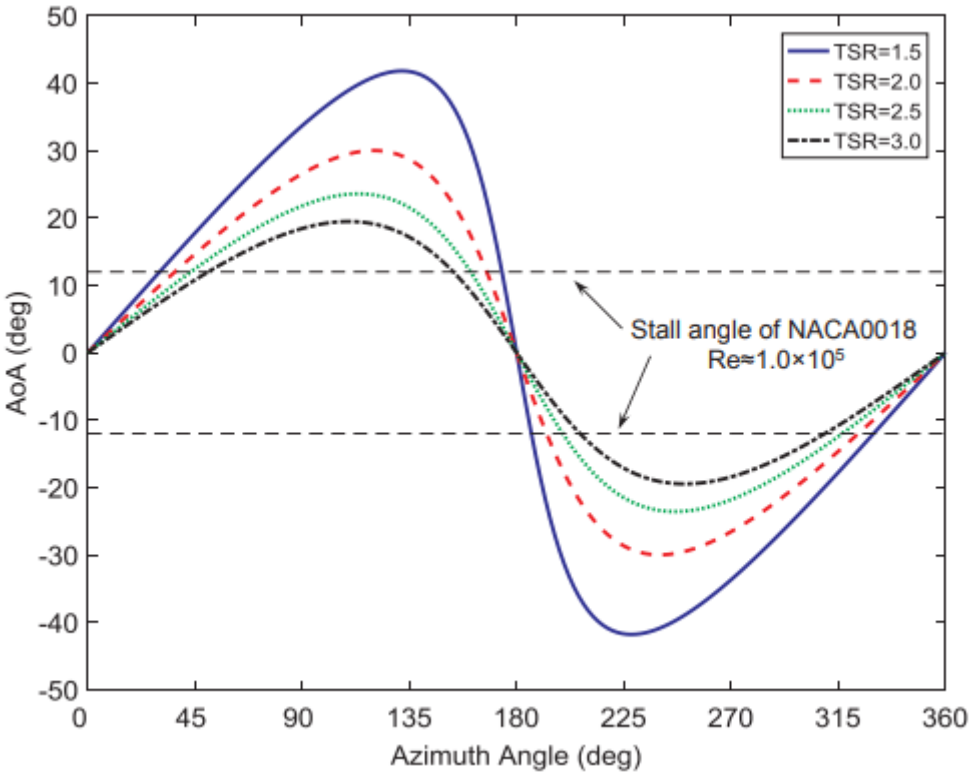

Figure 1.4: Relation between azimuth angle and AOA of rotating blade

attached to the surface. A leading-edge vortex (LEV) is formed at the leading edge, resulting in strong suction. The LEV gradually separates from the surface to form DSV. With increase in AOA, the DSV begins to convect towards the trailing edge and eventually separates from the trailing edge. During dynamic stall, an increase in the lift generated by the airfoil is observed during the airfoil pitch-up especially at high reduced frequency (κ or k) and is often a result of DSV formation. As the vortex convects downstream, the lift generated by the airfoil suddenly drops, and the airfoil goes into a state of deep stall. Choudhry *et al.* (2014) reported that DSV could be identified as a peak in lift coefficient as shown in Figure 1.5.

1.3 Flow Control

Flow control is the process of altering or manipulating a flow field to attain the desired design objective. Though flow control can be applied to various situations, we will limit our focus on the altering of the external wall-bounded flow developing on an airfoil surface. In addition to flow physics, other essential parameters, such as simplicity of design, cost-effectiveness, minimal maintenance, and robustness should be considered

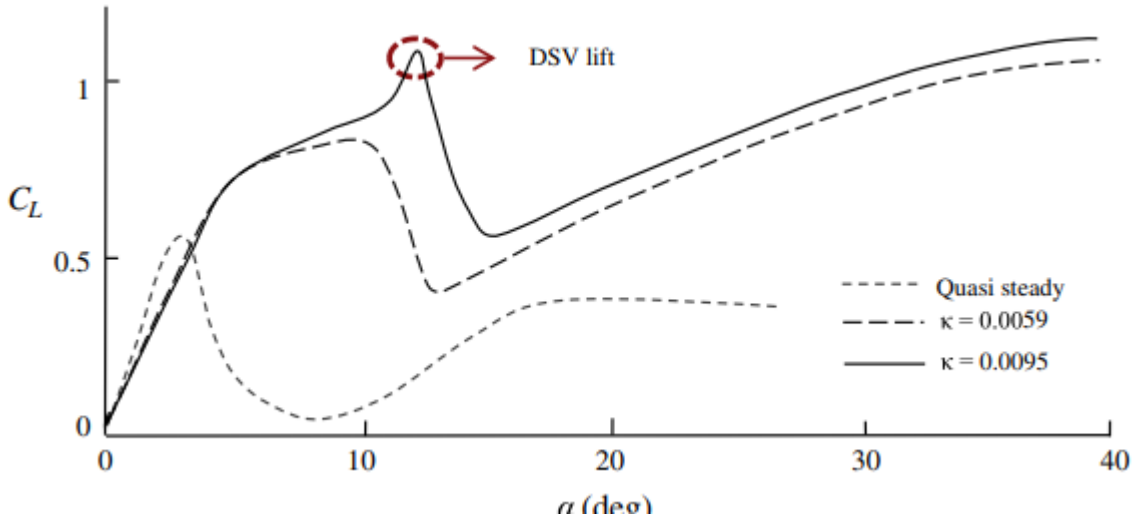

Figure 1.5: Lift coefficient of dynamic NACA 0021 airfoil (Choudhry *et al.*, 2014)

while choosing a flow control method. A key factor to consider in the context of flow control is the Re, as this non-dimensional parameter defines the nature of the boundary layer, whether it is laminar, transitional, or turbulent.

Flow control devices can be categorized based on the energy expenditure of the devices and the outcome of the devices. Based on energy expenditure of flow control devices are categorized into ***passive*** or ***active***. When the flow control device does not require an additional power, it is called ***passive***, and when it requires additional energy source, it is categorized as ***active***. Passive flow control is usually attained by adding non-movable elements to the airfoil surface or by changing airfoil geometry. Active control flow methods can offer advantages over passive methods like targeting specific instabilities, switching on and off, better adaptability to changes in flight conditions, etc. But implementing active control is more expensive and often more complicated than passive methods. Manufacturing complexity and maintenance are relatively high for active devices than passive ones. Hence it is relevant to investigate the scope of passive devices as they are generally more reliable and cost-effective.

Flow control devices can also be classified based on the design outcome of the device, whether it is ***'lift enhancement'*** or ***'drag reduction.'*** The lift generated by the airfoil can be increased by altering its shape, changing its inclination relative to the flow, minimizing the tip stall, and enhancing flow attachment and circulation. Lift augmentation can be achieved by increasing AOA, area of the wing, momentum exchange or the camber of airfoil and augmentation of circulation. The lift can also be increased by reducing or avoiding tip stall and delaying flow separation over the suction surface (suction surface refers to the upper surface of a horizontal wing, and its lower surface

is referred to as the pressure surface). Drag reducing flow control devices focus on mitigating the most significant components of drag, which for subsonic flow are the form drag, induced drag, and skin friction drag. Reducing drag in subsonic flows includes; reducing induced drag by reducing spanwise flow, reducing form drag by delaying flow separation, reducing skin friction drag by reducing coherence of turbulent structures, and creating favorable interaction with turbulent fluctuations. Since tubercles functions as lift enhancing passive device, a brief discussion limited to such devices shall be done in the following section.

1.3.1 Passive Devices for Lift Enhancement

Optimization of Airfoil Profile Shape

The most common method of performance enhancement is by altering the design shape of the airfoil. A wing generates an added lift for a given AOA and span, provided it has a higher camber and chord length. It can also be advantageous to reduce the skin friction drag by increasing the extent of the laminar boundary layer. In such cases, it is required to delay the flow transition to turbulent. This objective can be attained by designing an airfoil with its maximum thickness located as far aft as possible (Cebeci and Cousteix, 2005). Careful contouring of airfoil has to be done near the minimum pressure point to facilitate the transition of flow instead of separation (Gad-el Hak, 1990). It has to be noted that there are limitations for high Re and large sweep angles because of the early onset of transition due to the associated instabilities (Cebeci and Cousteix, 2005). In short, there exist a trade-off between the advantages of modifying the design airfoil shape and the disadvantages of off-design performance degradation.

Momentum Exchange/Separation Delay

Winglet-like devices in the shape of a small rectangle or delta used to delay flow separation and stall are called vortex generators, as shown in Figure 1.6. These devices have a height corresponding to boundary layer thickness and are placed along the chordwise direction (Lin, 2002). Later research has shown that the device height of 10% of the boundary layer could be effective and have considerably low drag (Godard and Stanislas, 2006). These vortex generators project into the boundary layer and create co-rotating or counter-rotating vortices depending on the orientation of the device. These vortices increase the momentum exchange in the boundary layer, thus giving a region

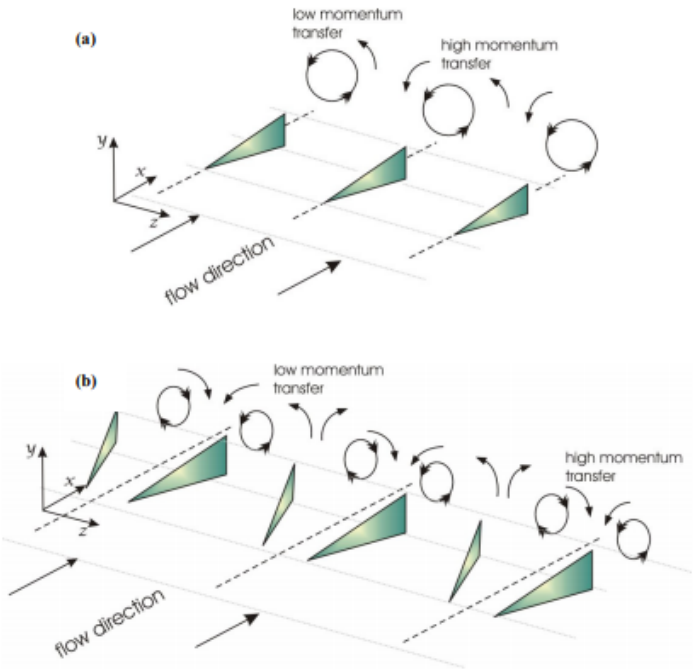

Figure 1.6: Schematic of vortex generators (Godard and Stanislas, 2006)

of mixing over the device almost three times the device height (Lin *et al.*, 1991).

Vortex generators can also reduce the Karman vortex street in the wake region and thus reduce the intensity of acoustic disturbance. Vortex generators are simple, robust, and inexpensive but add parasitic drag in flow regimes (e.g., cruise) where stall suppression is not required.

Counter-rotating streamwise vortices can also be generated on the suction surface of the airfoil by placing small serrations on the pressure surface just before the stagnation (Soderman, 1972) point, as shown in Figure 1.7. Incorporation of the serrations could increase the maximum lift coefficient with negligible drag effects at low AOA and reduced drag at high AOA. Placing the smallest serrations close to the stagnation point can result in the highest performance enhancements. Size, spacing, and position can also affect performance.

Some devices like leading-edge extensions (LEE) or strakes generate a high swirl vortex at moderate to high AOA, as shown in Figure 1.8, which helps maintain attached flow on the wing surface (Thompson, 1997) and results in creating lift well past the expected stall. A disadvantage of these leading extensions is the vortex bursting which can cause structural damage to the tail section of the aircraft and wing rock due to flow instability.

Yet another method to improve momentum exchange is tripping the boundary layer to a

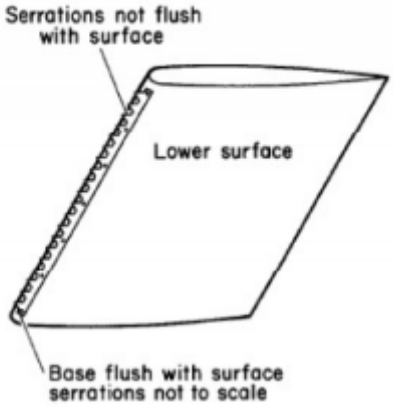

Figure 1.7: Schematic of serrations on leading edge of an airfoil (Soderman, 1972)

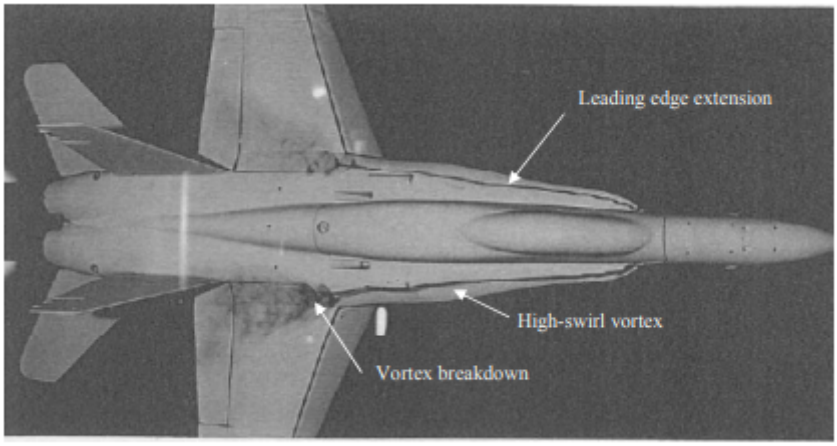

Figure 1.8: Flow pattern associated with LEE (Thompson, 1997)

turbulent one using a turbulator, which forms a thin raised strip, as shown in Figure 1.9. The effect of turbulators can also be brought about by distributed roughness elements (Braslow *et al.*, 1966). Momentum exchange between the freestream flow is higher for the turbulent boundary layer, and therefore flow separation is less likely to happen when there is an adverse pressure gradient (Simons, 2002). The disadvantage of tabulators is the high drag, especially at cruise. The turbulent boundary layer also has a higher skin friction drag than the laminar boundary layer, and therefore the position and height are important to ensure their efficiency.

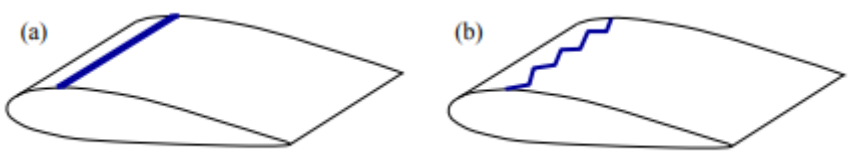

Figure 1.9: (a) Trip strip turbulator (b) Zig zag trip strip turbulator

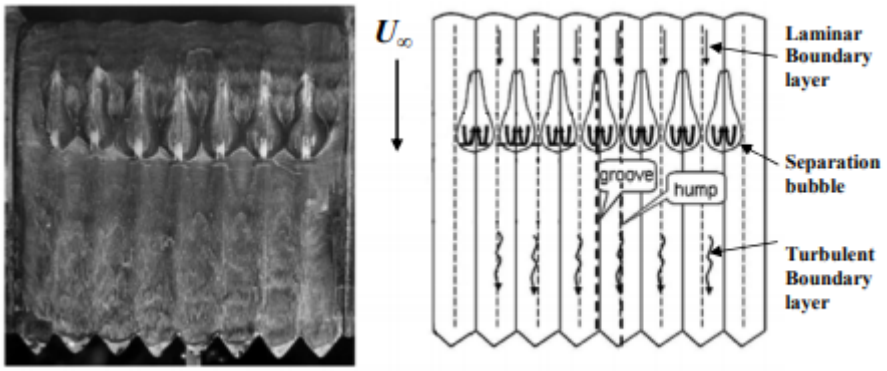

Figure 1.10: Flow pattern over wavy wing as seen in oil flow visualization and its interpretation (Zverkov *et al.*, 2008)

The use of rippled trailing edge, as shown in Figure 1.10 on an airfoil, can also help in altering the pressure gradients on the airfoil surface and thus delay the flow separation. The waviness of the airfoil causes small but significant lateral pressure gradients, which direct the low momentum boundary layer on the suction surface towards a bifurcation line between the trough and peak (Werle *et al.*, 1987). An increase in stall angle and maximum lift coefficient with nominal drag penalty using such modification was experimentally established by Werle *et al.* (1987). Significant variation in the structure of boundary layer was seen on the wavy wing when compared to the baseline wing at 0° AOA, as depicted in Figure 1.10. The transition from laminar to turbulent occurred 30% further downstream for a peak than for the trough. Further, the separation bubble was confined to the troughs and was not present over the humps. Such a boundary layer could endure a more significant adverse pressure gradient than a regular wing and thus provide higher performance (Zverkov *et al.*, 2008).

The feathers on the upper surface of a wing rise up when birds approach to land, and this observation inspired another method of flow separation delay, called flaps. During experiments involving movable flaps fitted to the suction surface of an airfoil, it was observed that the device would lift when the flow separation began as a response to local reversed flow, as seen in Figure 1.11, which would create a hindrance to the flow in moving further towards the leading edge (Meyer *et al.*, 1999). Flaps were made porous with jagged trailing with the intention to equalize static pressure on both sides, thus preventing premature deployment of flaps.

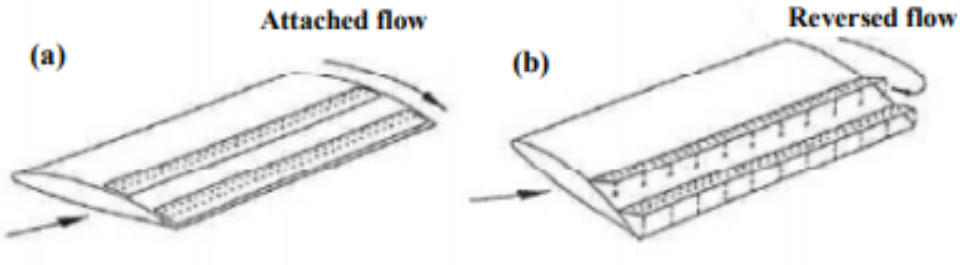

Figure 1.11: Schematic of movable flaps depicting (a) Attached flow at low AOA and (b) separated flow at high AOA (Bechert *et al.*, 1997)

Spanwise Flow Restriction

Flat plates fixed on the upper surface of the airfoil side along with the free stream flow, which obstructs the spanwise flow along the wing, are called wing fences and are depicted in Figure 1.12. Spanwise flow causes higher loading at the wingtips than at the inboard region, leading to stall initiation at the wingtip (Reithmaier and Reithmaier, 1995). Stalled wing tips cause reduced efficiency of ailerons at low speeds and high AOA. When the swept wing tip stalls, the center of pressure moves forward and causes a nose-up pitching moment, which becomes more and more prominent as the stall progresses from the tips to the inboard region. Vortex generators, saw-tooth leading edge, and notched leading edge are other methods to control spanwise flow. Even though they do not create any physical hindrance to the flow, they generate streamwise vortices and create a similar effect (Swatton, 2011).

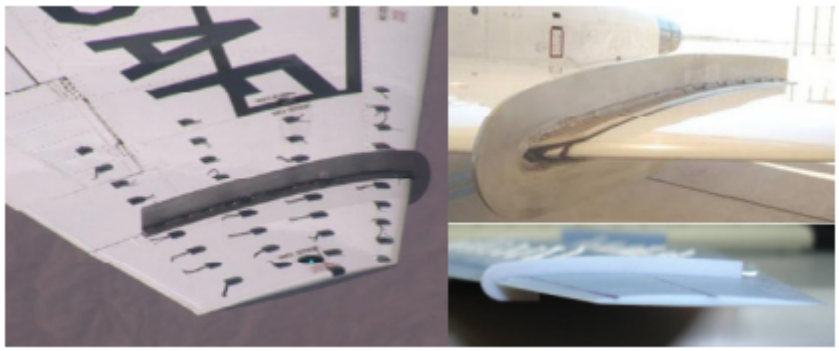

Figure 1.12: Wing fences (Williams, 2009)

1.4 Biomimicry-Lesson from Nature

Nature inspires us to find solutions to many engineering problems. Plant, animals, and even microorganisms provide brilliant engineering solutions through time-tested designs and methods. That is why biomimicry- a practice of learning and replicating nature's lessons to solve human technological problems- has gained much attention from the scientific community. A detailed description of biomimetics in the field of engineering and technology was conducted by Bar-Cohen (2006).

Though the word biomimetics is relatively new, the concept is centuries old. Nature has gone through evolution for over 3.8 billion years. It has time-tested various designs and processes, developing efficient life methods in the process. As a result, what we see in nature is most efficient, functional, and sustainable. This realization has inspired people to look into nature to solve many of their problems or make new devices. In our daily life, we come across many devices and machines inspired by nature, as simple as Velcro (inspired by burr seeds) to complex ones like aircraft (inspired by birds).

As far as the topics of flow control and aerodynamics are concerned, nature has provided many design inspirations. Leonardo da Vinci, a genius of his time, studied how birds fly and proposed designs of flying machines. Many design and devices we see today on aircraft also draw their design inspiration from nature, as in the case of the raindrop/teardrop shape of fuselage offering minimum resistance to air. Riblets on an aircraft wing, inspired by shark skin, are known for their advantage in drag reduction (Bechert *et al.*, 2000; Bhushan, 2012). Other nature-inspired adaptations include trailing edge flaps derived from bird feathers, winglets from eagles, and slots from the spit tail of falcon. During the landing approach of birds, we can observe that the covering feathers on the upper side of bird wings tend to pop up. The raised feathers impede the spreading of the flow separation from the trailing edge to the wing's leading edge. Self-activated movable flaps (artificial bird feathers) represent a high-lift system enhancing the maximum lift of airfoils up to 20%.

1.4.1 Flow control on Humpback whale flipper

The Humpback whale, *Megaptera novaeangliae*, is one of the largest rorqual species, where an adult whale could range between 12-16m. A significant feature of this species is its long flipper, about 25-30% of the total body length. The flippers have many functions, among which our consideration is maneuverability. Despite their colossal

size, Humpback whales are the most acrobatic among baleen whales (Leatherwood *et al.*, 1982). They are so agile that they can even perform somersaults underwater (Jurasz and Jurasz, 1979).

The maneuverability of the Humpback whale is related to its feeding habits. They devour a large amount of herring, capelin, and plankton (Dolphin, 1988), and the preying requires special techniques like sharp turning, diving, and surfacing. One feeding method is called "Lunge Feeding." The whale swims toward the prey from below at an angle 30° to 90°. Another technique is known as the "Inside Loop," where the whale moves away from the prey with its flippers abducted and protracted (Edel and Winn, 1978), then rolls 180 ° and makes a U-turn, and lunges toward its prey (Hain *et al.*, 1982). This turn is compact, requiring 1.5-2 body lengths. Yet another method is called "bubbling," where the whale swims upwards and exhales from its blowhole, a column of bubbles is produced. This results in a bubble net that encircles and concentrates the prey that can be consumed by the whale as it swims upward through the center of the net (Hain *et al.*, 1982). Reducing the turning radius could potentially increase the effectiveness of this feeding method as it could encircle and concentrate more prey within the bubble net. The turn radius of the whale can be represented by equation 1.2 from Weihs (1981).

$$R_t = \frac{m_v}{5.5 A_f C_L \rho_{s.w} \sin\phi} \tag{1.2}$$

The turning radius being inversely proportional to the coefficient of lift, it can be easily deduced that a sharp turn is possible when the lift coefficient is higher. It can be concluded that to enable the feeding requirement of this animal, the flipper has to maintain a tremendous amount of lift.

Nature has bestowed this species with a modification called tubercle on its flipper that helps in their preying and thus in their survival. Tubercles are a kind of protrusions on the leading edge of the flipper, as seen in Figure 1.13. The morphology and placement of leading-edge tubercles suggest that they function as enhanced lift devices to control flow over the flipper and maintain lift at high AOA (Fish and Battle, 1995). Tubercles can also help to increase the maximum lift coefficient with a nominal increase in drag (Miklosovic *et al.*, 2004). These characteristics of the tubercles help the Humpback whale significantly in its turning maneuver while feeding (Edel and Winn, 1978). The performance enhancement brought about by the tubercle is due to the creation of stream-wise vortices, which in turn re-energizes the boundary layer through enhanced

Figure 1.13: Humpback whale with tubercles on the flipper (Photo © Lisa Winchester)

momentum exchange (Edel and Winn, 1978; Fish and Battle, 1995). Some studies suggest the working mechanism of tubercles to be similar to vortex generating devices like tiny delta wings and strakes (Fish *et al.*, 2008). Another possible mechanism is eliminating of span-wise stall progression by compartmentalizing the flow (Miklosovic *et al.*, 2007).

1.5 Potential Application of Tubercles

The capability of tubercles to enhance lift with nominal drag penalties offers it great potential to be incorporated into many man-made systems. A significant characteristic of a man-made vehicle is that it is inflexible, just like much of the body of a Humpback whale. Thus, a good understanding of its locomotion mechanism can help incorporate it into the design of various aerodynamic and hydrodynamic surfaces.

UAVs are the most relevant among the potential applications for tubercles. These tiny aircraft operate at low velocities and, therefore, at low Reynolds number ranging from 15 000 to 500 000. Their wings typically operate in laminar and transitional regimes, and this causes the boundary layer to separate at low AOA (Mueller and DeLaurier, 2003). During the takeoff and landing, when flight speed is low, to ensure enough lift, high AOA is required, causing flow separation. The use of slats or flaps normally solves

this. Due to the excessive weight of the actuators associated, the incorporation of such devices could outweigh the potential benefits. In this scenario, tubercles could reduce the minimum stall speed without contributing significantly to the drag and weight of the vehicle.

When a helicopter requires high forward speed and carries a large load, it operates at high AOA (Tang and Dowell, 1992), increasing the chances of dynamic stall. Stall causes blade torsion, vibrations, and loads on control systems. Tubercles could increase the stall angle and smoothen the stall and could be advantageous to increase the service life, reduce fatigue, and improve safety.

STOL aircraft is used when there is a short runway length. Runway length being a function of minimum stall speed, it is desirable to reduce this parameter (Khurana, 2009). If the tubercle could increase the stall angle, the minimum stall speed would also be reduced and thus help in reducing the runway length. The softer stall characteristics of the tubercle also could be advantageous in improving the safety margin. sually

Wind turbines operate in low-speed wind conditions, and therefore it is desirable to generate maximum lift before the blade stalls so that more power can be generated (Johnson and Berg, 2008). Incorporating tubercles could extend the operational envelope of the blade by reducing the likelihood of stall. Studies by Howle (2009) indicated the potential of tubercles to substantially increase the electric power output leading to increased annual energy production. Incorporating tubercles on turbine blades could also reduce tonal noise, which is advantageous to the community. Tubercles could also potentially minimize stall on the blade, thereby reducing the fatigue rate and maintenance cost. Though large wind turbines operate at Re as large as 6×10^6 similar to the flow situation for Humpback whale , tubercles also have the potential to be used on small-scale wind turbines. Toronto-based Whalepower has already made attempts to integrate tubercle into wind turbines. The prototype of the blade, as seen in Figure 1.14 has shown the capability to capture more energy from lower speed winds.

Turning surfaces used by underwater vehicles called hydroplanes have a great deal of similarity with Humpback whale flippers (Edel and Winn, 1978). Tubercles could delay stall and increase maximum lift coefficient and thus enhance the maneuverability and stealth of these vehicles. Stream-wise vortices created by the tubercles could eliminate vortex shedding or reduce its coherence (Bearman and Owen, 1998). Propeller blades can also be incorporated with tubercles for the same purpose. Hydrofoils and propellers create characteristic tones (McAlpine *et al.*, 1999), thus identifiable by enemy hydrophones. Tubercle could be used to reduce this tonal noise.

Figure 1.14: Tubercle integrated wind turbine from *Whalepower*

Figure 1.15: Surfboard fin with tubercles

It is possible to use tubercles on hydrofoils such as keels and centerboards. Counterbalancing force to side forces are provided by hydrofoils on a yacht (Anderson, 2008), and therefore an increase in the lift would be advantageous. Increased lift means more force being exerted on the sail, thus allowing the yacht to move faster. Moreover, the size of the keel or centerboard could be reduced upon the addition of tubercles to obtain the same results as an unmodified hydrofoil. As the sail on a yacht requires to operate at high AOA, incorporating leading-edge tubercles (LET) could enhance its performance. Tubercles, when combined on surfboard fins, as shown in Figure 1.15 can provide greater lift and better control at lower speeds than conventional fins.

Application of tubercles is limited to certain devices. It can also be applied to car spoilers to facilitate high AOA operation. Increasing the stall angle can help in generating higher downforce, thus adding traction to the rear wheels and improving the acceleration aspect of the automobile.

Tubercles can also find their application on blades of various fluid handling devices like fans and compressors. A compressor achieves the highest performance near the stall, where the highest amount of work is obtained from each stage of the compressor

Figure 1.16: Fan integrated with leading edge tubercle

(Lord *et al.*, 2000). Tubercles could increase the operating margin of the compressor by increasing the maximum lift and reducing the severity of the stall.Regarding a fan, integrating tubercles, as seen in Figure 1.16 could help in circulating more air with increased efficiency and half the number of leaves. Increased efficiency of such fans can reduce the energy cost of dairy fans (Ontario-Power-Authority, 2010).

1.6 Motivation for Current Studies

From the discussion in Section 1.2.4, the limitation of the existing VAWT design is evident. It would be beneficial to control the flow on the VAWT blade so that the extent of the dynamic stall is reduced, which would enhance the power production and life span of the turbine.

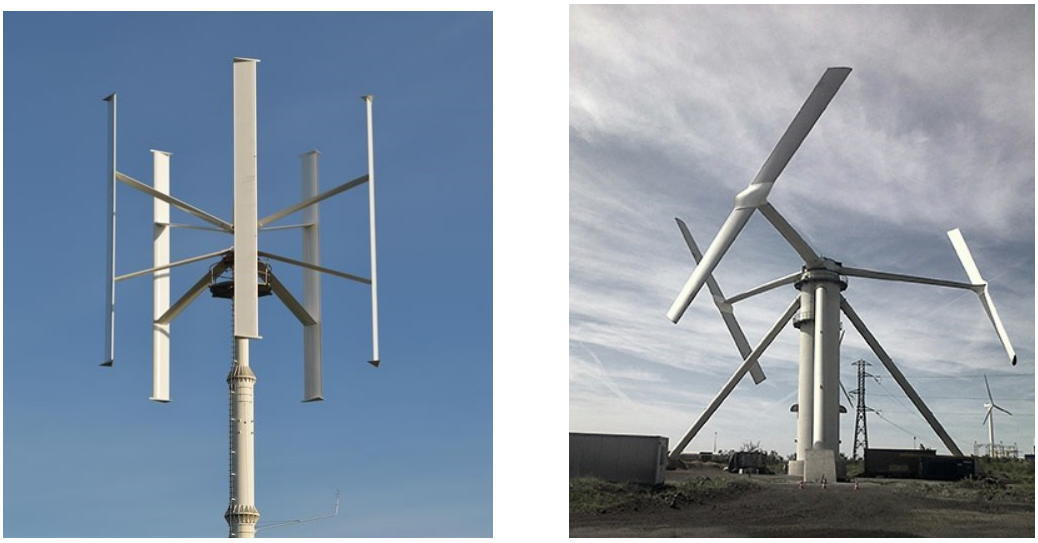

(a) Unswept blades (©Cision) **(b)** Swept blades (Sievert, 2015)

Figure 1.17: VAWT with different blade types

This study focuses on the possibility of incorporating Humpback whale-inspired tuber-

cles on VAWT blades to improve its performance. Figure 1.17 shows two commonly seen VAWT systems - one with unswept and another with swept blades. A comparison of the aerodynamic performance of these blades with blades incorporated with tubercles can give an insight into the possibility of application of leading-edge tubercles (LET) as flow control devices on VAWT blades.

1.7 Scope of the Study

This study investigates the potential of Humpback whale-inspired LET in enhancing the performance of VAWT blade. The main focus is on the aerodynamic effect of tubercles on the VAWT blade. The first part of the study is about finding the more functional aerodynamic surface planform on which the tubercle incorporation can result in significant performance enhancement. Effect of tubercles on rectangular and swept planform blades is studied. Based on the result, the effect of tubercle on the stall, hysteresis and LSB characteristics of static unswept/rectangular blade has been studied. Further, the effect of tubercle shape and geometrical parameters on the steady-state aerodynamic characteristics of the blade is analyzed. The VAWT blade being operational in unsteady flow conditions, the effect of tubercle on the unsteady aerodynamic characteristic is also studied. Though the study focuses on VAWT blade, it can also be extended to other aerodynamic devices.

1.8 Organization of the Thesis

This thesis is divided into five chapters. Chapter 1 gives an introduction to the topic of interest. Chapter 2 is dedicated to the literature survey. The chapter discusses various methods of flow control on VAWT blades and introduces tubercle as a potential flow control device for VAWT. Further, various researches pertaining to tubercle are discussed. The flow mechanism of LET, the effect of tubercle parameters on its performance, and the effect of LET on various devices based on earlier studies are described in the chapter.

The experimental procedures and results are discussed in four chapters. Chapter 3 is dedicated to the comparative study of swept and unswept blades. Details of the experimental blade models, their design, and fabrication procedures are discussed in the first section. The experimental setup and procedures are described in detail. The result of

the study is presented at the end of the chapter.

Chapter 4 is devoted to the detailed study on the effect of leading edge tubercles on static blade of rectangular planform. The details of model fabrication and experimental procedures of force and pressure measurement is described in the initial sections. The effect of tubercles on phenomena like LSB, stall, and hysteresis are discussed elaborately in the chapter.

The effect of tubercle parameters and shape on the steady-state aerodynamic characteristics of the blade is described in Chapter 5. The experimental setup and model fabrication method is described in the beginning of the chapter. The effect of tubercles parameter and shape on the static forces and moment of the blade is explained at the end of the chapter.

The effect of tubercles on dynamic blade is compiled in Chapter 6. The experimental setup and procedure is described in the beginning of the chapter. The effect of tubercles, their parameter and shape on the unsteady flow characteristics of the blades is detailed at the end of the chapter.

The conclusions of this study are presented in Chapter 7. A refined description of the effect of tubercles on VAWT blades is done here. Suggestions for future work are also provided here, based on the gaps identified during the research.

CHAPTER 2

LITERATURE SURVEY

This chapter is dedicated to familiarizing some of the earlier studies related to flow control on VAWTs and discussing earlier studies associated with the tubercles. The first section discusses some of the studies pertaining to flow control on VAWT blades. In the subsequent sections, earlier studies on tubercles and the performance enhancement brought about by them are discussed. Most of these are comparative studies involving baseline and tubercle models. The effect of varying Reynolds numbers on the performance of tubercles is discussed. Further, the flow patterns and flow control mechanisms associated with the tubercles are also outlined. Subsequently, the studies related to the application of tubercles on wind turbines are compiled. In the final section, the gap in the previous researches is identified and the objectives of the current study are laid out.

.

2.1 Dynamic Stall Control on VAWT

Dynamic stall control studies on various airfoils under incompressible conditions using different flow control techniques, has been extensively conducted. Some of the devices used in the flow control of pitch oscillating airfoils can also be for dynamic stall control on wind turbine blades.

Many effective methods for mitigating the dynamic stall of VAWTs have been proposed, which include both passive and active devices. Plasma actuators (Greenblatt *et al.*, 2015; Greenblatt and Lautman, 2015), leading-edge slot blowing (Sasson and Greenblatt, 2011), synthetic jet (Velasco *et al.*, 2017; Yen and Ahmed, 2013), and oscillating flap (Xiao *et al.*, 2013) are some of the active devices proposed to be used on VAWT blades to control dynamic stall. These active flow control techniques can delay or eliminate dynamic stall by adjusting the control parameters. However, complex control mechanisms, algorithms, and additional energy are needed for operation. On the contrary, passive flow control approaches are cheap, easier to implement, and require no extra energy, making them ideal for the application on VAWT. Choudhry *et al.* (2016) suggested using various passive devices like vortex generators, elevated wires,

and cavities exclusively for the application of wind turbine blades. The vortex generator and elevated wire function by creating counter-rotating vortices in streamwise and spanwise orientations, respectively. The cavity act as a reservoir for the reverse flow during pitch up. The experimental study suggested that these devices enhanced flow mixing and be used for dynamic stall control on wind turbine blades. Some other passive flow control approaches are vortex generator Gurney flap, leading-edge slat, and microtab (Zhu *et al.*, 2018). Ismail and Vijayaraghavan (2015) introduced a flow control approach for Darrieus Vertical AxisWind Turbine (DVAWT), combining a Gurney flap and an inward dimple, which was optimally placed on one side of a NACA 0015 airfoil near the trailing edge. Based on the lift and drag coefficients of the modified airfoil obtained numerically, the authors calculated the tangential force for one blade at different azimuth angles. The average tangential force increased by 40% for oscillating airfoil undergoing light dynamic stall. Sobhani *et al.* (2017) conducted a numerical study on the effect of a dimple on the blade, and the efficiency was improved by 18%. A numerical comparison of three passive devices- an airfoil with a leading-edge slat, airfoil with a non-circular gap, and a flow-deflecting airfoil showed that only the airfoil with a leading-edge slat could increase the power coefficients at all TSRs.

The dynamic stall phenomena on VAWTs is complex as the flow separation occurs on both sides of the blade. However, many of the above- mentioned passive devices are effective only on the side on which they are installed, and two-side installation might lead to performance degradation. For example, a three- bladed DVAWT of H-type with Gurney flaps on either side of the blades had a lower increment in power than the one with flaps only on the outboard side (Zhu *et al.*, 2018). A turbulence promoter of symmetrical shape is an effective method to reduce the intensity of DSV on either side of the VAWT blade(Fukudome *et al.*, 2004; Frunzulica *et al.*, 2014). Fukudome *et al.* (2004) used a tripping rod mounted on a symmetrical airfoil to act as a turbulence promoter. The experimental and numerical results showed that the tripping rod delayed the flow separation of the NACA 0018 airfoil at high AOAs. Frunzulica *et al.* (2014) further numerically simulated the effect of tripping rod on suppressing the flow separation on dynamic NACA 0012 airfoil. They found that the tripping rod could delay DSV formation and weaken its intensity. Experimental studies by Choudhry *et al.* (2016) also vouched for the capability of an off-surface rod in suppressing DSV formation on a pitching airfoil and suggested it to be a possible flow control device for VAWTs. The relevance of tubercles as passive flow control device arises due to their capability to function as turbulence promoters. Incorporating them on the leading edge can be useful as they can affect flow on both sides of the blade due to their symmetric nature.

2.2 Research into Tubercles

The focus on tubercles as a flow control device started after Fish and Battle (1995) reported that tubercles on the leading edge of Humpback whale flippers functioned as lift enhancement devices. These modifications on the whale flipper controlled the flow over the flipper and helped in maintaining lift at high angles, without stall. The flipper morphology is similar to that of wind turbine blade and aircraft wing. The cross-section at the mid-span of the flipper closely resembles NACA $63_4 - 021$ airfoil, as seen in Figure 2.1. This similarity between the flipper and various aerodynamic surfaces motivated researchers to study the effect of tubercles on various devices like an airfoil, wing, wind turbine blades, fans, etc. Many researchers have concluded that tubercles can improve performance on many aerodynamic devices. Some of the commonly seen improvements are delayed flow separation, increment in the maximum attainable lift, and stall angle. At the same time, some researchers have observed that tubercles could deteriorate performance in the pre- stall regime in certain circumstances. Even in such situations, tubercle proved advantageous, providing a softer stall and improved post-stall lift.

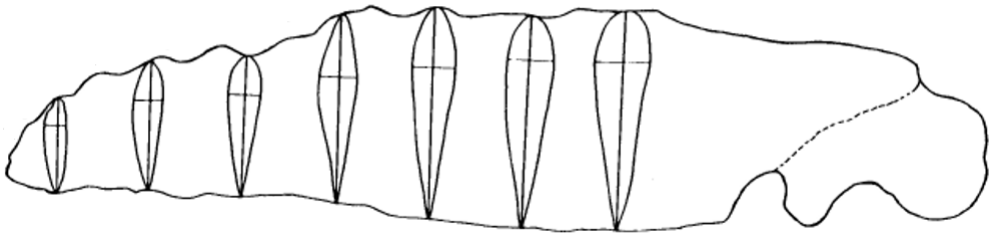

Figure 2.1: Flipper planform showing cross-section at different spanwise locations(Fish and Battle, 1995)

2.3 Performance Enhancement by Tubercles

A panel simulation method was developed that could be applied to a wing at a high Reynolds number, to evaluate the forces acting on the wing and study the influence of LET on the wing performance (Watts and Fish, 2001). Once the lift and drag were compared for wing with tubercles and without tubercles for AOA of 10°, a 4.8% increase in maximum lift, 10.9% decrease in drag, and 17.6% increase in lift to drag ratio (L/D) was observed for the wing with LET. The LET had no effect at an AOA of 0°,but

enhanced the performance at modest AOA. The researchers also observed that the tubercles were instrumental in delaying stall, thereby increasing the operational envelope of the control surface. The tubercles caused a variation in the span-wise lift distribution due to the presence of troughs. There was a substantial reduction in the strength wing tip vortex even while attaining enhanced lift (Watts and Fish, 2001). The tip vortex was no longer the contribution of the whole wing but primarily a response from the nearest tubercle.

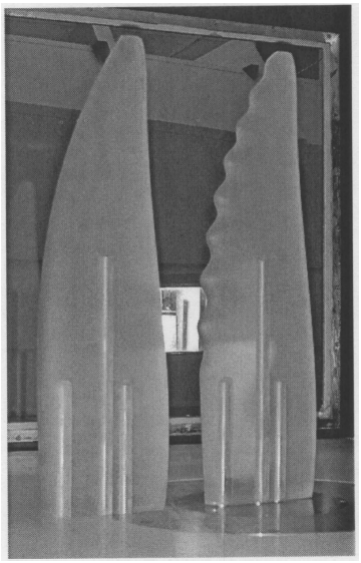

Figure 2.2: Humpback whale flipper models with and without tubercles (Miklosovic *et al.*, 2004, 2007)

Miklosovic *et al.* (2004) conducted an experimental study on an ideal scale Humpback whale flipper (with NACA 0020 cross-section) with and without tubercle, as shown in Figure 2.2, for Reynolds number ranging from 5.05×10^5 to 5.2×10^5. They reported that the stall angle improved by 40% compared to the model without tubercle. Further, a reduction in total drag at the post-stall region and a 6% increase in the maximum lift were also seen for the tubercle model. At all angles except $10^0 < \alpha < 12^0$, the L/D ratio for the tubercle model was greater than its baseline.

However, in a study at a Reynolds number of 2.5×10^5 for a 2D airfoil with LET of amplitude and spacing comparable to that of a Humpback whale, Stein and Murray (2005) suggested that there was a decrement in lift and increment in drag for an airfoil with tubercle when compared to its baseline. Stein and Murray (2005) also tried to compare the functioning of tubercle with vortex generators by using them both on the model. The lift performance was slightly improved with a nominal drag increase when vortex generators were used. It was thereby concluded that LET and vortex generators

do not function the same way.

Disadvantages of tubercle incorporated on NACA 63-021 at Reynolds number 1.8×10^5 in the pre-stall regime were also reported by Johari *et al.* (2007). It was experimentally found that the maximum lift coefficient and the stall angle were lower for the tubercle airfoil compared to the baseline. However, in the post-stall region, the tubercles seem to have a significant advantage as it increases the lift coefficient up to 50% higher than the baseline. Based on these findings, it was proposed that LET could be used as an active flow control device deployed only during stall conditions Johari *et al.* (2007). This concept of selectively using tubercles was previously mentioned in a patent by Watts and Fish (2006).

In another study comparing the performance of rudder with tubercle and unmodified baseline in water, at Reynolds number ranging from 2×10^5 to 8.8×10^5, it was reported that both models had a similar lift and drag performance in the pre-stall region (Weber *et al.*, 2010). It was also noted that the tubercle rudder stalled earlier than the baseline, thereby reducing the maximum lift coefficient and also increasing drag at those AOA. The reduced performance was attributed to the early onset of cavitation that was caused by the tubercles. Johari *et al.* (2007) reported of observing gradual stall for tubercle airfoils with water as the working fluid. In the post-stall region, lift enhancement was evident for the tubercle model. As the AOA was increased further, the difference in performance gradually diminished. He also suggested that there existed a critical Reynolds number, beyond which the maximum lift to drag ratio decreases for tubercle airfoil. The critical Reynolds number in this study was 7.1×10^5. The L/D ratio for the tubercle airfoil improved when compared to the baseline for Reynolds numbers lesser than the critical Reynolds number.

2.3.1 Effect of Tubercle Configuration

Geometrical parameters of the tubercle, like wavelength and amplitude, can significantly affect its performance. In a study conducted by Johari *et al.* (2007) using models of various wavelengths and amplitudes, the tubercle models had a lower lift than the baseline stall angle. In the post-stall region the tubercle model had as much as 50% higher lift than the baseline. The model with highest amplitude had an almost constant lift in the post stall region. The wavelength of the tubercles and the leading-edge radius had only a minor influence on the force and moment coefficients. The wavelength of the tubercle also had a minor effect on flow separation.

However, Weber *et al.* (2010) suggested wavelength could have a detrimental influence on the performance. They observed that at higher Reynolds number, rudders with tubercles of smaller wavelength were more prone to cavitation effects that deteriorated the performance. Hansen (2012) investigated the effect of amplitude and wavelength of tubercle and concluded that an optimal value existed for these parameters and represented it in terms of amplitude to wavelength ratio (A/W), for which the aerodynamic performance improved.

In addition to these two parameters, a key parameter called thickness to chord ratio determines the shape of an aerodynamic surface incorporated with LET. When tubercles are a mere addition to the leading edge, the thickness to chord ratio varies along the span, as found in Johari *et al.* (2007). Here, except for a small region in the leading edge, rest of the surface remain unchanged. Another method is to keep the thickness to chord ratio constant, as done by Hansen (2012) which creates ridges and valleys on the upper and lower surface of the airfoil. These undulations become more prominent when the amplitude to wavelength ratio of the tubercle is higher.

2.3.2 Reynolds Number Effects

When considering the significance of three-dimensional effects, it is crucial to consider the Reynolds number. Tubercles aided lift enhancement where the Reynolds number was between 5×10^5 and 6.31×10^5 (Miklosovic *et al.*, 2004, 2007; Carreira Pedro and Kobayashi, 2008). All these studies were done on the Humpback whale flipper model, implying that tubercles were only successful when applied to this geometry. The performance of the rudder deteriorated at Reynolds number 2×10^5 to 8.8×10^5 when tubercles were incorporated (Weber *et al.*, 2010). The worsening of performance was attributed to increased cavitation that caused comparatively lower pressure in the trough region (Weber *et al.*, 2010). A study of tubercles on Humpback whale flipper model at low Reynolds number in the range 0.4×10^5 to 1.2×10^5 by Stanway (2008) showed a reduction in maximum lift coefficient except for $Re = 1.2 \times 10^5$. The deterioration in performance was a strong indication that the Reynolds number is a significant parameter.

Studies by Miklosovic *et al.* (2007) also suggested that tubercles provided three dimensional benefits on semi-span models, but not on full-span models. It was seen that performance improved when tubercles were incorporated into the whale flipper model but caused performance degradation for a rectangular full-span planform (Miklosovic

et al., 2007). However, it has to be noted that the Reynolds number for the full span model was almost half of that was for the flipper model. This variation in Reynolds number could have also influenced the difference in performance.

2.3.3 Flow Patterns

Using numerical analysis,Watts and Fish (2001) obtained the pressure distribution and streamlines over airfoils with LET. The pressure behind the peak regions was higher than behind the trough regions. The streamlines were closer to each other in trough region indicating that the flow in this region had a higher velocity than in the peak region. This flow pattern obtained in the numerical analysis was consistent with the hypothesis made by Fish and Battle (1995). The limitation of the study was that an inviscid numerical model was used, and therefore boundary layer development and streamwise vorticity could not be captured.

Fish and Lauder (2006) accounted for the viscous effect using unsteady RANS formulation for the same airfoil used by Watts and Fish (2001). They observed that the flow separation was delayed behind the peak regions of the tubercle almost to the trailing edge. Behind the trough regions of the tubercles, streamlines indicate large streamwise vortices. This numerical study suggested that the flow accelerated behind the peak region of the tubercle, which was inconsistent with previous studies by Fish and Battle (1995) and Watts and Fish (2001).

Johari *et al.* (2007), using tuft visualization experiments, suggested that flow remains attached behind the tubercle peaks, whereas flow separation starts in the trough region, an observation consistent with results obtained by (Fish and Lauder, 2006). It was also reported that for tubercle integrated airfoils, flow separation started at lower AOAs. But the flow was attached over tubercle peaks for post-stall angles when flow separation happened for the baseline airfoil.

Custodio (2007) conducted dye visualization experiments for the same airfoil used by Johari *et al.* (2007). At Reynolds numbers close to 11.5×10^5 counter-rotating vortices in streamwise direction were generated in the trough regions of the tubercles. The flow is separated behind the trough but remained attached behind the tubercle peaks at post-stall. These findings agreed with those of Fish and Lauder (2006) and Johari *et al.* (2007).

Carreira Pedro and Kobayashi (2008) computationally established the presence of streamwise vortices at Reynolds number of 5.0×10^5. Simulation of flow around an idealized

model of Humpback whale flipper at AOA of 15°showed that tubercle changed the vorticity along the span. There was a reduction in tip vortex strength and an increase in vorticity downstream of the tubercles when compared to a baseline. There was also a reduction in the spanwise extent of leading-edge separation at the tip region.

Using PIV, Stanway (2008) found the velocity components in a plane parallel to the upper surface of an airfoil from the surface normal vorticity. Pair of counter-rotating vortices were seen downstream of each tubercle whose strength increased with AOA in the AOA range between 10°and 18°. Measurement of surface normal vorticity was based on a condition, that separation had taken place, so that one component of streamwise vortices would be perpendicular to the plane of measurement. The increased separation would have resulted in the increase in vorticity. Nevertheless,the existence of streamwise vortices was clear from the experiment.

2.4 Flow Control Mechanism of Tubercles

There are many proposed theories and explanations on how the tubercle enhances the performance of an aerodynamic surface, some of which are mentioned below:

- non-uniform flow separation (Van Nierop *et al.*, 2008; Carreira Pedro and Kobayashi, 2008; Johari *et al.*, 2007; Fish and Lauder, 2006)
- altering surface pressure distribution (Van Nierop *et al.*, 2008)
- enhance momentum exchange in the boundary layer (Carreira Pedro and Kobayashi, 2008; Johari *et al.*, 2007; Miklosovic *et al.*, 2004; Fish and Battle, 1995)
- compartmentalization of flow and tip stall reduction (Miklosovic *et al.*, 2007; Carreira Pedro and Kobayashi, 2008; Stein and Murray, 2005; Fish *et al.*, 2008)

Most of the time, the effects mentioned above are mutually inclusive, and many benefits can come about simultaneously. However, there is only little explanation on why LET fails to enhance performance in certain circumstances.

Custodio (2007) suggested that the local sweep angle of the tubercles affected the spanwise flow, resulting in the formation of vortices in the streamwise direction. Additional momentum exchange occured in the boundary layer due to the vortices, which keeps the flow attached over the surface for a longer time, thus enhancing the maximum attainable lift (Miklosovic *et al.*, 2004; Fish and Battle, 1995). Therefore, a similarity between tubercles and tab-like vortex generators was drawn.

Stein and Murray (2005) experimentally opposed the idea of similarity between tubercles and vortex generators. He suggested that tubercles were more analogous to wing fences for their similarity in preventing spanwise stall progression. Preventing stall progression along the span of a semi-span wing could overcompensate the premature flow separation in the trough regions of the tubercle (Miklosovic *et al.*, 2007). Tubercles create streamwise vortices and cause a physical barrier to flow, limiting the separation to the wing tip (Carreira Pedro and Kobayashi, 2008). Induced drag associated with semi-span wing can be decreased by reducing the strength of tip vortices, which can be achieved by tubercles by compartmentalizing the flow (Watts and Fish, 2001). Thus, it would be logical to state that the contradictory nature of tubercle (inferior performance in the case of conventional rectangular wings by superior performance for swept wing) is due to the three-dimensional effects (Miklosovic *et al.*, 2007; Stein and Murray, 2005). Another factor to be noted is that experiments pertaining to full-span models were done for low Reynolds numbers. The apparent effect of the Reynolds number makes it difficult to precisely determine whether momentum increase in the boundary layer or prevention of stall progression along the span is the dominant mechanism of flow control by tubercles.

Van Nierop *et al.* (2008) agreed with Stein and Murray (2005) to claim that tubercles could not function as vortex generators, given the fact that the amplitude and wavelength of tubercles are much higher than the thickness of boundary layer. Instead, it was suggested that since the airfoils at peak and trough sections have different thickness to chord ratio, the pressure gradient is higher for the trough from where the flow separation initiates. The non-uniform downwash component further delays the flow separation behind the tubercle peak, which causes a decrease in the effective AOA. The gradual onset of the global stall was described in terms of local stall angles being different along the span. It was thereby suggested to view stall angle as the point where lift decreases with AOA rather than when there is an abrupt loss of lift. Since the flow is still attached along the peak section, the airfoils with tubercles would only be partially stalled at this newly defined stall angle.

A different explanation for improved lift by tubercles, as given by Custodio (2007) using the method of images, was that the counter-rotating vortices move towards the troughs, as shown in Figure 2.3. The low pressure that is seen on the suction surface behind the trough regions is thought to be a result o the subsequent amalgamation of moving vortices. This results in an increase in lift as seen on a delta wing(Custodio, 2007).

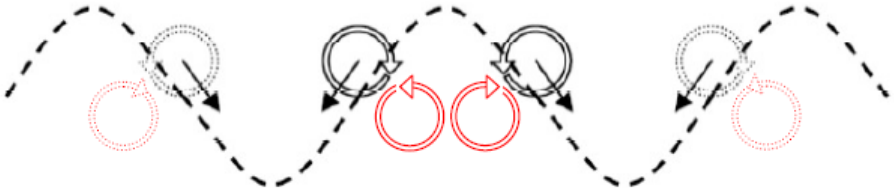

Figure 2.3: Schematic showing movement of vortices towards troughs as predicted using the method of images (Custodio, 2007).

2.5 Tubercles on Swept Wings

Bolzon *et al.* (2014, 2016, 2017) reported a series of experiments on a finite span NACA 0021 with a taper ratio of 0.4 and sweep of 35° at $Re = 2.25 \times 10^5$. Two wings were used in the study- one reference wing with no tubercles and a modified wing with tubercles in the streamwise direction. The researchers combined direct force measurements with wake velocity surveys to explore the relative changes in the induced and profile drag coefficients across the span. At pre-stall up to 8° it was found that tubercles reduced wing lift by 4-6% and profile drag by 7-9.5%, thereby increasing the lift to drag ratio by 2-6% (Bolzon *et al.*, 2017). The important finding in this study was that tubercles spatially modulated the profile drag across the span, reducing drag coefficients behind the peaks where attached flow occurs and increasing the drag coefficient behind the troughs where flow separation occurs. The opposite was found for induced drag- maxima occurred behind the peaks, and minima occurred behind the troughs. Results also revealed that tubercles reduced the drag coefficient near the wing tip at zero AOA but caused little to no change in the pre-stall AOAs (Bolzon *et al.*, 2017). The effect of single tubercle at the tip of swept wing was also studied (Bolzon *et al.*, 2016). In general, the change in the profile, induced, and total drag primarily occurred across the wing span with very little contribution from the wing tip region. LSB was found on both tubercle and baseline wing. However, the strength of tip vortices reduced by about 2.2% under the influence of the tubercle. Bolzon *et al.* (2016) also noted that sweeping a wing could cause asymmetry in the strengths of the vortices produced by a tubercle.

Wei *et al.* (2018) compared the hydrodynamic effect of spanwise varying tubercles aligned in the streamwise direction with those aligned normal to the leading edge on a swept and tapered wing at $Re = 2.2 \times 10^5$. It was seen that the difference in the alignment of tubercles did not significantly change the surface flow features. The tubercle aligned normal to leading-edge gave a higher lift to drag ratios at AOA between 2°and 7°. Flow visualization studies showed that each tubercle produces a pattern of

nodes and saddles in the surface flow that is significantly tilted due to the presence of the sweep angle. It was also noted that the streamwise vortex structures also disrupt the formation of large-scale recirculating regions that are associated with wing root stall.

2.6 Tubercle Application on Wind Turbine

Many early researches suggested tubercles to be highly beneficial for devices operating in low Reynolds numbers. It paved the path to incorporating tubercles on various devices like wind turbines, tidal turbines, aircraft wings, fans, compressor blades, etc.. The following section discusses some previous studies on tubercle incorporated wind turbine blades.

A numerical study on the effects of tubercles on the Annual Power Production (AEP) of HAWT was carried out by changing the parameters of tubercles (Abate and Mavris, 2017). It was seen that some cases of tubercle turbine outperformed the baseline in terms of shaft torque and AEP. It was also seen that tubercle configurations of low amplitude and high wavelength gave promising results in terms of AEP.

Huang *et al.* (2015) experimentally investigated the effect of LET on the aerodynamic performance of small-scale HAWT. The static 3D blade analysis suggested that change in wavelength and amplitude of the tubercle could affect the aerodynamic performance. The tests on rotating turbine models indicated that tubercles would successfully delay stall and thus improve turbine performance at low TSR.

The contribution of LET on the fatigue life of HAWT blades was numerically studied by Ng *et al.* (2017). On a turbine blade with tubercles occupying 20% to 95% span of the leading-edge, flapwise root-bending moment was found to be 6% lower than the unmodified configuration. The torsional moment was 17% lower due to the reduction in leading-edge suction along tubercle crests, further away from the elastic axis. In terms of tubercle positioning, having tubercles close to the blade tip enables performance enhancement during episodes of stall from large tip deflections and has significant contributions to root-bending moment due to a larger moment arm and higher relative flow speed. On the other hand, positioning tubercles close to the blade root may also be favoured as this region is prone to stall at low speeds while little effect on fatigue responses. Lin *et al.* (2016) conducted a numerical performance analysis of VAWT with a sinusoidal trailing edge. The modified blade achieved 0.38%-2.31% increase in maximum thrust than the baseline blade, depending on the wavelength and amplitude. A

blade configuration of higher wavelength and amplitude gave as much as 16% increase in the power coefficient.

The performance of VAWT is substantially affected by the dynamic stall phenomenon induced by variations of AOA of rotating blades, especially at low TSRs. Wang and Zhuang (2017) numerically investigated performance improvement of H-type VAWT using tubercles on blade leading edge. Compared to the standard blade, the tubercle blade increased the power generation at low TSR and the wind energy extraction capability at optimal TSR. The maximum enhancement in power coefficient was found to be approximately 18.7% at TSR of 2. Flow separation was also significantly controlled in the azimuth angle range of 75°to 160°, thus suppressing the dynamic stall in this region.

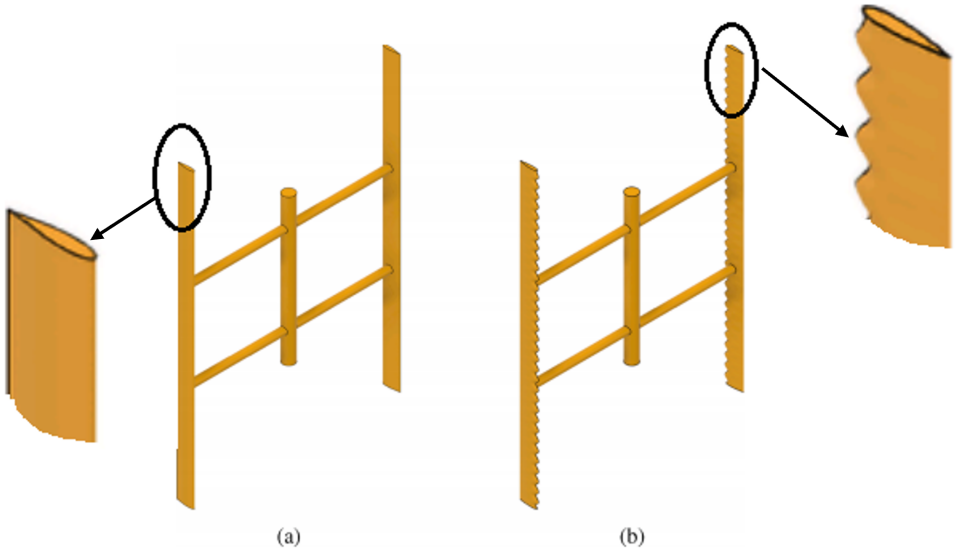

Figure 2.4: Baseline and tubercle VAWT (Sridhar *et al.*, 2022)

Sridhar *et al.* (2022) conducted a numerical study on the aerodynamic perspective of implementing tubercles of H-type VAWT, as shown in Figure 2.4. Performance and flow characteristics of four tubercle configurations were compared to a baseline. Results indicated that incorporation of tubercles on the leading edge of the blade generated counter-rotating vortices which helped in flow separation delay and dynamic stall control. Between azimuth angles 70°and 160°, flow separated only in trough regions of the blade and remained attached along the peak regions, thus providing more torque and power. In addition to the enhancements in the flow characteristics, a 28% increase in power coefficient was observed for the optimal configuration at the optimal tip speed ratio. Additionally, a 14% increase in maximum lift generated by the blade was observed. Preliminary aeroacoustics analysis revealed a 12% decrease in tonal noise along the

blade tip and a 20% decrease at the mid-plane of the turbine. It was suggested that tubercles effectively control dynamic stall, reduce noise emissions, and increase the power output in VAWTs.

2.7 Research Gap and Objectives of the Thesis

Most of the studies related to LET on swept wings are comparisons between a baseline and tubercle model swept at a particular angle. There has been no study to identify their effect with varying sweep angles to understand if LET function similarly on swept and unswept aerodynamic surfaces. Aerodynamic phenomena of LSB, stall, and hysteresis on conventional airfoils and wings are well documented. But experimental research on the effect of LET on these phenomena is limited. Though many experimental works are done on static airfoils and wings incorporated with LET, their effect on dynamic surfaces is not well explored. A systematic study of LET on VAWT blades can touch upon some of these gaps in the earlier research.

This work is aimed at studying the effect of LET on the aerodynamic performance of VAWT blades. The main objectives are:

1. Comparative study on the effect of LET on unswept and swept blades at a low chord-based Reynolds number of 10^5.
2. Experimental study on the effect of LET on LSB, stall, and hysteresis characteristics of the static unswept blade at Reynolds number ranging from 2.5×10^5 to 6.5×10^5 .
3. Experimental study on the effect of LET, their geometrical parameters and shape on the steady and unsteady aerodynamic characteristics of the blade.

CHAPTER 3

COMPARISON OF SWEPT AND UNSWEPT BLADES

This thesis is broadly divided into two parts, namely static and dynamic, based on whether the experimental data is obtained for a stationary or a moving blade model. The first part of the thesis is a comparative study on the effect of tubercles on static unswept and swept blades. The first objective was to select the better performing tubercle orientation on the swept blade from the two possible ones. Further, the effect of such tubercles on blades swept at different angles (10°, 20°, and 30°) are studied by comparing with respective baseline models and to unswept blade. This chapter discusses the methods involved in designing and fabricating the different experimental models and describes the experimental facilities used in the study. The aerodynamic performance of the static blades is analyzed in terms of the aerodynamic coefficient of lift, drag and L/D ratio. The objective of the study is to analyze if tubercles can be advantageous on both swept and unswept blades to the same extent.

3.1 Airfoil Selection

The first step is to select a suitable airfoil for the blade. The NACA 0021 was chosen because it is an uncambered or symmetric airfoil closely resembling the cross-section of the Humpback whale flipper. This profile has a maximum thickness of 21% of the chord length located at 30% of the chord. The instruments required for the experiments can easily be accommodated within the model due to the uncambered nature and high airfoil thickness. Thick symmetrical airfoils are also preferred on VAWT blades. Another significant reason to select a symmetrical airfoil was the availability of detailed literature.

3.2 Design and Fabrication of Experimental models

Different materials, design strategies, and manufacturing methods are used to fabricate the blade models to suit the requirements in each part of the experiment. Blade models made of wood are used in the comparative study of unswept and swept blades study. A

detailed description of the blade geometry, design strategy, and manufacturing method used in the comparison study of blades is done in this section.

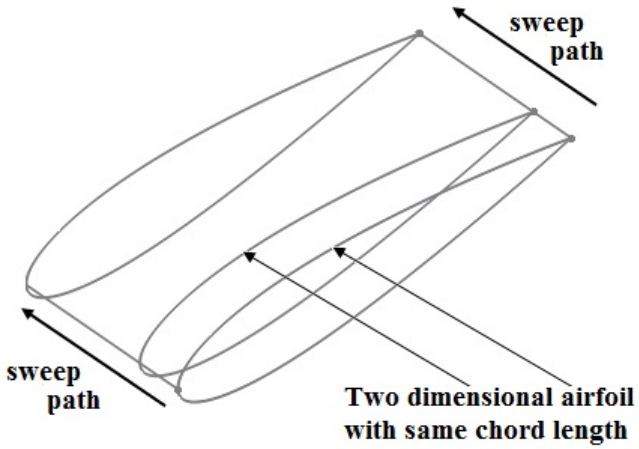

Figure 3.1: Schematic showing the process involved in the modeling of baseline blades

Comparative studies of unswept and swept blades consist of baseline models and tubercle models swept at 0° (unswept), 10°, 20°, and 30°. Though multiple models are used, the modeling procedure remains relatively similar. All blades are designed using the computer-aided design (CAD) software, " Solid Works." Baseline models are designed by drawing the two-dimensional NACA 0021 airfoil along the span of the blade, as shown in Figure 3.1. The two-dimensional airfoil profile is drawn along guide paths which are straight lines at the leading and trailing edge, creating a series of equal-length airfoils along the span. The resulting model has a straight leading edge. However, the guide paths for tubercle models are sinusoidal curve at the leading edge and straight line at the trailing edge creating a series of NACA 0021 airfoils of varying chord lengths along the span of the blade as shown in Figure 3.2.

While using the above approach for modeling a tubercle blade, a wavy surface is created on the upper and lower side due to the variable chord length along the span, as shown in Figure 3.3. Some earlier experimental (Hansen *et al.*, 2011) and numerical studies (Skillen *et al.*, 2015) have used this approach for modeling. This undulated surface or ridge-type formation on the surfaces becomes very prominent when the amplitude of the guiding sinusoidal curve (tubercle amplitude) is higher. As will be discussed later in Chapter 5, the experimental models for dynamic studies would be fabricated in a modular manner such that there is a common trailing edge section and replaceable leading edges of different tubercle amplitudes. A wavy surface would adversely affect the compatibility between the common trailing edge and different leading edges. Keeping this in mind a design approach is devised so that the blade surface is not wavy.

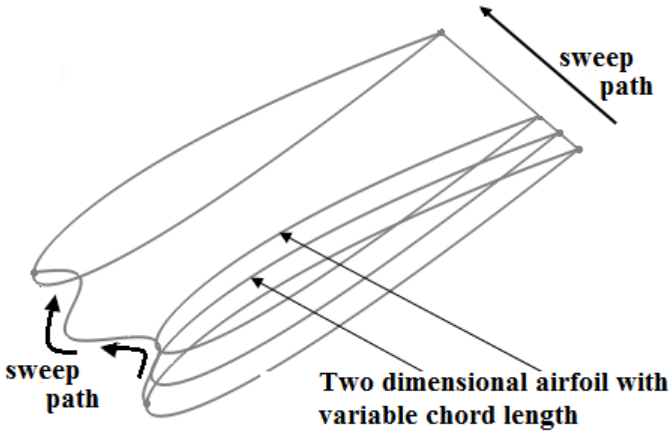

Figure 3.2: Schematic showing the process involved in the modeling of tubercled blades

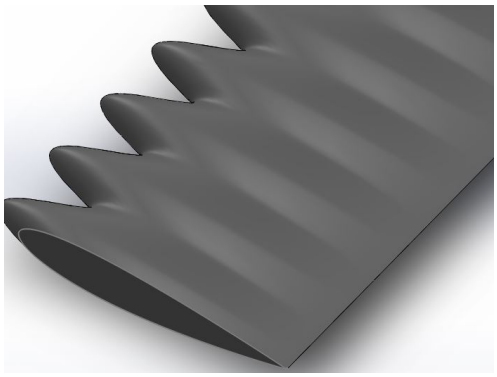

Figure 3.3: Wavy surface of the model

The problem of the wavy surface is resolved by replacing the trailing section (70% of the chord) of the tubercle models with the trailing section of the baseline model, as shown in Figure 3.4. This approach ensures that the wavy surface is limited only to the leading edge, and the rest of the surface is smooth and non-wavy as the baseline models. In short, tubercle models are created by retrofitting baseline models with tubercled leading edges, similar to those used by Johari *et al.* (2007) and Custodio *et al.* (2015).

The same approach discussed before is used in modeling the swept blades. The guide curves are inclined at different angles (10°, 20°, and 30°) for different swept blades. Since models required for swept blade studies have a small dimension and do not require any pressure ports, the most economical method was to manufacture them out of light wood using computerized numerical control (CNC) machining process.

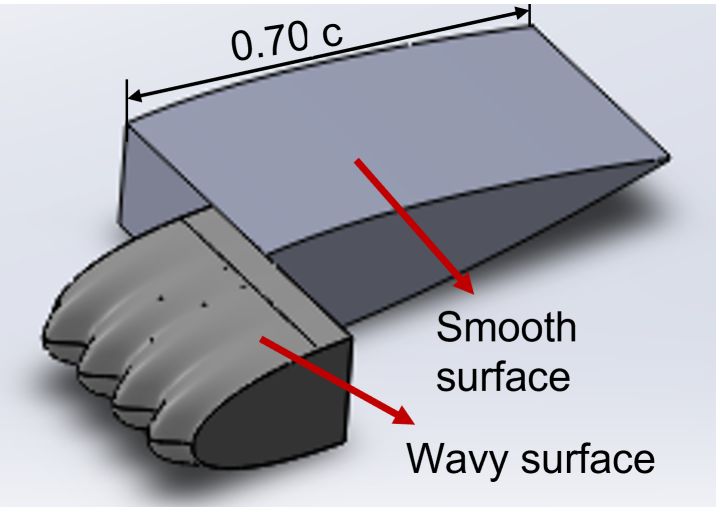

Figure 3.4: Wavy tubercle leading section combined with smooth trailing section

3.2.1 Models for Tubercle Alignment Study

There are two possible ways to arrange tubercles on a swept blade, unlike in the case of a regular rectangular (unswept) blade. One configuration (configuration A) of the swept tubercle blade can be obtained by placing the tubercles in the stream-wise direction. Another design (configuration B) is to place the tubercles perpendicular to the blade leading edge. Figure 3.5 shows the two configurations of tubercle on 30°swept blade. A preliminary study is conducted to choose the configuration with better aerodynamic performance. The tubercle configuration with superior aerodynamic characteristics is chosen for the rest of the survey involving swept blades. The study tubercle orientation on swept blades is a topic for detailed research involving many swept blades and different Reynolds numbers. However, due to financial constraints, a preliminary study using only one set of swept blades is conducted prior to studying the effects of tubercle on different swept blades. For configuration B of tubercles, the angle γ, formed between the tubercles and the flow direction is same as the blade sweep angle, λ. The blade of highest sweep angle (30°), is chosen for the tubercle orientation study, so that there is a significant γ, which enables a clear comparison between configurations A and B. The configuration with better aerodynamic performance ratio shall be used on other swept blades involved in this study. The wavelength and amplitude of tubercles are 21% and 6% of the chord length, respectively.

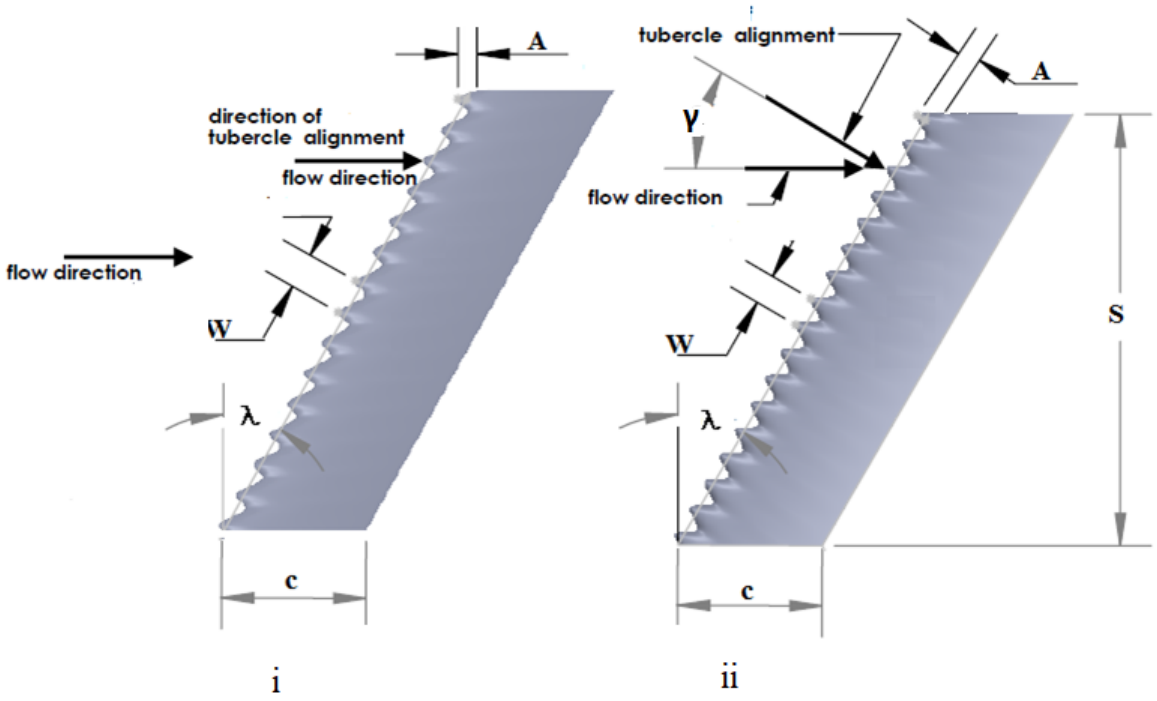

Figure 3.5: Schematic of the swept blades used for tubercle alignment study- (i) configuration A (ii) configuration B

Table 3.1: Geometrical parameters of the swept blades used in tubercle alignment study

S.No	**Label**	λ	**A**	**W**	**c**	**S**	γ
-	-	(°)	(mm)	(mm)	(mm)	(mm)	(°)
i	30 tubercle-A	30°	9	31	150	450	0
ii	30 tubercle-B	30°	9	31	150	450	30

3.2.2 Unswept and Swept Blades

The swept blade study used the better-performing tubercle orientation (configuration A). A set of blades swept at different angles (0°, 10°, 20°, 30°) and tubercles aligned in the stream-wise direction together with their baseline models are used. The wavelength and amplitude of tubercles are 21% and 6% of the chord, respectively, the same as used in the tubercle configuration study. The swept blades are made from wood through the CNC machining process. Figure 3.6 shows the various baseline and tubercle swept blades used, and the geometrical parameters of these blades are listed in Table 3.2. The wood models have a surface roughness of 25 microns.

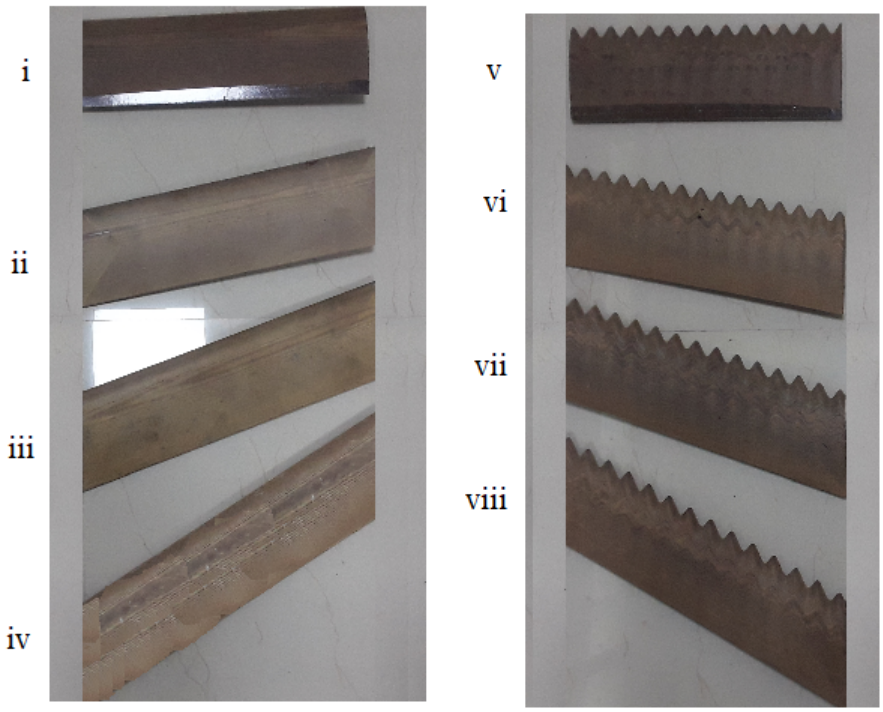

Figure 3.6: Experimental models made of wood for swept blade studies (i-iv) Baseline models (v-viii) Tubercle models

Table 3.2: Geometrical parameters of unswept and swept blade used in the comparative study

S. No	**Label**	λ	**A**	**W**	**c**	**s**
-	-	(°)	(mm)	(mm)	(mm)	(mm)
i	0 baseline	0	-	-	150	450
ii	10 baseline	10	-	-	150	450
iii	20 baseline	20	-	-	150	450
iv	30 baseline	30	-	-	150	450
v	0 tubercle	0	9	31	150	450
vi	10 tubercle	10	9	31	150	450
vii	20 tubercle	20	9	31	150	450
viii	30 tubercle	30	9	31	150	450

3.3 Wind Tunnel

The experimental study has been split between two low speed, open-circuit wind tunnel (OCWT) facilities. The first part of the study, which is a comparison between swept and unswept blades is conducted at at the low speed wind tunnel facility in the Department of Mechanical Engineering at the National Institute of Technology, Karnataka, which has been designated as Tunnel I in this thesis and is depicted in Figure 3.7. The rest of the study, pertaining to unswept blades, as will be discussed in the next chapters, is

conducted at the OCWT in the Department of Aerospace Science Engineering at the Indian Institute of Science, Bangalore, Karnataka, which is named Tunnel II. The basic structure and functioning of both tunnels are similar except for the size. Tunnel I has a test section of 1m x1m, whereas Tunnel II is more extensive with a test section size of 4.25 m x 2.75 m. A brief description of the structure and components of an OCWT is as follows.

Figure 3.7: OCWT at NITK, Surthakal (Tunnel I)

Table 3.3: Specifications of the Tunnel I

Parameters	Value
Shape of test section	Square
Length of test section	$2m$
Test section area	$1.0m^2$
Contraction ratio	$9:1$
No of driving fans	1
Maximum RPM	715
Power of driving motor	$11kW$
Max. flow velocity	$30m/s$
Turbulence intensity	0.5%

An open circuit wind tunnel primarily consists of an inlet section, test section, diffuser, and fan drive. The inlet section consists of a region of contraction with a rectangular inlet opening converging to a test section. The shape of the test section is square for

Tunnel I and octagonal for Tunnel II. A honeycomb structure is provided at the beginning of the inlet to streamline the air entering the tunnels. The test section of Tunnel I has a 1mx1m cross-section and is almost 2 meters long. The test section of Tunnel 11 is 4.25 m x 2.75 m and is about 6 m long. The horizontal and vertical sides of the octagon are parallel, whereas the other sides are provided divergence to compensate for the boundary layer growth. Large plexiglass windows are provided on the vertical sides of the test section in both tunnels to ensure the visibility of the experimental model.

The test section is followed by a diffuser that opens to the surrounding. The square test section of Tunnel I changes to a circular cross-section, gradually increasing the diameter. The octagonal section of the Tunnel II changes to a rectangular one gradually with semi-circular sides at the outlet end. Tunnel II has an additional component - a deflector located at about 10 inches behind the diffuser outlet. It guides the air at the outlet of the diffuser in the vertical direction. It also acts as a barrier and reduces interference of outside atmospheric flow. Towards the end of the diffuser, a fan drive is located. Tunnel I has one fan connected to the motor, whereas Tunnel II has two fans working side by side and directly connected by means of shaft extension and flexible coupling to two wound rotor induction motors.

3.4 Force Balance

The most frequently used method for obtaining force measurements on a model is to use a balance system (Barlow *et al.*, 1999). Since strain gauges have been used satisfactorily and are relatively simple to set up and calibrate, this was the chosen method for lift, drag, and pitching moment measurement. The study involving static swept blades was conducted in Tunnel I and used a box-type external force balance.

External balances are placed outside the experimental model, mostly fixed to the wind tunnel floor, and are usually large. A box-type three-component balance from Sunshine Measurements is used in Tunnel I to measure aerodynamic forces of lift and drag on the swept blade models. The balance specifications typically depend on the loads to be measured, the size of the models, and the wind tunnel. The maximum loads taken by the external balance used in the study are lift of 5 kg, drag of 2 kg, and pitching moment of 5 kg-m. This balance is fitted beneath the test section. The strut of the balance extends to inside the test section on which the experimental models are mounted. The force balance is built with a scale and mechanism to manually change the AOA. The force balance is connected to a data acquisition and signal conditioning instrument, which is

Figure 3.8: Box-type external force balance loaded used a pulley system for calibration-check procedure

further connected to a computer. Operating this balance is relatively easy being factory calibrated. It is enough to zero the device, and appropriate offsets can be automatically determined. However, a calibration-check procedure has to be done by the work-back load method, which involves loading the balance with known weights using a pulley system and checking the corresponding output load. Figure 3.8 shows the external balance in the check calibration process.

3.4.1 Brief Theory on Force Measurement

The cross-section of an aerodynamic surface is usually an airfoil, as shown in Figure 3.9. When air flows over the airfoil, it exerts stress $\vec{f}$ on each point of the body, whose normal and tangential components are pressure, p (due to pressure difference between lower and upper surface), and the shear stress, τ (due to the viscosity of air) respectively. The stress distribution $\vec{f}$, integrated over the surface, gives a resultant force $\vec{R}$ and a moment M about a certain chosen reference point. The resultant force $\vec{R}$ can be reconstituted into perpendicular components along any axes chosen. Two particularly used axes are the freestream axis and the body axis.

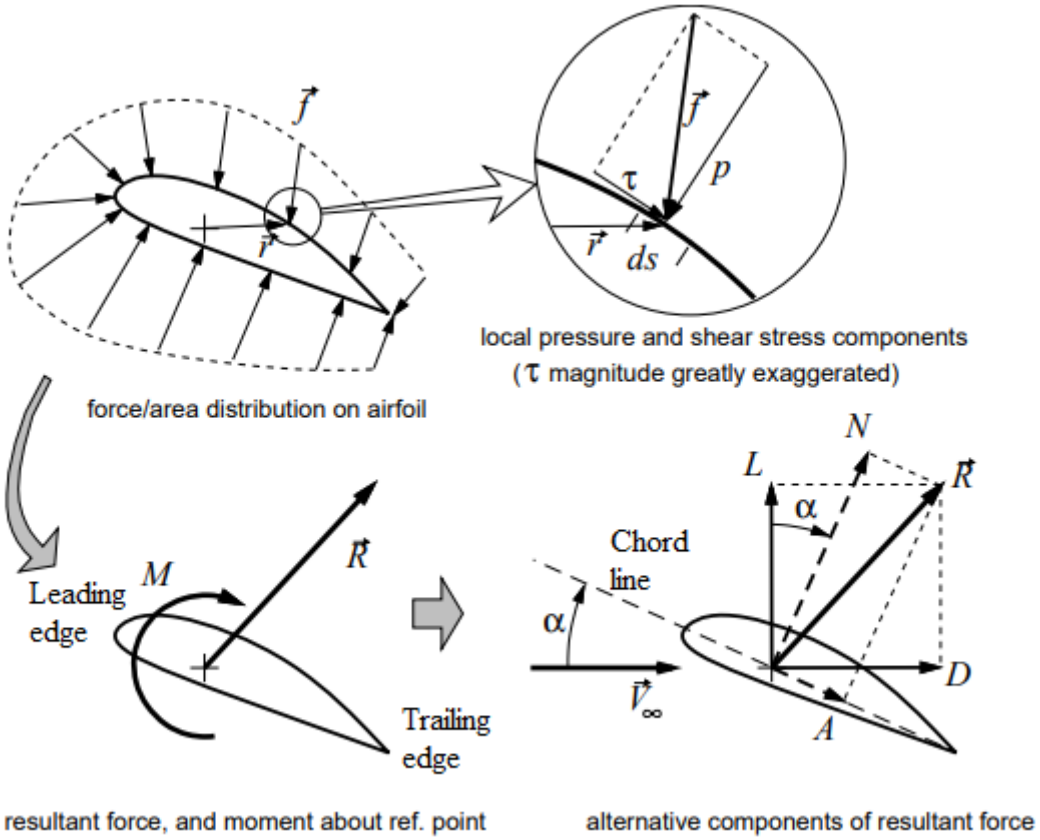

Figure 3.9: Airfoil terminology and forces acting on airfoil (Lozano, 2008)

Body Axis: The components of $\vec{R}$ are axial force, A (along the airfoil chord line), and normal force, N (perpendicular to the chord line).
Freestream Axis: The components of $\vec{R}$ are drag, D (along the freestream flow direction) and lift, L (perpendicular to the freestream flow direction).

Force balance fitted inside the experimental model registers the forces in the body axis. Lift and drag forces are obtained by axis transformation of AOA (α), using equation 3.1 and 3.2. Further, the coefficients of lift, drag and moment are obtained from equations 3.3,3.4, and 3.5.

$$L = Ncos\alpha - Asin\alpha \tag{3.1}$$

$$D = Nsin\alpha + Acos\alpha \tag{3.2}$$

$$C_L = \frac{L}{0.5\rho V_\infty^2 A_b} \tag{3.3}$$

$$C_D = \frac{D}{0.5\rho V_\infty^2 A_b} \tag{3.4}$$

$$C_M = \frac{M}{0.5\rho V_\infty^2 A_w c} \tag{3.5}$$

3.5 Model Mounting and Data Acquisition

The mounting procedure of the experimental models differs according to the wind tunnel. This section details the mounting process of the experimental model on the force balance within the wind tunnel. The tunnel I has a circular cutout on the test section floor where the external box type force balance is fixed. The circular plate on the force balance completely seals off the circular opening on the tunnel floor once it is fixed to the floor. Figure 3.10 shows the force balance mounted beneath the test section of Tunnel I. The experimental model is rigidly fixed to the strut of the force balance using base plates fitted on the experimental model.

Figure 3.10: Three component balance fitted to test section of Tunnel I

Data acquisition and processing instruments are available together with the external

balance and can be easily operated. Measurements are conducted in wind-off and wind-on mode, and aerodynamic forces acting on the model are obtained by subtracting the wind-off forces from wind-on forces.

3.5.1 Uncertainty Analysis

A variable is expressed with its uncertainty as:

$$X_i = X_i(measured) + \delta X_i \tag{3.6}$$

The uncertainty in the experimental result Q obtained from the experiment can be found by applying the Root Sum Square (RSS) method with respect to the contributing variables as:

$$\delta Q_{X_i} = \frac{\partial Q_{X_i}}{\partial X_i} \delta X_i \tag{3.7}$$

When there is more than one contributing variable to the measured quantity, the total uncertainty is measured as follows:

$$\delta Q_{X_i} = \sqrt{\sum_{i=1}^{N} \left(\frac{\partial Q_{X_i}}{\partial X_i} \delta X_i \right)^2} \tag{3.8}$$

The uncertainty in lift coefficient derived with respect to lift force, flow velocity, planform area of the experimental model can be expressed as:

$$\delta C_L = \sqrt{\left(\frac{\delta L}{0.5 \rho V_{\infty A_p}^2} \right)^2 + \left(\frac{-4L\delta U}{\rho V_\infty^3 A_p} \right)^2 + \left(\frac{-2L\delta \rho}{\rho^2 V_\infty^2 A_p} \right)^2 + \left(\frac{-2L\delta A_p}{\rho V_\infty^2 A_p^2} \right)^2} \tag{3.9}$$

The percentage error in lift coefficient is expressed as

$$\varepsilon_{C_L} = \left(1 - \frac{C_L + \delta C_L}{C_L} \right) 100 \tag{3.10}$$

The same procedure is followed to obtain the error in other aerodynamic coefficients of drag and moment, except that for moment, additional error associated with chord length also would be considered.

Significant sources of error were the uncertainties in the AOA, free stream velocity, and measured forces. The angular uncertainty in the pitching scale was estimated to be ± 0.5 degrees. Uncertainty in force measurement was calculated by loading the force balance

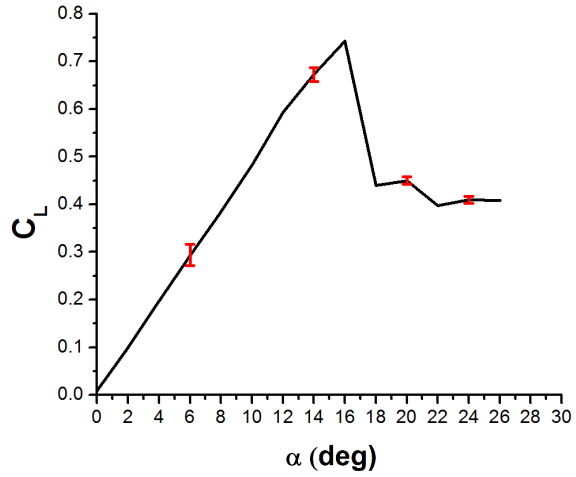

(a) Lift coefficient

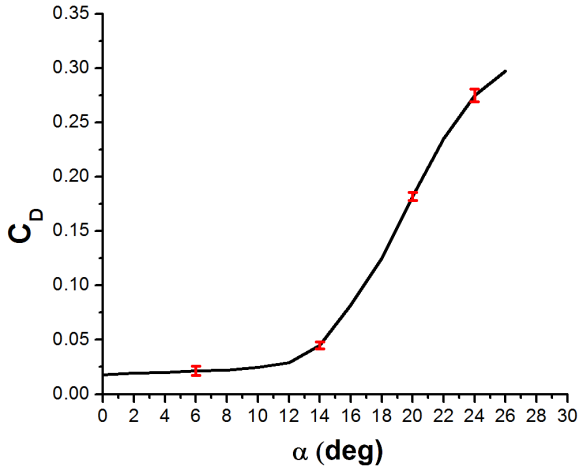

(b) Drag coefficient

Figure 3.11: Force coefficients of unswept baseline (0 baseline) blade with error bars at AOA of 6°, 14°,20°and 24°

with different known weights. The balance used in force measurement has a maximum uncertainty of 1.5N. The error due to the machining process resulted in a difference of $\pm 0.2mm$ in the chord and span of the blade models. Uncertainty in free stream velocity was about $\pm 1m/s$. The percentage error in lift coefficient is 7.9%, 2.09%, 1.9%, and 1.8% at an AOA of 6°, 14°, 20°, and 24°, respectively. The percentage error in drag coefficient is 18%, 9%, 3%, and 2.1% for the same angles of attack. The trend is that the error percentage decreases with increasing loads. Maximum uncertainties for lift and drag occur at low angles of attack where the forces are very low . The error bars for lift and drag coefficients with increasing AOA for baseline unswept blade (0 baseline) are depicted in Figure 3.11a and Figure 3.11b, respectively.

3.6 Results and Discussion

This section discusses the result obtained from the comparison of steady-state force analysis of the swept and unswept blades. It includes the preliminary studies on swept and unswept blades at a low Reynolds number of 10^5. The main objective is to compare the performance of the tubercles on blades swept at different angles by comparing them to the respective baselines and to unswept blades. This enables us to understand the extent of performance enhancement brought about by tubercles on swept and unswept blades.

3.6.1 Validation

A comparison of results obtained in this study with an earlier study would be a good approach for validation.Hansen (2012) conducted experiments for NACA 0021 finite airfoil, which is identical to the '0 baseline blade' in this study at $Re_c = 1.2 \times 10^5$. Figure 3.12 depicts the lift graph obtained for '0 baseline' blade at $Re_c = 10^5$ from this study and identical finite airfoil at $Re_c = 1.2 \times 10^5$ from earlier study done by Hansen (2012). The stall angle for half span NACA-0021 airfoil at was 15° with $C_{L_{max}}$ close to 0.9 as shown in Figure 3.12b. After the stall, the C_L fell to about 0.4. The stall angle, $C_{L_{max}}$, and post-stall C_L in this study are 16°, 0.76 and 0.37 respectively. Though there is a variation in $C_{L_{max}}$ and C_L in post-stall region, the general trend is quite similar in both studies. The difference in these coefficients between this study and the one conducted by Hansen (2012) was due to the fact the model mounting was done vertically with one tip fixed to the tunnel leaving only one free tip. However, in this study, model mounting was done horizontal, leaving both tips free to produce tip vortices and therefore decreasing the lift. Hansen (2012) used tripped model, whereas no tripping was done in this study, which lead to the difference in slope of lift curve in both cases.

3.6.2 Effect of Sweep on Blades

Before finding out the effect of tubercles on swept blades, it would be beneficial to briefly discuss how sweep affects the aerodynamic performance of unmodified blades at a low Re of 10^5. The aerodynamic characteristics of s baseline blades are depicted in Figure 3.13. The slope of the lift curve goes on decreasing with an increase in sweep angle, as seen in Figure 3.13a. The maximum lift coefficient, $C_{L_{max}}$, also decreases

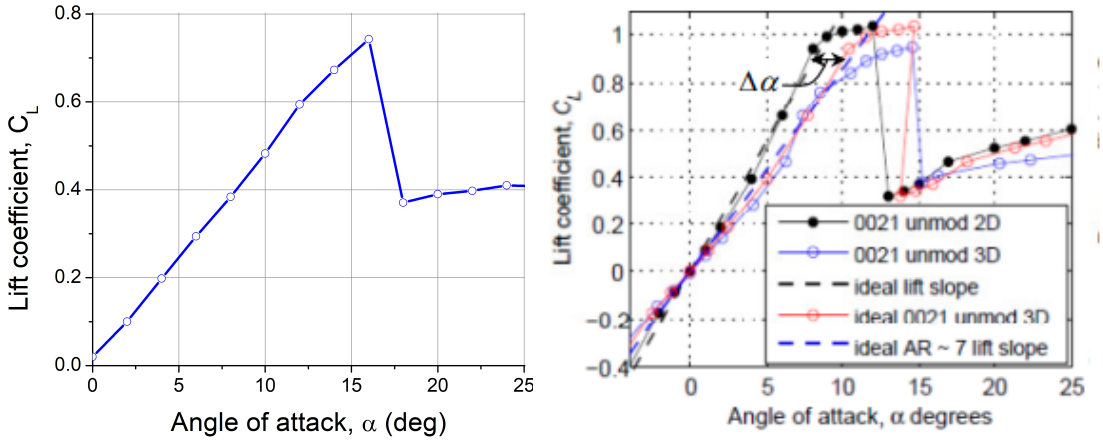

(a) **(b)**

Figure 3.12: Lift coefficient comparison of baseline blade of (a) the current study with that of that of (b) Hansen (2012)

with an increase in sweep angle. The drag of the unswept blade (0 baseline) is the lowest in the pre-stall and increases with an increase in AOA. It has the highest drag in the post-stall region. Among the swept blades, the blade swept at 10° (10 baseline) has the least drag in the post-stall region and the drag increases with an increase in sweep angle in the post-stall region.

The combined effect of lift and drag is reflected in the lift to drag ratio, L/D which is an indicator of aerodynamic efficiency (Anderson Jr, 2010) of the finite airfoil section. The L/D for the baseline blades are depicted in Figure 3.13c. The highest L/D is for the unswept blade (0 baseline) and as the sweep of the blade increases, L/D goes on decreasing. When the blade is swept at 30°, the L/D ratio is less than half of that for the unswept blade. The nature of the L/D curve is affected by the decrease in lift and increase in drag for the swept blades. Thus, it can be concluded that at a low Reynolds number, unswept and low sweep blades are more aerodynamically efficient than the blades of high sweep. The L/D value drops from 22 at AOA of 12° to 4 at AOA of 18° for the unswept blade, whereas for a high sweep blade (30 baseline) it is dropped from 10 at AOA of 12° to 5 at AOA of 18°. The high sweep blades have relatively smaller changes in the post-stall L/D compared to the abrupt fall in L/D of the low sweep blades.

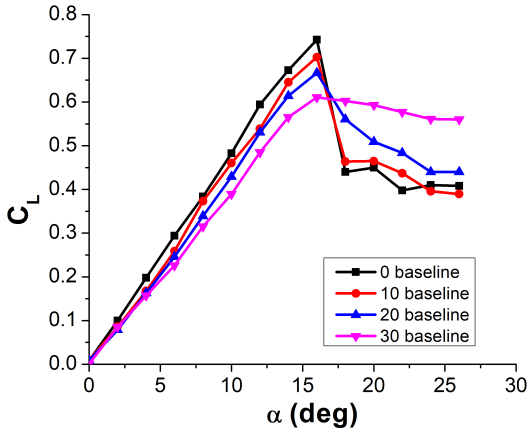

(a) Lift coefficient

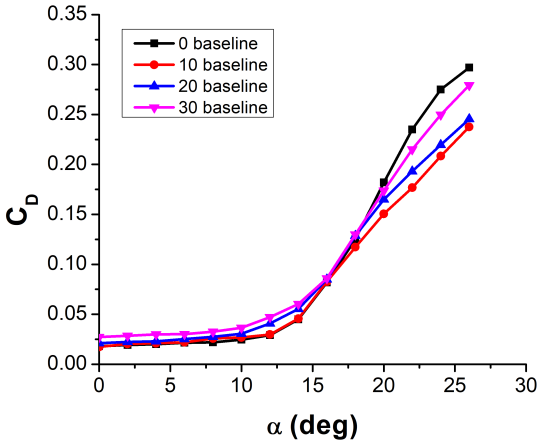

(b) Drag coefficient

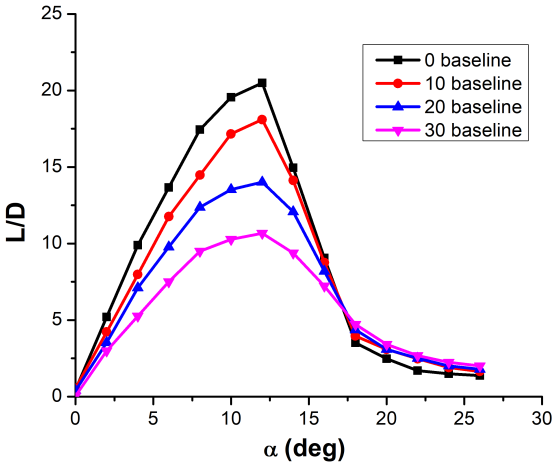

(c) Lift to drag ratio

Figure 3.13: Aerodynamic characteristics of baseline swept blades at $Re_c = 10^5$

3.6.3 Effect of Tubercle Orientation

One of the objectives of this study is to identify the effect of tubercles swept blades at a low Reynolds number. Since the tubercles on the swept blade could have two orientations, as explained in Section 3.2.1, it is necessary to choose the configuration with better aerodynamic performance. The angle formed by the tubercle with the incoming flow is the same as the swept angle. Therefore the blade swept at an angle of 30°, the highest swept blade in the group, was chosen for this part of the study to clearly differentiate the tubercle orientation and its effect.

The aerodynamic characteristics of the 30° blades of different tubercle orientations are presented in Figure 3.14. From the lift characteristics shown in Figure 3.14a, configu-

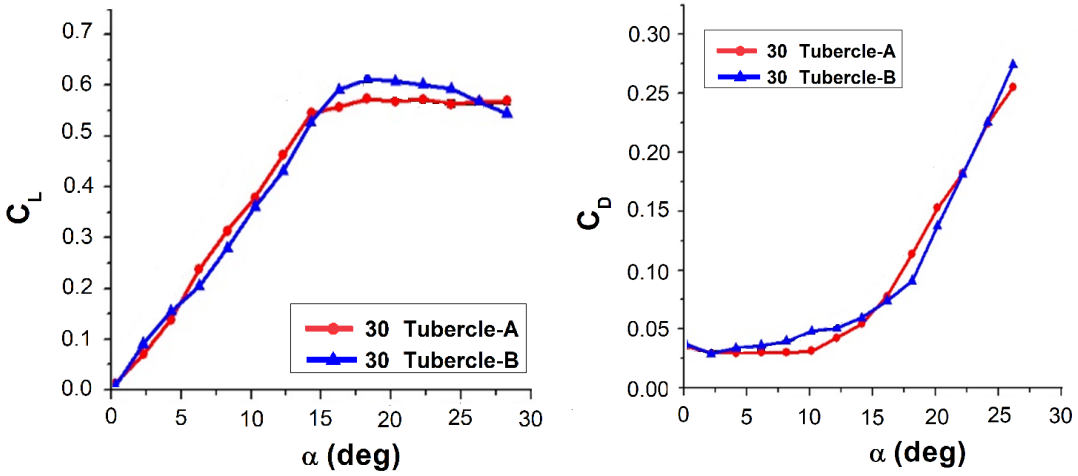

(a) Lift coefficient

(b) Drag coefficient

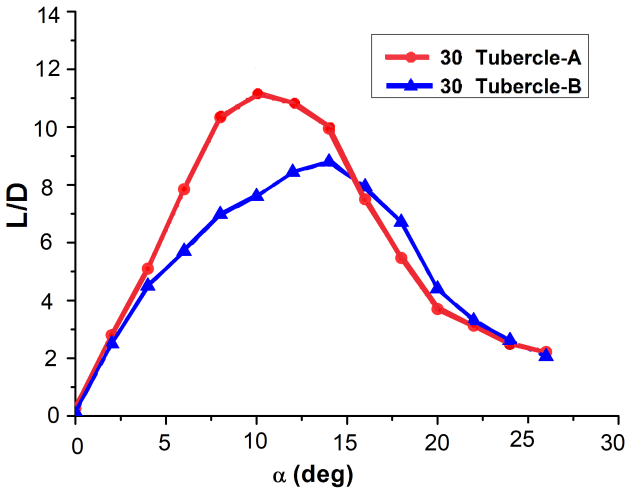

(c) Lift to drag ratio

Figure 3.14: Aerodynamic characteristics of 30° blades with distinct tubercle orientation at $Re_c = 10^5$

ration A (tubercles oriented along the flow direction) have a higher lift in the pre-stall region than configuration B (tubercles arranged normal to the leading edge) and vice-versa in the post-stall region. The drag characteristics presented in Figure 3.14b shows that the blade configuration B has a higher drag in the pre-stall region. In the immediate post-stall region configuration-B has lower drag than A but eventually becomes higher than A as AOA further increases.

A conclusion on the aerodynamic efficiency of both tubercle configurations cannot be drawn from the lift and drag curves, but can be done from the L/D ratio. The L/D curve for 30° blades with two different orientation of tubercles is shown in Figure 3.14c. The blade of configuration B has a low aerodynamic efficiency than configuration A in

the pre-stall region and slightly higher efficiency in the post-stall region. In general, the blade of tubercle configuration A has a higher aerodynamic efficiency. Hence, the configuration-A of tubercles would be used on all swept blades in further study. The 30 Tubercle-A blade will now be named 30 Tubercle as this will be the only configuration used further.

3.6.4 Effect of Tubercles on Swept Blades

As we have now understood that the tubercles aligned along the airflow have more aerodynamic efficiency than those aligned normal to the leading edge, we shall now analyze the effect of such tubercles on blades swept at different angles by comparing them with corresponding baselines.

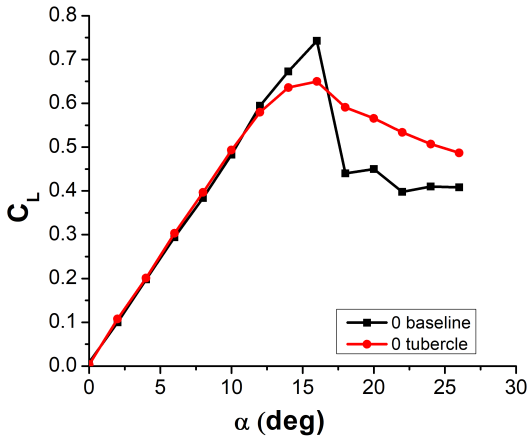

(a) 0 degree blades

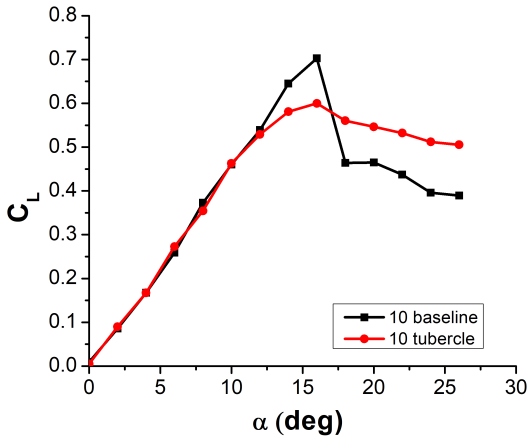

(b) 10 degree blades

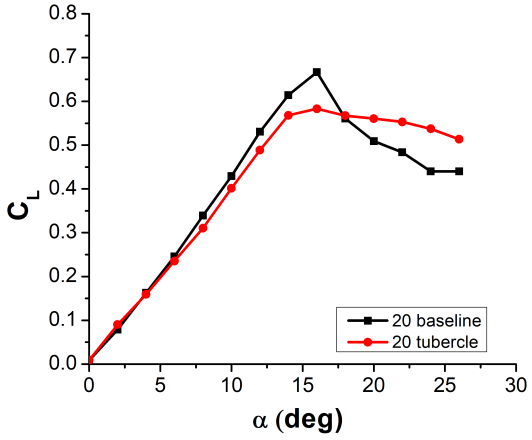

(c) 20 degree blades

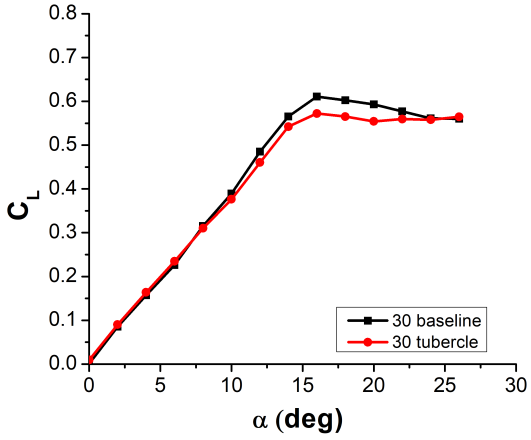

(d) 30 degree blades

Figure 3.15: Lift characteristics of swept blades at $Re_c = 10^5$

Figure 4.2 depicts the lift characteristics of 0°, 10°, 20° and 30° blades. From the lift characteristic of unswept blades (0 baseline and 0 tubercle) shown in Figure 3.15a, it is seen that both the baseline blade and tubercle blade have same lift characteristics in the pre-stall region. The '0 baseline blade' stall at 16° and has a $C_{L_{max}}$ of 0.76. After the stall, the lift coefficient for baseline drops to about 0.43. The $C_{L_{max}}$ for unswept tubercle blade (0 tubercle) is 0.67, which is approximately 12% less than the baseline.The significant effect of the tubercle is visible in the post-stall region. When the baseline abruptly stalls, dropping C_L to 0.430, the tubercle blade presents a smooth stall characteristic.

A similar trend is observed for 10° and 20° swept blades. When 10° baseline has a $C_{L_{max}}$ of 0.702 and falls abruptly to 0.446 at stall, the tubercle variant has a $C_{L_{max}}$ of 0.589 which smoothly falls to 0.560. For 20° baseline and tubercle blades the $C_{L_{max}}$ is 0.661 and 0.583 respectively while the post-stall C_L for these blades are 0.560 and 0.567. However, there is a prominent difference for 30° blades. $C_{L_{max}}$ for baseline blade is 0.61 and stalls smoothly to a C_L of 0.603, unlike all the other baseline models. The 30° tubercle model has $C_{L_{max}}$ of 0.57, which also smoothly decreases to 0.562 at stall.

The unswept tubercle blade (0 tubercle) has an average 27.4% hike in C_L in the post-stall region compared to its baseline (0 baseline). However, this percentage hike in the post-stall region for swept blades decreases with an increase in the sweep. Tubercle variant for 10° swept blade (10 tubercle) has an average of 23.8% greater lift than its baseline (10 baseline), while for 20° swept tubercle (20 tubercle) the increment is only 12.9%. As the sweep further increases to 30°, the lift coefficient of the tubercle blade (30 tubercle) is 2.9% higher than the corresponding baseline. It is also seen that all baseline and tubercle blades stall at 16°. If the experimental studies were conducted such that force measurements were recorded with AOA increasing in steps of 0.5°, it would have been possible to see more precise difference in the stall angle

Figure 3.16 depicts the comparison of drag for baseline and tubercle blades at various swept angles. For all swept angle variants, both tubercle and baseline blades produce identical drag in the pre-stall region. However, the tubercle blade configuration for each swept variant has a decreased drag than its corresponding baseline in the stall and post-stall region. The tubercle variant of 0°, 10°, 20° and 30° shows an average of 19.62%, 21.11%, 18.62% and 10.87% reduction in drag in the post-stall region, respectively. However, at a very high AOA, beyond 24°tubercle blades produced drag comparable to or even slightly higher than the baselines.

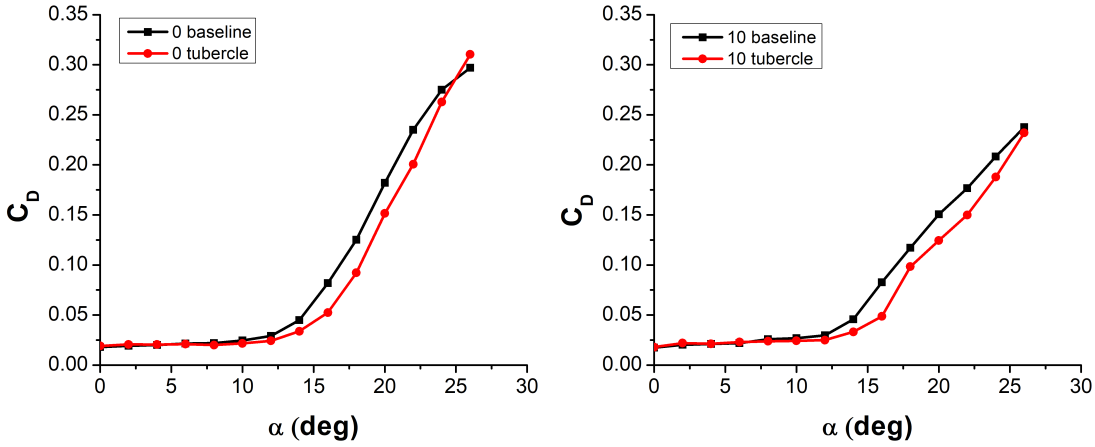

(a) 0 degree blades

(b) 10 degree blades

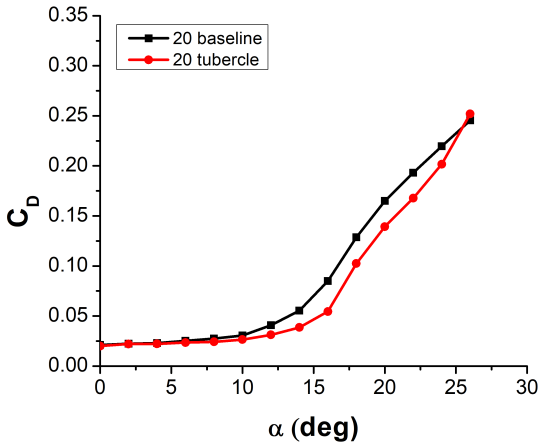

(c) 20 degree blades

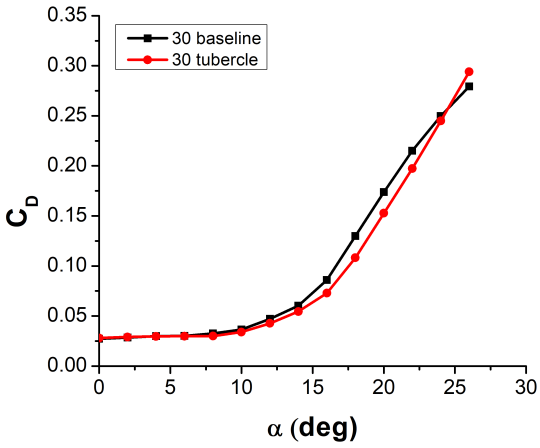

(d) 30 degree blades

Figure 3.16: Drag characteristics of swept blades at $Re_c = 10^5$

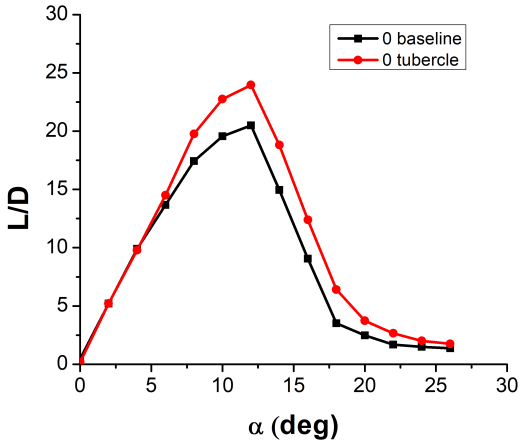

(a) 20 degree blades

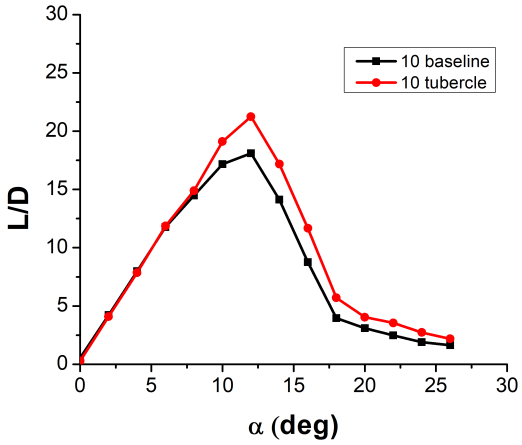

(b) 30 degree blades

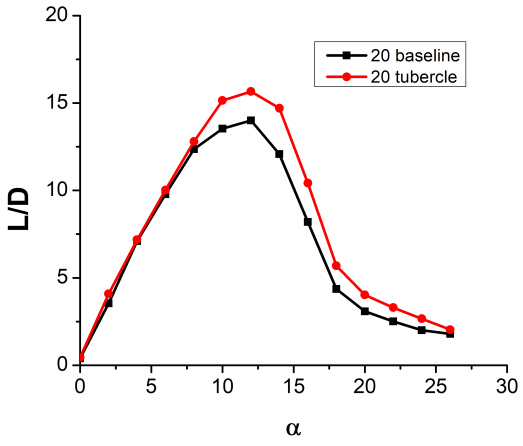

(c) 20 degree blades

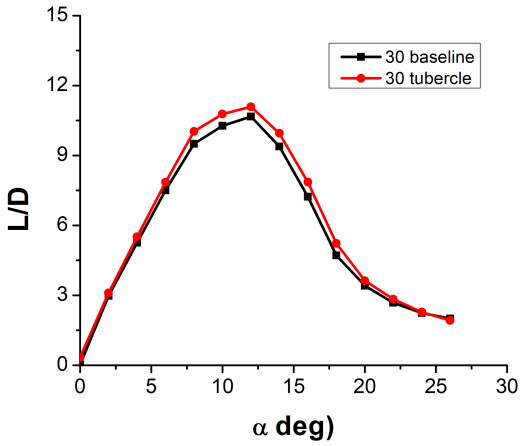

(d) 30 degree blades

Figure 3.17: Lift to drag ratio of swept blades at at $Re_c = 10^5$

A comparison of lift and drag may not help fully understand the potential benefits of tubercle blades. The L/D ratio for the blade act as an indicator of aerodynamic efficiency and provide a clear and easy understanding of the feasibility of using tubercle blades in various applications. Figure 3.17 shows the L/D curve with respect to AOA for the different swept blades. The unswept tubercle blade (0 tubercle) has a 20 % increase in maximum lift to drag ratio, $(L/D)_{max}$ when compared to its baseline (0 baseline). For 10° and 20° blades the hike in $(L/D)_{max}$ for the tubercle variant is 17.6% and 11.7%, respectively. However, for 30° the increment is a mere 3.8% for tubercle variant (30 tubercle) over the corresponding baseline (30 baseline). It can clearly be seen that at a very high swept angle of 30°, tubercles do not appear to be beneficial compared to the baseline. From earlier works done on tubercles (Custodio, 2007; Carreira Pedro and Kobayashi, 2008), it was suggested that the tubercles created counter-rotating vortices

that re-energized the boundary flow delaying flow separation and thereby improving aerodynamic characteristics. The inefficiency of the high swept tubercle blade could be explained in terms of the span-wise flow component over the blade. The counter-rotating vortices created by the tubercles lose their strength and eventually disintegrate as the span-wise flow washes over them. It is known that as the swept angle increases, the span-wise flow is also greater. At low Reynolds numbers, the vortices produced by the leading edge tubercle get washed out over the span when the swept angle of the blade is large. This could be the reason for the decrease in aerodynamic efficiency for the tubercle blade with an increase in swept angle.

CHAPTER 4

EFFECT OF TUBERCLES ON LSB, STALL AND HYSTERESIS

From the discussion in the last chapter, it was seen that tubercles are more beneficial on rectangular planform unswept blades than on swept blades. Based on those observations, a detailed study on the effect of tubercles on static unswept blade is conducted in this chapter. Some common phenomena on a conventional blade are LSB, stall, and hysteresis. The effect of LET on these phenomena, is studied from the simultaneous force and pressure analysis of a baseline and tubercle blade. The detailed discussion of the design and fabrication of experimental models, experimental setup, and result analysis are done in this chapter.

4.1 Fabrication of Experimental Models

The second objective of the thesis involves pressure and force measurements on static blade in the laminar, transition, and turbulent flow regime (Reynolds number varying from 2.5×10^5 to 6.5×10^5). The approach to designing the experimental model is the same as described in Chapter 3. However, the fabrication process is different. This part of the study requires larger models so that the high Reynolds number required for the study can be achieved. The large size of the model also is beneficial as it offers ample space inside to accommodate various instruments. The blade models are made from Fibre Reinforced Plastic (FRP). These models have a surface roughness of 17 microns. Figure.4.1 shows the schematic of the blade models used in the study of static unswept blades, and the geometrical parameters of the blades are given in Table 4.1.

Table 4.1: Geometrical parameters of unswept blades

Sl.No	Label	A (mm)	W (mm)	c (mm)	s (mm)
i	Baseline	-	-	400	1440
ii	Tubercle	20	40	400	1440

The blades are manufactured in nine modular segments, each 160 mm in span. Steel tubes of 1mm diameter are embedded normal to the surface in one of the sections (S2 in

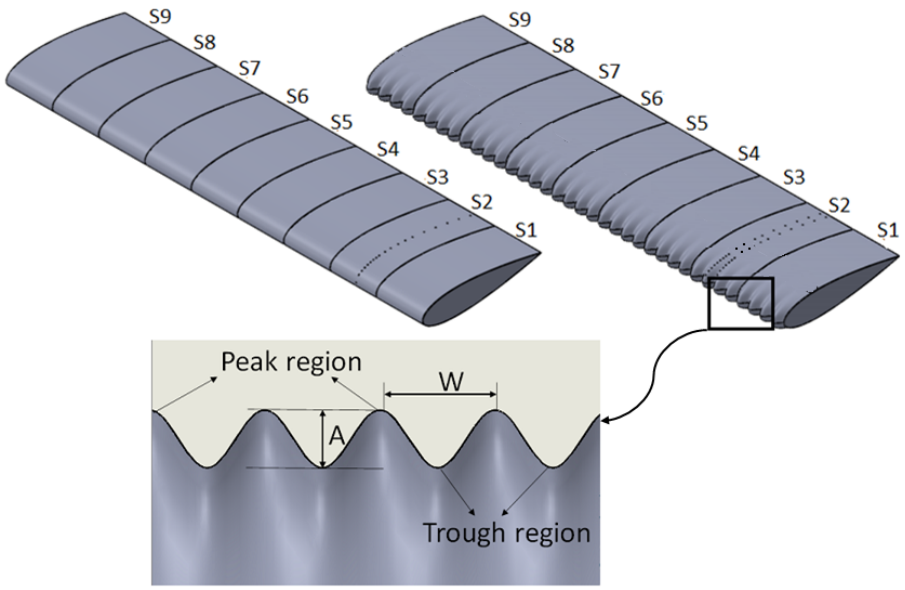

Figure 4.1: Schematic of the unswept blades used in static study

(a) **(b)**

Figure 4.2: Modular sections of baseline blade showing (a) pressure scanner and (b) spar arrangement

Figure 4.1) of each blade for static pressure measurement. The cavity within this section has the provision to install the pressure scanner. Figure 4.2a shows the modular sections of the baseline blade, where the pressure scanner is fitted to one of the sections. The central unit (S5 in Figure 4.1) has two reinforced ribs embedded on both ends and three spars (two at the leading-edge and one at the trailing edge) fixed to them. A base plate is also installed in this section to facilitate the connection of the model to the sting of the wind tunnel. The spars are threaded rods on which the modular units can slide and be fixed using nuts. Figure 4.2b shows the spar positioning with one modular section slid out.

The modular section that would carry the pressure scanner on the baseline blade is

designed so that it has 33 pressure ports (B1-B33) in a single row, as depicted in Figure 4.3a. The corresponding section of the tubercle blade has 66 pressure ports (T1-T66) arranged in two rows- 35 in the peak region and 31 in the trough region, as depicted in Figure 4.3b. Since the blades are made in a modular manner, the section with pressure ports can be moved to a different location along the span by sliding it over the threaded spars and fixing it at the desired location using nuts. The location of the pressure ports along the chord for the baseline and tubercle blade is depicted in Fig.4.4. Table 4.2 gives the non-dimensional location of each pressure port with respect to the chord length of the airfoil.

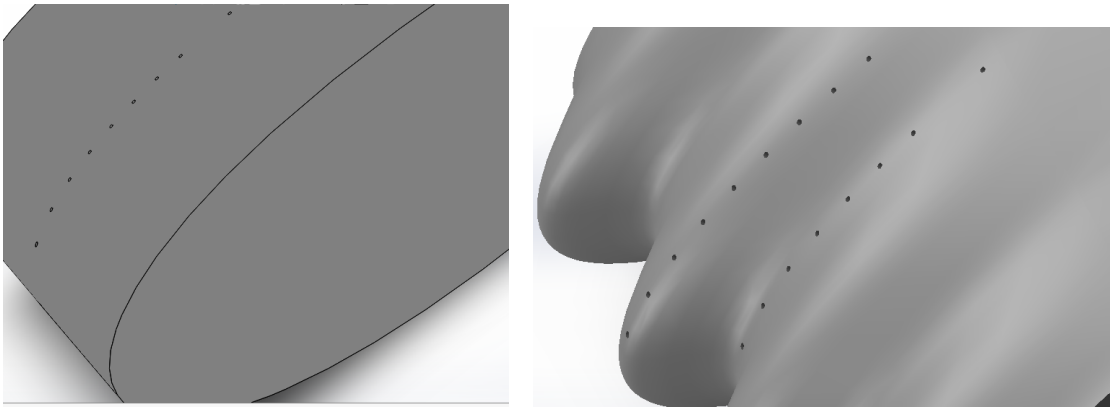

(a) Baseline blade **(b)** Tubercle blade

Figure 4.3: Pressure ports on baseline and tubercle blades

Since the model is modular, as discussed earlier, the section with pressure ports can take the position of sections S1 to S9 except for the fixed section S5. For reference, a right-handed coordinate system with the x-axis along the flow direction is assumed to be fixed on the leading edge at the mid-span of the blade. Thus, any non-dimensional spanwise location can be represented by $-0.5 \leq y/s \leq +0.5$. As the section with the pressure port takes various spanwise positions, the non-dimensional location of the pressure ports along the span is specified in Table 4.3.

4.2 Wind Tunnel

The study on the effect of tubercles on LSB, stall and hysteresis characteristics of blade is conducted at the OCWT in the Department of Aerospace Science Engineering at the Indian Institute of Science, Bangalore, Karnataka, which is designated Tunnel II in the thesis. The aerial view of Tunnel II is shown in Figure 4.5. The specification of Tunnel II is enlisted in Table 4.4. The basic structure and functioning of Tunnel I and Tunnel

Table 4.2: Chord wise location of pressure tubes on unswept blades

Sl.No.	Baseline	x/c	Tubercle Peak	x/c	Tubercle Trough	x/c
1	B1	0.91	T1	0.96	T36	0.99
2	B2	0.81	T2	0.86	T37	0.89
3	B3	0.69	T3	0.77	T38	0.79
4	B4	0.60	T4	0.67	T39	0.69
5	B5	0.52	T5	0.57	T40	0.59
6	B6	0.43	T6	0.47	T41	0.5
7	B7	0.35	T7	0.41	T42	0.44
8	B8	0.29	T8	0.35	T43	0.38
9	B9	0.23	T9	0.29	T44	0.32
10	B10	0.16	T10	0.24	T45	0.27
11	B11	0.13	T11	0.19	T46	0.22
12	B12	0.09	T12	0.17	T47	0.19
13	B13	0.06	T13	0.15	T48	0.17
14	B14	0.02	T14	0.12	T49	0.15
15	B15	0	T15	0.09	T50	0.12
16	B16	0.02	T16	0.07	T51	0.09
17	B17	0.05	T17	0.05	T52	0.07
18	B18	0.07	T18	0.02	T53	0.05
19	B19	0.09	T19	0	T54	0.08
20	B20	0.12	T20	-0.02	T55	0.11
21	B21	0.15	T21	-0.01	T56	0.15
22	B22	0.17	T22	0.02	T57	0.19
23	B23	0.20	T23	0.05	T58	0.25
24	B24	0.24	T24	0.09	T59	0.31
25	B25	0.29	T25	0.13	T60	0.37
26	B26	0.35	T26	0.16	T61	0.46
27	B27	0.41	T27	0.22	T62	0.54
28	B28	0.47	T28	0.28	T63	0.63
29	B29	0.57	T29	0.35	T64	0.71
30	B30	0.65	T30	0.43	T65	0.83
31	B31	0.77	T31	0.52	T66	0.96
32	B32	0.87	T32	0.67	-	-
33	B33	0.96	T33	0.69	-	-
34	-	-	T34	0.81	-	-
35	-	-	T35	0.93	-	-

Table 4.3: Location of pressure port along the blade span (y/s) for baseline and tubercle blades

Sl.No.	Label	Baseline	Tubercle Peak	Tubercle Trough
i	S1	-0.46	-0.46	-0.44
ii	S2	-0.35	-0.35	-0.33
iii	S3	-0.24	-0.24	-0.22
iv	S4	-0.12	-0.12	-0.11
v	S6	0.43	0.43	0.44
vi	S7	0.32	0.32	0.33
vii	S8	0.21	0.21	0.22
viii	S9	0.097	0.12	0.11

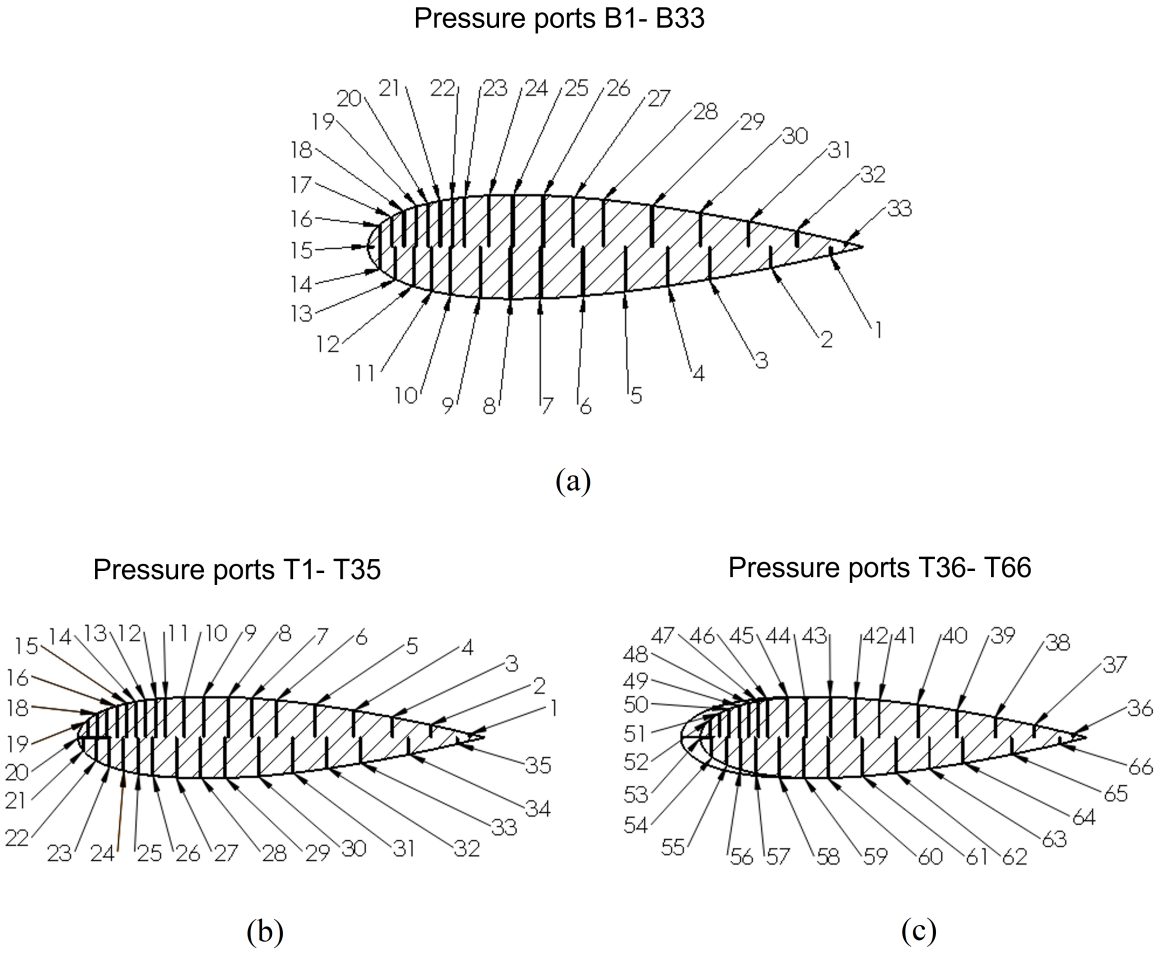

Figure 4.4: Schematic showing the location of pressure ports along the chord (a) baseline (b) tubercle peak (c) tubercle trough

II is similar, except that Tunnel II is a more extensive research facility, where a wide range of models can be studied.

Table 4.4: Specifications of Tunnel II

Parameters	Tunnel II
Shape of test section	Octahedron
Length of test section	$6m$
Test section area	$11.5m^2$
Contraction ratio	$14:1$
No of driving fans	2
Maximum RPM	720
Power of driving motor	$480kW$
Max. flow velocity	$90m/s$
Turbulence intensity	0.14%

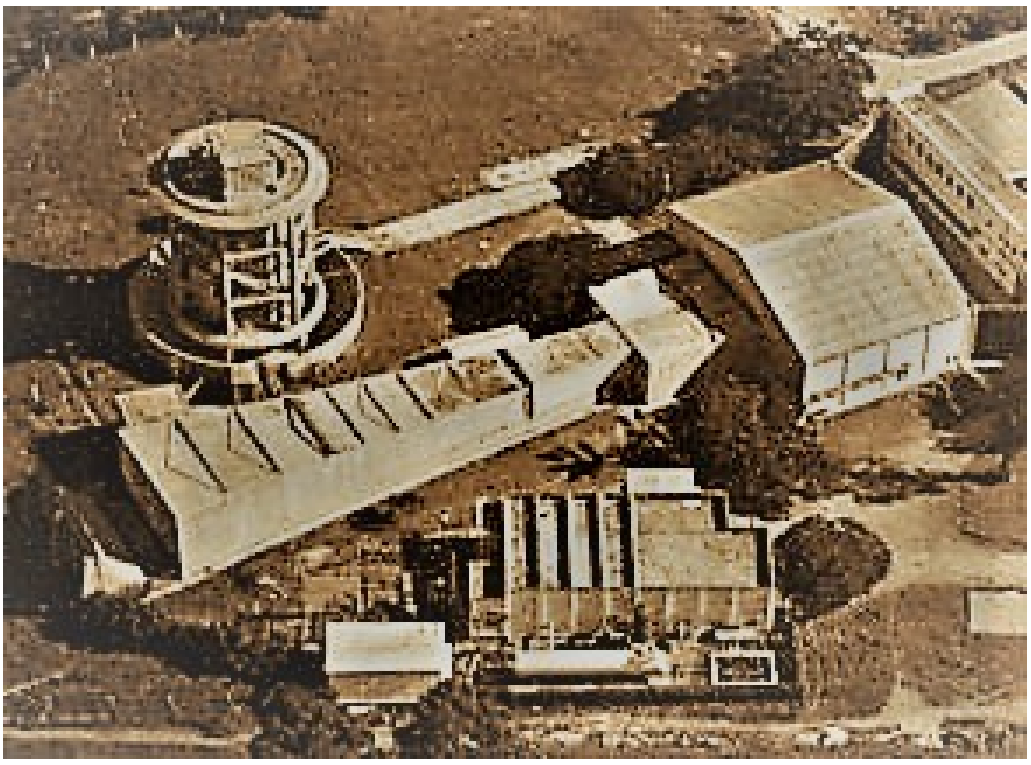

Figure 4.5: OCWT at IISc, Bangalore (Tunnel II)(Photo courtesy: APC, IISc)

4.3 Force Balance

The force measurement for the static blade is done using an internal force balance. Internal balances are compact and small enough to be accommodated within the testing model. The body of the balance is made of monolithic steel and is heat-treated to increase the yield point and the fatigue life, as the balance is tested with repetitive cycles of load. The balance body is accurately machined and shaped, as seen in Figure 4.6, such that the strains at specific sections of the balance are very sensitive to specific forces and moments acting on it while remaining insensitive to others. The internal balance uses strain gauges, which are foil-type resistances encased in epoxy glue and applied to the balance. When a load is applied to the strain-cell, there is a change in the geometry of the foil, and this in turn, alters the resistance to the excitation voltage and changes the output voltage. The remarkable change in output voltage is directly related to the applied load. The internal balance used in the measurement forces and moment on static blade is designated as WT5, with reference to the internal reports of the wind tunnel laboratory. The dimensions and component ratings of WT5 balance are presented in Table.4.5.

When used, one end of the balance (the model end) is rigidly fixed to the model while

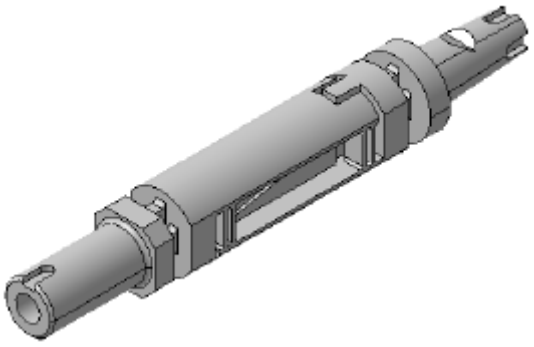

Figure 4.6: CAD model of WT5 balance

Table 4.5: Balance rating for WT5 balance

Component	Rating
Normal force	50 kgf
Side Force	25 kgf
Axial Force	25 kg
Pitching Moment	5 kg-m
Yawing Moment	2.5 kg-mm
Rolling Moment	2 kg-m

the other end (the sting end) is rigidly fixed to the sting of the wind tunnel sector. During the wind tunnel operation, the balance produces six electrical outputs, which are linearly related to the six aerodynamic forces/moments acting on the model. The balance is calibrated in such a way that it measures six force/moment components relative to an axis system fixed to the balance with its origin at the geometric center of the balance.

4.3.1 Calibration of Internal Force Balance

Low-speed wind-tunnel balances are calibrated using a single bridge element calibration rig with accurate dead weights. A six-component strain gauge balance has the following bridge stations for measuring the aerodynamic forces and moments acting on a model during a wind tunnel test.

1. Normal force (N1, N2)
2. Axial force (A1, A2)
3. Side force (S1, S2)
4. Rolling moment (RM)

The six-component strain gauge balance has been designed to minimize the interaction terms for each main component loading. The calibration of an internal strain gauge balance will yield a set of equations that can be used to determine the aerodynamic loads on the model during a wind tunnel test. The calibration of internal balance is done by applying known set of standard weights as loads to the balance mounted on the calibration rig. The location of applied loads is done in normal, axial, and side directions (relative to the balance axis) using a calibration body. During calibration of each element (N1, N2 ...), loading is done in ascending and descending orders to check the hysteresis. Usually, balance is calibrated for the range of expected loads. A typical N1/S1 element loading during calibration is shown in Figure 4.7.

Figure 4.7: Internal balance WT11 under calibration

The balance sensitivity matrix is obtained as a linear relationship between the applied forces/moments and the electrical response (electrical output in volts) as

$$\{R\} = [C]\{F\} \tag{4.1}$$

where, $\{\mathrm{R}\}$ is the electrical response which is a column matrix of the sensitivities to the applied forces $\{\mathrm{F}\}$, and [C] is a 6x6 calibration matrix. Ideally, [C] would be a diagonal matrix as the non-diagonal terms represent cross sensitivities of the measuring element

and are made negligible by careful design of the balance body. For further use the above relation can be inverted to obtain:

$$\{F\} = [U]\{R\} \tag{4.2}$$

where, [U]is the inverse of [C] and is called the user matrix. During the wind tunnel test, $\{R\}$ will be measured, and the aerodynamic forces $\{F\}$ can be calculated. These can be converted into suitable aerodynamic force/moment coefficients by further calculation. These forces/moments specified in the balance axis system can be transformed into any other axis (for example, the wind axis system) by using a suitable coordinate transformation. The calibration report for WT11 is presented in appendix A as an example.

4.4 Model Mounting

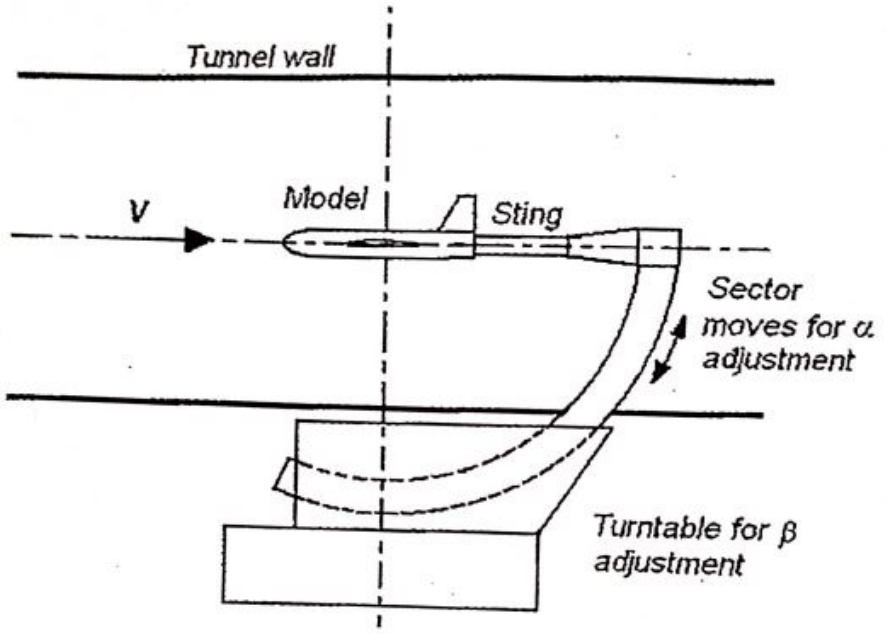

Figure 4.8: Schematic of sector arrangement in Tunnel II

The Tunnel II has a sector with two degrees of freedom (DOF) to facilitate the movement of the experimental model in pitch (α) and yaw (β) directions. A schematic depicting the sector is shown in Figure 4.8. The experimental model is fitted to a sting connected to the sector. The sting balance is placed at an offset below the model as it was difficult to accommodate the balance within the experimental model due to the

interference from spars. A pylon that connects the model to the sting also houses the balance, as shown in Figure 4.9. An adapter locks the force balance on the pylon constraining its axial movements.

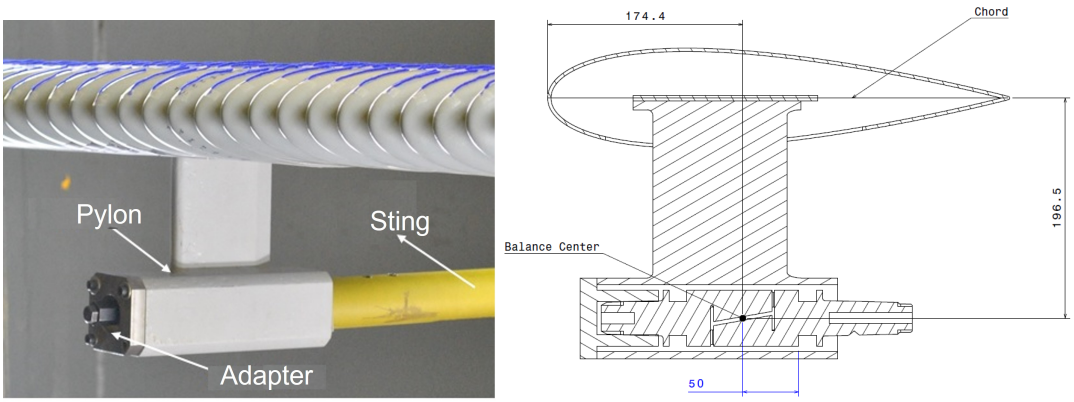

(a) (b)

Figure 4.9: (a)Unswept blade mounted to sting using a pylon (b)Cross sectional view showing positioning of balance within the pylon

4.5 Data Acquisition

The data acquisition system for steady-state aerodynamic force/moment consists of devices from National Instruments® as below:

1. A PXie 16 channel Analog to digital converter (ADC) board with 250ks/sec sampling rate. The number of differential channels is limited to 8.
2. A universal signal conditioner amplifier system (SCXI 1520 R) configured for custom voltage with excitation mode for strain gauge signal conditioning and SCXI-1000 series channel enclosure for communication with a computer.

Individual balance channels (N1, N2, S1, S2, A1, A2, and RM bridge elements) are connected to the Universal amplifier input using a special interfacing connector SCXI-1314. Individual gain, excitation (5 V), and type of input (differential) for all the seven bridge elements have to be individually programmed. A worksheet for data logging was developed using LabVIEW®. A standard sampling rate of 1ks/s was used for force data acquisition. Raw voltage values were recorded from the corresponding channels, and post-processing was done offline using MATLAB®. Instrumentation requires warm-up for at least 60 minutes for thermal stability. The data acquisition devices, and the control unit for the AOA, is shown in Figure 4.10.

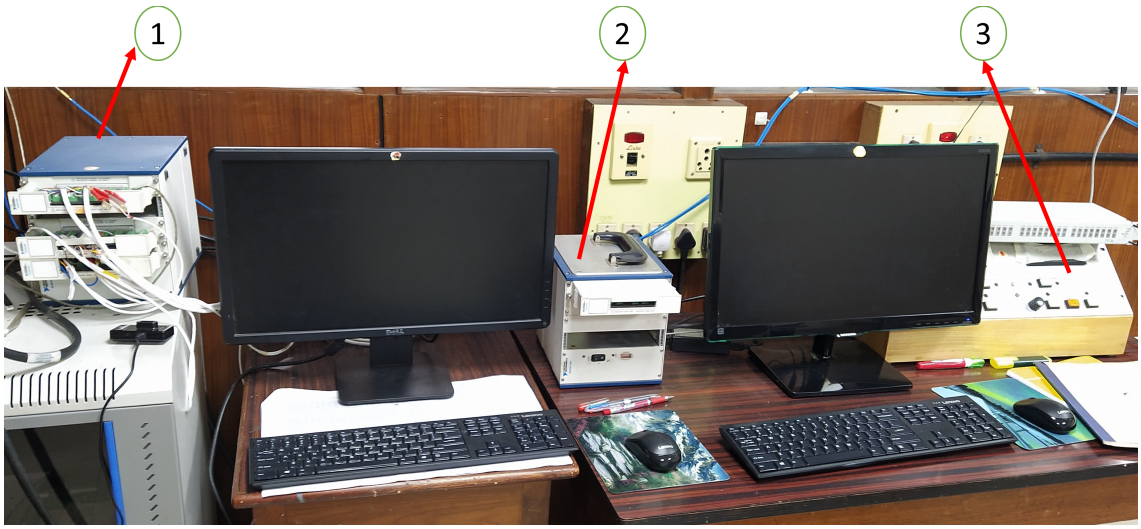

Figure 4.10: Data acquisition panel for static blade models 1.ADC, 2. Amplifier 3. AOA control unit

4.6 Force Measurement

In order to validate the force measurement system, known loads are applied to the system and work back the load using the analysis program. The load on balance varies from 0.5kg to 10 kg, and the system calculates the work-back. Figure 4.11 shows the variation in applied load with work-back load obtained from the force balance. The maximum error was about 4.5%.

Wind-on Experiments :- The steady-state flow analysis of unswept blades are done for different tunnel velocities corresponding to the chord Reynolds number of 2.5×10^5, 3.5×10^5, 5×10^5, and 6.5×10^5, and data is collected for AOA ranging from -4° to 28°, in steps of 2°. The experimental model experiences both aerodynamic load (generated due to the flow) and inertial load(due to its weight).

Wind-off Experiments :- Here, the wind tunnel is not switched on, and the data is collected for the above-mentioned AOA range . The data collected contain only the inertial loads.

To exclude the inertial forces, data obtained from wind-off operations is subtracted from the corresponding wind-on files. Correction for wind tunnel effects is also conducted for the blade model. The maximum solid blockage ratio (ratio of model frontal area to test section area) was 0.02 at an AOA of 28°. Additional corrections of wind tunnel effects for finite span experimental model include wake blockage, streamline curvature, and downwash, using methods described in (Barlow *et al.*, 1999). These corrections resulted in a increase of AOA and C_D by 0.5% and 4.7%, respectively, and a decrease

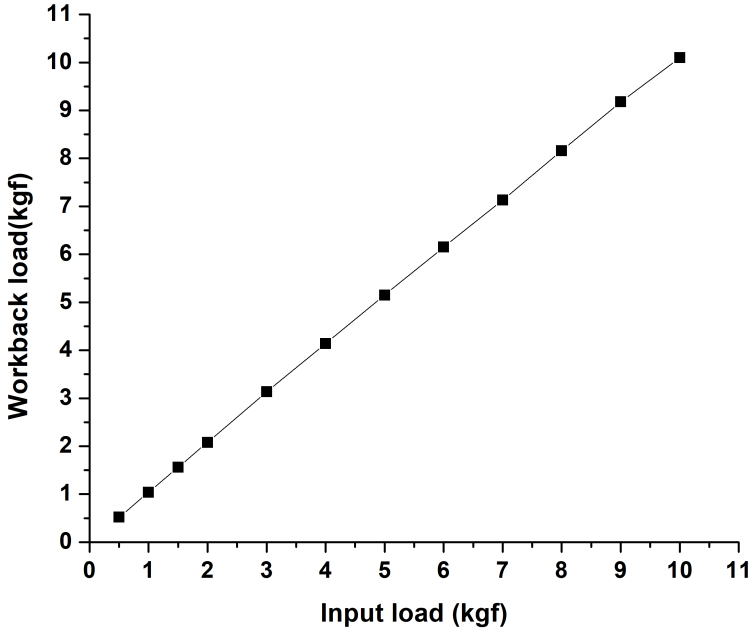

Figure 4.11: Relation between input and work-back load on WT5

in C_L by 2.3% for the baseline blade at the highest angle in the pre-stall region (20°) at $Re_c = 2.5 \times 10^5$.

4.7 Pressure Measurement

As discussed in Section.4.1, the static blades have pressure tubing connected perpendicular to the surface to measure the surface pressure. The baseline blade has 33 pressure tubing arranged in a single row, whereas the tubercle blade has 66 tubes arranged in two rows, as shown in Figure 4.3. Steel tubes of 1 mm diameter are embedded along the chord during model fabrication. Flexible silicone tubes are used to connect the steel tubes to the pressure scanner.

The aerodynamic performance of an aerodynamic surface can be studied easily from the distribution of pressure over the surface. This distribution is usually expressed in terms of the pressure coefficient as expressed in equation 4.3.

$$C_P = \frac{P - P_\infty}{0.5\rho V_\infty^2} \tag{4.3}$$

4.7.1 Pressure Scanner

Electronic pressure scanner ZOC33/64xX2 from Scanivalve Corp., as shown in Figure 4.12 is used for pressure measurement. This module has 64 individual piezoresistive pressure sensors in eight packs and accepts up to 128 pneumatic inputs. Each sensor has two pneumatic inputs: Bank A and Bank B. The inputs are switched pneumatically by enabling the duplexing valve. Even though there are 128 pressure inputs combined from the two banks, only 64 pressure inputs from one bank can be used at a time. This scanner's calibration and wind tunnel operation process is elaborated in Appendix B.

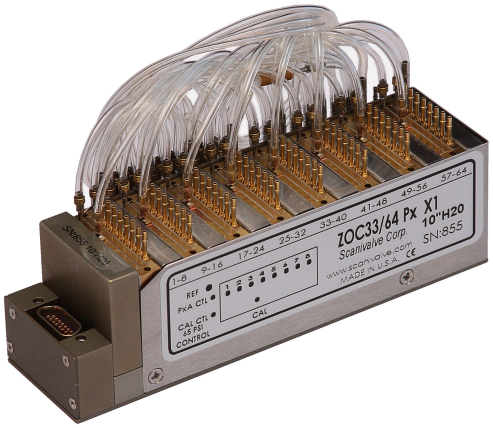

Figure 4.12: Pressure scanner used in the study

4.8 Uncertainty Analysis

The uncertainty in AOA is $\pm 0.1^{\circ}$ stemming from the pitching sector mechanism. Balance calibration coefficients are obtained from the standard procedure similar to that reported in AIAA-091A-2020 (AIAA, 2020) which is also reported in Appendix A. The accuracy of these coefficients is validated on a calibration rig by using check loads and moments at a specific location on balance. The maximum deviations of loads and moments obtained from the balance using the calibration coefficients were within 0.55% FS (Full Scale) and 0.2% FS, respectively. The sampling rate of the ADC connected to the force balance is 1 kHz. At least 1000 samples were collected for each AOA, and the mean value was used. Another source of error is the uncertainty in velocity, which was estimated to be $\pm 0.5 m/s$ with a pitot-static tube. The temperature fluctuations can contribute to an error in density which is assumed to be 5%. The fabrication process can

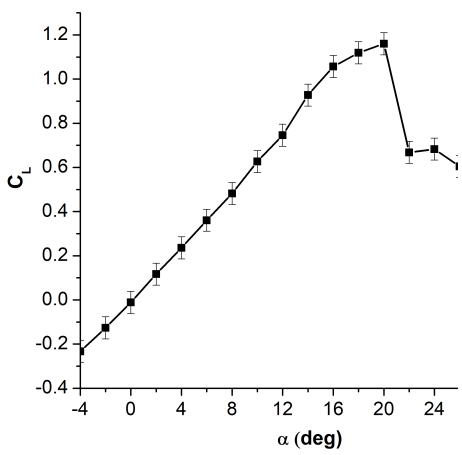

(a) Lift coefficient

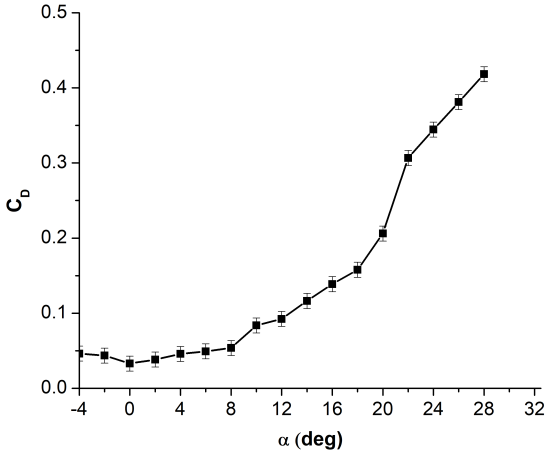

(b) Drag coefficient

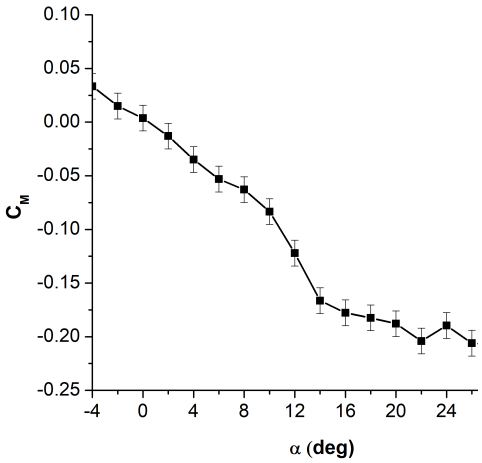

(c) Moment coefficient

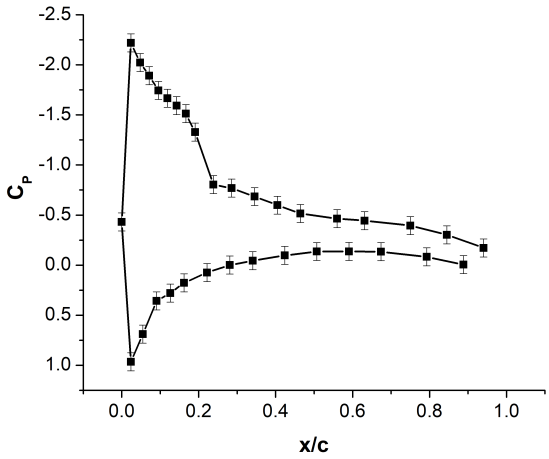

(d) Pressure coefficient

Figure 4.13: Uncertainty in aerodynamic coefficients

result in an error of$\pm 0.2mm$ in chord and span. The total uncertainty is calculated using procedures mention in Chapter 3 . The uncertainty in various aerodynamic coefficients are depicted in Figure 4.13.

4.9 Results and Discussion

In the previous chapter, a comparison of unswept blades and various swept blades was made, and it was observed tubercles seem more beneficial on the unswept blade or rectangular planform blades than on swept blades at a low Reynolds number. Based on those results, further investigations are conducted on the unswept blades. The force and

surface pressure measurements at various Reynolds numbers discussed in this section can provide an insight into the effect of tubercles, on phenomena like LSB, stall, and hysteresis.

4.9.1 Laminar Separation Bubble

As discussed in the introduction chapter, the typical method to recognize LSB is from the pressure distribution data over the blade. The pressure distribution over the blades at section S4 is utilized to study the LSB. Section S4 being close to the midspan of the blade ensures minimum interference from the tip vortices. Pressure analysis over section S1 (the tip section) justified this choice as LSB was completely absent for all AOA studied, as the flow of air from the pressure surface to the suction surface causes high turbulence and does not allow LSB formation near the blade tips.

The first recognizable pattern of LSB for the static baseline blade is obtained at AOA of 6°. Figure 4.14 shows pressure distribution over the baseline blade at an AOA 6°. The beginning of the LSB is marked by S, the point of separation, which occurs at $x/c = 0.24$. The point of reattachment, R, which occurs at $x/c = 0.35$, marks the end of the LSB.

The development of LSB with the increase in AOA is depicted in Figure 4.15, which shows the surface pressure of the baseline blade at AOA of 10°, 16°, and 22°. The LSB is present for all AOA mentioned. At 10°, point of separation is at $x/c = 0.19$ and point of reattachment is at $x/c = 0.29$. The point of separation at 16° and 22° are $x/c = 0.17$ and $x/c = 0.07$, respectively. The point of reattachment for these AOA are $x/c = 0.24$ and $x/c = 0.15$, respectively. The characteristics of LSB at different AOA are listed in Table 4.6, which shows that as the AOA increases, the onset point of LSB tends to move forward towards the leading edge. The LSB sustains until an AOA of 22° beyond which the blade stalls. The size of the LSB also tends to decrease with an increase in AOA. The LSB occupied about 11% of the chord at AOA of 6°, whereas at AOA of 22°, the size of LSB was just about 7.31% of the chord. The Reynolds number also affects the formation of LSB on the baseline blade. Figure 4.16 depicts the pressure distribution of baseline blade at 8° for Reynolds number 2.5×10^5 and 5×10^5, which are the laminar and transition flow regime, respectively. Figures 4.16a and 4.16b are very similar to one another, except that there is a region of LSB in 4.16a, indicating the presence of LSB in the laminar regime of fluid flow and its absence in the transition regime. The high energy of flow during the transition prevents the formation of LSB.

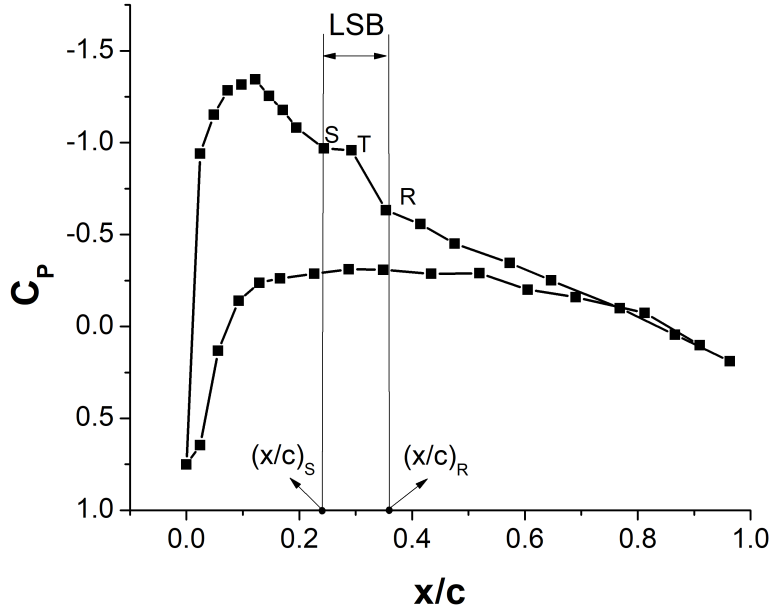

Figure 4.14: Pressure distribution over baseline blade at AOA of 6° showing region of LSB at $Re_c = 2.5 \times 10^5$

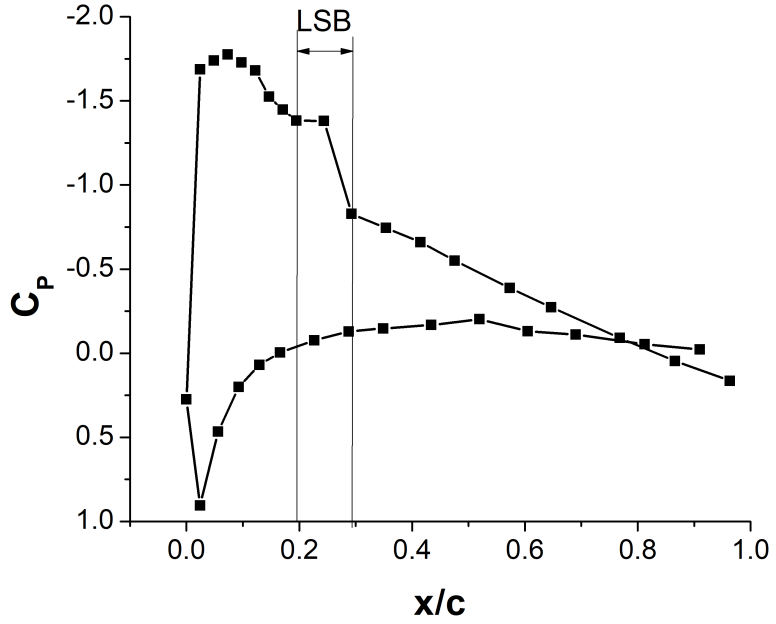

(a) AOA= 10°

Figure 4.15: Pressure distribution over baseline blade at various AOA showing region of LSB at $Re_c = 2.5 \times 10^5$

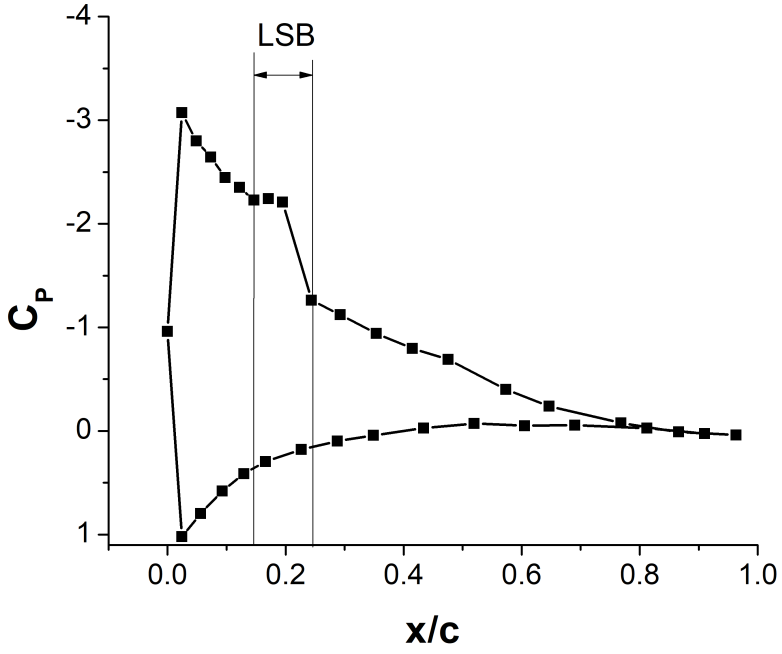

(b) AOA= 16°

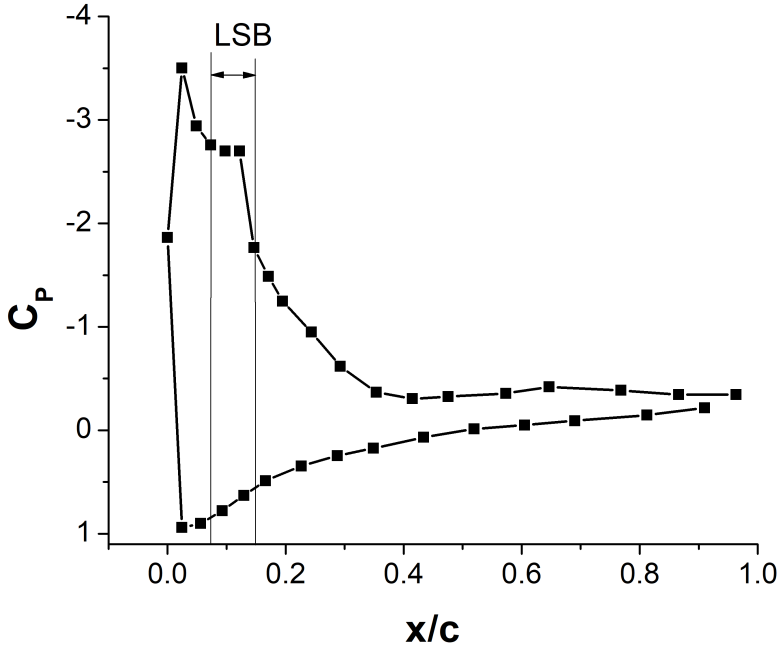

(c) AOA= 22°

Figure 4.15: Pressure distribution over baseline blade at various AOA showing region of LSB at $Re_c = 2.5 \times 10^5$ (cont.)

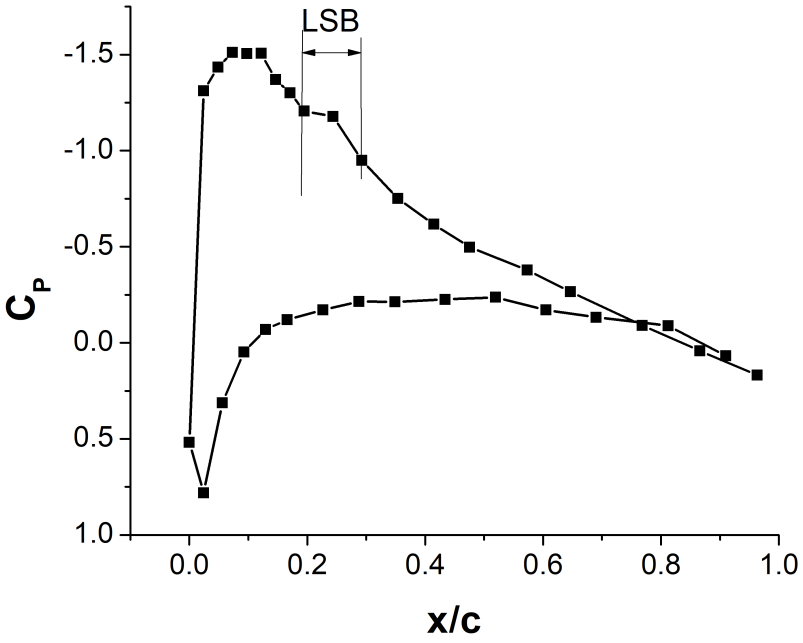

(a) $Re_c = 2.5 \times 10^5$

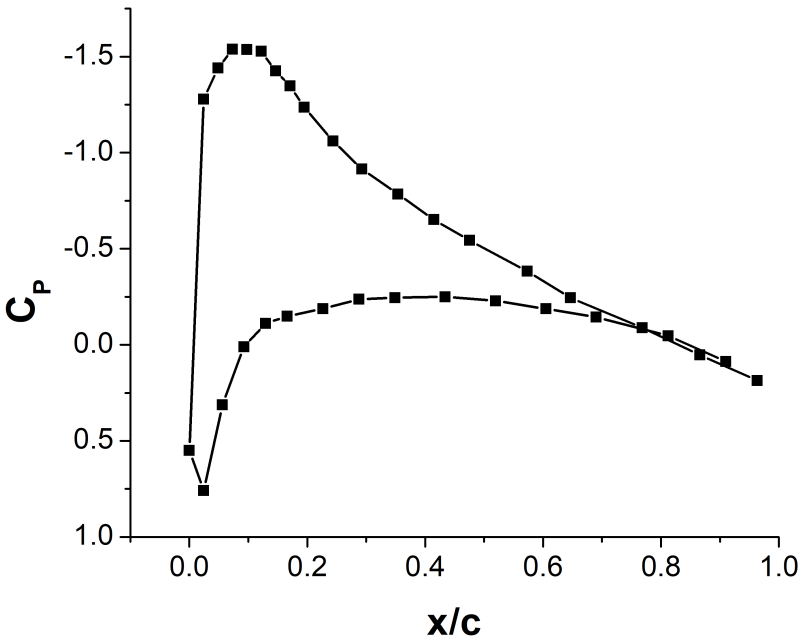

(b) $Re_c = 5 \times 10^5$

Figure 4.16: Pressure distribution of baseline blade at different Reynolds numbers

Table 4.6: LSB characteristics of baseline blade

α (deg)	$(x/c)_S$	$(x/c)_R$	l_{LSB}(%c)
6°	0.24	0.35	10.98
8°	0.24	0.35	10.98
10°	0.19	0.29	9.76
16°	0.17	0.24	7.32
22°	0.07	0.14	7.31

Figure 4.17 shows the pressure distribution over the tubercle blade at AOA of 6° and 16° at Reynolds number of 2.5×10^5. No region of LSB can be seen in the peak and the trough regions of the tubercle. The effect of tubercles in preventing LSB is evident. In other words, tubercles can energize the flow and keep the flow turbulent. Energized flow cannot separate from blade surface and form LSB.

4.9.2 Stall

The stall characteristics are studied primarily from the lift and drag coefficients of the static blades (baseline and tubercle). A better understanding of the stall phenomenon can be drawn from the pressure distribution over these blades.

The aerodynamic coefficients for the baseline blade in the laminar flow regime, at chord Reynolds number, $Re_c = 2.5 \times 10^5$ are depicted in Figures 4.18. It can be seen from Figure 4.18a that the slope of the lift coefficient curve in the linear region for the tubercle blade is slightly lesser than the baseline counterpart. This observation is different from that seen for the unswept blades (0 baseline and 0 tubercle) in section 3.6.4 where the slopes were identical. The difference in slope among baseline and tubercle models can be attributed to the geometrical parameters of the tubercle. Custodio *et al.* (2015) also observed a similar trend for slope for finite NACA 0020 airfoil at a Reynolds number of 4.5×10^5. He observed that based on the amplitude and wavelength of tubercles, the slope could coincide or fall below the baseline. A similar observation was also made by Hansen (2012), where a finite NACA 0021 airfoil incorporated with tubercles at Reynolds number of 1.2×10^5 had a lower slope for lift C_L curve compared to the baseline.

At $Re_c = 2.5 \times 10^5$, the baseline blade stalls at AOA of 20°, and has a $C_{L_{max}}$ of 1.12. The stall causes for loss of lift by about 46%, marking a post stall lift coefficient, ($C_{L_{p.s}}$) of 0.6. For the above-mentioned Re, the tubercle blade exhibited premature stall at 16° with $C_{L_{max}} = 0.798$, which is about 28% lower than the $C_{L_{max}}$ of baseline. The

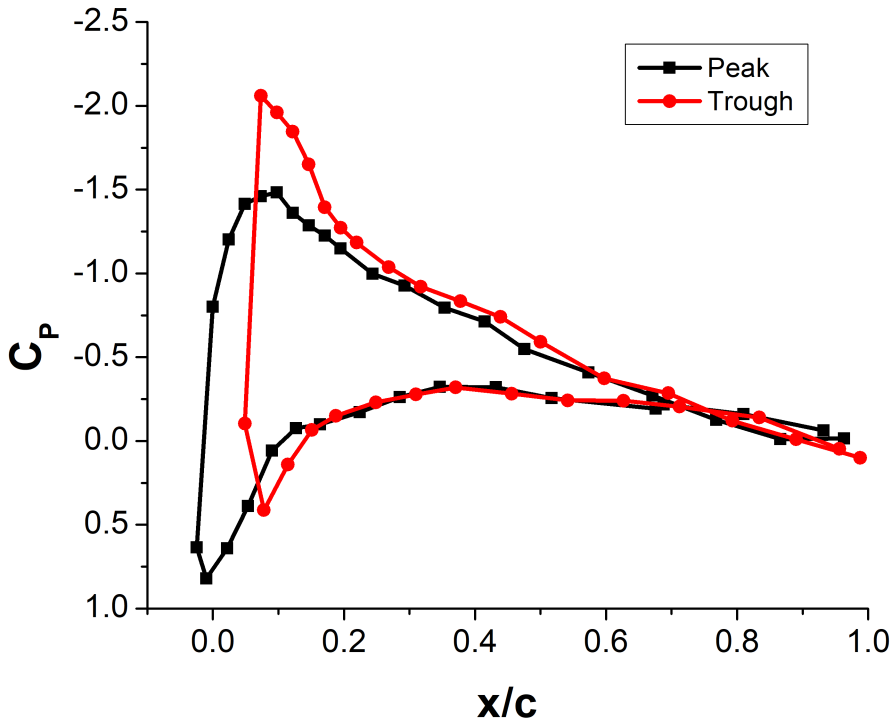

(a) AOA= 6°

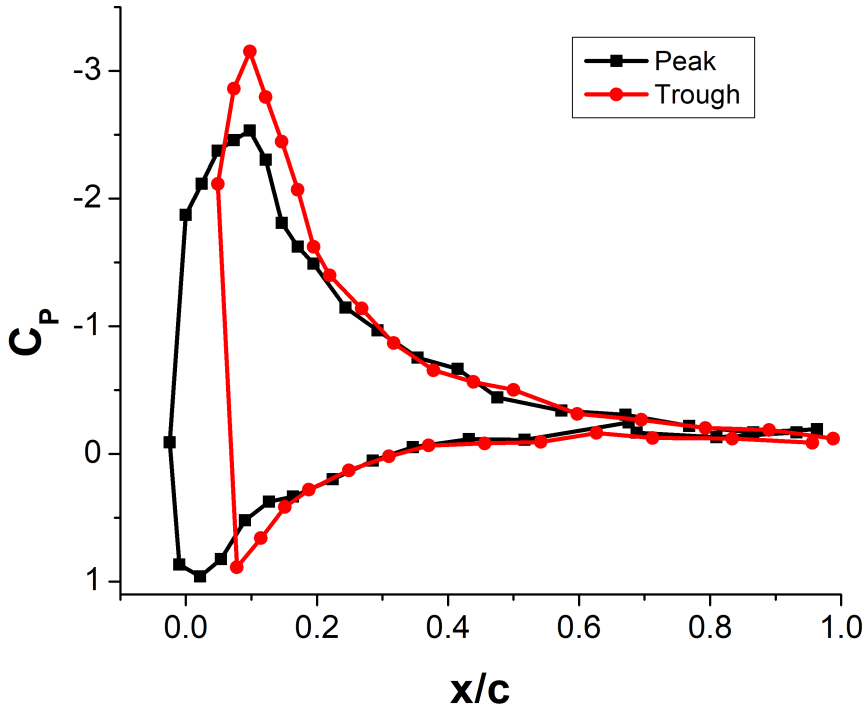

(b) AOA= 16°

Figure 4.17: Pressure distribution over tubercle blade at $Re_c = 2.5 \times 10^5$

Table 4.7: Lift characteristics of baseline blade

	Re_c	α_{stall}	$C_{L_{max}}$	$C_{L_{p.s}}$	$\% \downarrow$ in C_L (after stall)
Baseline	2.5×10^5	22	1.122	0.607	46
	5.0×10^5	24	1.164	0.735	37
	6.5×10^5	26	1.172	0.816	31
Tubercle	2.5×10^5	16	0.798	0.653	28
	5.0×10^5	17	0.924	0.714	23
	6.5×10^5	18	0.983	0.735	27

$C_{L_{p.s}}$ of tubercle blade is close to 0.65, indicating loss of lift by 18%. The percentage decrease in C_L for both blades at various Reynolds numbers has been presented in Table 4.7. Although the tubercle blade stalls earlier than the baseline blade, it has better stall characteristics. As seen in Figure 4.18a, the stall occurs abruptly in a single step for the baseline blade, whereas the tubercle blade does not lose lift suddenly and abruptly. The stall occurs gradually and smoothly for the tubercle blade in multiple stages. The drag coefficient of blades at Reynolds number $Re_c = 2.5 \times 10^5$ is depicted in Fig.4.18b. The tubercle blade has a greater drag than the baseline at this Reynolds number, especially in the post-stall region. As AOA increases beyond 24°, drag values for the baseline and tubercle blades are closely identical.

Figures 4.19 and 4.20 shows the aerodynamic characteristic of the unswept blades at a higher Reynolds number in the transition ($Re_c = 5 \times 10^5$) and the turbulent flow ($Re_c = 6.5 \times 10^5$) regimes, respectively. The baseline blade stalls at 24° and 26° ,whereas the tubercle blades stall at 17° and 18°, respectively, for above-mentioned Reynolds numbers. There is also a significant reduction in $C_{L_{max}}$ for the tubercle blade compared to the baseline for all the Reynolds numbers. However, as the Reynolds number increases, there is a decrease in the difference for $C_{L_{max}}$ between a baseline and tubercle blade. The lift characteristics of unswept blades at different Reynolds number are summarized in Table 4.7. The drag of the tubercle blade is nominally greater than the baseline blade at very low AOA, up to 4° . Beyond 4°, drag remains almost the same for both blades till the stall angle. The tubercle blade has a higher drag than the baseline in the immediate post-stall region. As AOA further increases beyond 24° the difference in drag values between the baseline and tubercle blades starts to decline.

Figure 4.21 shows a comparison of the lift coefficient obtained for the finite NACA 0021 wing with that obtained by Custodio *et al.* (2015) for NACA 0020 finite wing at comparable Reynolds numbers. The trend for lift coefficient is quite similar for both studies, except for the linear range. This dissimilarity is due to the difference in experimental fluids. It has to be noted that the working fluid in experiments conducted

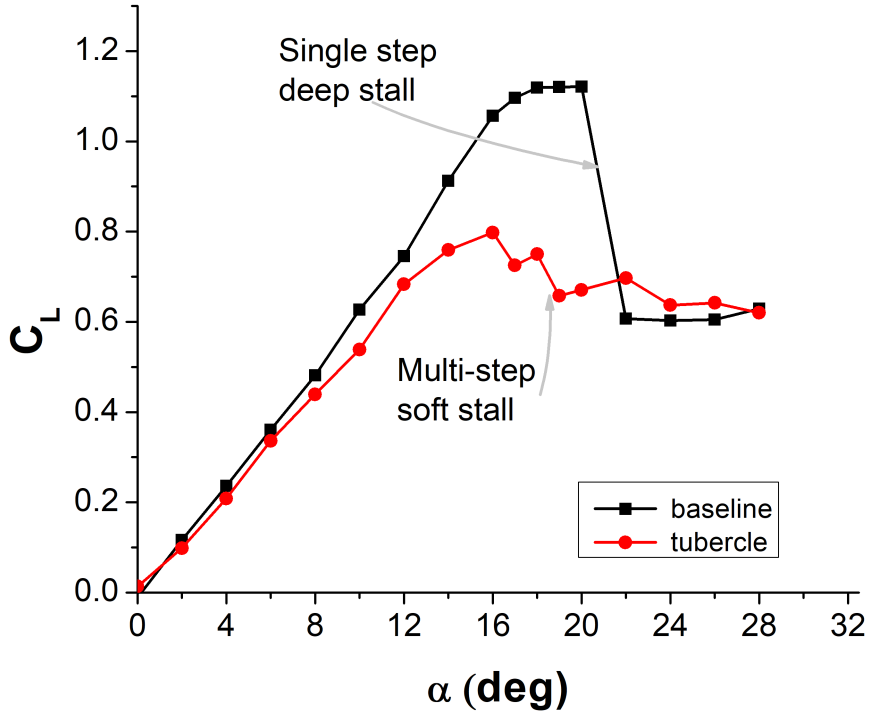

(a) Lift coefficient

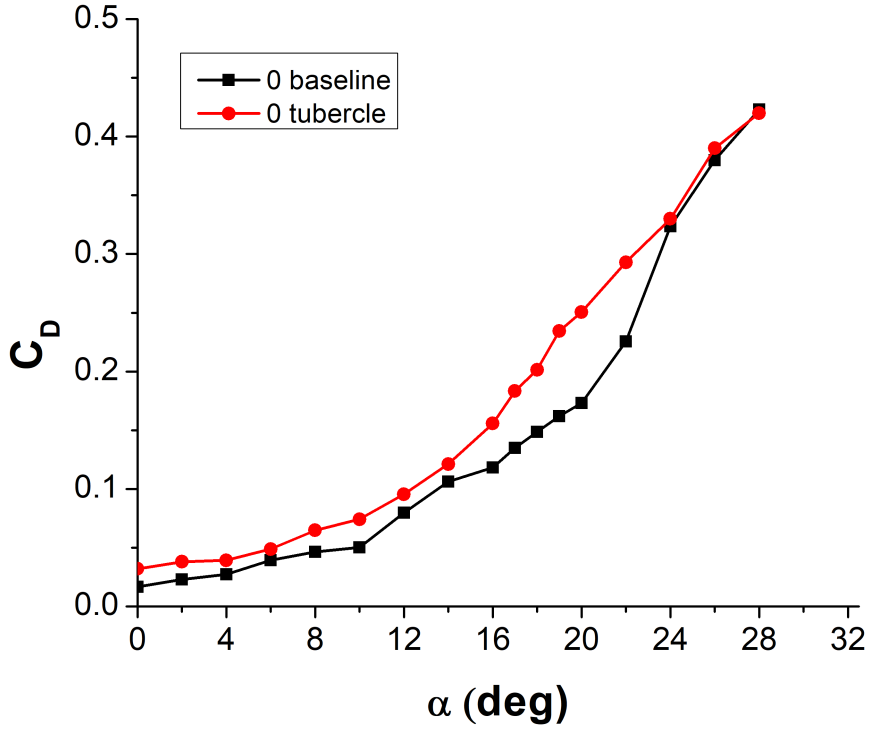

(b) Drag coefficient

Figure 4.18: Aerodynamic characteristics of baseline and tubercle blade at $Re_c = 2.5 \times 10^5$

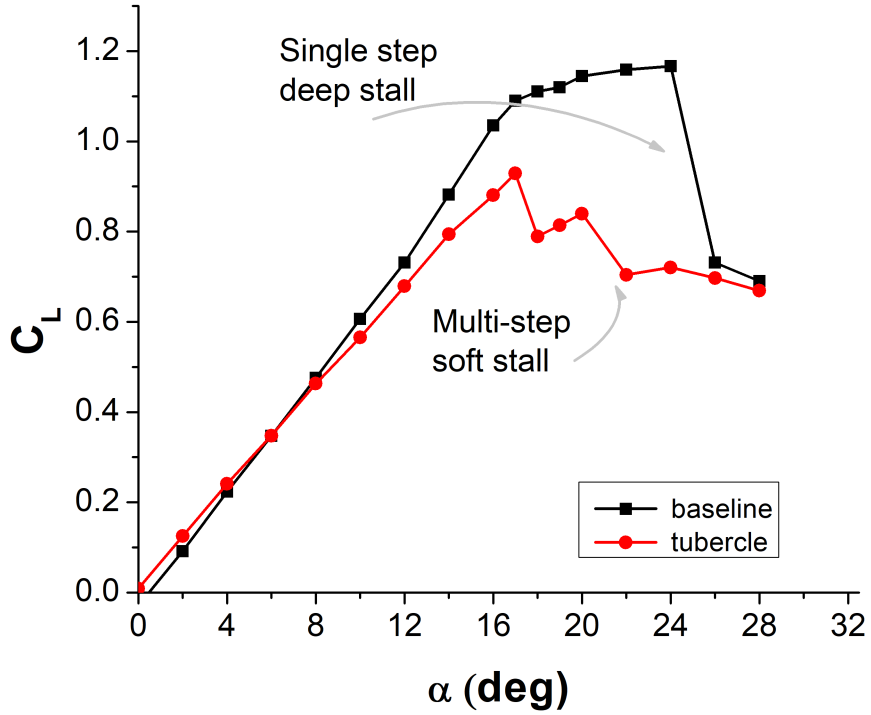

(a) Lift coefficient

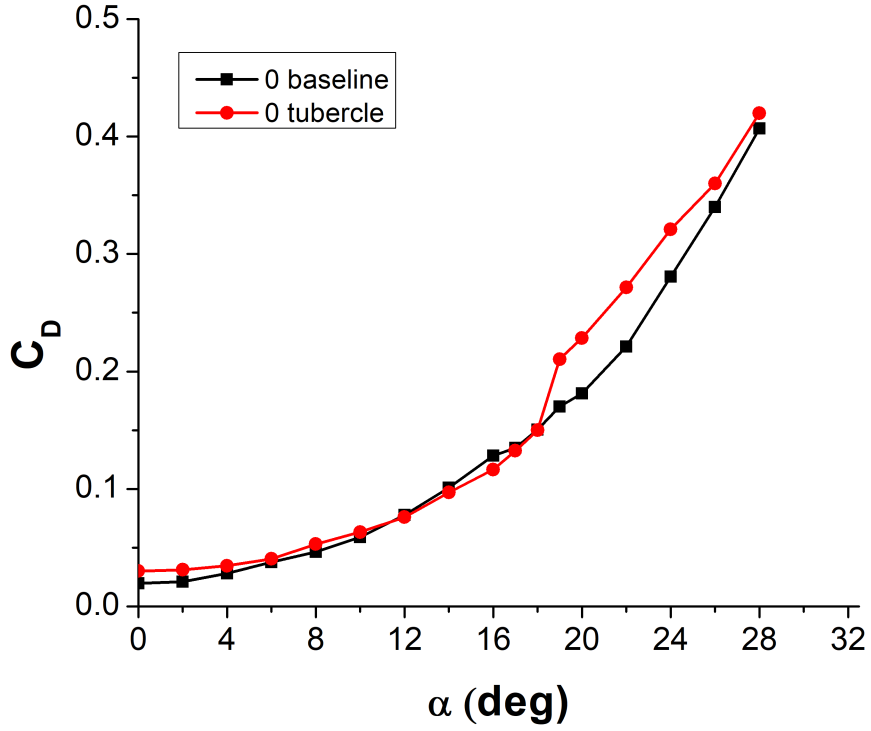

(b) Drag coefficient

Figure 4.19: Aerodynamic characteristics of baseline and tubercle blade at $Re_c = 5 \times 10^5$

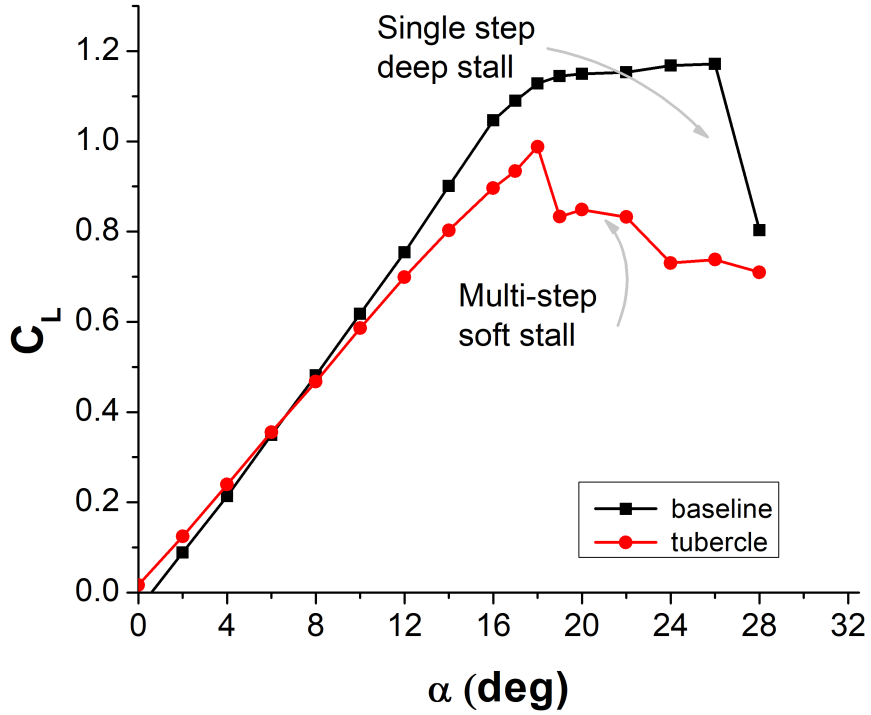

(a) Lift coefficient

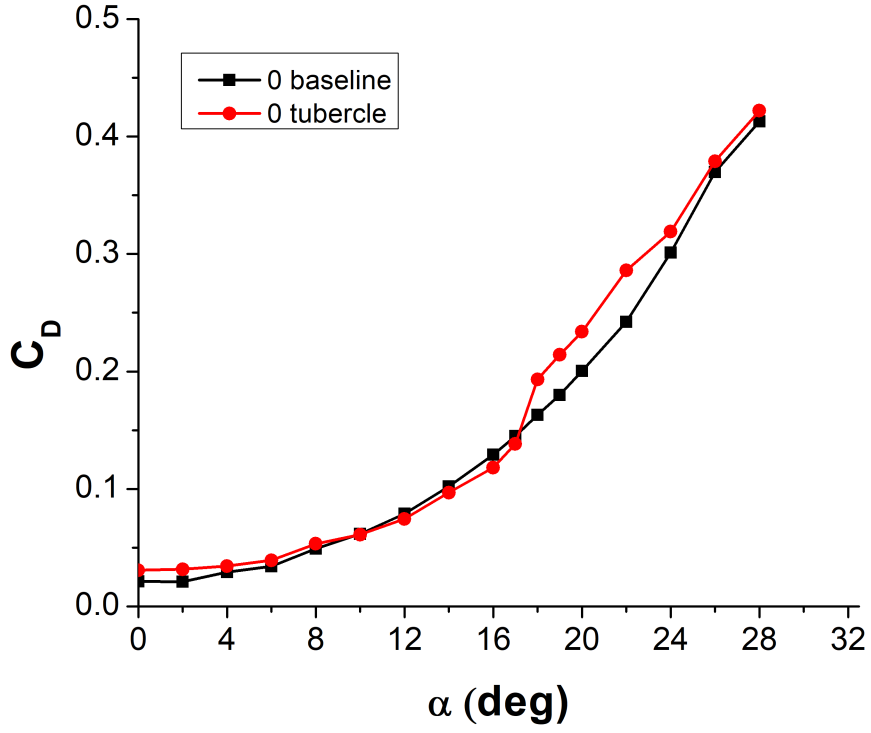

(b) Drag coefficient

Figure 4.20: Aerodynamic characteristics of baseline and tubercle blade at $Re_c = 6.5 \times 10^5$

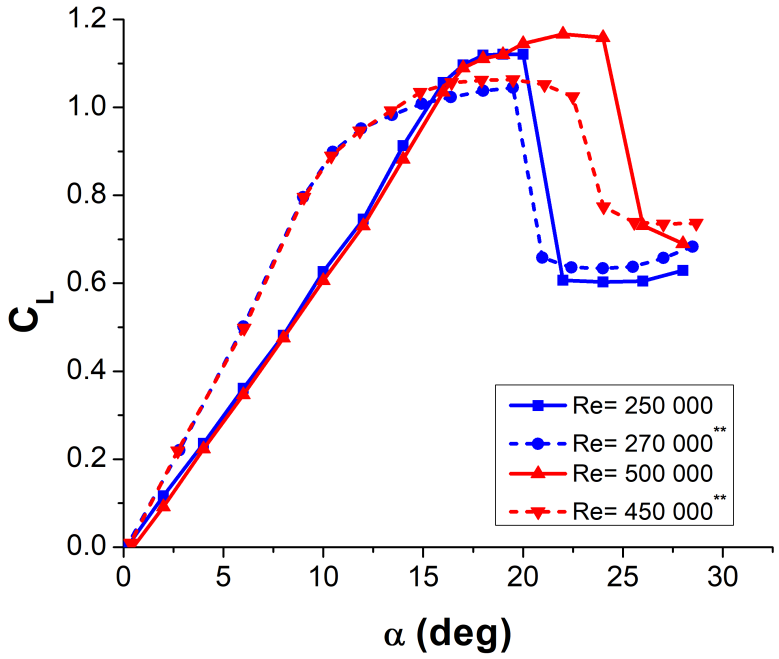

Figure 4.21: Comparison of lift coefficient of baseline blade with that of finite NACA 0020 airfoil obtained by Custodio *et al.* (2015)**

by Custodio *et al.* (2015) was water, whereas air is the working fluid in this study.

The effect of tubercles on the stall phenomenon of blades is further studied from the surface pressure distribution. Fig.4.22 shows the pressure distribution for both the baseline and tubercle blades in their respective stall AOAs. The tip sections (S1 and S9) on both have the least pressure along the chord-wise direction and gradually increase towards the blade's mid-span (S4 and S5) as expected for a finite wing. For the tubercle blade, pressure distribution along the span on the upper surface is also in the form of peaks and valleys. The suction peaks in the trough regions of the tubercle blade are higher than the suction peaks at the peak regions of the blade, as seen in Figure 4.22b The pressure on the lower surface of the blade is not significantly affected by the tubercles as it is on the upper surface.

Stall progression along the span of the blade with increasing AOA can be seen in Figures 4.23 to 4.25, where the surface pressure at three consecutive post-stall angles for each blade is depicted. Figure 4.23a shows the pressure envelope over the baseline blade at 22°. A constant pressure region extending from the leading edge to the trailing edge is seen over sections S4 and S5, indicating flow separation at these regions. Compared to the pressure distribution at stall angle (Fig. 4.22a), there is a decrease in pressure for all spanwise sections, which indicates loss of lift and during the stall. As the AOA is

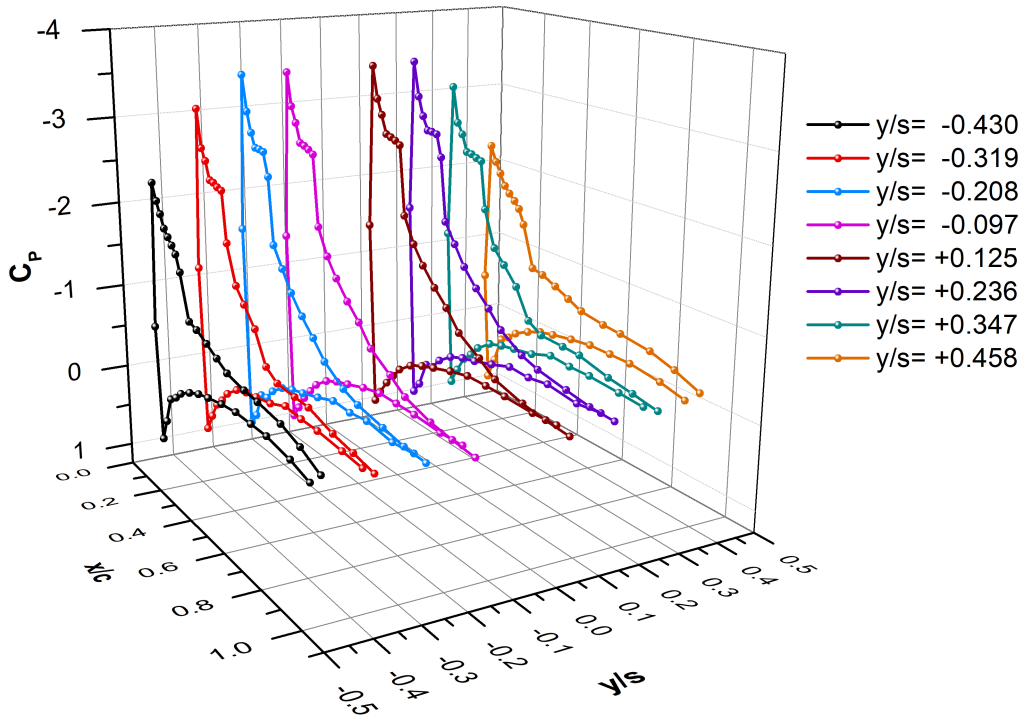

(a) Baseline blade at AOA=20°

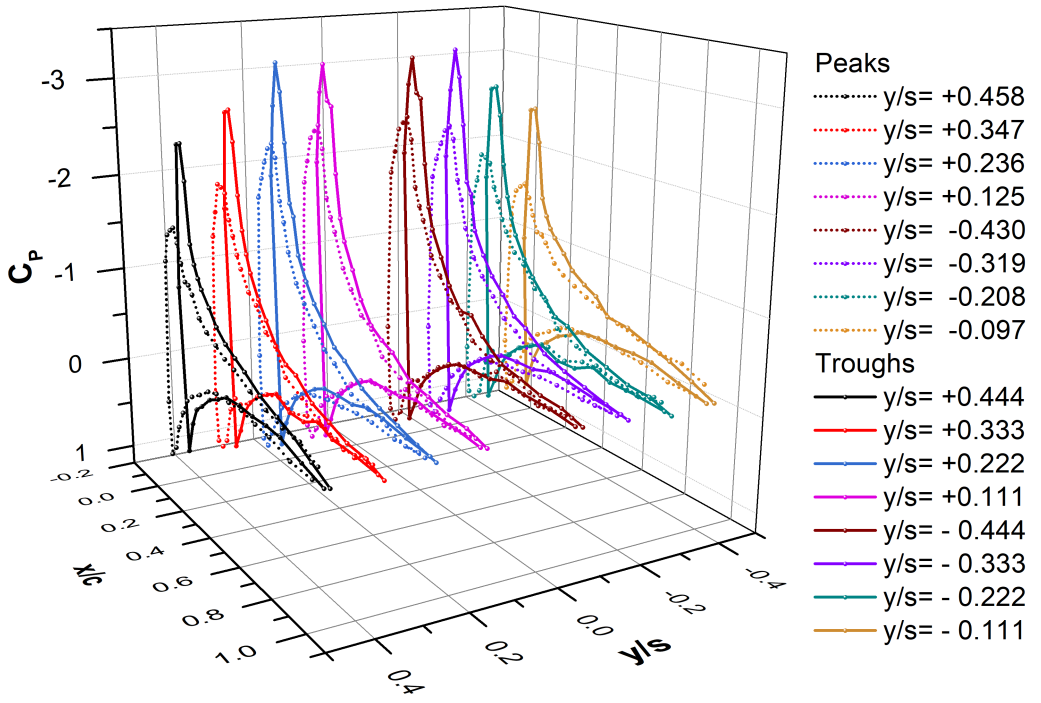

(b) Tubercle blade at AOA=16°

Figure 4.22: Spanwise pressure distribution for baseline and tubercle blade at stall region

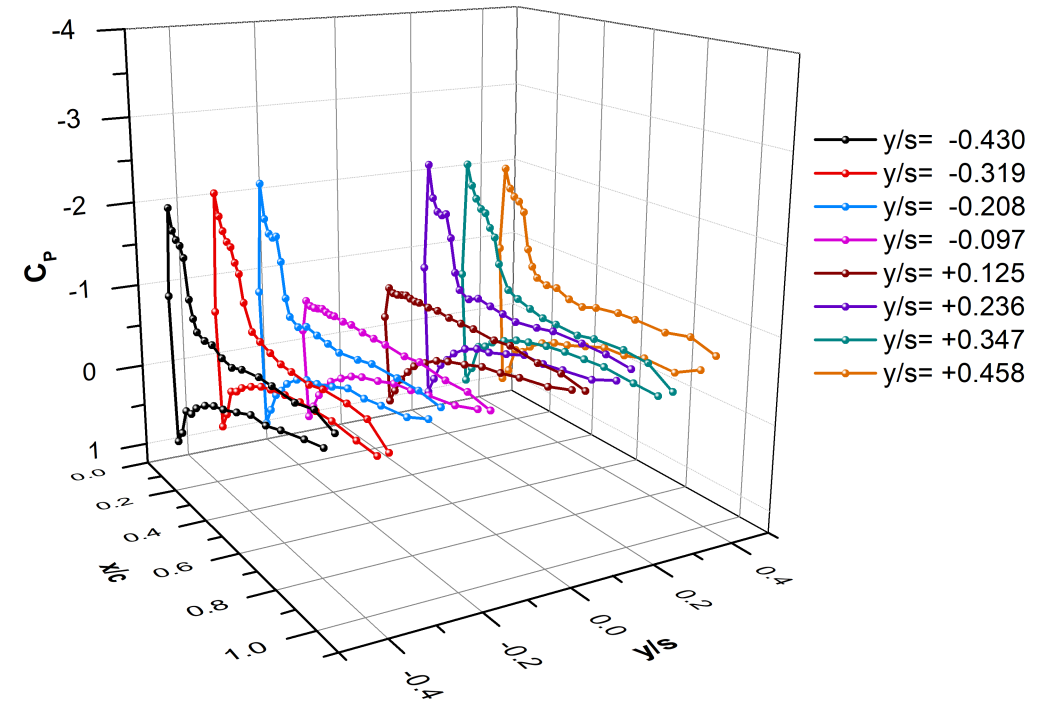

(a) Baseline blade at AOA=22°

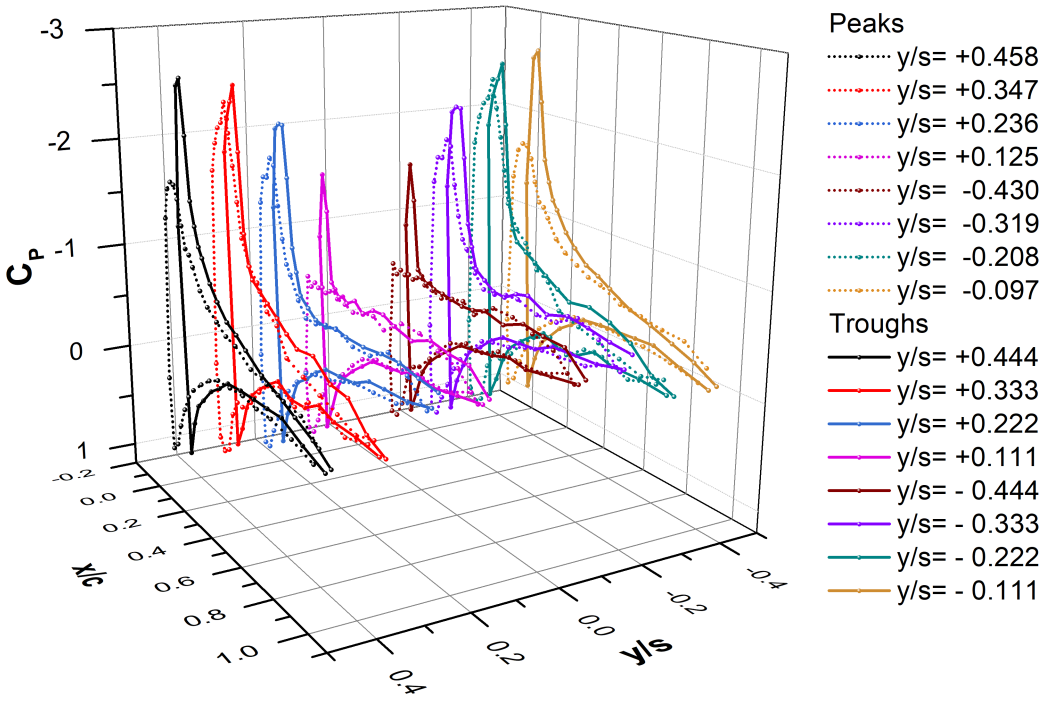

(b) Tubercle blade at AOA=18°

Figure 4.23: Spanwise pressure distribution for baseline and tubercle blades at first post-stall angle

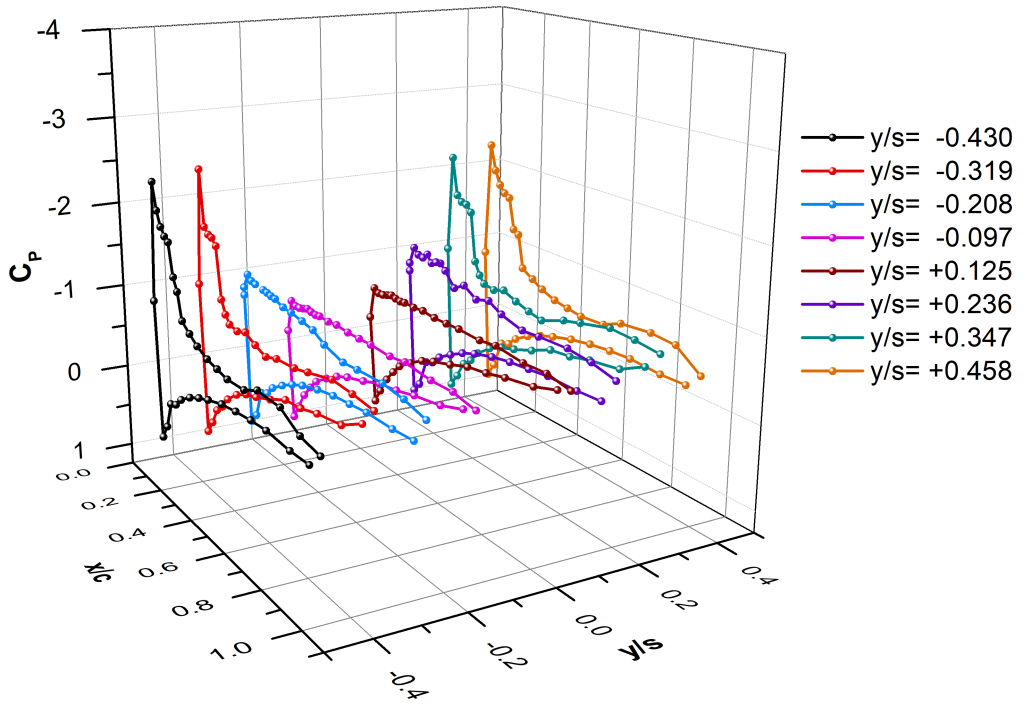

(a) Baseline blade at AOA=24°

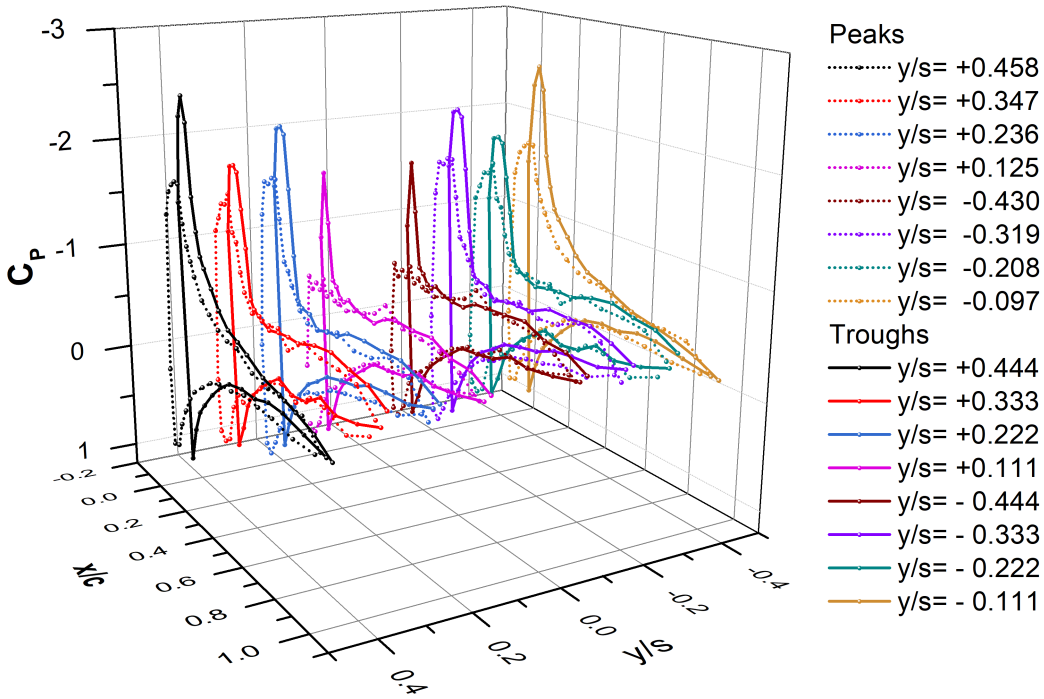

(b) Tubercle blade at AOA=20°

Figure 4.24: Spanwise pressure distribution for baseline and tubercle blades at second post-stall angle

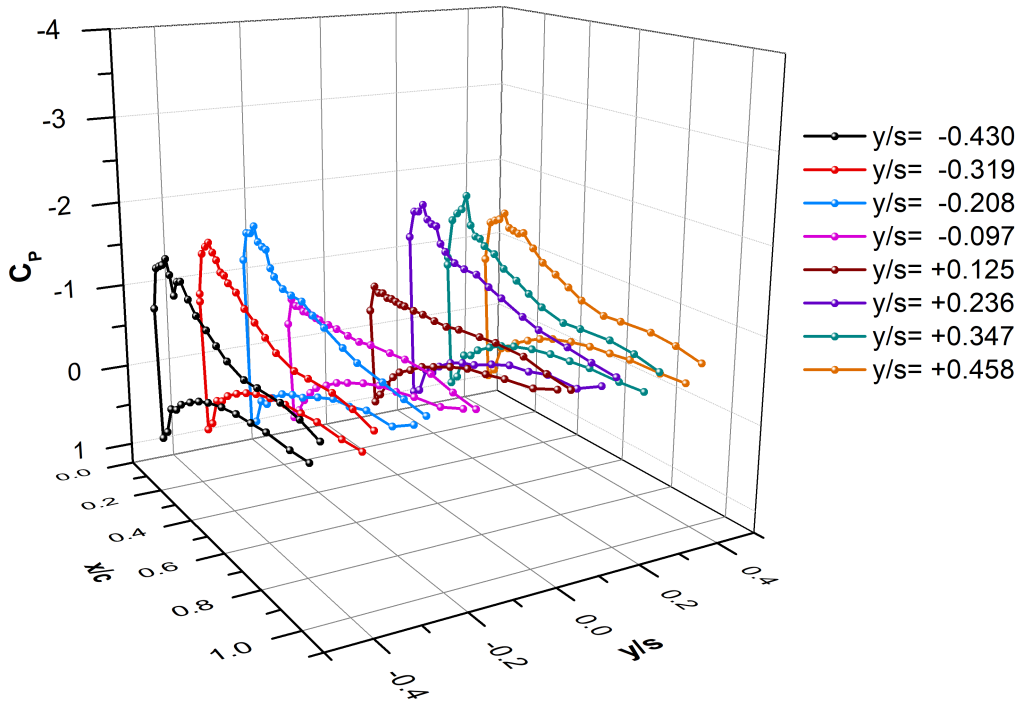

(a) Baseline blade at AOA=26°

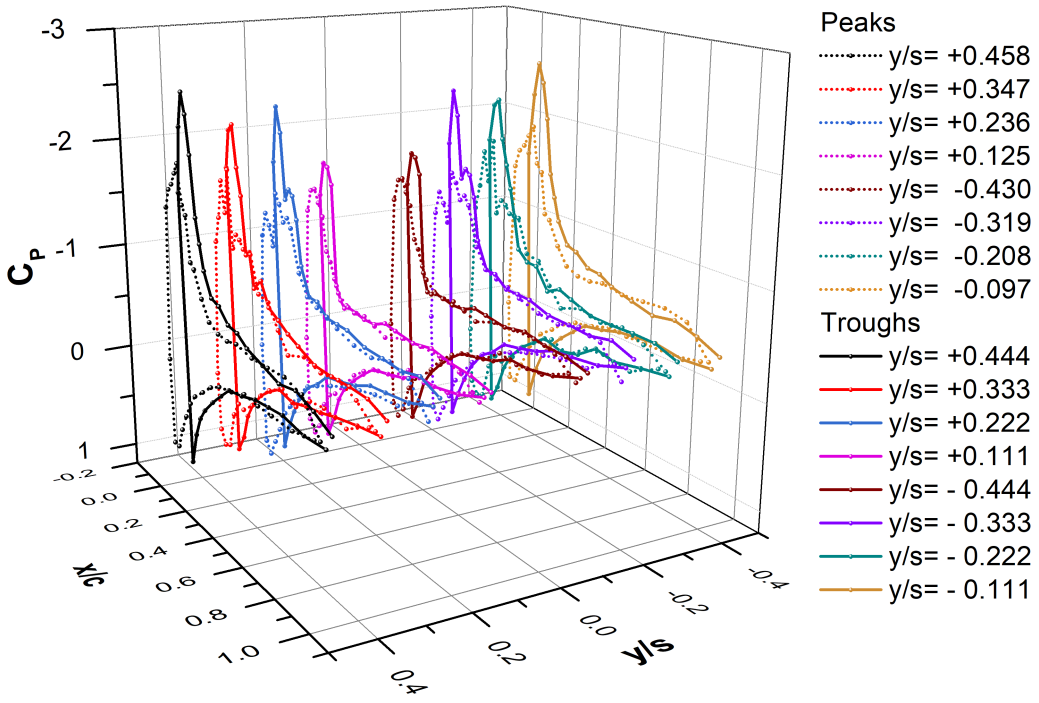

(b) Tubercle blade at AOA=22°

Figure 4.25: Spanwise pressure distribution for baseline and tubercle blades at third post-stall angle

increased to 24°, the region of flow separation has moved over to adjacent sections S3 and S6, as seen in Figure 4.24a). As AOA is further increased to 26°, as shown in Figure 4.25a, there is a drop in pressure for all spanwise sections. At α_{stall}, the maximum C_P over the tip sections S1 and S9 were close to -2.5, whereas at 26° it has dropped to about -1.5. Analyzing the Figures 4.23a, 4.24a, and 4.25a, it can be said that the stall initially occurs in the mid-span of the blade, which progresses towards the tips with the increase in AOA.

For the tubercle blade, at post-stall AOA of 18°, the flow separation over the mid-span of the blade (S4 and S5) occurs, as seen in Figure 4.23b. As AOA is increased to 20° (Figure 4.24b), there is a decrease in the pressure peaks when compared to that of 18°AOA. However, a rapid progression of flow separation from sections S4 and S5 to adjacent sections S3 and S6, as in the case of baseline blade, is not seen. Further increase in AOA (Fig.4.25b) causes a decrease in pressure for all spanwise sections, but the stall does not progress from the midsection to the blade tips. At AOA of 22°, the tubercle peaks on the tip sections still have a maximum C_P of -2.5 as it was during the stall angle. Thus, it becomes evident that tubercles on a blade prevent the stall progression from the mid-blade to the blade tips.

4.9.3 Hysteresis

Hysteresis characteristics of the blades are studied by conducting simultaneous force and pressure measurements for blades with increasing and decreasing AOA. Figure 4.26 shows the lift coefficient as a function of AOA for the baseline blade and tubercle blade. The linear region of the lift curve remains insensitive towards the direction of AOA change. The lift coefficient is identical in the linear region for increasing and decreasing branches of AOA. Hysteresis of the lift coefficient curve is seen between 14° and 28° based on the Reynolds number. The hysteresis loop is clockwise for lift coefficient (Fig.4.26a), similar to the one seen on a Lissaman-7769 airfoil (Mueller, 1985). As a result of hysteresis, C_L has a distinct value at a given AOA within the loop. For example, at $Re = 2.5 \times 10^5$, the $C_L = 1.04$ at AOA of 16° in the increasing branch, and 0.652 for the decreasing branch. Figure 4.26b represents the lift coefficient for the tubercle blade at the two extreme Reynolds numbers studied. The lift coefficients have close top identical values for increasing and decreasing branches of AOA. Therefore, no hysteresis can be seen on the lift curve of the tubercle blade.

Figures 4.27 and 4.28 depict the drag coefficient and moment coefficient, respectively,

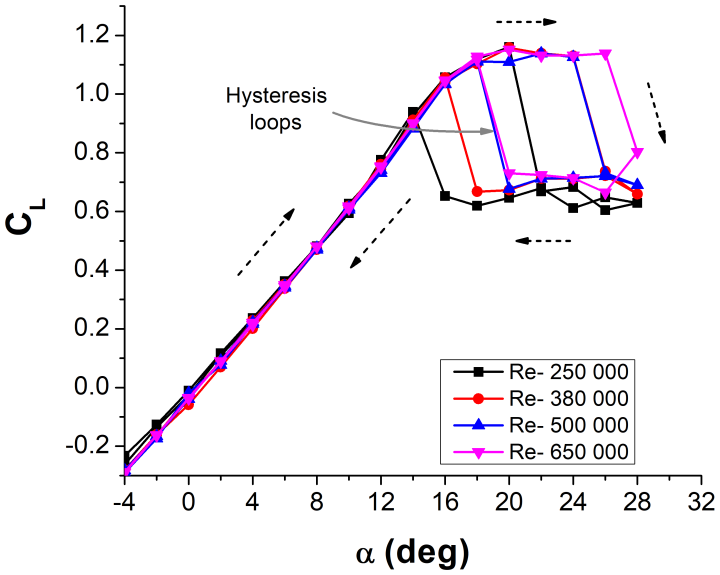

(a) baseline blade

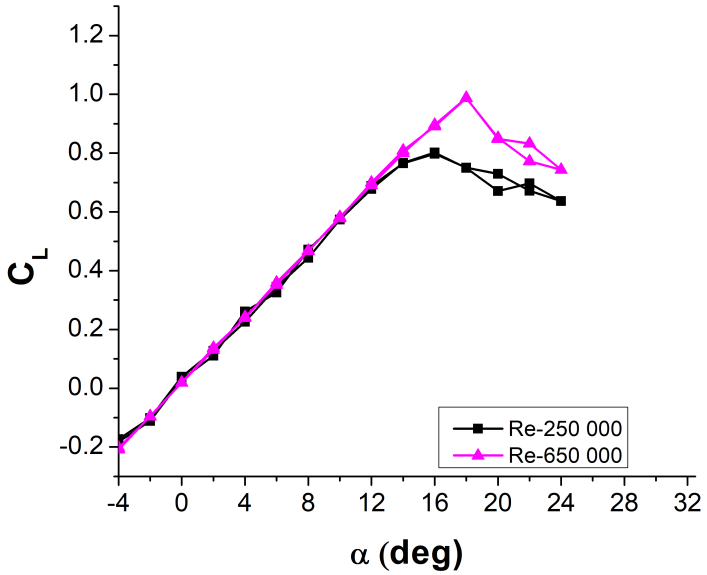

(b) tubercle blade

Figure 4.26: Aerodynamic coefficients showing hysteresis characteristics of baseline and tubercle blade

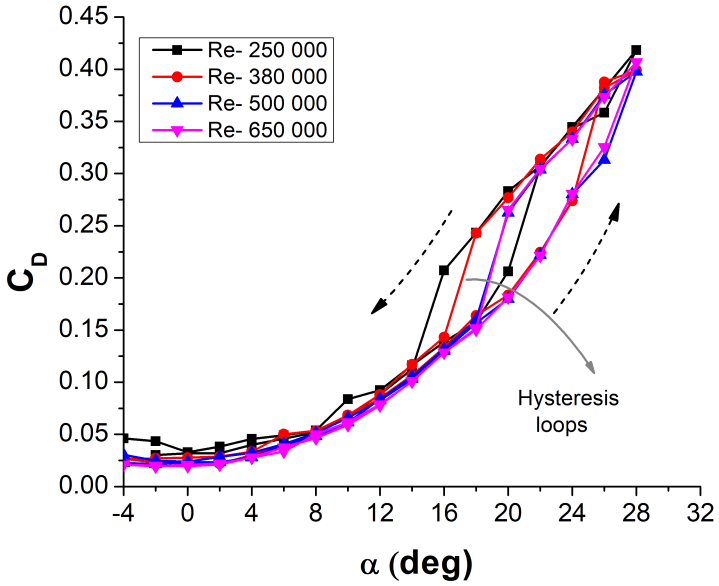

(a) Baseline blade

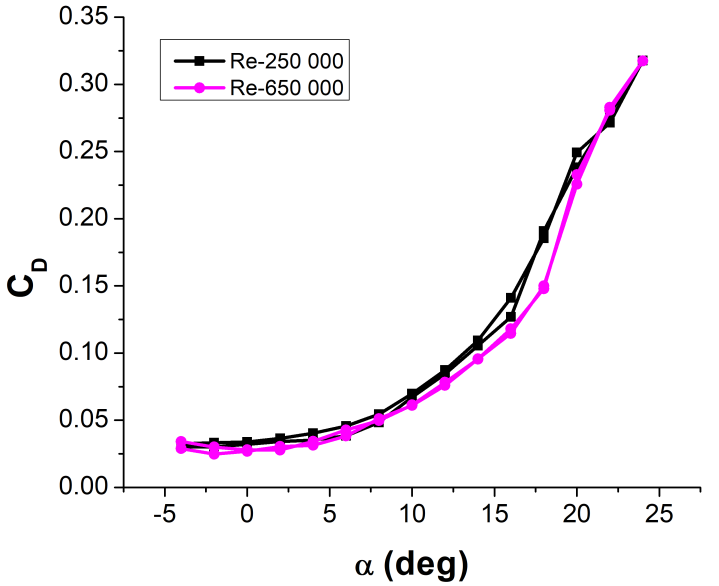

(b) Tubercle blade

Figure 4.27: Aerodynamic coefficients showing hysteresis characteristics of baseline and tubercle blade

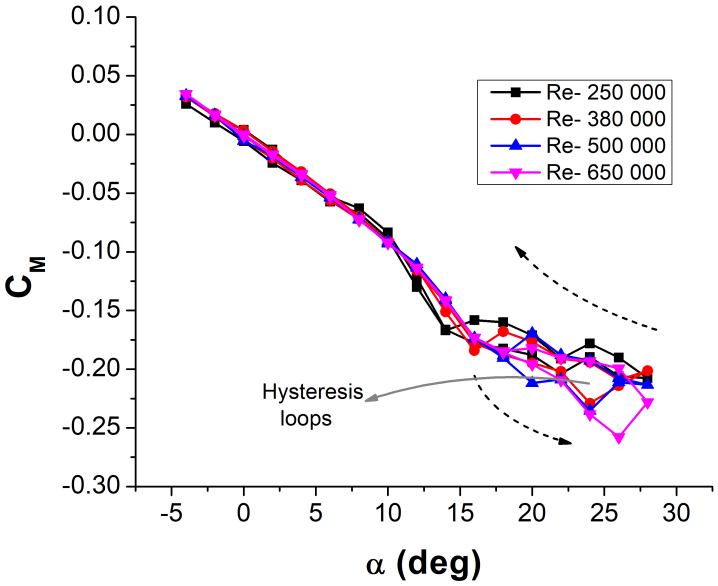

(a) Baseline blade

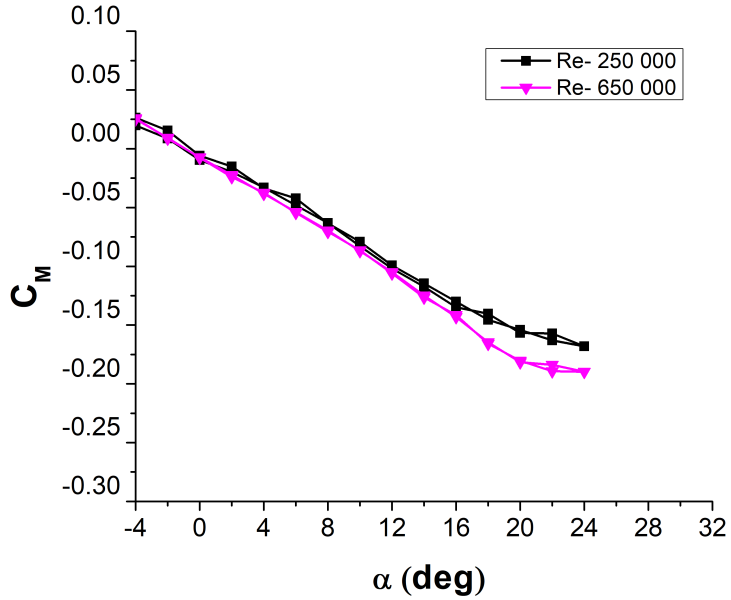

(b) Tubercle blade

Figure 4.28: Aerodynamic coefficients showing hysteresis characteristics of baseline and tubercle blade

Table 4.8: Hysteresis characteristics of baseline blade

Re_c	$C_{L_{max}}$	L/D_{max}	α_{stall}	α_{rec}	$\alpha_{h.l}$
2.5×10^5	1.122	8.96	20	14	6
3.8×10^5	1.158	9.16	22	15	7
5.0×10^5	1.164	9.84	24	16	8
6.5×10^5	1.172	10.48	26	17	9

for the baseline and tubercle blade. The baseline blade produces hysteresis loops beyond 14°AOA. The hysteresis loop is in anticlockwise direction for drag and moment (Fig.4.27a & 4.28a). Figures 4.27b and 4.28b represent the drag and moment coefficients for the tubercle blade. It is seen that no significant hysteresis is formed. Lift and drag curves trace the same path whether the blade was moving up (increasing AOA) or down (decreasing AOA). The absence of hysteresis for this blade helps it in easy stall recovery. The negative slope of the moment coefficient for the tubercle blade (Fig. 4.28b) is higher than that of the baseline (4.28a), implying higher stability of the tubercle blade in the post-stall region. The experiment was initially done for AOA changing in steps of two. However, once hysteresis was detected, force measurements were done again in steps of one to better understand the extent of the hysteresis loop. The hysteresis parameters of the baseline blade are detailed in Table 4.8. Fine-tuning of AOA could have resulted in obtaining an accurate extent of hysteresis. However, it can be seen that the size of the hysteresis loop increases with an increase in Reynolds number.

Surface pressure measurements are done to further analyze the effect of tubercles on hysteresis. Surface pressure is measured for static blades when the AOA is increased and decreased. From the force measurement, it is seen that $\alpha_{stall} = 20^\circ$ and $\alpha_{rec} = 14^\circ$ for the blade at a Reynolds number of 2.5×10^5. Therefore, the surface pressure measurement at $\alpha = 20^\circ$, which falls inside the hysteresis loop of the baseline blade, is depicted in Figure 4.29. The surface pressure on the lower side of the blade does not change significantly whether AOA is increasing or decreasing, whereas the pressure on the upper surface responds significantly to the direction of change of AOA. For the increasing angle, the C_P at the leading edge of the suction side was seen to rapidly reach its negative high, after which the pressure recovers over the blade. A pressure plateau (region of constant pressure) is seen at the chordwise location $x/c \approx 0.1 - 0.15$, beyond which a sudden increase in pressure occurs at $0.1 \leq x/c \leq 0.25$. Such pressure plateau followed by a sudden pressure rise indicates the formation of LSB Russell (1979), which can be seen between 11% and 25% of the chord. Further downstream boundary layer reattaches to the airfoil surface, causing pressure to recover gradually and smoothly. For AOA of 20°in the decreasing branch, the suction peak pressure was

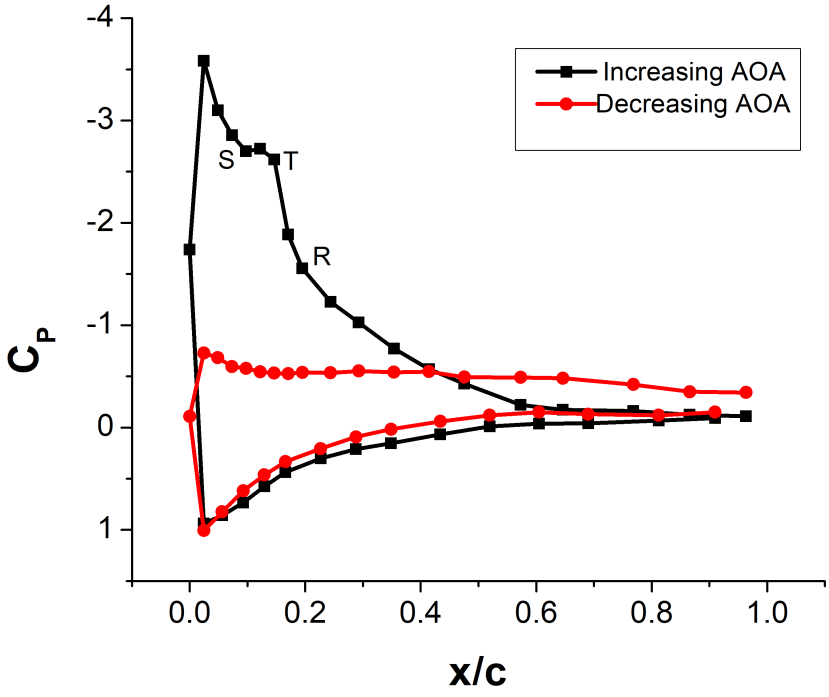

Figure 4.29: Pressure distribution of baseline blade in the hysteresis loop region, A0A= 20°

seen to decrease drastically. The surface pressure on the upper surface was seen to be nearly constant. Such a pressure distribution would indicate significant flow separation on the suction surface and thus stall. The pressure distribution over a baseline blade is consistent with a similar study on thick airfoil by Hu *et al.* (2007).

From the force analysis, it was seen that no particular region of hysteresis was present for the tubercle blade. Therefore, the surface pressure of the tubercle blade in the pre-stall and post-stall regions was analyzed. The α_{stall} for tubercle blade at $Re = 2.5 \times 10^5$ is 16°. Therefore we present the surface pressure at $\alpha = 14°$, which is the pre-stall region (Fig.4.30a) and $\alpha = 20°$ which is the post-stall region (4.30b). At AOA of 14°, there is a suction peak for trough and peak near the leading edge, followed by gradual pressure recovery. At 20°, the flow has fully separated in the peak and trough regions. At AOA of 14° and 20°, surface pressures in the trough and peak region of the tubercle blade remain almost identical irrespective of whether the AOA was increasing or decreasing.

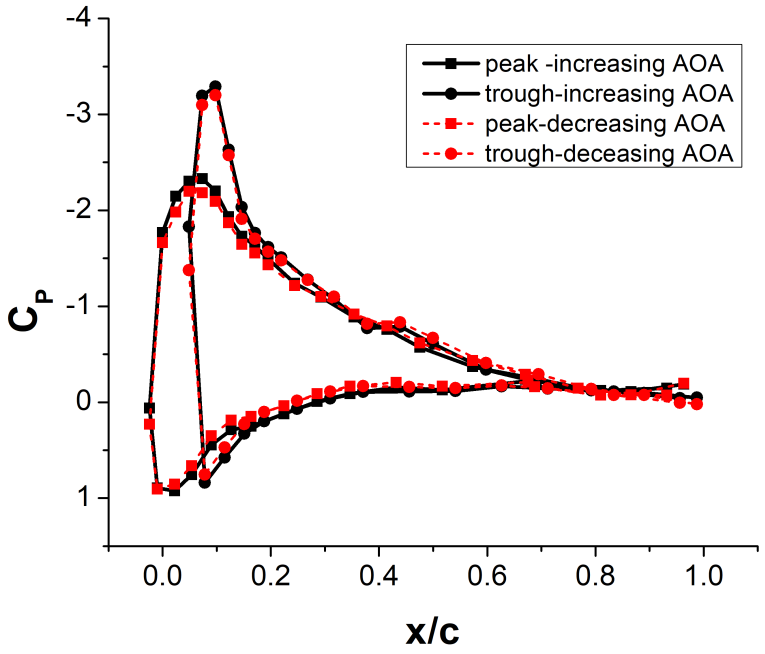

(a) Pre-stall region (A0A= 14°)

Figure 4.30: Surface pressure distribution of tubercle blade near stall region

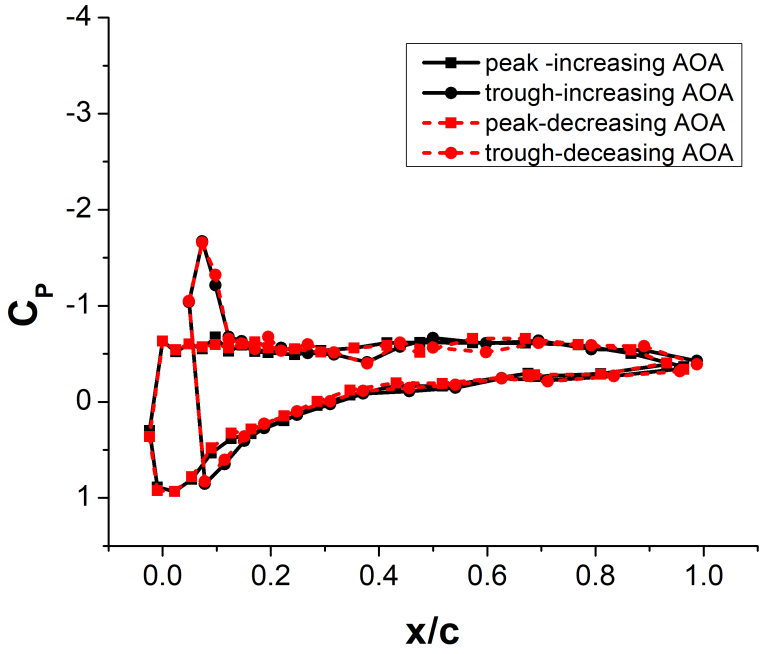

(b) post-stall region(A0A= 20°)

Figure 4.30: Surface pressure distribution of tubercle blade near stall region (cont.)

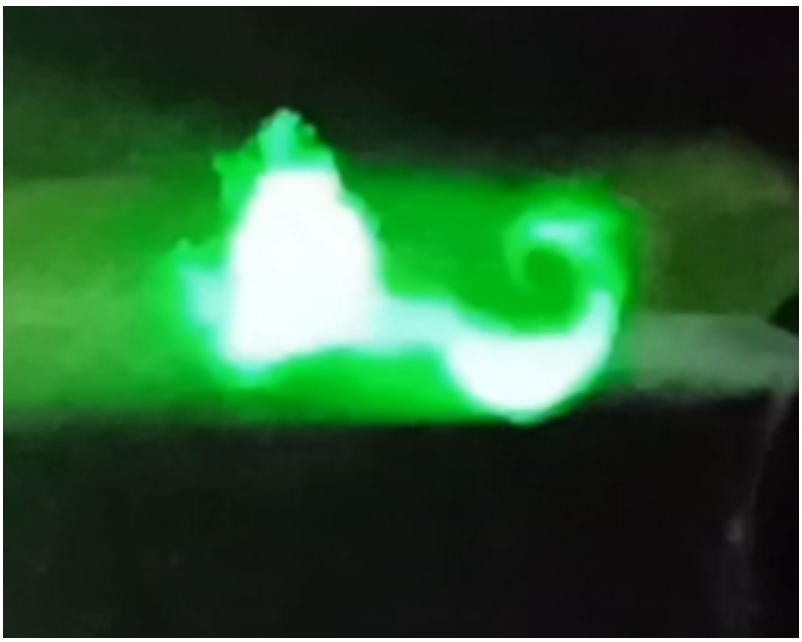

Figure 4.31: Counter-rotating vortices in the wake region of tubercle blade as seen in smoke visualization

4.9.4 Flow Control Mechanism of Tubercles

Smoke is released at the leading edge of the blade, and a plane in the wake region is illuminated using a laser. The illuminated plane in the wake region of the tubercle blade shows regions of counter-rotating vortices, as shown in Figure 4.31. The tubercles on the leading edge of the blade create counter-rotating vortices along the streamwise direction. The high-energy counter-rotating vortices energize the flow over the blade and prevent it from separating from the surface.

CHAPTER 5

EFFECT OF TUBERCLE PARAMETERS ON STEADY-STATE AERODYNAMIC CHARACTERISTICS

The study on the effect of tubercle geometry parameters on the static aerodynamic characteristics is done in this chapter. The aerodynamic performance of two distinct geometries of tubercles - sinusoidal and triangular-shaped tubercles is studied and compared. The effect of amplitude and wavelength of the tubercle is also studied by considering the A/W ratio. For this study, blades are tested at $Re = 5 \times 10^5$, and the steady-state forces acting on the blades are measured. The experimental procedure and results obtained from the steady-state analysis of blades are presented in this chapter.

5.1 Experimental Models

The experimental blade models for the steady-state analysis are designed using the same procedures described in chapter 3. The fabrication method is different from the approaches mentioned in previous chapters. The blades are made in a modular manner such that there is a common trailing section and many leading-edge sections. Figure 5.1 shows the different leading-edge sections used in the study, consisting of a baseline and six tubercle sections. Four tubercle sections are in a sinusoidal shape, and two are in a triangular shape of varying amplitude to wavelength ratio. The different amplitude to wavelength ratio is obtained by keeping the wavelength constant and changing the amplitude. One of the sinusoidal blades of amplitude and wavelength 20mm and 40 mm respectively (labeled as Sin-A/W=0.50) is identical to the blade mentioned in Chapter 3 and is considered as a reference. Keeping Sin-A/W=0.50 blade as a reference, three more sinusoidal blades are selected, one with lower A/W (Sin-A/W=0.25)and two with higher A/W (Sin-A/W=0.75 and Sin-A/W=1.00). The two blades with triangular LET- Tri-A/W=0.50 and Tri-A/W=1.00, have identical tubercle parameters as of Sin-A/W=0.50 and Sin-A/W=1.00, respectively. These models are also used to study the unsteady aerodynamic characteristic of the blades, which shall be discussed in the next chapter. The models are made from FRP to ensure the light weight required for

the unsteady flow study. The geometrical parameters of these models are detailed in Table.5.1.

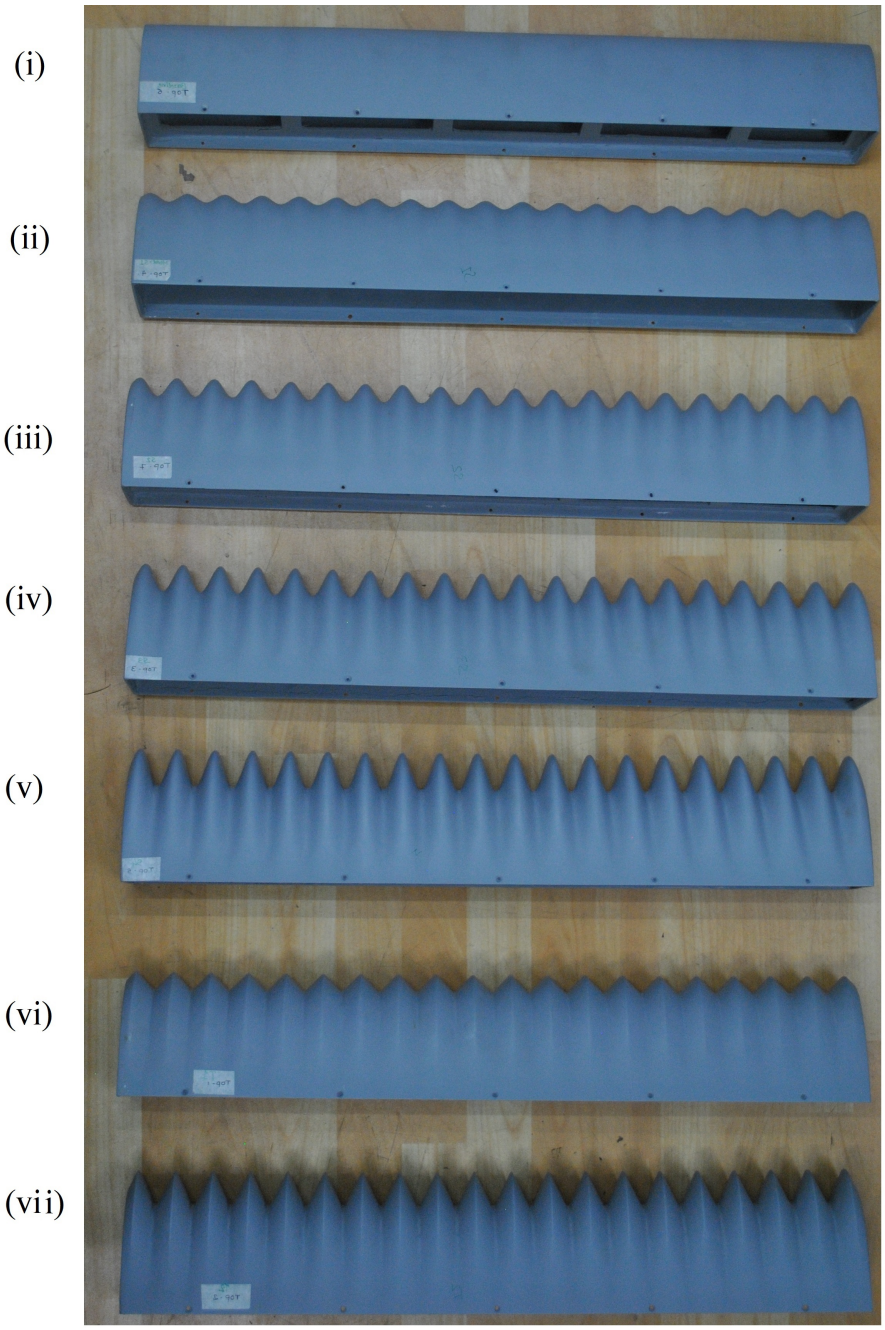

Figure 5.1: Leading-edge sections of blade models (i) Baseline (ii) Sin-A/W=0.25 (iii) Sin-A/W=0.50 (iv) Sin-A/W=0.75 (v) Sin-A/W=1.00 (vi) Tri-A/W=0.50 (vii) Tri-A/W=1.00

As shown in Figure 5.2, the common trailing edge section is fabricated so that sting and balance are connected to this section. An adapter is embedded in this section to which the internal balance would be fixed. This adapter is used to constrain the axial movement of the balance. The adapter also has a provision for a locking pin so as to

Table 5.1: Details of geometrical parameters of the blades used in dynamic study

Sl.No -	Label -	A (mm)	W (mm)	A/W -	c (mm)	s (mm)	Shape of the leading edge
i	Baseline	-	-	-	400	780	straight
ii	Sin-A/W=0.25	10	40	0.25	400	780	sinusoidal
iii	Sin-A/W=0.50	20	40	0.50	400	780	sinusoidal
iv	Sin-A/W=0.75	30	40	0.75	400	780	sinusoidal
v	Sin-A/W=1.00	40	40	1.00	400	780	sinusoidal
vi	Tri-A/W=0.50	20	40	0.50	400	780	triangular
vii	Tri-A/W=1.00	40	40	1.00	400	780	triangular

constrain the rotational motion of the balance. The balance is connected to the sting, which enters the model through a cut-out provided at the end. The adapter can be accessed by a removable panel. The trailing section fitted with the balance remains attached to the sting, and the leading sections can be replaced one after another after each experimental cycle.

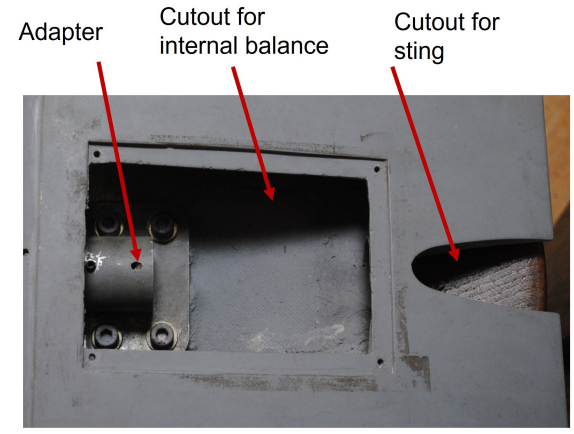

(a)

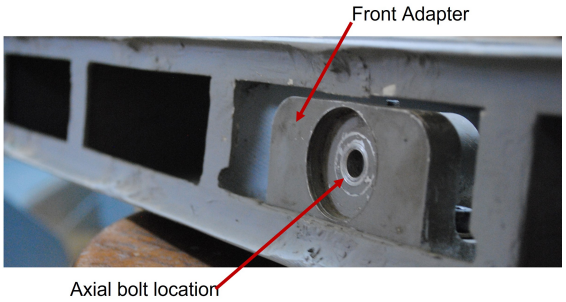

(b)

Figure 5.2: Standard trailing edge section of blade models

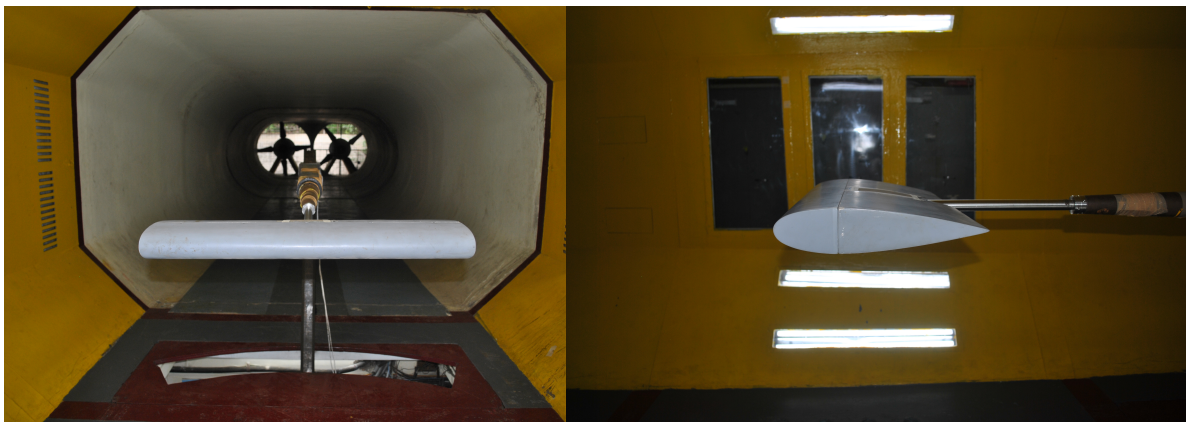

Figure 5.3: Mounting of blade models on tunnel sector arm

5.2 Experimental Setup

The steady-state analysis is conducted in Tunnel II, and the experimental procedure is similar to that explained in the previous chapter. The experimental model is mounted to the tunnel sector arm,and the tunnel is operated to maintain a flow velocity of 20m/s, which corresponds to $Re_c = 5 \times 10^5$. The force balance arrangement is slightly different from that described in Chapter 4. The force balance is fitted within the model without using any pylon, as shown in Figure 5.3. The experimental models do not have any strengthening elements in the spanwise direction, which gives ample space within the model to carry the force balance.

The balance used for the study is designated as WT 11 with reference to internal reports in the wind tunnel lab. The component rating of the WT11 balance is listed in Table 5.2

Table 5.2: Component rating for WT11 internal balance

Component	Rating
Normal force	80 kgf
Side Force	20 kgf
Axial Force	20 kgf
Pitching Moment	4 kg-m
Yawing Moment	2 kg-m
Rolling Moment	2 kg-m

5.3 Results and Discussion

5.3.1 Effect of Tubercle Parameters

The effect of tubercle amplitude and wavelength on the static aerodynamic characteristics is studied using blades of varying amplitude to wavelength ratio. Figure 5.4 depicts the lift characteristics for blades of sinusoidal LET (Figure 5.4a) and triangular LET (Figure 5.4b). As seen in Figure 5.4a, the slope of the lift curve for the Sin-A/W=0.25 blade is nominally greater than the baseline, whereas all other tubercle blades have a lower slope than the baseline. Though nominal, the slope of the blade decreases with an increase in A/W of the tubercles. The baseline attains a $C_{L_{max}}$ of 0.922 and stalls at an AOA of 25°. The C_L drops by 55% to 0.41 after stall. The blades with sinusoidal LET stall earlier than the baseline. The general trend is that the blade stalls more prematurely with an increase in A/W of the tubercles. For example, the blade with the lowest A/W tubercle (Sin-A/W=0.25) stalls at 22°, and the blade of the highest A/W (Sin-A/W=1.00) stalls at 17°. The $C_{L_{max}}$ for Sin-A/W=0.25 is slightly greater than the baseline. However, with increase in A/W the $C_{L_{max}}$ goes on decreasing for the sinusoidal LET blades. As discussed in the previous chapter, the advantage of sinusoidal LET is they help in attaining smooth stall characteristics. With increase in A/W the stall becomes smoother. The blades with sinusoidal LET has superior lift characteristics than the baseline in the post-stall regime. The tubercle with the lowest A/W has a maximum lift in the post-stall region. The lift decreases with an increase in A/W in the post-stall region.

The effect of the tubercle parameter is also studied using the blades of triangular LET. As shown in Figure 5.4b, tubercle blades stall earlier than the baseline, and the $C_{L_{max}}$ is lower than of baseline. The effect of tubercle parameters on lift characteristics for triangular LET is identical to that of sinusoidal LET blade. The lift characteristics of baseline, sinusoidal, and tubercle blades are summarized in Table 5.3. With an increase in A/W, the stall angle and $C_{L_{max}}$ decreases for blades with triangular LET. The loss of lift during stall decreases with an increase in A/W.

The drag comparison of sinusoidal and triangular LET with baseline is shown in Figures 5.5. As seen in 5.5a, the drag coefficient for baseline blade and blades with sinusoidal LET is identical at low AOA, $\alpha \leq 10°$. For $10° \leq \alpha \leq 17°$, the tubercle blades have a higher drag than the baseline nominally. Beyond 17°, which is the stall region, the drag of the tubercle blades is significantly higher than that of the baseline. The drag increases with an increase in A/W in the stall region. At high AOA, usually beyond

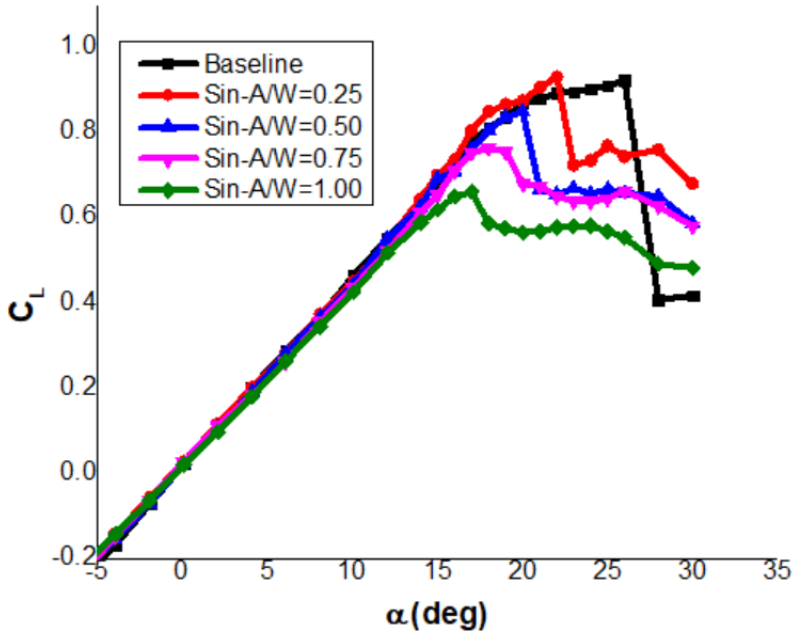

(a) Sinusoidal tubercle

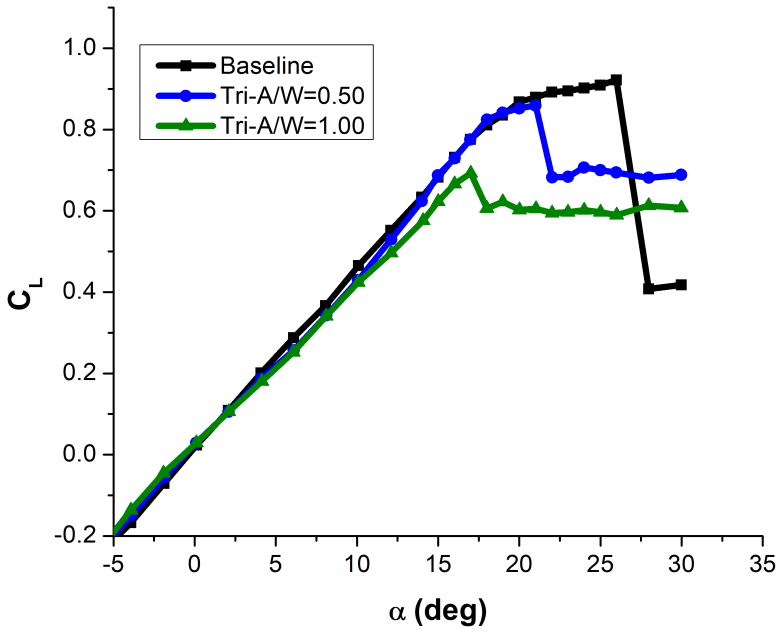

(b) Triangular tubercle

Figure 5.4: Lift characteristics for blades of sinusoidal and triangular LET at $Re_c = 5 \times 10^5$

30°the difference in drag coefficient for baseline and tubercle blade starts to diminish. Similar observations are made in the case of blades with triangular LET, as seen in

Table 5.3: Static lift characteristics of baseline and tubercle blades

Blade	α_{stall}	$C_{L_{max}}$	$C_{L_{p.s}}$	$\% \downarrow$ in C_L (after stall)
Baseline	25°	0.92	0.41	55.7
Sin-A/W=0.25	22°	0.93	0.72	22.2
Sin-A/W=0.50	20°	0.85	0.67	21.7
Sin-A/W=0.75	19°	0.76	0.68	10.5
Sin-A/W=1.00	17°	0.66	0.59	10.6
Tri-A/W=0.50	18°	0.86	0.68	20.9
Tri-A/W=1.00	17°	0.69	0.61	11.5

Figure 5.5b.

Figure 5.6 depicts the pitching moment about the quarter chord point for sinusoidal and triangular blades. For a given AOA, the nose-down pitching moment (negative pitching moment) is higher for sinusoidal and triangular tubercle blades than the baseline, indicating higher static stability of tubercle blades. A significant difference in nose-down pitching moment between baseline and tubercle blade happens beyond the stall angle. Blades of lower A/W have a higher negative moment than blades of higher A/W.

The effect of varying tubercle amplitude is closely identical for blades with sinusoidal and triangular LET. Both sinusoidal and triangular blades exhibit a decrease in $C_{L_{max}}$ and α_{stall} with an increase in A/W of the tubercle. The drag and nose-down pitching moment of blade increase with increase in amplitude to wavelength ratio of the tubercles.

5.3.2 Effect of Tubercle Geometry

The sinusoidal and triangular tubercles are similar, except that the sinusoidal tubercles are blunt. The effect of the tubercle geometry on the aerodynamic characteristics of lift, drag, and moment is depicted in Figures 5.7, 5.8, and 5.9, respectively. Figures 5.7a and 5.7a show the lift characteristic of the blades with the two distinct tubercle geometry at A/W=0.5 and A/W=1, respectively. It is seen that there is no significant change in the lift coefficient between blades of sinusoidal and triangular LET of corresponding tubercle parameters in the pre-stall region. A nominal increase may be pointed in the post-stall, but the improvement is very insignificant. However, at very high AOA, $\alpha \geq 27°$, the triangular LET attains greater lift than of the sinusoidal.

The drag coefficient also does not show a significant difference between a sinusoidal and triangular LET. The L/D curve depicted in Figure 5.10 shows the aerodynamic

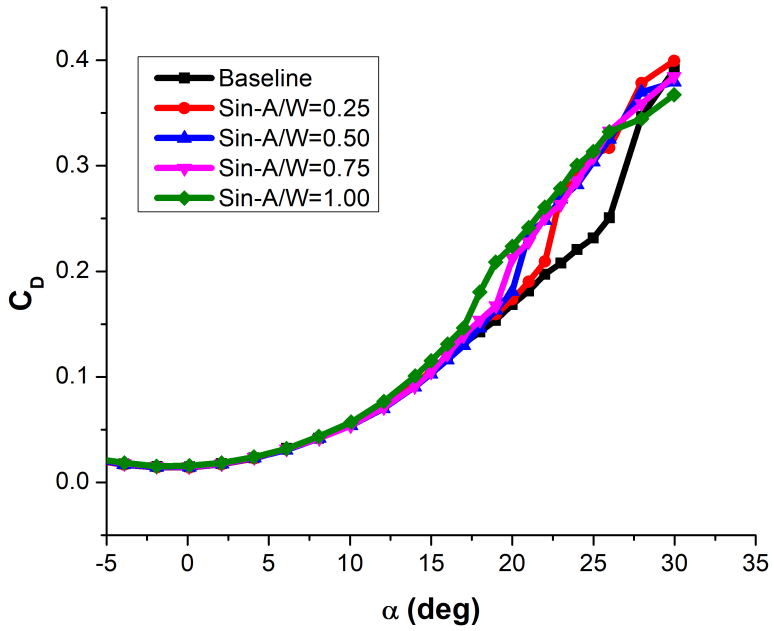

(a) Sinusoidal tubercle

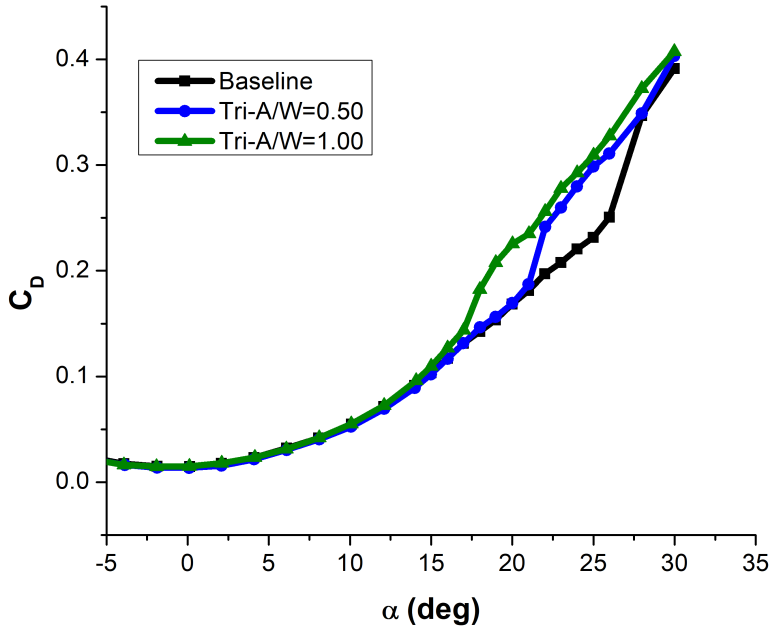

(b) Triangular tubercle

Figure 5.5: Drag characteristics for blades of sinusoidal and triangular LET at $Re_c = 5 \times 10^5$

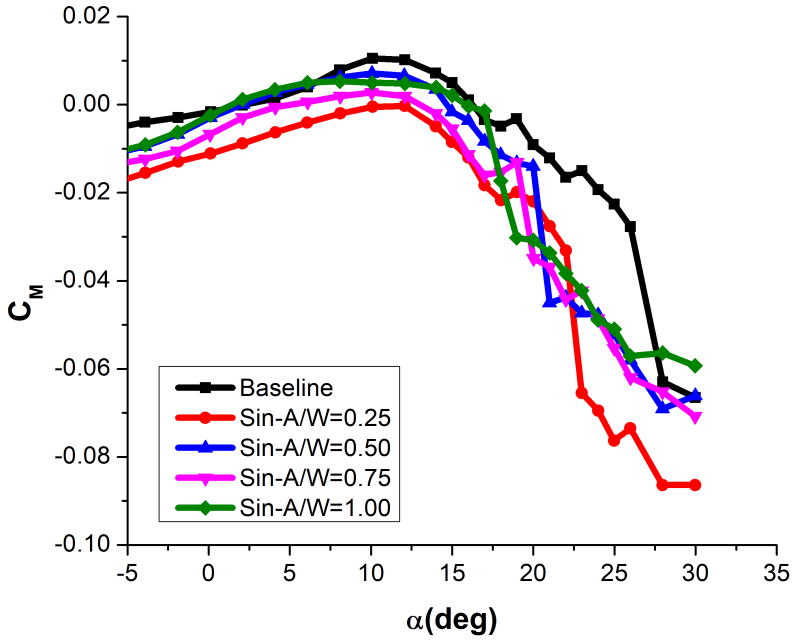

(a) Sinusoidal tubercle

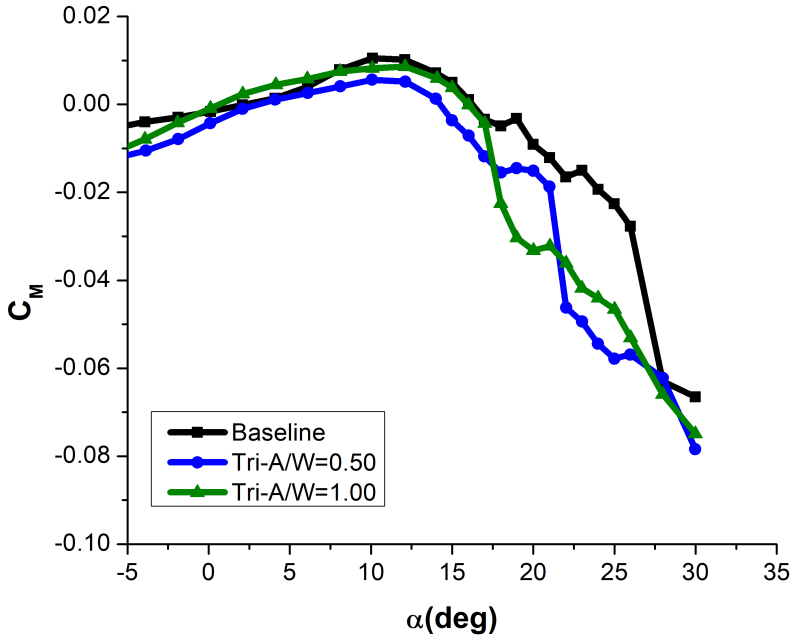

(b) Triangular tubercle

Figure 5.6: Moment characteristics for blades of sinusoidal and triangular LET $Re_c = 5 \times 10^5$

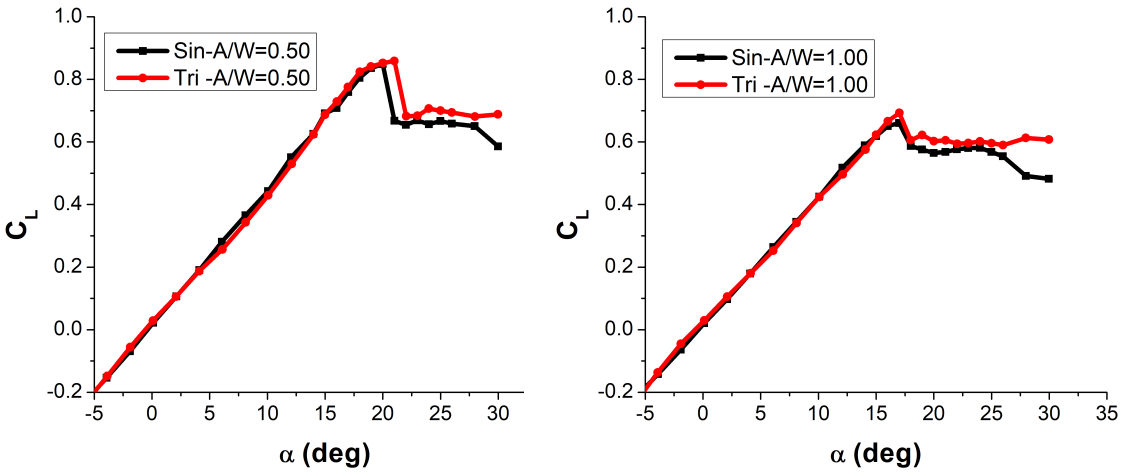

(a) A/W= 0.5 **(b)** A/W= 1

Figure 5.7: Comparison of lift coefficient for blades of sinusoidal and triangular LET

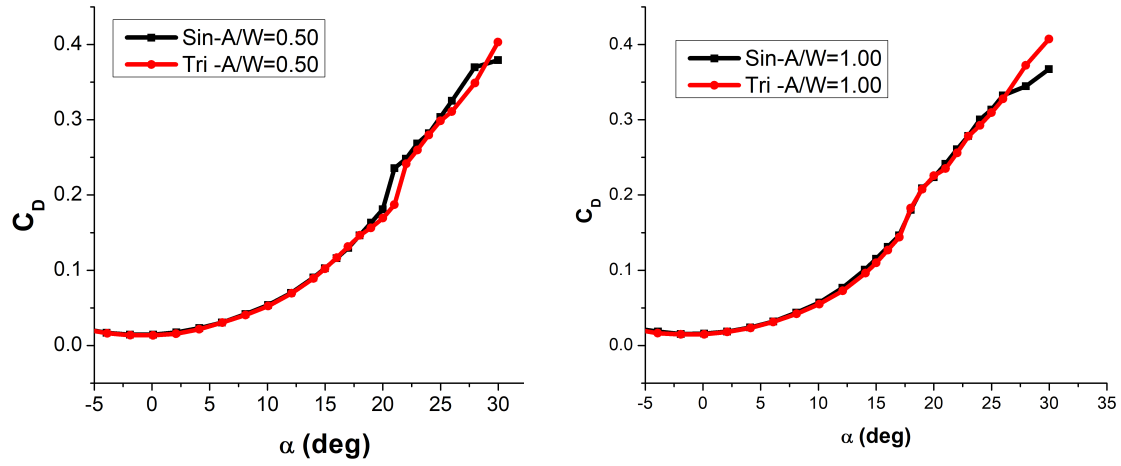

(a) A/W= 0.5 **(b)** A/W= 1

Figure 5.8: Comparison of drag coefficient for blades of sinusoidal and triangular LET

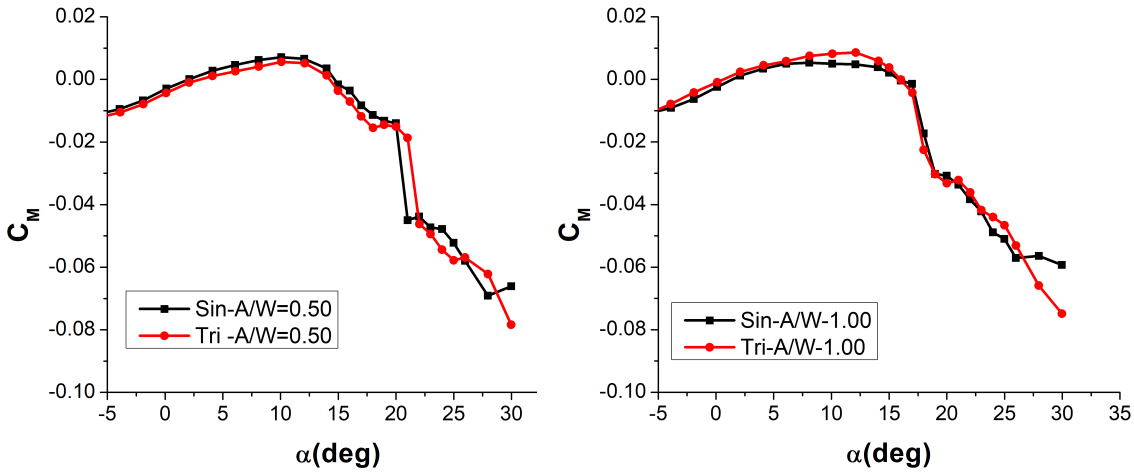

(a) A/W=0.5 **(b)** A/W=1

Figure 5.9: Comparison of moment coefficient for blades of sinusoidal and triangular LET

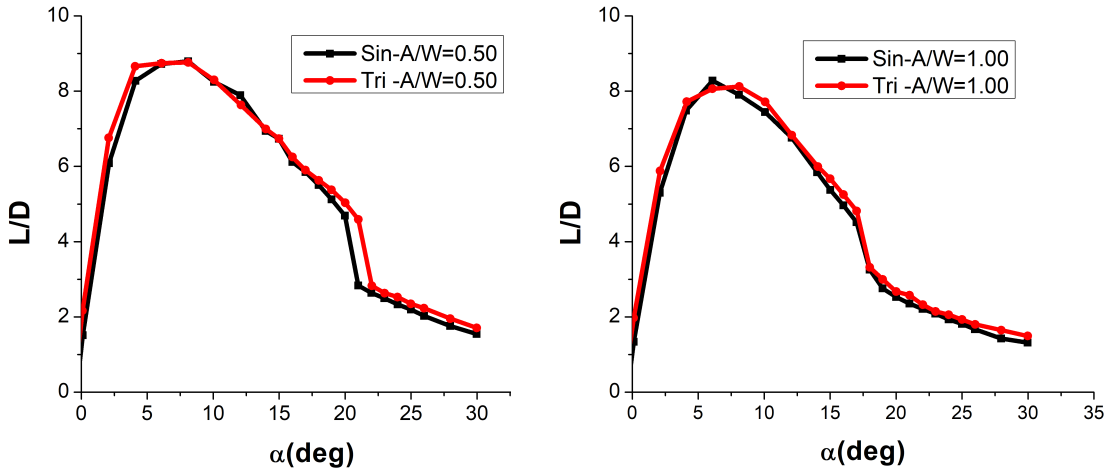

(a) A/W=0.5 **(b)** A/W=1

Figure 5.10: Comparison of L/D for blades ofsinusoidal and triangular LET

efficiency of both tubercle geometry. The aerodynamic efficiency for both sinusoidal and triangular tubercles of corresponding parameters remains almost the same. It can be said that the static aerodynamic characteristics are closely identical for sinusoidal and triangular tubercles. For static applications, sinusoidal or triangular LET can provide the same aerodynamic effects, especially when the operational range of AOA is low.

CHAPTER 6

EFFECT OF TUBERCLE PARAMETERS ON UNSTEADY STATE AERODYNAMIC CHARACTERISTICS

The key objective of this chapter is to investigate the ability of LET to control flow on a VAWT blade. The blade rotation is substituted with pitch oscillation, so the effective AOA changes continuously and periodically. The effect of tubercles, their geometrical parameter, and shapes on pitch-oscillating blades is studied in this chapter. The details of the experimental models and the experimental setup used in the study are explained in section 6.1. The results obtained and discussion is presented in section 6.2.

6.1 Experimental Setup for Dynamic Study

The experiments are conducted in Tunnel II. However, for the study of the dynamic blades, the experimental modes are not mounted on the sector as discussed in Section 4.4. The experiments require the blade model to be in continuous oscillation. Therefore the sting is removed, and the sector arm is fully retracted (Refer to Figure 4.8). The sector arm is completely hidden below the tunnel floor when fully retracted, causing no hindrance to the airflow. A specially designed rig called forced oscillation rig (FOR) or high alpha rig that can facilitate continuous oscillation of the experimental model is moved into the tunnel for the dynamic blade study. The schematic of the rig is depicted in Figure 6.1. A detailed description of the forced oscillation is given below.

6.1.1 Forced Oscillation Rig

The floor of Tunnel II is made of reinforced concrete with a provision for mounting FOR in the test section. Since the wind tunnel is used for various tests, the forced oscillation rig has to be installed during the dynamic tests and later dismantled and stored. Further, the rig is placed in the air stream; therefore a careful rig design is required from the point of tunnel blockage. The high alpha rig has a square platform 1900 mm long and

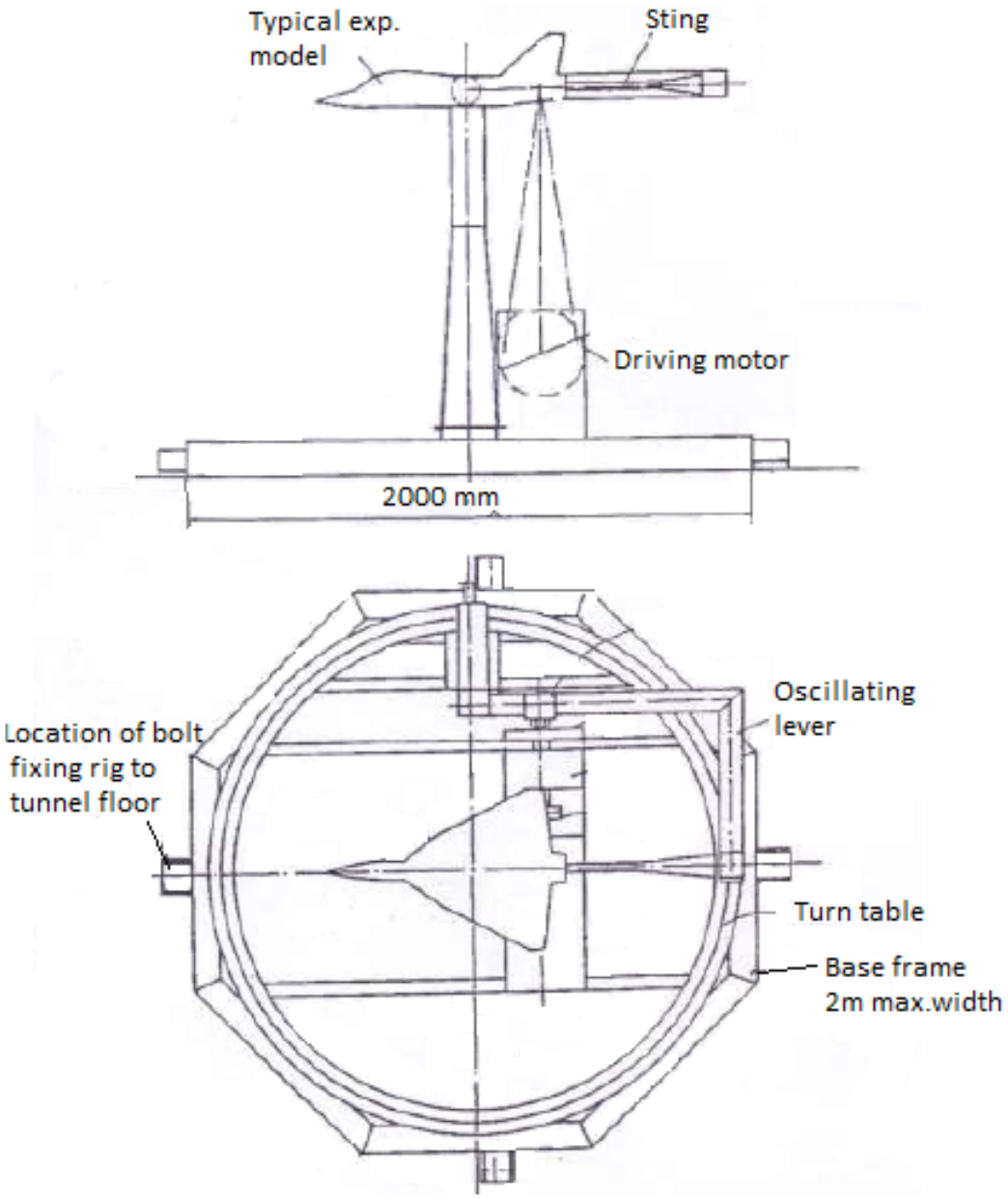

Figure 6.1: Top and profile view of high alpha rig

100 mm deep. The platform is provided with wheels and is fabricated from light steel tubes, and has a turntable bearing of a diameter of 1750 mm. The platform can be fixed to the test section floor by means of four through bolts and bushings. The turntable carries all hardware required for the oscillation rig. The main components of the rig, as shown in Figure 6.2 are:

1. Turntable

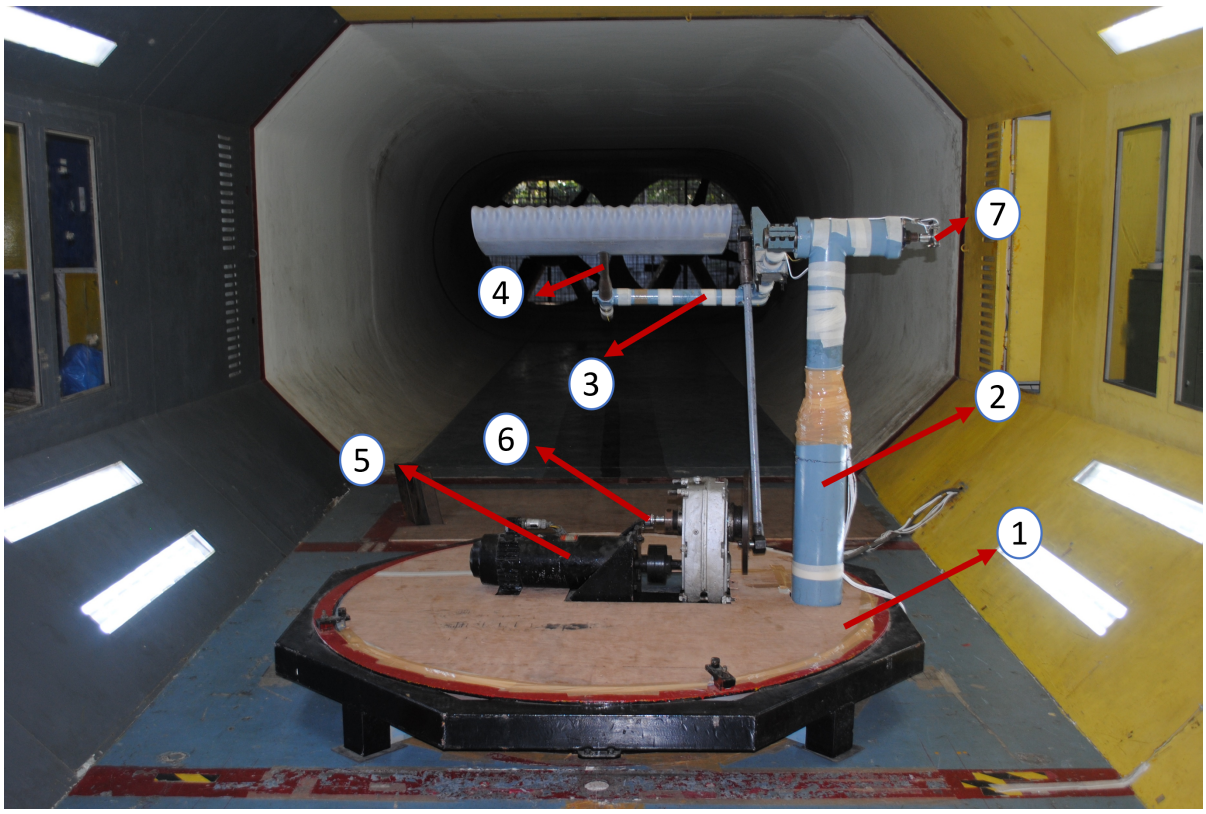

Figure 6.2: Main components of high alpha rig

2. Supporting column
3. Oscillating lever
4. Sting and balance
5. Drive system
6. Drive shaft position encoder
7. Oscillating lever position sensor

Turntable

The platform supports the turntable, which supports the vertical column carrying the oscillating lever and the drive system. The angular position of the turn table is indicated on the graduated scale. Provision is made for locking the turn table at any angular position by clamps that lock the races of the bearing together. This is done to ensure that the turn table does not rotate accidentally during the normal operation of the rig.

Supporting Column

The column is bolted to the turntable at the lower end and. It carries housings for the two bearings which support the shaft forming a part of the oscillation system consisting of the oscillating lever, sting, and the model. The shaft carries the oscillating lever on one end and a position encoder at the other. The supporting column has to be strong and has a larger diameter at the lower end.

Oscillating Lever

The oscillating lever is an L-shaped member fabricated from a steel tube of 7 mm diameter and is firmly attached to one end of the supporting column. The other end of the oscillating lever has the provision of securing the sting. This member is kept as light as possible to ensure that the inertia forces are as low as possible. The oscillation of this lever is made possible by a connecting rod fixed to the driving gear and a pin on the oscillating lever. The pin is provided with a suitable ball bearing. The pin can be fixed at a different location on the lever (on a specially fabricated fitting that can be bolted at any location on the lever) to vary the mean position and amplitude of the oscillation. The end of the lever that carries the sting is provided with a pinch fitting so that the rotation of the sting is possible. This ensures that both pitch and yaw oscillation can be performed without altering the oscillating lever in any manner.

It must be noted that if the model reference point is strictly along the axis of the tunnel and the turntable axis, the span of the experimental model would be limited to a maximum of 1 m. However, considering the large width of the tunnel, it would not make a significant change to the result even if the model axis is offset to the tunnel axis by around 0.3 m making it possible for models of span 1.2 meters to be tested without any changes. This would only require a new oscillating lever of greater arm length. An alternative is to enlarge the turntable and keep the model on the axis of the tunnel. But the enormous increase in weight and cost of the turntable makes it a less preferred option. Different oscillating levers can be easily fabricated based on the size of the experimental models. Models of span less than 1 meter are strictly aligned to the tunnel axis, whereas larger models would be slightly off the tunnel axis, which is acceptable considering the large size of the tunnel. The experimental models are 780mm in this study, and they are aligned to the tunnel axis.

Sting and Balance

The oscillating lever is connected to the experimental model through sting and balance. Different experimental models would require different lengths for sting, so that the axis of oscillation coincides with the reference point on the model. The model was fixed on the rig such that its axis of rotation passed through the center of gravity of the experimental model. The sting was reinforced to minimize twist and elastic deflection. The WT11 balance used in the static analysis is used for the dynamic force/moment measurement.

Drive System

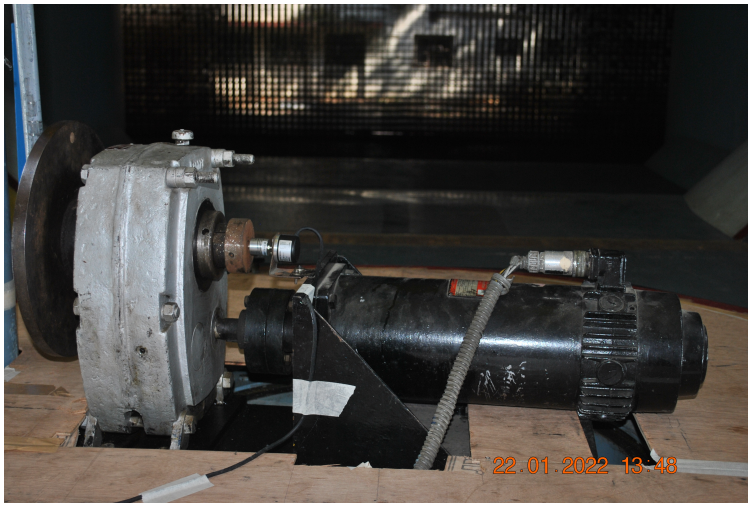

Figure 6.3: Drive system- Motor and gearbox

The drive system consists of a motor and a gearbox combination driving a crank disk, all mounted on a common base, as shown in Figure 6.3. The crank pin of the disc drives the connecting rod, which is connected to a driven pin carried on fitting mounted on the oscillating lever. The amplitude of oscillation can be varied by changing the position of the crank pin on the disc. Fine adjustment of the amplitude is possible by moving the drive unit on the turn table and simultaneously altering the position of the driving pin on the oscillating lever. Some provision is made for such an adjustment. It is also possible to vary the mean alpha by changing the position of the driven pin on the fitting carrying it.

Drive shaft position encoder

The drive unit is incorporated with a digital position encoder, as shown in Figure 6.4. The encoder produces signal once a revolution on one channel and certain number (up to 3600) of signals at equally spaced angular positions within a revolution. A computer can read the two channels of the signal and sequence all data acquisition operations with respect to the signal.

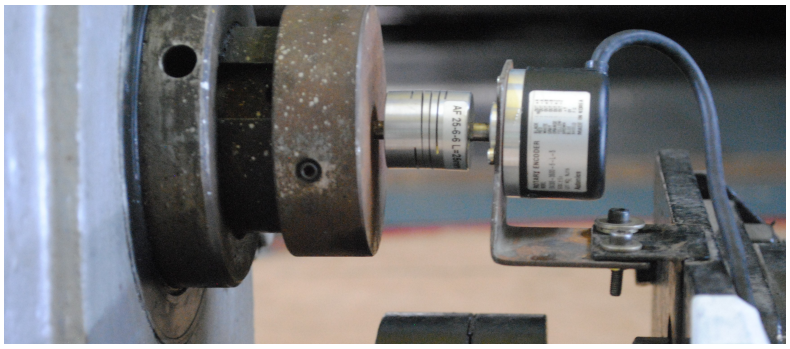

Figure 6.4: Encoder coupled with drive system

In order to acquire the aerodynamic information acting on the model that is executing periodic motion during the wind tunnel testing at regular intervals over several cycles a precise hardware trigger for data acquisition at pre-determined angle intervals is required. A pulse encoder was used in the experiment, which generates two types of pulses:

- One pulse/rev: M- pulse
- 360 pulses/rev: A- pulse

While the M pulse is used to mark the beginning of a revolution, the A pulse is used for angular resolution (1 °). The required hardware was implemented to acquire data at 1° interval, giving 360 points per revolution.

AOA position sensor

To obtain the aerodynamic forces at varying sting angles during an oscillation, both the balance data and the sting position are to be acquired at many positions during a cycle. For this purpose, a potentiometer-type position sensor is incorporated on the shaft connected to the oscillating lever, as shown in Figure 6.5. The computer acquires

both the balance signal and the potentiometer output on receiving timing signals from the drive unit position encoder on the gearbox shaft.

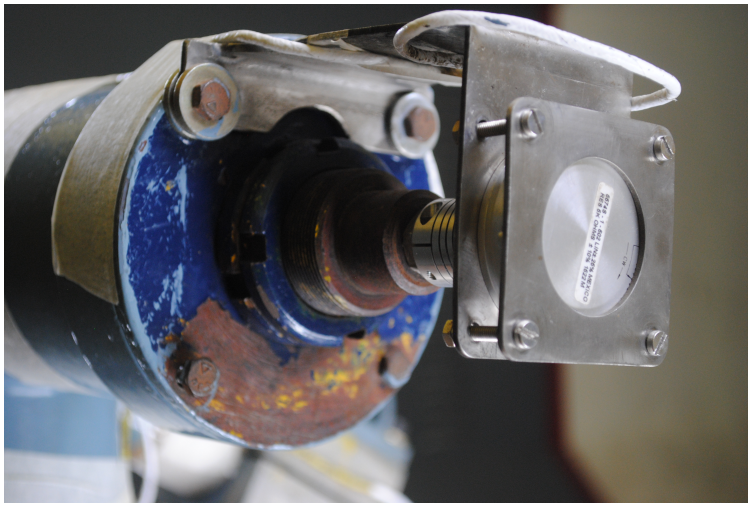

Figure 6.5: Potentiometer connected to lever arm

6.1.2 Requirements of Experiment model

The selection and fabrication of experimental models for dynamic measurement must be made considering several factors. One of the main requirements is that the model has to be lightweight. This is important because the inertial forces on the model depend directly on the mass and moment of the inertia of the model and the square of angular frequency of oscillation. The inertia of the experimental model should be kept as low as possible in order not to mask unsteady aerodynamic forces. The experimental model must be rigid to avoid distortion during dynamic testing. Proper selection of materials has to be done so that the model is not only rigid but also lightweight. FRP is used for model fabrication in this study. Yet another requirement is that the model size should be such that the blockage is minimum in the wind tunnel. The blockage factor should be less than 2%, so that reliable results without any compensation for the tunnel boundary layer can be obtained.

6.1.3 Model Mounting

The forced oscillation rig is moved to the wind tunnel and fixed to the floor with the sting axis aligned to the tunnel axis. The force balance is attached firmly to the sting of the forced oscillation rig, and any rotation is constrained using pins. The common

trailing section of the experimental model is slid onto the sting and balance. An adapter is fixed within the model (trailing edge section), as shown in Figure 5.2b, which is used to fix the model to sting by means of an axial bolt. Figure 6.6 depicts the connection between the front adapter and sting balance.

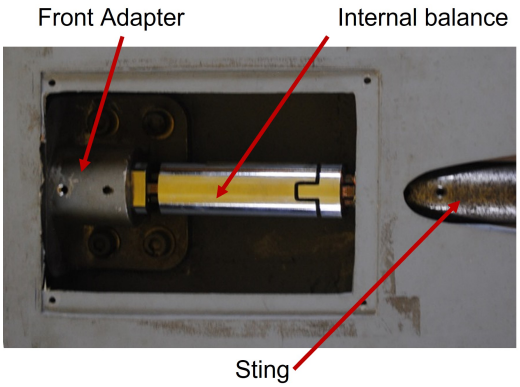

Figure 6.6: Connection of sting balance within the experimental model

The sting balance on the dynamic model is not placed at an offset from the center of gravity of the model as in te case of the static blade. It is placed within the trailing section and is aligned with sting, as shown in Figure 6.7

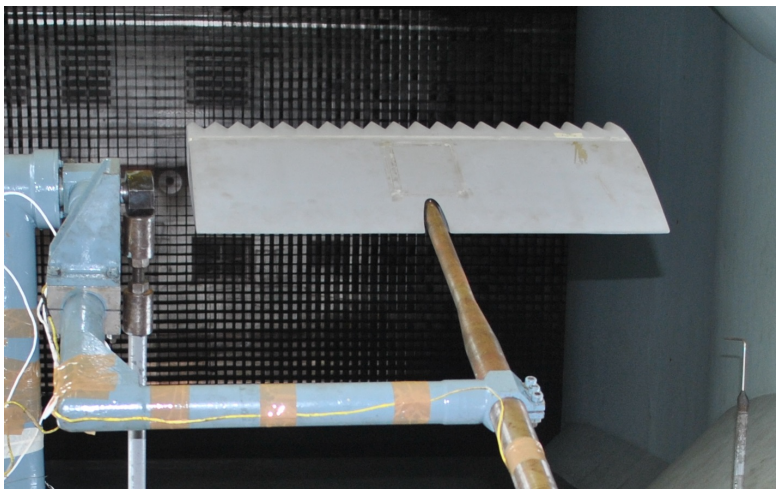

Figure 6.7: Mounting of dynamic blade models on high alpha rig

6.1.4 Data Acquisition (DAQ)

The sensors from the strain gauge detect the physical phenomenon and provide voltage output to the signal conditioning devices, which amplifies the detected signal and sends it to the data acquisition and modular instruments. Customized software was developed

with LabView for data acquisition using NI boards. The phase synchronous triggering was implemented in the software. The software has the provision for online waveform display. Data were acquired continuously by events marking the bias, wind-off, and wind-on segments. During the offline processing, it is required to specify the time intervals for extracting the relevant data from the collected data. The offline program uses the collected data and created data file, containing averaged sensor bias value, wind-off data vector, and wind-on data vector. These data files go as input to the load analysis program, developed in Matlab, for computing the motion time history in terms of non-dimensional body axis derivatives as a function of AOA.

Amplifier

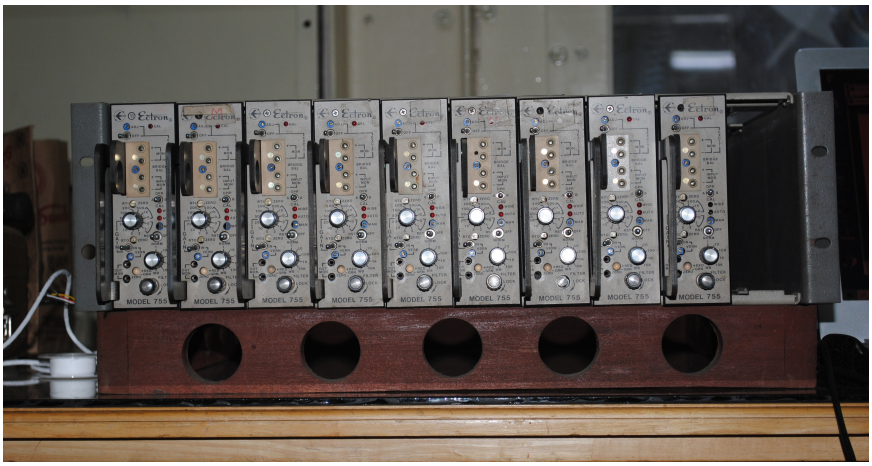

Figure 6.8: Amplifier Unit

A signal conditioning amplifier from Ectron Corporation, as shown in Figure 6.8 is used, which consists of a resistive transducer bridge which is a network of resistors whose resistance varies due to the change in some physical condition(i.e. change in strain as sensed by the strain gauges). It is impossible to produce an electrical signal proportional to these changes in the physical quantity, which can be amplified and used to monitor and control the physical process. The data acquisition system accepts the balance output data, outputs from the potentiometer for AOA, cyclic counts, and pulses for every revolution from the encoder. The amplifier can be used to obtain an input voltage of 1 to 10 volts and have a Gain setting of 1-2500. It also consists of Bessel filters that can be used with half and full-bridge configurations.

Figure 6.9 is the schematic of the phase synchronized for high alpha or forced oscillation rig.

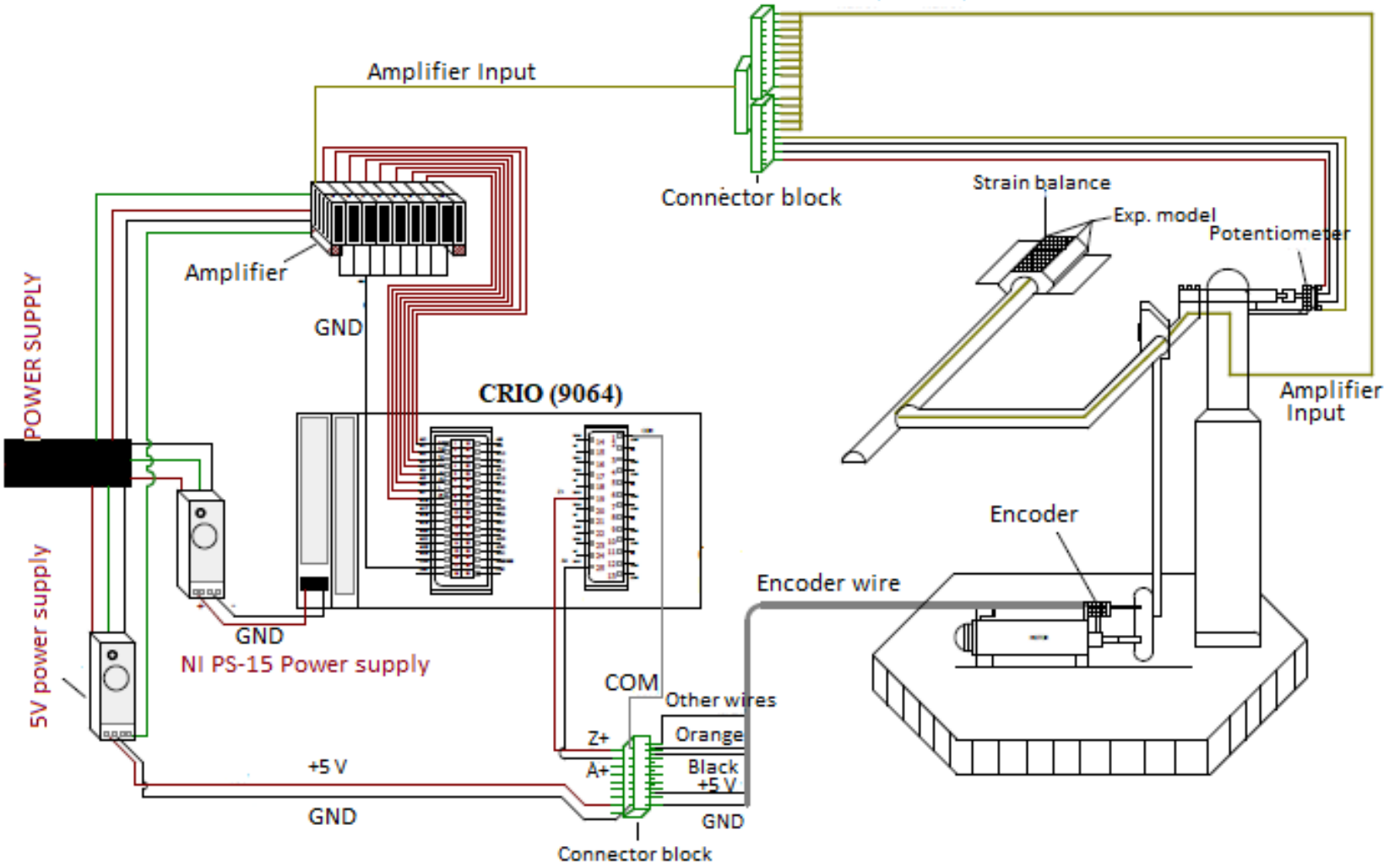

Figure 6.9: Schematic of phase synchronized data acquisition for high alpha rig

6.1.5 System Validation

The dynamic balance, after being mounted on the force oscillation rig, is subjected to a validation procedure same as that of the static test. The loading on balance is varied from 1 kg to 10 kg. Work back load was also computed by tying a kg weight to the balance and setting a low-frequency oscillation. Data were acquired over a few cycles, averaged, and analyzed. Variation of a 5kg load in the same range of AOA was numerically computed using Matlab. The results obtained from numerical and experimental procedures are depicted in Figure 6.10. The maximum difference obtained was less than 4%. This ensures that the data acquisition, phase synchronous sampling, load computation modules, amplifier, LabVIEW software are all working properly.

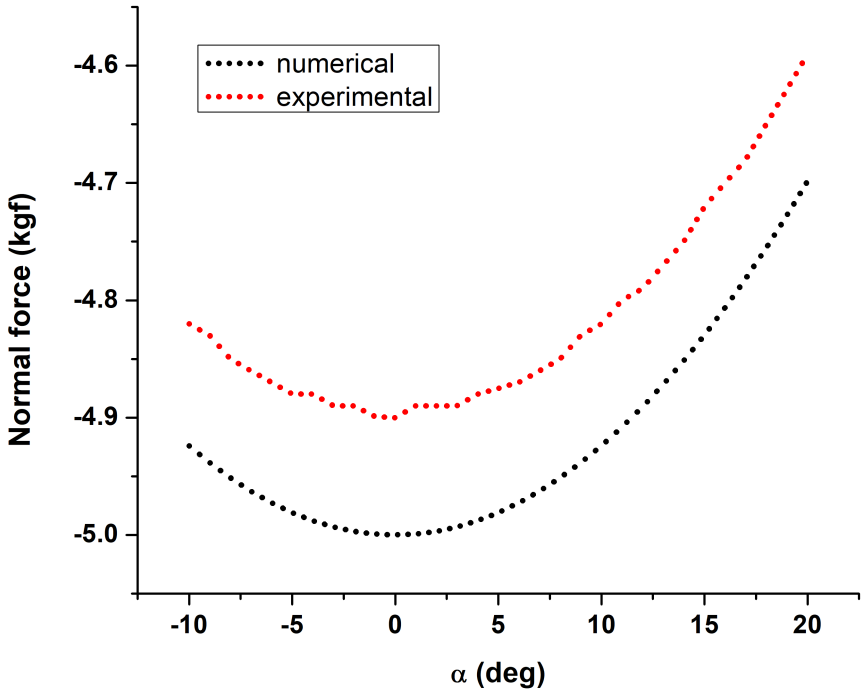

Figure 6.10: Work back loading on dynamic rig compared with calculated load

6.1.6 Working Method

While studying unsteady aerodynamics, an important parameter to take into account is the reduced frequency (k). Reduced frequency is a non-dimensional parameter used to

indicate the unsteadiness of flow given by equation 6.1.

$$k = \frac{\omega c}{V_\infty} = \frac{2\pi f c}{V_\infty} \tag{6.1}$$

Based on reduced frequency flow can be roughly classified as:

(a) Steady state:-$k = 0$
(b) Quasi-steady :-$0 \leq k \leq 0.05$
(c) Unsteady :- $k > 0.05$
(d) Highly unsteady:-$k > 0.2$

The FOR installed in the wind tunnel can provide oscillation at various angular rates (ω) by controlling the speed of the drive system. Thus the reduced frequency can be controlled either by changing the angular rate of oscillation or tunnel velocity (V_∞). Here, varied reduced frequency is attained by changing the rate of oscillation. Tunnel flow velocity, V_∞ is maintained at 20 m/, which corresponds to Re_c of 2.5×10^5.

6.2 Results and Discussion

In this section, we analyze the performance of dynamic blades incorporated with tubercles of different amplitude and geometry. Since the phenomenon of stall and hysteresis are best seen in the normal force coefficient curve, it will be used as the main tool in this part. To make a comparison with static results, the configuration of the tubercle blade used in static analysis will be used in the dynamic analysis also as a reference. The dynamic model, designated as Sin-A/W=0.50 has the identical wavelength and amplitude as the tubercle blade used in static blade study in Chapter 4, and shall be considered a reference together with the baseline blade.

6.2.1 Validation of Results

The oscillations of the blade is first conducted at a low range of AOA, $-8^\circ \leq \alpha \leq 24^\circ$, which is the linear region of lift on the static baseline blade. This is conducted to validate the dynamic experimental procedure. At very low reduced frequency, $k \leq 0.05$, the flow is considered to be quasi-steady and closely resembles the steady-state. Figure 6.11 shows the lift and drag coefficients of the oscillating blade at different reduced frequencies compared to the static results. At low reduced frequencies, k=0.0085 and

k=0.032, both lift and drag coefficients fully coincide with the static results. Oscillations in the low AOA range is conducted only for validation purpose, and further studies will be conducted for the high AOA range, $8° \leq \alpha \leq 35°$.

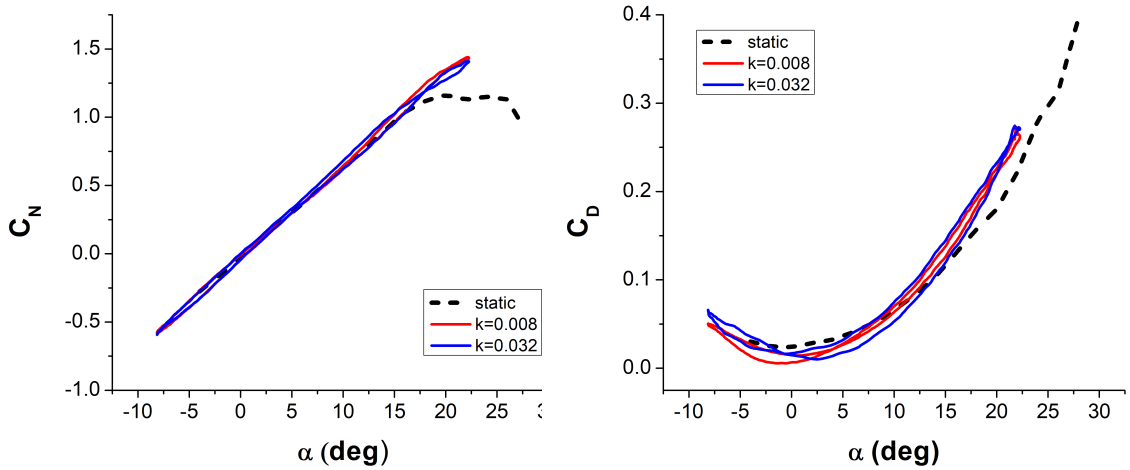

(a) Coefficient of normal force **(b)** Coefficient of axial force

Figure 6.11: Comparison of aerodynamic coefficients for static and dynamic blades at low AOA

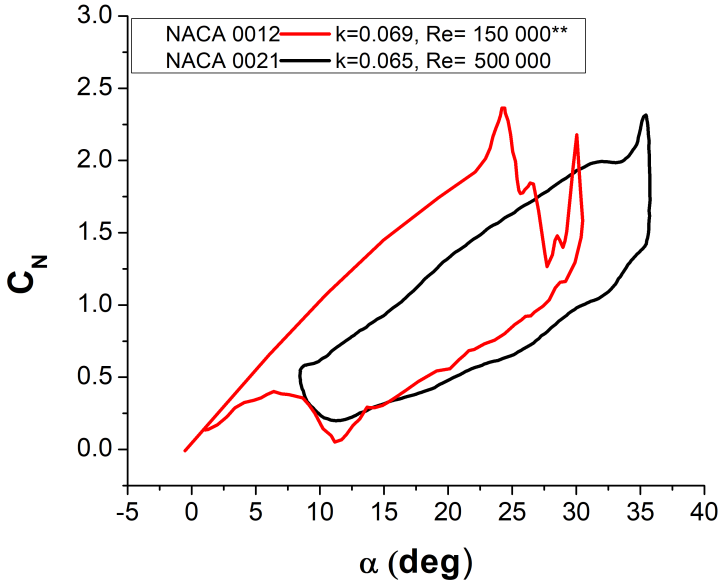

Figure 6.12: Comparison of normal force coefficient with Wei *et al.* (2021)

Further validation, especially at high AOA oscillation, is done by comparing the normal force coefficient to the results obtained in a similar study by Wei *et al.* (2021). They conducted an experimental study of NACA 0012 infinite wing/airfoil in pitch oscillation

at a tunnel velocity corresponding to $Re_c = 1.5 \times 10^5$. The current study is done for NACA 0021 finite wing at a tunnel velocity corresponding to $Re_c = 2.5 \times 10^5$. Though differences exist in the flow Reynolds number and the airfoil used, the experimental procedure closely resembles for both the studies. Figure 6.12 shows the comparison for C_N obtained in the current study at k=0.065 to the one obtained by Wei *et al.* (2021), which shows a close resemblance in the result obtained.

6.2.2 Effect of Reduced Frequency

Figures 6.13a and 6.13b show the variation in normal force coefficient for baseline and tubercle model (Sin-A/W=0.50), respectively, at different reduced frequencies. The steady-state normal force coefficient, C_N obtained from the static blade studies has been included. For the baseline blade, as seen in Figure 6.13a, there is a significant increase in normal force for the oscillating/ pitching blade as compared to the static blade due to the formation of DSV. The DSV is characterized by a small plateau on the force coefficient curve followed by a sudden increase in its slope, as seen on Figure 6.13a (more clearly on Figure 6.16c). With increase in AOA, the forward-moving reversed flow creates a strong suction vortex at the leading edge. With further increase in AOA, this leading-edge vortex (LEV) separates from the airfoil and forms DSV. As AOA further increases, the convection of DSV towards the trailing edge starts. At the same time, secondary vortices are created on the leading edge, and the onset of vortices also begins at the trailing edge. The trailing edge vortices and DSV completely detach from airfoil when AOA is further increased, causing complete flow separation and thus the dynamic stall (Wei *et al.*, 2021). The formation and convection of DSV are important in the dynamic stall process. From the C_N curve of the baseline blade, it can be seen that DSV formation and convection are prominent, and it increases with an increase in reduced frequency. The size of the hysteresis loop increases with increase in reduced frequency. A similar trend is observed for the tubercle blade. Maximum lift coefficient increases with an increase in reduced frequency. The size of the hysteresis loop also increases with an increase in reduced frequency. However, the DSV characteristics are not present for tubercle blades even at very high reduced frequencies. There is a significant difference between the stall and hysteresis characters of baseline and tubercle blades which shall be discussed in the following section.

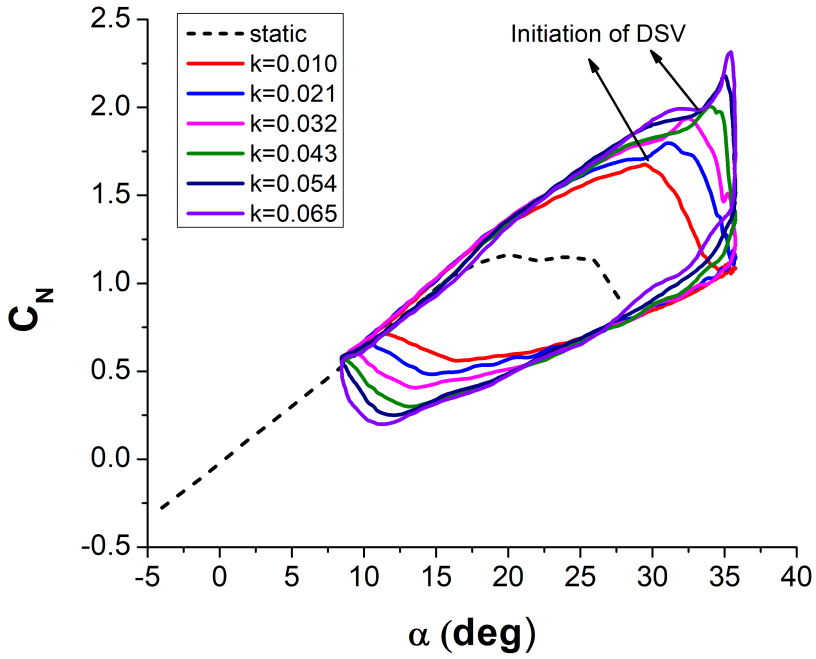

(a) Baseline blade

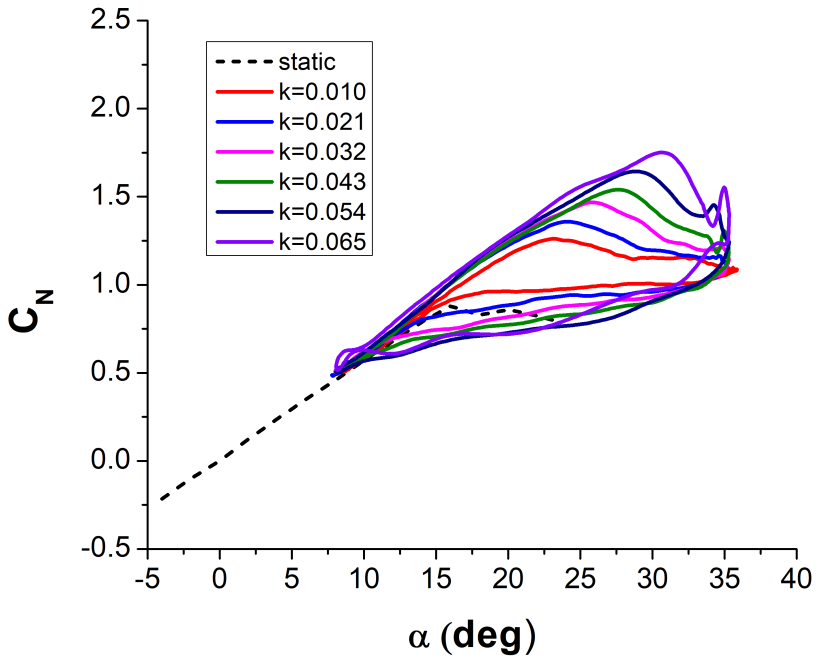

(b) Tubercle blade (model Sin-A/W=0.5)

Figure 6.13: Variation in normal force coefficient with AOA for different reduced frequencies

6.2.3 Effect of Tubercle on Dynamic Blade

The stall and hysteresis pattern of the tubercle blade is significantly different from that of an unmodified blade. Figure 6.14 depicts the C_N curve of baseline blade and Sin-A/W=0.50 tubercle blade at different reduced frequencies. The static normal force coefficient for these blades at Re_c of 5×10^5 (tunnel velocity 20m/s) has also been included to compare between the dynamic and static hysteresis. The maximum coefficient of normal force, $C_{N_{max}}$, for dynamic baseline blade is 1.75, 1.98, and 2.1 at reduced frequencies of 0.010, 0.032, and 0.065, respectively, whereas for the tubercle blade, it is 1.12, 1.48, and 1.82. It is clear that the tubercle blade do not outperform the baseline blade in terms of lift creation. The dynamic stall angle, $\alpha_{d.stall}$ for baseline is 28°, whereas for tubercle blade is 22°. This difference in dynamic stall angle $\alpha_{d.stall}$ between baseline and tubercle decreases as the reduced frequency increases. The advantage of tubercle comes into the picture in the extent of stall and hysteresis. The baseline blade creates a large parallelogram-shaped clockwise hysteresis loop. Just like the extent of static hysteresis loop for baseline increased with Reynolds number, the dynamic stall size increases with reduced frequency.

The tubercle blade has a smoother stall and a significantly smaller hysteresis loop than the baseline. At reduced frequency of 0.010, the hysteresis loop is just a quarter of that of the baseline. Much of the difference between baseline and tubercle blade is for the decreasing branch of AOA. Reattachment of flow occurs much later on baseline than the tubercle blade. Flow reattachment during the pitching down oscillation is seamless and smooth for tubercle blade, whereas it is abrupt for the baseline blade. Another notable difference is that for the decreasing branch, the normal force produced for baseline is much lower than in the static case. However, for the tubercle blade, the dynamic force is roughly the same as it was for the static tubercle blade. Analyzing the C_N curves, it can be said that tubercles energize the flow over the blade. The variation in load during a cycle of operation is much lower on the tubercle blade than on a conventional blade. This is advantageous on turbine blades where large variation in load cycle leads to fatigue in the structural components.

6.2.4 Effect of Tubercle Parameter

An important parameter defining tubercle is its amplitude to wavelength ratio (A/W). The effect of tubercle A/W on stall is studied using four blades of sinusoidal LET and two blades of triangular LET of varying A/W. Figure 6.15 depicts the C_N for sinusoidal

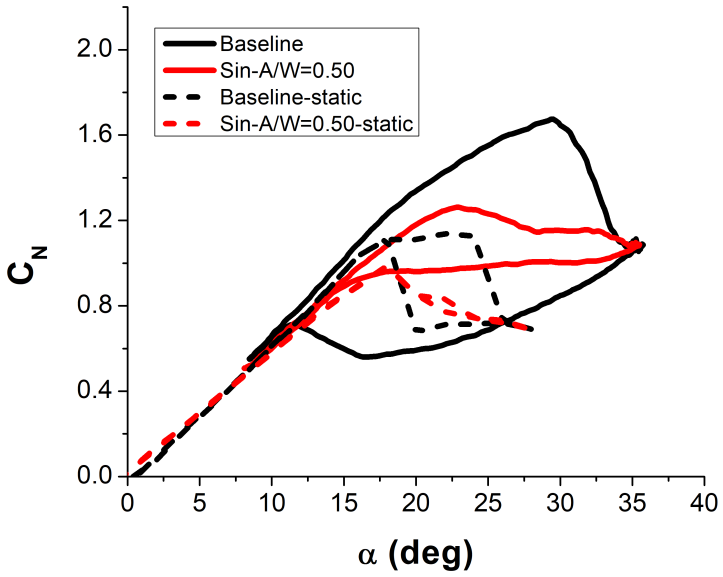

(a) k=0.010

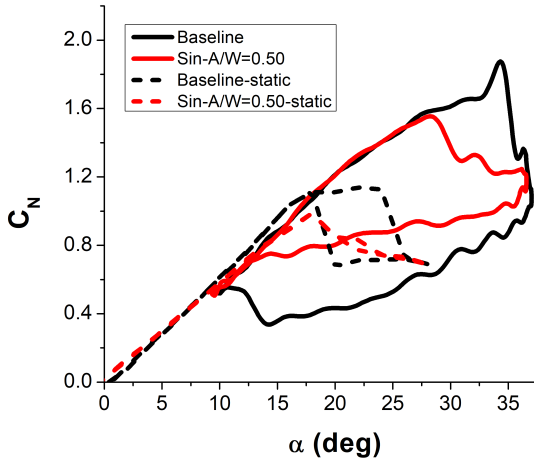

(b) k=0.032

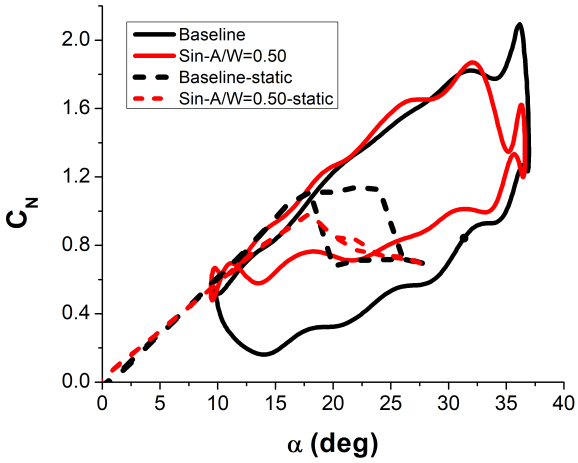

(c) k=0.060

Figure 6.14: Comparison of unsteady normal force coefficients for baseline and tubercle blade with respective steady forces at different reduced frequencies

blades in comparison with baseline at different reduced frequencies. The A/W of the tubercle seems to have an important effect on the performance of the dynamic blade. At k= 0.010, the $C_{N_{max}}$ for blades of sinusoidal LET, Sin-A/W=0.25, Sin-A/W=0.50, Sin-A/W=0.75, and Sin-A/W=1 are 1.387, 1.275, 1.123 and 1.075, respectively, which indicates that the maximum attainable normal force decreases with increase in A/W of the tubercles. Similar observations are made for higher reduced frequencies of 0.032 and 0.065. The blade with the highest A/W has the $C_{N_{max}}$, but lower than baseline at

a very low reduced frequency. With increase in reduced frequency, the normal force of this blade starts to catch up with the baseline. However, with an increase in A/W there is a significant decrease in the size of the hysteresis loop for all reduced frequencies studied. The stall characteristics seem to improve with an increase in A/W which can be seen in C_N (Figures 6.15a, 6.15c and 6.15e) and $C_{M.b}$ curves (Figures 6.15b, 6.15d and 6.15f). At all reduced frequencies the C_N curve shows smooth and gradual stall for Sin-A/W=1.00 blade. The stall characteristic is also evident from the moment coefficient with respect to body axis, $C_{M.b}$. For all reduced frequencies, the stall is characteristic by the sudden drop in $C_{M.b}$ for the baseline blade. A less prominent drop in $C_{M.b}$ is observed for tubercle blades. The drop in $C_{M.b}$ decreases with increase in A/W of the blade.

Blades of triangular LET also have identical behavior of sinusoidal LET blades in terms of variation in A/W. Figure 6.16 shows the C_N and $C_{M.b}$ for triangular LET blades. Similar to the sinusoidal LET blades, the blade with low A/W has a higher normal force. However, a large hysteresis loop is created for the blade with low A/W. The effect of tubercle A/W becomes evident from the results obtained from sinusoidal and triangular LET blades. Tubercles with high A/W are advantageous in obtaining higher normal force but disadvantageous in terms of hysteresis losses.

6.2.5 Effect of Tubercle Geometry

The geometrical shape of tubercles could influence the performance, which is studied using the two distinct shapes of tubercles- sinusoidal and triangular. Two sets of the blade with tubercle A/W of 0.5 and 1 are used to compare the effect of geometrical shape. These blades have quite similar planforms, except that the troughs and peaks of the sinusoidal leading edge are blunter than the triangular. The effect of varying tubercle geometry is studied from the normal force coefficient of sinusoidal and triangular tubercle blades. Figure 6.17 shows the C_N for blades of triangular and sinusoidal LET of corresponding A/W at different reduced frequencies. It is seen that the size of hysteresis loops is approximately of the same size for sinusoidal and triangular blades for all reduced frequencies. However, the triangular blades produce s slightly higher force throughout the range of AOA studied. With the manufacturing complexity of both blades being the same, it would be beneficial to use triangular tubercles than sinusoidal. An additional advantage of a triangular LET blade is that there is no wavy formation of normal force curve in the decreasing branch of AOA, as seen for sinusoidal blade, especially at high reduced frequency (Figures 6.17e & 6.17f). This wave

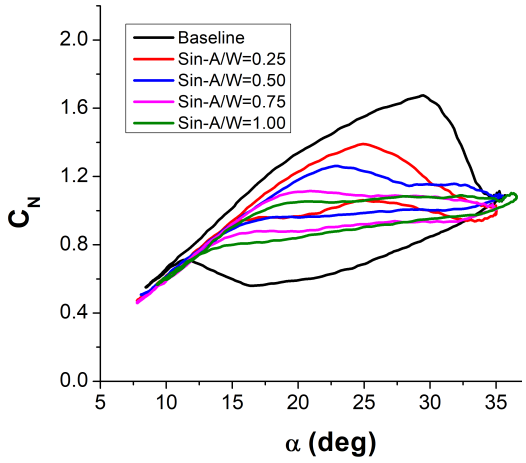

(a) Moment (k=0.010)

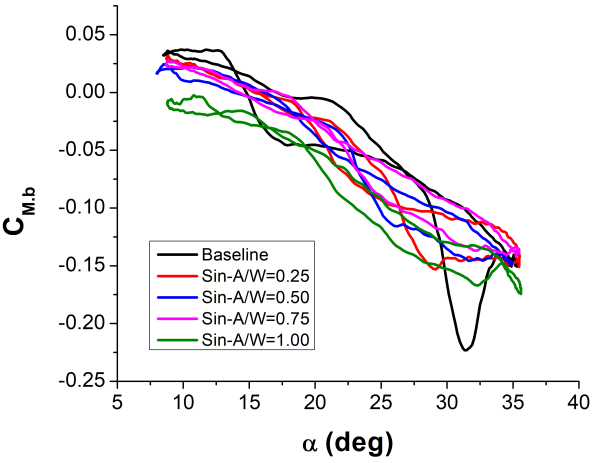

(b) Moment (k=0.010)

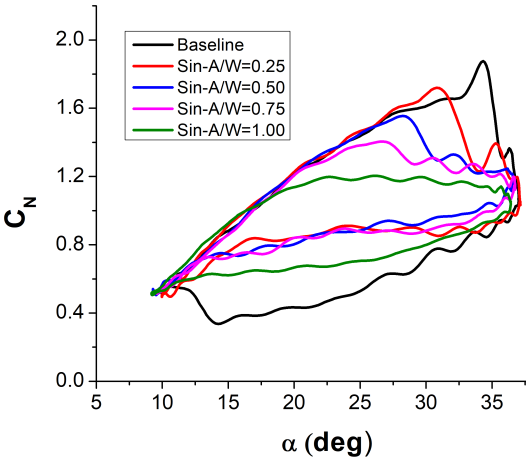

(c) Normal force (k=0.032)

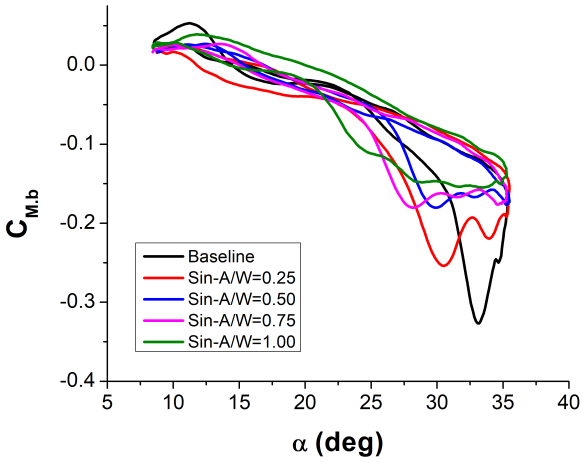

(d) Moment (k=0.032)

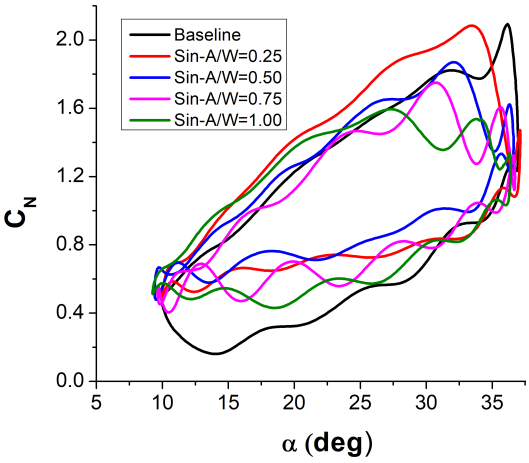

(e) Normal force (k=0.065)

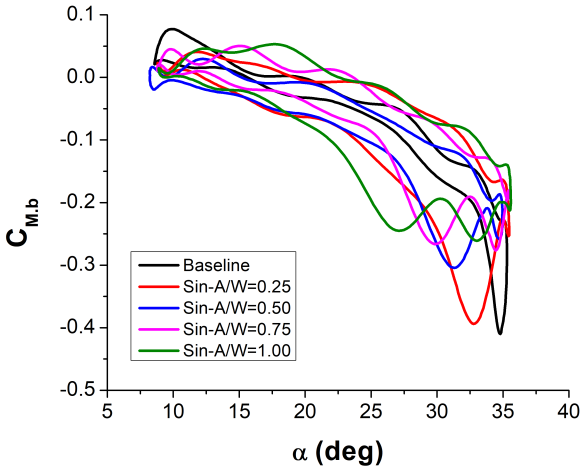

(f) Moment (k=0.065)

Figure 6.15: Aerodynamic coefficients with respect to body axis for sinusoidal LET at different reduced frequencies

formation is the effect of intense vortex shedding that usually happens at a high reduced frequency. The process of vortex shedding is prominent for the blade with a sinusoidal LET compared to the triangular one.

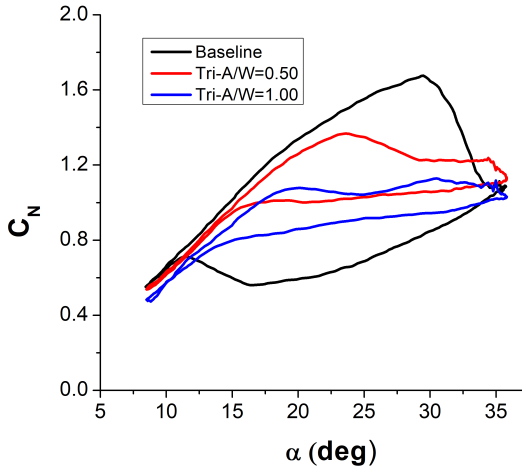

(a) Normal force(k=0.010)

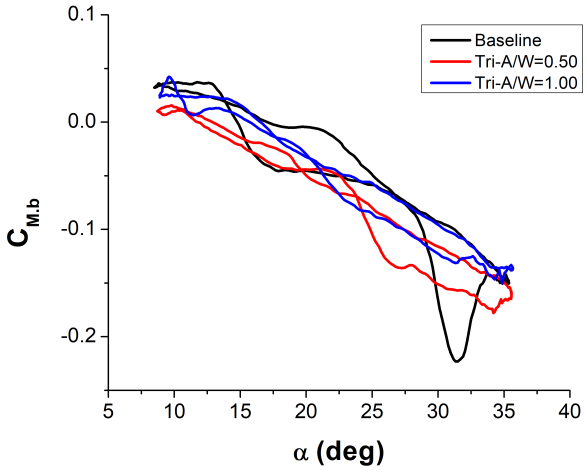

(b) Moment (k=0.010)

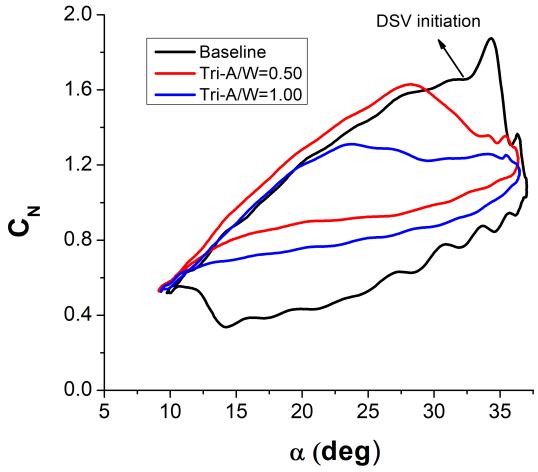

(c) Normal force (k=0.032)

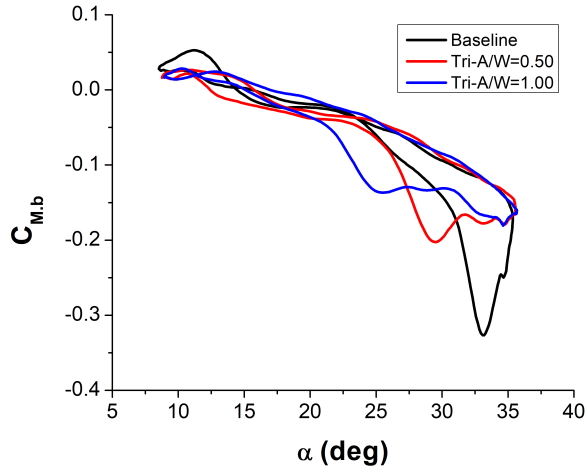

(d) Moment (k=0.032)

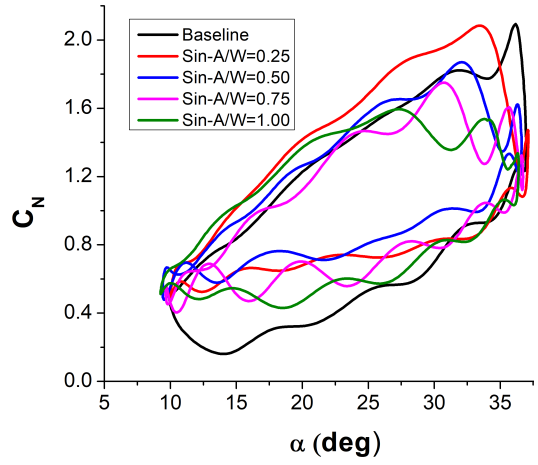

(e) Normal force (k=0.065)

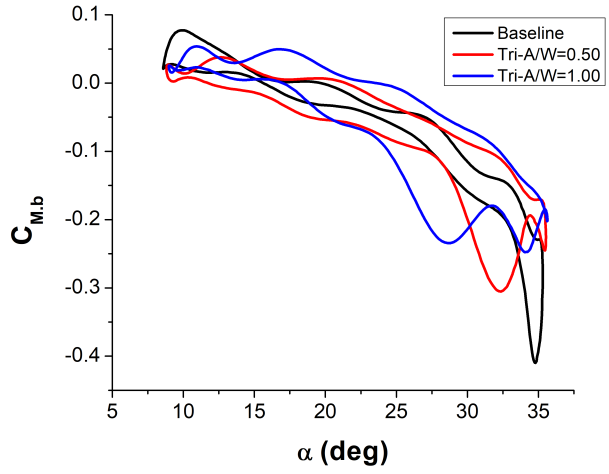

(f) Moment (k=0.065)

Figure 6.16: Aerodynamic coefficients with respect to body axis for triangular LET at different reduced frequencies

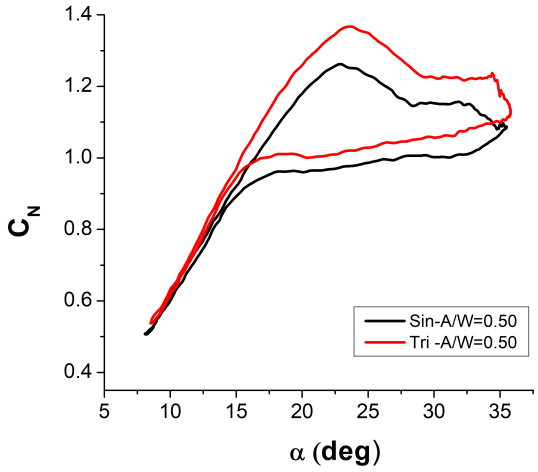

(a) A/W=0.5, k=0.010

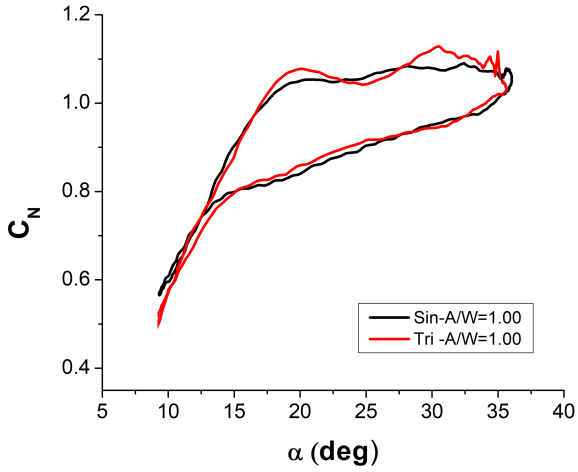

(b) A/W=1, k=0.010

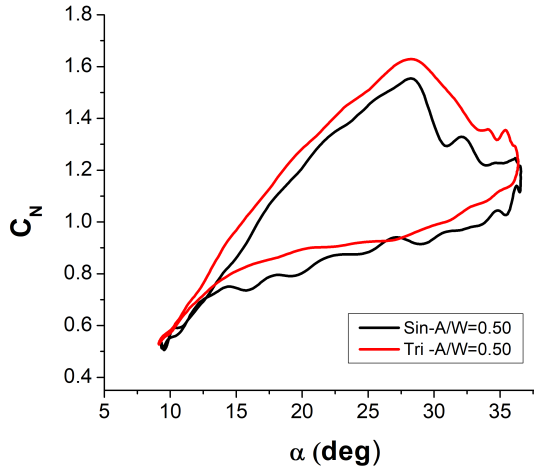

(c) A/W=0.5, k=0.032

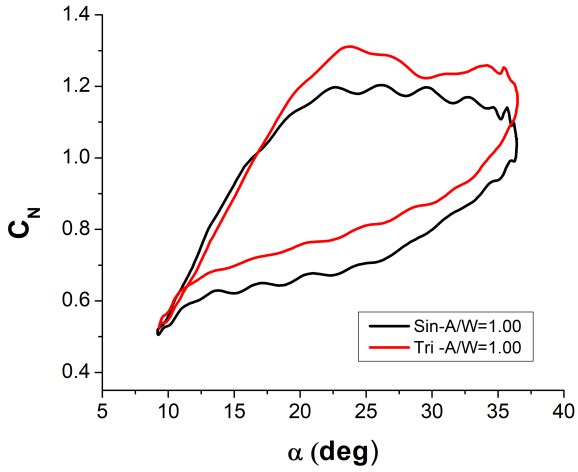

(d) A/W=1, k=0.032

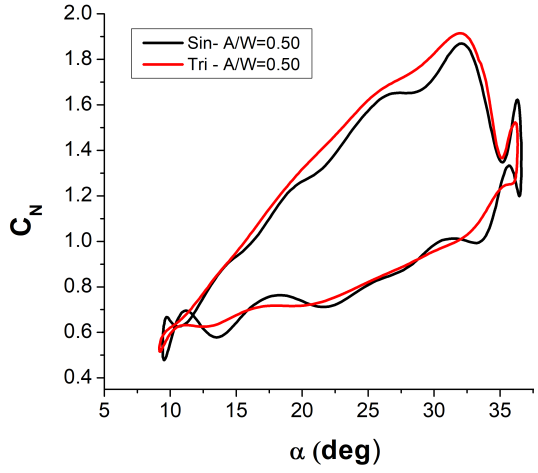

(e) A/W=0.5, k=0.065

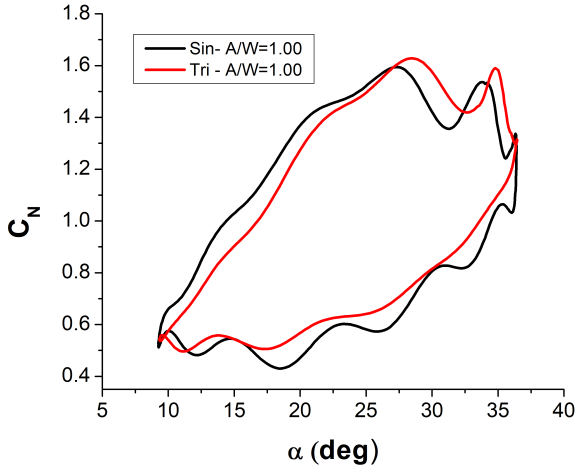

(f) A/W=1 , k=0.065

Figure 6.17: Normal force coefficient comparison for sinusoidal and triangular LET

CHAPTER 7

CONCLUSIONS

This work is an experimental study carried out to determine and analyze the capability of Humpback whale-inspired LET to control the flow on VAWT blade. Static force analysis of swept and unswept VAWT blade incorporated with LET is initially conducted at a low Reynolds number, to identify the effect of LET on both the planforms. Based on the results obtained, a more extensive study on the various effects of LET on static unswept blades is conducted at different Reynolds number. Further, the effect of varying tubercle parameters and geometric shape on the steady-state aerodynamic forces and moment of the blade is studied. In the final part, a study on the effect of LET, their geometrical parameters and shape on the unsteady aerodynamic characteristics is conducted.

First part of the study is to determine the effect of LET on swept and unswept static blades at a low Reynolds, $Re_c = 10^5$. Preliminary study was conducted to identify the aerodynamically efficient tubercle alignment on swept blades from the two possible methods. Based on the analysis of L/D ratio, it was concluded that the orientation of tubercle in the streamwise direction on swept wing helps in attaining higher L/D ratio compared to tubercle aligned normal to the leading edge. Further, streamwise tubercles were incorporated on blades swept 10°, 20°and 30°, and their performance were compared to unswept blade (0°) and to respective baselines. It was seen that at low Reynolds number, LET improved the aerodynamic performance of unswept blade(0°) and low sweep blade (10°). Tubercles do not significantly affect the performance of blades swept at high angles (30°). Incorporating LET on the blade can provide it with a soft stall characteristic. However, the difference in the aerodynamic efficiency for swept blade with tubercles to its corresponding baseline is not as predominant as for the unswept blade. This is because when blade is swept, the stall characteristic starts to improve. Further addition of tubercles to swept wing do not significantly enhance the aerodynamic performance.

The second part of the study involves detailed analysis of force and surface pressure on unswept blades at Reynolds number in laminar, transition and turbulent flow regimes. The unswept tubercle blade and its baseline is studied at various Reynolds number ranging from 2.5×10^5 to 6.5×10^5. The incorporation of LET to blade helped in

improving many aerodynamic characteristics. The baseline blade showed distinct area of LSB on its suction surface at a Reynolds number of 2.5×10^5. The LSB region moved towards the leading edge of the blade and decreased in size with increase in AOA. With incorporation of tubercles on the leading edge of the blade, formation of LSB was prevented. The stall characteristic of the blades also pointed to the performance enhancement brought about by the LET. When the baseline stalled abruptly in a single step, tubercle blade stalled softly and gradually in multiple steps. Tubercle blade also proved advantageous as it eliminated the hysteresis of force and moment curves that existed for the baseline. However, the tubercles blade had a decreased α_{stall} and $C_{L_{max}}$ than the baseline.

The effect of geometrical shape and parameters of tubercle on the steady aerodynamic characteristics of the blade is studied at $Re_c = 5 \times 10^5$, using blades of sinusoidal and triangular tubercles of various A/W ratio. Effect of varying A/W on the lift, drag, and moment characteristics is closely identical for blades of sinusoidal and triangular shaped tubercles. The lift characteristics of tubercles blades (sinusoidal and triangular) are inferior to that of the baseline at angles less than baseline stall angle. The $C_{L_{max}}$ decreases with an increase in A/W. However, at AOA greater than the baseline stall angle the tubercle blades have higher lift than the baseline. In the post-stall region the blades of lower A/W have higher lift. Drag remains identical of baseline and tubercle blades at low AOA. In the immediate post-stall region, the drag for tubercle blades are higher and drag is higher for blades with tubercles of higher A/W. While comparing the steady-state aerodynamic characteristics between blade of sinusoidal and triangular shaped tubercles of identical tubercle parameters, no significant difference is identified.

In the last part of the work, study of dynamic blade is conducted by measuring aerodynamic loads on oscillating blades. Sinusoidal and triangular leading edges of different A/Ws are used. Most advantageous effect of tubercle (sinusoidal and triangular) on dynamic blade is that it significantly decreases the hysteresis and dynamic stall of the unmodified blade. With increase in A/W of the tubercle the maximum coefficient of normal force reduces. The size of hysteresis loop also reduces with increase in A/W for sinusoidal and triangular tubercle. Though sinusoidal and triangular tubercle blade have similar hysteresis and stall characteristics, the maximum coefficient of normal force is nominally higher for triangular than sinusoidal.

The important findings of the study are summarized below:

- The LET are beneficial on improving the stall characteristics of unswept and low sweep blades at low Reynolds numbers. The LET fail to enhance aerodynamic

performance of blades swept at high angles.

- On a static blade, the effect of LET is manifested on the LSB, stall, and hysteresis characteristics of the blade. The LET prevents the formation of LSB on the suction surface of the blade.
- The LET improves the stall characteristic of the blade by preventing deep abrupt stall and facilitating smooth gradual stall. Tubercles reduce the rate of stall progression from blade centre to the tips. Stall characteristics tends to become smoother with increase in amplitude of the tubercles.
- The LET energizes the boundary layer flow on the blade, thus preventing the static hysteresis seen on the force and moment coefficient curves.
- The tubercle blades have lower $C_{L_{max}}$ and α_{stall} than the baseline. The $C_{L_{max}}$ decreases with increase in amplitude of the tubercles. However, the tubercle blades have higher post-stall lift than the baseline.
- For a static blade, sinusoidal and triangular shaped LET of identical tubercle parameters have closely identical aerodynamic characteristics.
- The LET are advantageous on dynamic blade as it help to mitigate dynamic stall and reduces the size of the dynamic hysteresis loop, which results in reducing the variation in cyclic loads acting on the turbine.
- The geometric parameter of tubercle, specifically the A/W ratio significantly affects the performance of LET on dynamic blade. Blades of high A/W tubercle are advantageous in terms of stall and hysteresis. These blades have a very smooth stall and significantly small hysteresis loop. However, the normal force generated by such blades are lower than blades with tubercles of low A/W.
- A triangular shaped tubercle can be more advantageous than a sinusoidal shaped of corresponding A/W, as the triangular tubercle can create higher normal force with no significant difference on stall and hysteresis characteristics.

7.1 Scope for Future Work

This work has been done for the simplest shapes of VAWT blade. The effect of tubercle on complex blade types- like helical and D-Type VAWT blades would be beneficial in better understanding of potential benefits of tubercle in practical applications. The

pressure distribution over the span of unswept blade in this study has given an insight into the stall progression mechanism on such blades. Such an approach on swept blades with tubercles would also beneficial for better understanding of tubercle mechanism on swept blades. Moreover, the study of swept blades are limited to a single Reynolds number. Since sweeping is a feature that is advantageous at high velocities, detailed study at various Reynolds number would be beneficial. The acoustics and vibration studies of tubercle incorporated VAWT can also be a topic of vast research.

LIST OF PUBLICATIONS

1. Jeena Joseph, A. Sathyabhama (2022) "Leading edge tubercle on wind turbine blade to mitigate problems of stall, hysteresis, and laminar separation bubble". ***Energy Conversion and Management.***
   https://doi.org/10.1016/j.enconman.2022.115337

2. Jeena Joseph, A. Sathyabhama, S.Surya (2022) "A Detailed Study on the Effects of Wing Sweep on Tubercle Wings". ***Aircraft Engineering and Aerospace Technology.***
   https://doi.org/10.1108/AEAT-04-2021-0114

3. Jeena Joseph, A. Sathyabhama (2021) "Experimental study on the effect of tubercles on lift drag characteristic of swept wing at low Reynolds number". ***Iranian Journal of Science and Technology, Transactions of Mechanical Engineering.***
   https://doi.org/10.1007/s40997-021-00455-z

Conferences

1. Jeena Joseph, A. Sathyabhama."Numerical study on the effect of tubercle on symmetrical airfoil at low Reynolds number". *The International Journal of Engineering and Science* (IJES)ISSN (e): 2319 – 1813 ISSN (p):23-19 – 1805, PP 65-71, 2020.

2. Jeena Joseph, A. Sathyabhama. "Experimental study on the effect of leading-edge tubercle on high swept wing at low Reynolds number". 3^{rd} International Heat and Mass Transfer Conference IHMTC-2019, IIT Roorkee, 28-31 December 2019

3. Jeena Joseph, Surya S, A. Sathyabhama. "A Comparison on the Effect of Leading Edge Tubercle on Straight and Swept Wing at Low Reynolds Number". Proceedings of the 46th National Conference on Fluid Mechanics and Fluid Power (FMFP) 2019, PSG College, Coimbatore, 9-11 December 2019.

REFERENCES

Abate, G. and D. N. Mavris (2017). CFD analysis of leading edge tubercle effects on wind turbine performance. 15^{th} International Energy Conversion Engineering Conference, 4626.

AIAA (2020). Calibration and use of internal strain-gage balances with application to wind tunnel testing (AIAA R-091A-2020).

Anderson, B. D. (2008). The physics of sailing. *Physics Today*, 61(2), 38.

Anderson Jr, J. D., *Fundamentals of aerodynamics*. Tata McGraw-Hill Education, 2010.

Bar-Cohen, Y. (2006). Biomimetics—using nature to inspire human innovation. *Bioinspiration & biomimetics*, 1(1), p–1.

Barlow, J. B., W. H. Rae, and A. Pope, *Low-speed wind tunnel testing*. John wiley & sons, 1999.

Bearman, P. W. and J. C. Owen (1998). Reduction of bluff-body drag and suppression of vortex shedding by the introduction of wavy separation lines. *Journal of Fluids and Structures*, 12(1), 123–130.

Bechert, D., M. Bruse, W. Hage, and R. Meyer (2000). Fluid mechanics of biological surfaces and their technological application. *Naturwissenschaften*, 87(4), 157–171.

Bechert, D., M. Bruse, W. Hage, R. Meyer, D. Bechert, M. Bruse, W. Hage, and R. Meyer (1997). Biological surfaces and their technological application-laboratory and flight experiments on drag reduction and separation control. 28^{th} Fluid dynamics conference, p–1960.

Bhushan, B. (2012). Shark skin surface for fluid-drag reduction in turbulent flow. Biomimetics: Bioinspired Hierarchical-Structured Surfaces for Green Science and Technology, 227–265.

Bianchi, S., A. Corsini, A. G. Sheard, and C. Tortora (2013). A critical review of stall control techniques in industrial fans. *International Scholarly Research Notices*, 52(6), 192–197.

Bolzon, M., R. Kelso, and M. Arjomandi (2014). The effects of tubercles on swept wing performance at low angles of attack. Proceedings of the 19^{th} Australasian fluid mechanics conference, 8–11.

Bolzon, M. D., R. M. Kelso, and M. Arjomandi (2016). Formation of vortices on a tubercled wing, and their effects on drag. *Aerospace Science and Technology*, 56, 46–55.

Bolzon, M. D., R. M. Kelso, and M. Arjomandi (2017). Force measurements and wake surveys of a swept tubercled wing. *Journal of Aerospace Engineering*, 30(3), 04016085.

Braslow, A. L., R. M. Hicks, and R. V. Harris (1966). Use of grit-type boundary-layer-transition trips on wind-tunnel models. NASA,TN-D-3579.

Carr, L. and K. McAlister (1983). The effect of a leading-edge slat on the dynamic stall of an oscillating airfoil.

Carr, L. W. (1988). Progress in analysis and prediction of dynamic stall. *Journal of aircraft*, 25(1), 6–17.

Carr, L. W., K. W. McAlister, and W. J. McCroskey (1977). Analysis of the development of dynamic stall based on oscillating airfoil experiments. NASA TN D-8382.

Carreira Pedro, H. and M. Kobayashi (2008). Numerical study of stall delay on humpback whale flippers. 46^{th} AIAA aerospace sciences meeting and exhibit, 584.

Cebeci, T. and J. Cousteix (2005). Transition in three-dimensional incompressible flows. Modeling and Computation of Boundary-Layer Flows: Laminar, Turbulent and Transitional Boundary Layers in Incompressible and Compressible Flows, 261–306.

Chandrasekhara, M., L. Carr, and M. Wilder (1994). Interferometric investigations of compressible dynamic stall over a transiently pitching airfoil. *AIAA journal*, 32(3), 586–593.

Choudhry, A., M. Arjomandi, and R. Kelso (2016). Methods to control dynamic stall for wind turbine applications. *Renewable energy*, 86, 26–37.

Choudhry, A., R. Leknys, M. Arjomandi, and R. Kelso (2014). An insight into the dynamic stall lift characteristics. *Experimental Thermal and Fluid Science*, 58, 188–208.

Craig, A. E., J. O. Dabiri, and J. R. Koseff (2017). Low order physical models of vertical axis wind turbines. *Journal of Renewable and Sustainable Energy*, 9(1), 013306.

Custodio, D. (2007). The effect of humpback whale-like leading edge protuberances on hydrofoil performance. Worcester Polytechnic Institute.

Custodio, D., C. Henoch, and H. Johari (2015). Aerodynamic characteristics of finite span wings with leading-edge protuberances. *AIAA journal*, 53(7), 1878–1893.

De Tavernier, D., C. Ferreira, A. Viré, B. LeBlanc, and S. Bernardy (2021). Controlling dynamic stall using vortex generators on a wind turbine airfoil. *Renewable Energy*, 172, 1194–1211.

Diwan, S. S. and O. Ramesh (2007). Laminar separation bubbles: Dynamics and control. *Sadhana*, 32(1), 103–109.

Dolphin, W. F. (1988). Foraging dive patterns of humpback whales, *Megaptera novaeangliae*, in southeast alaska: a cost–benefit analysis. *Canadian Journal of Zoology*, 66(11), 2432–2441.

Edel, R. and H. Winn (1978). Observations on underwater locomotion and flipper movement of the humpback whale megaptera novaeangliae. *Marine Biology*, 48(3), 279–287.

Ekaterinaris, J. A. and M. F. Platzer (1998). Computational prediction of airfoil dynamic stall. *Progress in aerospace sciences*, 33(11-12), 759–846.

Ericsson, L. E. and J. P. Reding (1971). Unsteady airfoil stall, review and extension. *Journal of Aircraft*, 8(8), 609–616.

Fish, F. and G. Lauder (2006). Passive and active flow control by swimming fishes and mammals. *Annu. Rev. Fluid Mech.*, 38, 193–224.

Fish, F. E. and J. M. Battle (1995). Hydrodynamic design of the humpback whale flipper. *Journal of Morphology*, 225(1), 51–60.

Fish, F. E., L. E. Howle, and M. M. Murray (2008). Hydrodynamic flow control in marine mammals. *Integrative and Comparative Biology*, 48(6), 788–800.

Frunzulica, F., A. Dumitrache, and B. Suatean (2014). Numerical investigations of passive flow control elements for vertical axis wind turbine. International Conference on Mathematical Problems in Engineering. American Institute of Physics, 331–340.

Fukudome, K., M. Watanabe, A. Iida, and A. Mizuno (2004). Separation control of high angle of attack airfoil for vertical axis wind turbines. *Journal of the Visualization Society of Japan*, 24(2), 59–62.

Gad-el Hak, M. (1990). Control of low-speed airfoil aerodynamics. *AIAA journal*, 28(9), 1537–1552.

Gaster, M. (1967). The structure and behaviour of laminar separation bubbles. Technical Report R. & M. No. 3597, Aeronautical Research Council. London.

Godard, G. and M. Stanislas (2006). Control of a decelerating boundary layer. part 1: Optimization of passive vortex generators. *Aerospace Science and Technology*, 10(3), 181–191.

Greenblatt, D. and R. Lautman (2015). Inboard/outboard plasma actuation on a vertical-axis wind turbine. *Renewable Energy*, 83, 1147–1156.

Greenblatt, D., H. Müller-Vahl, R. Lautman, A. Ben-Harav, and B. Eshel (2015). Dielectric barrier discharge plasma flow control on a vertical axis wind turbine. Active flow and combustion control 2014, 71–86.

Hain, J. H., G. R. Carter, S. D. Kraus, C. A. Mayo, and H. Winn (1982). Feeding behavior of the humpback whale, megaptera novaeangliae, in the western north atlantic. *Fishery Bulletin*, 80(2), 259–268.

Hansen, K. L. (2012). Effect of leading edge tubercles on airfoil performance. University of Adelaide, Austrailia.

Hansen, K. L., R. M. Kelso, and B. B. Dally (2011). Performance variations of leading-edge tubercles for distinct airfoil profiles. *AIAA journal*, 49(1), 185–194.

Hoerner, S. F. (1965). Fluid dynamic drag. Hoerner Fluid Dynamics, BrickTown, N.J. USA.

Howle, L. E. (2009). A report in the efficiency of a whale-power corp. 5 meter prototype wind turbine blade. Whalepower Wenvor Blade, BelleQuant, LLC, Durham.

Hu, H., Z. Yang, and H. Igarashi (2007). Aerodynamic hysteresis of a low-reynolds-number airfoil. *Journal of Aircraft*, 44(6), 2083–2086.

Huang, G.-Y., Y. Shiah, C.-J. Bai, and W. Chong (2015). Experimental study of the protuberance effect on the blade performance of a small horizontal axis wind turbine. *Journal of Wind Engineering and Industrial Aerodynamics*, 147, 202–211.

Islam, M. R., S. Mekhilef, and R. Saidur (2013). Progress and recent trends of wind energy technology. *Renewable and Sustainable Energy Reviews*, 21, 456–468.

Ismail, M. F. and K. Vijayaraghavan (2015). The effects of aerofoil profile modification on a vertical axis wind turbine performance. *Energy*, 80, 20–31.

Johari, H., C. W. Henoch, D. Custodio, and A. Levshin (2007). Effects of leading-edge protuberances on airfoil performance. *AIAA journal*, 45(11), 2634–2642.

Johnson, S. J. and D. E. Berg (2008). Active load control techniques for wind turbines.

Jurasz, C. M. and V. P. Jurasz (1979). Feeding modes of the humpback whale (*Megaptera novaengliae*) in southeast alaska. Whale Research Institute.[LGB-L].

Khurana, K. (2009). Aviation management: global perspectives. Global India Publications.

Laneville, A. and P. Vittecoq (1986). Dynamic stall: The case of the vertical axis wind turbine. *Journal of Solar Energy Engineering*, 108, 141–145.

Leatherwood, S., R. R. Reeves, W. F. Perrin, W. E. Evans, and L. Hobbs (1982). Whales, dolphins, and porpoises of the eastern north pacific and adjacent arctic waters: A guide to their identification. US Department of Commerce, National Oceanic and Atmospheric Administration.

Leishman, J. (1990). Dynamic stall experiments on the naca 23012 aerofoil. *Experiments in Fluids*, 9(1), 49–58.

Lin, J., F. Howard, and G. Selby (1991). Exploratory study of vortex-generating devices for turbulent flow separation control. AIAA 29^{th} Aerospace Sciences Meeting, Reno, NV, January 7-10, AIAA Paper 91–0042,.

Lin, J. C. (2002). Review of research on low-profile vortex generators to control boundary-layer separation. *Progress in Aerospace Sciences*, 38(4-5), 389–420.

Lin, S.-Y., Y.-Y. Lin, C.-J. Bai, and W.-C. Wang (2016). Performance analysis of vertical-axis-wind-turbine blade with modified trailing edge through computational fluid dynamics. *Renewable Energy*, 99, 654–662.

Lissaman, P. (1983). Low-reynolds-number airfoils. *Annual review of fluid mechanics*, 15(1), 223–239.

Lord, W., D. MacMartin, and G. Tillman (2000). Flow control opportunities in gas turbine engines. Fluids 2000 Conference and Exhibit, 2234.

Lozano, P. (2008). Fluid mechanics and aerodynamics. `https://web.mit.edu/16.unified/www/FALL/fluids/Lectures/f03.pdf`. Accessed: 2022-06-05.

McAlpine, A., E. Nash, and M. Lowson (1999). On the generation of discrete frequency tones by the flow around an aerofoil. *Journal of Sound and Vibration*, 222(5), 753–779.

McCroskey, W. J. (1982). Unsteady airfoils. *Annual review of fluid mechanics*, 14(1), 285–311.

Meyer, R., D. Bechert, and W. Hage (1999). Windtunnel experiments with artificial bird feathers for passive separation control on airfoils. IUTAM Symposium on Mechanics of Passive and Active Flow Control, 99–100.

Miklosovic, D., M. Murray, L. Howle, and F. Fish (2004). Leading-edge tubercles delay stall on humpback whale (*Megaptera novaeangliae*) flippers. *Physics of fluids*, 16(5), L39–L42.

Miklosovic, D. S., M. M. Murray, and L. E. Howle (2007). Experimental evaluation of sinusoidal leading edges. *Journal of aircraft*, 44(4), 1404–1408.

Mizoguchi, M., Y. Kajikawa, and H. Itoh (2014). Static stall hysteresis of low-aspect-ratio wings. 32^{th} AIAA Applied Aerodynamics Conference, Atlanta,Georgia, 2014.

Mueller, T. J. (1985). The influence of laminar separation and transition on low Reynolds number airfoil hysteresis. *Journal of aircraft*, 22(9), 763–770.

Mueller, T. J. and S. M. Batill (1982). Experimental studies of separation on a two-dimensional airfoil at low reynolds numbers. *AIAA journal*, 20(4), 457–463.

Mueller, T. J. and J. D. DeLaurier (2003). Aerodynamics of small vehicles. *Annual review of fluid mechanics*, 35(1), 89–111.

Ng, B. F., T. H. D. New, and R. Palacios (2017). Bio-inspired leading-edge tubercles to improve fatigue life in horizontal axis wind turbine blades. 35^{th} Wind energy symposium, 1381.

Noll, R. and N. Ham (1982). Effects of dynamic stall on SWECS. *Journal of Solar Energy Engineering*, 104, 96–101.

Ontario-Power-Authority (2010). Energy efficient fans take their cue from the humpback whale. http://archive.powerauthority.on.ca/Storage/122/16957-AgNews-July231.pdf.

Paulsen, U. S., H. A. Madsen, K. A. Kragh, P. H. Nielsen, I. Baran, J. Hattel, E. Ritchie, K. Leban, H. Svendsen, and P. A. Berthelsen (2014). Deepwind-from idea to 5 mw concept. *Energy Procedia*, 53, 23–33.

Pohlen, L. J. and T. J. Mueller (1984). Boundary layer characteristics of the miley airfoil at low reynolds numbers. *Journal of aircraft*, 21(9), 658–664.

Reithmaier, L. and L. W. Reithmaier (1995). Mach 1 and beyond: The illustrated guide to high-speed flight. McGraw Hill Professional.

Rezaeiha, A., I. Kalkman, and B. Blocken (2017). Cfd simulation of a vertical axis wind turbine operating at a moderate tip speed ratio: Guidelines for minimum domain size and azimuthal increment. *Renewable energy*, 107, 373–385.

Russell, J. M., Length and bursting of separation bubbles: A physical. *In NASA Conference Publication*, 2085. Scientific and Technical Information Office, National Aeronautics and Space., 1979.

Sasson, B. and D. Greenblatt (2011). Effect of leading-edge slot blowing on a vertical axis wind turbine. *AIAA journal*, 49(9), 1932–1942.

Schmitz, F. W. (1967). Aerodynamics of the model airplane. part 1-airfoil measurements. NASA-TM-X-60976, Washington DC.

Selig, M., J. Guglielmo, A. Broern, and P. Giguere (1996). Experiments on airfoils at low reynolds numbers. AIAA 34^{th} Aerospace Sciences Meeting, Reno, Nevada, AIAA Paper 96–0062.

Sheldahl, R. E. and P. C. Klimas (1981). Aerodynamic characteristics of seven symmetrical airfoil sections through 180-degree angle of attack for use in aerodynamic analysis of vertical axis wind turbines. Technical report, Sandia National Labs., Albuquerque, NM (USA).

Shih, C., L. Lourenco, L. Van Dommelen, and A. Krothapalli (1992). Unsteady flow past an airfoil pitching at a constant rate. *AIAA journal*, 30(5), 1153–1161.

Shyy, W., Y. Lian, J. Tang, D. Viieru, and H. Liu (2007). Aerodynamics of low Reynolds number flyers. Cambridge University Press.

Sievert, T. (2015). New technology forum - vertiwind project's first prototype tested in southern france. *https://w3.windfair.net/wind-energy/news/17936-new-technology-forum-vertiwind-project-s-first-prototype-tested*. Accessed: 2022-05-05.

Simons, M. (2002). Model aircraft aerodynamics. Special Interest Model Books, Dorset, England, U.K., p. 112.

Skillen, A., A. Revell, J. Favier, A. Pinelli, and U. Piomelli (2013). Investigation of wing stall delay effect due to an undulating leading edge: An les study. 8^{th} International Symposium on Turbulence and Shear Flow Phenomena.

Skillen, A., A. Revell, A. Pinelli, U. Piomelli, and J. Favier (2015). Flow over a wing with leading-edge undulations. *Aiaa Journal*, 53(2), 464–472.

Sobhani, E., M. Ghaffari, and M. J. Maghrebi (2017). Numerical investigation of dimple effects on darrieus vertical axis wind turbine. *Energy*, 133, 231–241.

Soderman, P. T. (1972). Aerodynamic effects of leading-edge serrations on a two-dimensional airfoil. NASA TMX-2643, Washington, D.C.

Sridhar, S., J. Joseph, and J. Radhakrishnan (2022). Implementation of tubercles on vertical axis wind turbines (VAWTs): An aerodynamic perspective. *Sustainable Energy Technologies and Assessments*, 52, 102109.

Stanway, M. J. (2008). Hydrodynamic effects of leading-edge tubercles on control surfaces and in flapping foil propulsion. Massachusetts Institute of Technology.

Stein, B. and M. Murray (2005). Stall mechanism analysis of humpback whale flipper models. *Proceedings of Unmanned Untethered Submersible Technology (UUST), UUST05*, 5.

Stoop, J. and J. De Kroes (2012). Stall shield devices, an innovative approach to stall prevention. Air Transport and Operations: Proceedings of the Third International Air Transport and Operations Symposium 2012, Delft, 18-20 June 2012. Ed. R. Curran, Delft University of Technology.

Swatton, P. J. (2011). Principles of flight for pilots. John Wiley & Sons.

Tang, D. and E. Dowell (1992). Flutter and stall response of a helicopter blade with structural nonlinearity. *Journal of Aircraft*, 29(5), 953–960.

Tani, I. (1964). Low-speed flows involving bubble separations. *Progress in Aerospace Sciences*, 5, 70–103.

Thompson, D. (1997). Effect of the leading-edge extension (LEX) fence on the vortex structure over the F/A-18. Technical report, Defence Science and Technology Organisation, Canberra, Australia.

Timmer, W. (2008). Two-dimensional low-reynolds number wind tunnel results for airfoil NACA 0018. *Wind engineering*, 32(6), 525–537.

Tummala, A., R. K. Velamati, D. K. Sinha, V. Indraja, and V. H. Krishna (2016). A review on small scale wind turbines. *Renewable and Sustainable Energy Reviews*, 56, 1351–1371.

Van Nierop, E. A., S. Alben, and M. P. Brenner (2008). How bumps on whale flippers delay stall: An aerodynamic model. *Physical review letters*, 100(5), 054502.

Velasco, D., O. L. Mejia, and S. Laín (2017). Numerical simulations of active flow control with synthetic jets in a darrieus turbine. *Renewable Energy*, 113, 129–140.

Wang, Z. and M. Zhuang (2017). Leading-edge serrations for performance improvement on a vertical-axis wind turbine at low tip-speed-ratios. *Applied Energy*, 208, 1184–1197.

Watts, P. and F. Fish (2006). Scalloped leading edge advancements. US Patent App. 11/093,722.

Watts, P. and F. E. Fish (2001). The influence of passive, leading edge tubercles on wing performance. 12^{th} International Symposium Unmanned Untethered Submersible Technology,Autonomous Undersea System Insttute, Durham New Hampshire.

Weber, P. W., L. E. Howle, and M. M. Murray (2010). Lift, drag, and cavitation onset on rudders with leading-edge tubercles. *Marine technology*, 47(1), 27–36.

Wei, B., Y. Gao, and D. Li (2021). Physics of dynamic stall vortex during pitching oscillation of dynamic airfoil. *International Journal of Aeronautical and Space Sciences*, 22(6), 1263–1277.

Wei, Z., T. H. New, and Y. Cui (2018). Aerodynamic performance and surface flow structures of leading-edge tubercled tapered swept-back wings. *AIAA Journal*, 56(1), 423–431.

Weihs, D. (1981). Effects of swimming path curvature on the energetics of fish motion. *Fishery Bulletin*, 79, 171–176.

Werle, M., R. Paterson, and W. Presz Jr (1987). Trailing-edge separation/stall alleviation. *AIAA journal*, 25(4), 624–626.

Williams, D. R., F. Reißner, D. Greenblatt, H. Müller-Vahl, and C. Strangfeld (2017). Modeling lift hysteresis on pitching airfoils with a modified Goman–Khrabrov model. *AIAA Journal*, 55(2), 403–409.

Williams, M. D. (2009). Wind tunnel analysis and flight test of a wing fence on a T-38. Master of Science Thesis, Air Force Institute of Technology, Wright-Patterson Air Force Base, Ohio.

Xiao, Q., W. Liu, and A. Incecik (2013). Flow control for vatt by fixed and oscillating flap. *Renewable Energy*, 51, 141–152.

Yen, J. and N. A. Ahmed (2013). Enhancing vertical axis wind turbine by dynamic stall control using synthetic jets. *Journal of Wind Engineering and Industrial Aerodynamics*, 114, 12–17.

Zhong, J., J. Li, P. Guo, and Y. Wang (2019). Dynamic stall control on a vertical axis wind turbine aerofoil using leading-edge rod. *Energy*, 174, 246–260.

Zhu, H., W. Hao, C. Li, Q. Ding, and B. Wu (2018). A critical study on passive flow control techniques for straight-bladed vertical axis wind turbine. *Energy*, 165, 12–25.

Zverkov, I., B. Zanin, and V. Kozlov (2008). Disturbances growth in boundary layers on classical and wavy surface wings. *AIAA journal*, 46(12), 3149–3158.

APPENDIX A

Calibration of Six Component Internal Strain Gauge Balance (WT11)

Dynamic blade measurements are conducted using WT11 balance and its calibration report has been presented here. The important dimensions of the balance are presented in the Table.1 and its rating in Table.2. The wiring color code has been presented in Table.3. Further, tables 4-11 are obtained by loading each bridge element with known weights.

Table 1: Dimensions of WT11 balance

Maximum diameter	30mm
Overall length	200 mm
Distance between centres of N1 and N2 gauges	99mm
Balance center distance from N1 gauge	48.5mm

Table 2: Component rating of the balance

Component		Component	
Normal force	80 kgf	Pitching Moment	4 kg-m
Side Force	20 kgf	Yawing Moment	2 kg-m
Axial Force	20 kgf	Rolling Moment	2 kg-m

Table 3: Wiring color code for balance

INPUT VOLTAGE	3-5 Volts DC max

INPUT	POSITIVE	NEGATIVE
—	Red	black
OUTPUT		
A	Orange	Orange
N1	Blue	Blue
N2	White	White
S1	Grey	Grey
S2	Yellow	Yellow
RM	Violet	Violet

TABLE - 4

Loading : N1 negative

LOAD(kgf)	EX(v)	N1(v)	N2(v)	S1(v)	S2(v)	A1(v)	L1(v)
0.0000	5.0000	-0.2339	-0.4330	0.1736	0.4329	-0.1690	0.5900
5.0000	5.0000	-0.9520	-0.4373	0.1639	0.4341	-0.1597	0.5895
10.0000	5.0000	-1.6703	-0.4420	0.1540	0.4355	-0.1512	0.5894
15.0000	5.0000	-2.3879	-0.4479	0.1443	0.4368	-0.1433	0.5898
20.0000	5.0000	-3.1076	-0.4515	0.1355	0.4380	-0.1363	0.5870
25.0000	5.0000	-3.8276	-0.4551	0.1245	0.4394	-0.1287	0.5892
30.0000	5.0000	-4.5436	-0.4629	0.1174	0.4408	-0.1235	0.5873
35.0000	5.0000	-5.2601	-0.4706	0.1062	0.4423	-0.1174	0.5886
40.0000	5.0000	-5.9794	-0.4755	0.0999	0.4431	-0.1127	0.5831
35.0000	5.0000	-5.2641	-0.4679	0.1088	0.4420	-0.1184	0.5845
30.0000	5.0000	-4.5522	-0.4569	0.1175	0.4406	-0.1242	0.5833
25.0000	5.0000	-3.8318	-0.4546	0.1256	0.4397	-0.1300	0.5925
20.0000	5.0000	-3.1055	-0.4580	0.1394	0.4383	-0.1513	0.5854
15.0000	5.0000	-2.3897	-0.4499	0.1470	0.4373	-0.1454	0.5883
10.0000	5.0000	-1.6711	-0.4451	0.1560	0.4362	-0.1532	0.5893
5.0000	5.0000	-0.9527	-0.4404	0.1652	0.4349	-0.1614	0.5899
0.0000	5.0000	-0.2344	-0.4352	0.1743	0.4338	-0.1699	0.5902

drift corrected data, normalised by excitation voltage

LOAD(kgf)	N1(v)	N2(v)	S1(v)	S2(v)	Ax(v)	L(v)
0.0000	0.0000	0.0000	0.0000	0.0000	0.0000	0.0000
5.0000	-0.1436	-0.0008	-0.0020	0.0002	0.0019	-0.0001
10.0000	-0.2873	-0.0017	-0.0039	0.0005	0.0036	-0.0001
15.0000	-0.4308	-0.0029	-0.0059	0.0008	0.0052	-0.0000
20.0000	-0.5747	-0.0036	-0.0077	0.0010	0.0066	-0.0006
25.0000	-0.7187	-0.0043	-0.0099	0.0012	0.0081	-0.0002
30.0000	-0.8619	-0.0058	-0.0113	0.0015	0.0092	-0.0006
35.0000	-1.0052	-0.0073	-0.0136	0.0018	0.0104	-0.0003
40.0000	-1.1490	-0.0083	-0.0148	0.0020	0.0113	-0.0014
35.0000	-1.0060	-0.0067	-0.0130	0.0017	0.0102	-0.0011
30.0000	-0.8636	-0.0045	-0.0113	0.0014	0.0091	-0.0014
25.0000	-0.7195	-0.0040	-0.0097	0.0012	0.0079	0.0005
20.0000	-0.5742	-0.0047	-0.0069	0.0010	0.0037	-0.0009
15.0000	-0.4311	-0.0030	-0.0054	0.0007	0.0049	-0.0004
10.0000	-0.2874	-0.0020	-0.0036	0.0005	0.0033	-0.0002
5.0000	-0.1437	-0.0011	-0.0018	0.0002	0.0017	-0.0001
0.0000	0.0000	0.0000	0.0000	0.0000	0.0000	0.0000

normalised by load applied

5.00000000	-0.02872314	-0.00016628	-0.00039040	0.00004595	0.00037279	-0.00001908
10.00000000	-0.02872593	-0.00017374	-0.00039352	0.00005003	0.00035769	-0.00001182
15.00000000	-0.02871821	-0.00019282	-0.00039280	0.00005009	0.00034549	-0.00000265
20.00000000	-0.02873597	-0.00017930	-0.00038336	0.00004847	0.00032969	-0.00003053
25.00000000	-0.02874841	-0.00017105	-0.00039498	0.00004947	0.00032484	-0.00000709
30.00000000	-0.02872994	-0.00019356	-0.00037692	0.00005066	0.00030559	-0.00001834
35.00000000	-0.02871965	-0.00020920	-0.00038727	0.00005119	0.00029683	-0.00000862
40.00000000	-0.02872625	-0.00020722	-0.00037041	0.00004889	0.00028366	-0.00003476
35.00000000	-0.02874258	-0.00019245	-0.00037257	0.00004925	0.00029172	-0.00003216
30.00000000	-0.02878648	-0.00015038	-0.00037731	0.00004793	0.00030202	-0.00004551
25.00000000	-0.02878043	-0.00016035	-0.00038817	0.00004941	0.00031678	0.00001899
20.00000000	-0.02871231	-0.00023385	-0.00034728	0.00004753	0.00018312	-0.00004711
15.00000000	-0.02873921	-0.00020175	-0.00036222	0.00004872	0.00032441	-0.00002499
10.00000000	-0.02873628	-0.00020374	-0.00036408	0.00005075	0.00033151	-0.00001706
5.00000000	-0.02873187	-0.00021444	-0.00036200	0.00004773	0.00033745	-0.00001304

average values

-0.02873711	-0.00019001	-0.00037755	0.00004907	0.00031357	-0.00001958

TABLE - 5

LOADING : N1 Positive

LOAD(kgf)	EX(v)	N1(v)	N2(v)	S1(v)	S2(v)	A1(v)	L1(v)
0.0000	5.0000	0.6071	-0.3328	0.1915	0.4332	-0.1689	0.5885
5.0000	5.0000	1.3259	-0.3286	0.2054	0.4320	-0.1767	0.5875
10.0000	5.0000	2.0475	-0.3274	0.2197	0.4309	-0.1844	0.5892
15.0000	5.0000	2.7605	-0.3172	0.2337	0.4299	-0.1929	0.5903
20.0000	5.0000	3.4812	-0.3142	0.2475	0.4286	-0.2018	0.5898
25.0000	5.0000	4.1980	-0.3077	0.2615	0.4273	-0.2114	0.5870
30.0000	5.0000	4.9166	-0.3028	0.2762	0.4258	-0.2218	0.5816
35.0000	5.0000	5.6314	-0.2937	0.2883	0.4246	-0.2323	0.5799
40.0000	5.0000	6.3525	-0.2914	0.3020	0.4235	-0.2433	0.5827
35.0000	5.0000	5.6412	-0.3031	0.2880	0.4248	-0.2325	0.5814
30.0000	5.0000	4.9224	-0.3073	0.2745	0.4262	-0.2214	0.5846
25.0000	5.0000	4.2057	-0.3138	0.2608	0.4276	-0.2109	0.5886
20.0000	5.0000	3.4878	-0.3190	0.2468	0.4289	-0.2014	0.5874
15.0000	5.0000	2.7679	-0.3229	0.2332	0.4301	-0.1922	0.5907
10.0000	5.0000	2.0501	-0.3281	0.2193	0.4310	-0.1836	0.5871
5.0000	5.0000	1.3295	-0.3308	0.2053	0.4324	-0.1757	0.5889
0.0000	5.0000	0.6086	-0.3332	0.1913	0.4335	-0.1682	0.5885

drift corrected data, normalised by excitation voltage

LOAD(kgf)	N1(v)	N2(v)	S1(v)	S2(v)	Ax(v)	L(v)
0.0000	0.0000	0.0000	0.0000	0.0000	0.0000	0.0000
5.0000	0.1437	0.0008	0.0028	-0.0002	-0.0016	-0.0002
10.0000	0.2880	0.0011	0.0056	-0.0005	-0.0031	0.0001
15.0000	0.4306	0.0031	0.0084	-0.0007	-0.0048	0.0004
20.0000	0.5748	0.0038	0.0112	-0.0009	-0.0066	0.0003
25.0000	0.7181	0.0050	0.0140	-0.0012	-0.0086	-0.0003
30.0000	0.8618	0.0060	0.0170	-0.0015	-0.0106	-0.0014
35.0000	1.0047	0.0079	0.0194	-0.0017	-0.0127	-0.0017
40.0000	1.1489	0.0083	0.0221	-0.0020	-0.0149	-0.0012
35.0000	1.0067	0.0060	0.0193	-0.0017	-0.0128	-0.0014
30.0000	0.8629	0.0052	0.0166	-0.0014	-0.0106	-0.0008
25.0000	0.7195	0.0038	0.0139	-0.0011	-0.0085	0.0000
20.0000	0.5759	0.0028	0.0111	-0.0009	-0.0066	-0.0002
15.0000	0.4319	0.0020	0.0084	-0.0007	-0.0048	0.0004
10.0000	0.2883	0.0010	0.0056	-0.0005	-0.0031	-0.0003
5.0000	0.1442	0.0005	0.0028	-0.0002	-0.0015	0.0001
0.0000	0.0000	0.0000	0.0000	0.0000	0.0000	0.0000

normalised by load applied

5.00000000	0.02874919	0.00016943	0.00055520	-0.00004907	-0.00031321	-0.00004024
10.00000000	0.02880449	0.00011029	0.00056412	-0.00004695	-0.00031250	0.00001346
15.00000000	0.02870932	0.00020901	0.00056232	-0.00004562	-0.00032238	0.00002479
20.00000000	0.02873759	0.00018771	0.00056063	-0.00004684	-0.00033049	0.00001355
25.00000000	0.02872360	0.00020189	0.00056017	-0.00004825	-0.00034222	-0.00001205
30.00000000	0.02872635	0.00020138	0.00056502	-0.00005017	-0.00035443	-0.00004574
35.00000000	0.02870684	0.00022477	0.00055382	-0.00004964	-0.00036407	-0.00004885
40.00000000	0.02872337	0.00020812	0.00055293	-0.00004896	-0.00037371	-0.00002877
35.00000000	0.02876167	0.00017127	0.00055217	-0.00004863	-0.00036557	-0.00004048
30.00000000	0.02876266	0.00017210	0.00055391	-0.00004791	-0.00035279	-0.00002564
25.00000000	0.02878095	0.00015394	0.00055544	-0.00004598	-0.00033979	0.00000081
20.00000000	0.02879604	0.00014068	0.00055503	-0.00004472	-0.00033021	-0.00001038
15.00000000	0.02879546	0.00013650	0.00055788	-0.00004457	-0.00031842	0.00002909
10.00000000	0.02883473	0.00010171	0.00055900	-0.00004787	-0.00030606	-0.00002828
5.00000000	0.02884289	0.00009625	0.00056072	-0.00003961	-0.00029696	0.00001556

average values

0.02876368	0.00016567	0.00055789	-0.00004699	-0.00033485	-0.00001221

nn2f_1

TABLE - 6

LOADING : N2 NEGATIVE

LOAD(kgf)	EX(v)	N1(v)	N2(v)	S1(v)	S2(v)	A1(v)	L1(v)
0.0000	5.0000	-0.0588	-0.5803	0.1816	0.4169	-0.1398	0.5980
5.0000	5.0000	-0.0664	-1.2950	0.1815	0.4362	-0.1371	0.6101
10.0000	5.0000	-0.0738	-2.0101	0.1814	0.4553	-0.1335	0.6203
15.0000	5.0000	-0.0791	-2.7271	0.1813	0.4739	-0.1304	0.6271
20.0000	5.0000	-0.0866	-3.4424	0.1812	0.4927	-0.1270	0.6362
25.0000	5.0000	-0.0939	-4.1580	0.1809	0.5118	-0.1238	0.6480
30.0000	5.0000	-0.0970	-4.8774	0.1809	0.5309	-0.1202	0.6592
35.0000	5.0000	-0.1047	-5.5923	0.1807	0.5502	-0.1161	0.6759
40.0000	5.0000	-0.1250	-6.2953	0.1808	0.5673	-0.1128	0.6735
35.0000	5.0000	-0.1073	-5.5905	0.1807	0.5490	-0.1170	0.6631
30.0000	5.0000	-0.0979	-4.8777	0.1811	0.5304	-0.1202	0.6546
25.0000	5.0000	-0.0887	-4.1645	0.1811	0.5114	-0.1239	0.6448
20.0000	5.0000	-0.0827	-3.4478	0.1813	0.4928	-0.1271	0.6370
15.0000	5.0000	-0.0769	-2.7311	0.1813	0.4741	-0.1304	0.6283
10.0000	5.0000	-0.0713	-2.0143	0.1814	0.4552	-0.1335	0.6192
5.0000	5.0000	-0.0654	-1.2974	0.1815	0.4360	-0.1369	0.6090
0.0000	5.0000	-0.0590	-0.5811	0.1816	0.4166	-0.1401	0.5981

drift corrected data, normalised by excitation voltage

LOAD(kgf)	N1(v)	N2(v)	S1(v)	S2(v)	Ax(v)	L(v)
0.0000	0.0000	0.0000	0.0000	0.0000	0.0000	0.0000
5.0000	-0.0015	-0.1429	-0.0000	0.0039	0.0005	0.0024
10.0000	-0.0030	-0.2859	-0.0000	0.0077	0.0013	0.0044
15.0000	-0.0040	-0.4293	-0.0001	0.0114	0.0019	0.0058
20.0000	-0.0055	-0.5724	-0.0001	0.0152	0.0026	0.0076
25.0000	-0.0070	-0.7155	-0.0001	0.0190	0.0032	0.0100
30.0000	-0.0076	-0.8594	-0.0001	0.0228	0.0039	0.0122
35.0000	-0.0092	-1.0023	-0.0002	0.0267	0.0048	0.0156
40.0000	-0.0132	-1.1429	-0.0001	0.0301	0.0054	0.0151
35.0000	-0.0097	-1.0019	-0.0002	0.0265	0.0046	0.0130
30.0000	-0.0078	-0.8594	-0.0001	0.0228	0.0040	0.0113
25.0000	-0.0059	-0.7167	-0.0001	0.0189	0.0032	0.0093
20.0000	-0.0048	-0.5734	-0.0001	0.0152	0.0026	0.0078
15.0000	-0.0036	-0.4300	-0.0000	0.0115	0.0019	0.0060
10.0000	-0.0025	-0.2867	-0.0000	0.0077	0.0013	0.0042
5.0000	-0.0013	-0.1433	-0.0000	0.0039	0.0006	0.0022
0.0000	0.0000	0.0000	0.0000	0.0000	0.0000	0.0000

normalised by load applied

5.00000000	-0.00030340	-0.02858363	-0.00000432	0.00077385	0.00010843	0.00048259
10.00000000	-0.00029835	-0.02859409	-0.00000362	0.00076848	0.00012598	0.00044497
15.00000000	-0.00026926	-0.02862211	-0.00000377	0.00076043	0.00012614	0.00038693
20.00000000	-0.00027730	-0.02861823	-0.00000399	0.00075927	0.00012840	0.00038148
25.00000000	-0.00027993	-0.02861919	-0.00000525	0.00075993	0.00012894	0.00039924
30.00000000	-0.00025429	-0.02864512	-0.00000466	0.00076110	0.00013142	0.00040747
35.00000000	-0.00026191	-0.02863814	-0.00000465	0.00076258	0.00013624	0.00044491
40.00000000	-0.00033043	-0.02857284	-0.00000366	0.00075282	0.00013557	0.00037712
35.00000000	-0.00027653	-0.02862703	-0.00000481	0.00075591	0.00013105	0.00037161
30.00000000	-0.00025989	-0.02864599	-0.00000292	0.00075843	0.00013185	0.00037668
25.00000000	-0.00023787	-0.02866877	-0.00000404	0.00075764	0.00012858	0.00037375
20.00000000	-0.00023758	-0.02866935	-0.00000311	0.00076204	0.00012978	0.00038883
15.00000000	-0.00023984	-0.02866907	-0.00000295	0.00076614	0.00012843	0.00040257
10.00000000	-0.00024601	-0.02866545	-0.00000352	0.00077104	0.00013109	0.00042093
5.00000000	-0.00025864	-0.02865609	-0.00000392	0.00077848	0.00012849	0.00043473

average values

-0.00026875	-0.02863301	-0.00000395	0.00076321	0.00012869	0.00040625

TABLE - 7

LOADING : N2 Positive

LOAD(kgf)	EX(v)	N1(v)	N2(v)	S1(v)	S2(v)	A1(v)	L1(v)
0.0000	5.0000	0.4340	-0.1579	0.1878	0.4326	-0.1675	0.5869
5.0000	5.0000	0.4387	0.5662	0.1886	0.4292	-0.1699	0.5780
10.0000	5.0000	0.4400	1.2936	0.1890	0.4255	-0.1718	0.5702
15.0000	5.0000	0.4488	2.0144	0.1894	0.4217	-0.1739	0.5599
20.0000	5.0000	0.4507	2.7420	0.1899	0.4178	-0.1760	0.5482
25.0000	5.0000	0.4548	3.4673	0.1904	0.4138	-0.1779	0.5415
30.0000	5.0000	0.4624	4.1892	0.1909	0.4095	-0.1801	0.5298
35.0000	5.0000	0.4709	4.9101	0.1914	0.4037	-0.1822	0.5231
40.0000	5.0000	0.4782	5.6320	0.1919	0.3961	-0.1834	0.5126
35.0000	5.0000	0.4686	4.9148	0.1917	0.4014	-0.1816	0.5210
30.0000	5.0000	0.4652	4.1904	0.1906	0.4083	-0.1806	0.5278
25.0000	5.0000	0.4583	3.4684	0.1904	0.4116	-0.1782	0.5376
20.0000	5.0000	0.4526	2.7450	0.1896	0.4168	-0.1766	0.5479
15.0000	5.0000	0.4476	2.0207	0.1891	0.4209	-0.1746	0.5605
10.0000	5.0000	0.4429	1.2952	0.1887	0.4247	-0.1725	0.5698
5.0000	5.0000	0.4384	0.5696	0.1883	0.4284	-0.1702	0.5778
0.0000	5.0000	0.4344	-0.1565	0.1877	0.4320	-0.1682	0.5862

drift corrected data, normalised by excitation voltage

LOAD(kgf)	N1(v)	N2(v)	S1(v)	S2(v)	Ax(v)	L(v)
0.0000	0.0000	0.0000	0.0000	0.0000	0.0000	0.0000
5.0000	0.0009	0.1448	0.0002	-0.0007	-0.0005	-0.0018
10.0000	0.0012	0.2903	0.0002	-0.0014	-0.0009	-0.0033
15.0000	0.0029	0.4344	0.0003	-0.0022	-0.0013	-0.0054
20.0000	0.0033	0.5799	0.0004	-0.0029	-0.0017	-0.0077
25.0000	0.0041	0.7249	0.0005	-0.0037	-0.0020	-0.0090
30.0000	0.0057	0.8693	0.0006	-0.0046	-0.0025	-0.0114
35.0000	0.0073	1.0135	0.0007	-0.0057	-0.0029	-0.0127
40.0000	0.0088	1.1578	0.0008	-0.0072	-0.0031	-0.0148
35.0000	0.0069	1.0144	0.0008	-0.0062	-0.0027	-0.0131
30.0000	0.0062	0.8695	0.0006	-0.0048	-0.0025	-0.0117
25.0000	0.0048	0.7251	0.0005	-0.0041	-0.0020	-0.0098
20.0000	0.0037	0.5804	0.0004	-0.0031	-0.0017	-0.0077
15.0000	0.0027	0.4355	0.0003	-0.0022	-0.0013	-0.0052
10.0000	0.0017	0.2904	0.0002	-0.0015	-0.0009	-0.0033
5.0000	0.0008	0.1452	0.0001	-0.0007	-0.0004	-0.0017
0.0000	0.0000	0.0000	0.0000	0.0000	0.0000	0.0000

normalised by load applied

5.00000000	0.00018481	0.02896165	0.00003008	-0.00013405	-0.00009439	-0.00035379
10.00000000	0.00011875	0.02902707	0.00002262	-0.00014045	-0.00008537	-0.00033233
15.00000000	0.00019555	0.02896041	0.00002176	-0.00014414	-0.00008415	-0.00035896
20.00000000	0.00016597	0.02899487	0.00002138	-0.00014639	-0.00008382	-0.00038519
25.00000000	0.00016545	0.02899784	0.00002058	-0.00014872	-0.00008187	-0.00036186
30.00000000	0.00018845	0.02897724	0.00002105	-0.00015223	-0.00008209	-0.00037936
35.00000000	0.00020953	0.02895633	0.00002050	-0.00016376	-0.00008240	-0.00036293
40.00000000	0.00022011	0.02894602	0.00002077	-0.00018078	-0.00007796	-0.00037006
35.00000000	0.00019617	0.02898243	0.00002264	-0.00017648	-0.00007839	-0.00037439
30.00000000	0.00020659	0.02898269	0.00001898	-0.00015961	-0.00008423	-0.00039118
25.00000000	0.00019246	0.02900223	0.00002174	-0.00016465	-0.00008186	-0.00039063
20.00000000	0.00018270	0.02901855	0.00001862	-0.00015368	-0.00008589	-0.00038472
15.00000000	0.00017748	0.02903289	0.00001880	-0.00014989	-0.00008716	-0.00034450
10.00000000	0.00017058	0.02903725	0.00002082	-0.00014745	-0.00008773	-0.00033065
5.00000000	0.00016231	0.02904699	0.00002276	-0.00014367	-0.00008193	-0.00033997

average values

0.00018246	0.02899496	0.00002154	-0.00015373	-0.00008395	-0.00036403

TABLE – 8 LOADING : S1 Negative

LOAD(kgf)	EX(v)	N1(v)	N2(v)	S1(v)	S2(v)	A1(v)	L1(v)
0.0000	5.0000	0.1974	-0.3752	-0.4443	0.3765	-0.1741	0.5886
2.0000	5.0000	0.2006	-0.3758	-0.8739	0.3648	-0.1821	0.5885
4.0000	5.0000	0.2037	-0.3763	-1.3097	0.3594	-0.1901	0.5895
6.0000	5.0000	0.2067	-0.3767	-1.7376	0.3459	-0.1983	0.5893
8.0000	5.0000	0.2099	-0.3776	-2.1748	0.3416	-0.2067	0.5915
10.0000	5.0000	0.2129	-0.3778	-2.6086	0.3335	-0.2152	0.5890
12.0000	5.0000	0.2157	-0.3783	-3.0366	0.3197	-0.2236	0.5899
14.0000	5.0000	0.2187	-0.3788	-3.4647	0.3062	-0.2324	0.5882
16.0000	5.0000	0.2217	-0.3794	-3.8961	0.2955	-0.2412	0.5883
18.0000	5.0000	0.2246	-0.3798	-4.3229	0.2801	-0.2501	0.5897
20.0000	5.0000	0.2276	-0.3806	-4.7650	0.2800	-0.2597	0.5887
18.0000	5.0000	0.2246	-0.3800	-4.3319	0.2875	-0.2505	0.5870
16.0000	5.0000	0.2215	-0.3793	-3.8989	0.2959	-0.2416	0.5869
14.0000	5.0000	0.2184	-0.3789	-3.4671	0.3054	-0.2328	0.5862
12.0000	5.0000	0.2152	-0.3784	-3.0361	0.3159	-0.2241	0.5864
10.0000	5.0000	0.2123	-0.3778	-2.6054	0.3263	-0.2152	0.5866
8.0000	5.0000	0.2095	-0.3773	-2.1740	0.3367	-0.2067	0.5871
6.0000	5.0000	0.2060	-0.3768	-1.7420	0.3463	-0.1985	0.5880
4.0000	5.0000	0.2034	-0.3761	-1.3091	0.3547	-0.1901	0.5886
2.0000	5.0000	0.2002	-0.3756	-0.8780	0.3651	-0.1819	0.5887
0.0000	5.0000	0.1969	-0.3752	-0.4474	0.3761	-0.1740	0.5883

drift corrected data, normalised by excitation voltage

LOAD(kgf)	N1(v)	N2(v)	S1(v)	S2(v)	Ax(v)	L(v)
2.0000	0.0006	-0.0001	-0.0859	-0.0023	-0.0016	-0.0000
4.0000	0.0013	-0.0002	-0.1730	-0.0034	-0.0032	0.0002
6.0000	0.0019	-0.0003	-0.2586	-0.0061	-0.0048	0.0001
8.0000	0.0025	-0.0005	-0.3460	-0.0070	-0.0065	0.0006
10.0000	0.0031	-0.0005	-0.4327	-0.0086	-0.0082	0.0001
12.0000	0.0037	-0.0006	-0.5183	-0.0113	-0.0099	0.0003
14.0000	0.0043	-0.0007	-0.6039	-0.0140	-0.0117	-0.0001
16.0000	0.0049	-0.0008	-0.6901	-0.0162	-0.0134	-0.0000
18.0000	0.0055	-0.0009	-0.7754	-0.0192	-0.0152	0.0002
20.0000	0.0061	-0.0011	-0.8638	-0.0193	-0.0171	0.0000
18.0000	0.0055	-0.0010	-0.7772	-0.0177	-0.0153	-0.0003
16.0000	0.0049	-0.0008	-0.6906	-0.0161	-0.0135	-0.0003
14.0000	0.0043	-0.0007	-0.6041	-0.0142	-0.0117	-0.0004
12.0000	0.0036	-0.0006	-0.5179	-0.0121	-0.0100	-0.0004
10.0000	0.0031	-0.0005	-0.4318	-0.0100	-0.0082	-0.0004
8.0000	0.0025	-0.0004	-0.3454	-0.0079	-0.0065	-0.0003
6.0000	0.0018	-0.0003	-0.2590	-0.0060	-0.0049	-0.0001
4.0000	0.0013	-0.0002	-0.1724	-0.0043	-0.0032	0.0001
2.0000	0.0007	-0.0001	-0.0861	-0.0022	-0.0016	0.0001

normalised by load applied

2.00000000	0.00032022	-0.00005607	-0.04294366	-0.00115881	-0.00079402	-0.00000924
4.00000000	0.00031887	-0.00005462	-0.04325586	-0.00085241	-0.00079642	0.00004476
6.00000000	0.00031315	-0.00005097	-0.04309509	-0.00101777	-0.00080675	0.00002290
8.00000000	0.00031607	-0.00005880	-0.04324746	-0.00086990	-0.00081462	0.00007469
10.00000000	0.00031318	-0.00005132	-0.04327079	-0.00085650	-0.00082214	0.00001020
12.00000000	0.00030795	-0.00005107	-0.04318929	-0.00094486	-0.00082554	0.00002328
14.00000000	0.00030681	-0.00005140	-0.04313337	-0.00100125	-0.00083233	-0.0000042s8
16.00000000	0.00030603	-0.00005182	-0.04313207	-0.00101056	-0.00083827	-0.00000262
18.00000000	0.00030434	-0.00005055	-0.04307953	-0.00106869	-0.00084468	0.00001335
20.00000000	0.00030438	-0.00005392	-0.04319136	-0.00096314	-0.00085579	0.00000199
18.00000000	0.00030516	-0.00005372	-0.04317591	-0.00098579	-0.00084952	-0.00001629
16.00000000	0.00030488	-0.00005170	-0.04315947	-0.00100484	-0.00084369	-0.00001903
14.00000000	0.00030524	-0.00005317	-0.04315355	-0.00101178	-0.00083839	-0.00003202
12.00000000	0.00030276	-0.00005279	-0.04316051	-0.00100585	-0.00083401	-0.00003383
10.00000000	0.00030566	-0.00005214	-0.04317543	-0.00099807	-0.00082314	-0.00003602

8.00000000	0.00031151	-0.00005315	-0.04317894	-0.00098757	-0.00081738	-0.00003314
6.00000000	0.00030121	-0.00005389	-0.04316698	-0.00099426	-0.00081391	-0.00001403
4.00000000	0.00032143	-0.00004712	-0.04309685	-0.00106945	-0.00080473	0.00001344
2.00000000	0.00032748	-0.00004613	-0.04306774	-0.00109969	-0.00078888	0.00003343

average values

0.00031033	-0.00005234	-0.04315125	-0.00099480	-0.00082338	0.00000198

TABLE – 9 LOADING : S1 Positive

LOAD(kgf)	EX(v)	N1(v)	N2(v)	S1(v)	S2(v)	A1(v)	L1(v)
0.0000	5.0000	0.1875	-0.4068	0.8018	0.4974	-0.1614	0.5867
2.0000	5.0000	0.1872	-0.4062	1.2304	0.5096	-0.1527	0.5869
4.0000	5.0000	0.1868	-0.4058	1.6614	0.5194	-0.1443	0.5862
6.0000	5.0000	0.1865	-0.4052	2.0903	0.5315	-0.1360	0.5873
8.0000	5.0000	0.1861	-0.4046	2.5204	0.5427	-0.1278	0.5861
10.0000	5.0000	0.1856	-0.4041	2.9511	0.5532	-0.1196	0.5873
12.0000	5.0000	0.1854	-0.4036	3.3831	0.5625	-0.1114	0.5861
14.0000	5.0000	0.1852	-0.4028	3.8135	0.5733	-0.1036	0.5860
16.0000	5.0000	0.1847	-0.4025	4.2399	0.5883	-0.0961	0.5824
18.0000	5.0000	0.1846	-0.4021	4.6703	0.5998	-0.0885	0.5824
20.0000	5.0000	0.1845	-0.4016	5.0978	0.6138	-0.0813	0.5811
18.0000	5.0000	0.1847	-0.4019	4.6682	0.6028	-0.0886	0.5835
16.0000	5.0000	0.1855	-0.4026	4.2388	0.5912	-0.0964	0.5833
14.0000	5.0000	0.1860	-0.4031	3.8106	0.5788	-0.1039	0.5839
12.0000	5.0000	0.1864	-0.4034	3.3824	0.5663	-0.1116	0.5840
10.0000	5.0000	0.1868	-0.4038	2.9550	0.5529	-0.1196	0.5851
8.0000	5.0000	0.1875	-0.4044	2.5256	0.5414	-0.1276	0.5857
6.0000	5.0000	0.1880	-0.4049	2.0964	0.5299	-0.1357	0.5862
4.0000	5.0000	0.1883	-0.4053	1.6646	0.5208	-0.1440	0.5860
2.0000	5.0000	0.1890	-0.4061	1.2350	0.5096	-0.1525	0.5856
0.0000	5.0000	0.1895	-0.4065	0.8064	0.4972	-0.1605	0.5857

drift corrected data, normalised by excitation voltage

LOAD(kgf)	N1(v)	N2(v)	S1(v)	S2(v)	Ax(v)	L(v)
2.0000	-0.0001	0.0001	0.0857	0.0024	0.0017	0.0001
4.0000	-0.0002	0.0002	0.1718	0.0044	0.0034	-0.0001
6.0000	-0.0003	0.0003	0.2576	0.0068	0.0050	0.0001
8.0000	-0.0004	0.0004	0.3435	0.0091	0.0067	-0.0001
10.0000	-0.0005	0.0005	0.4296	0.0112	0.0083	0.0002
12.0000	-0.0005	0.0006	0.5160	0.0130	0.0099	-0.0001
14.0000	-0.0006	0.0008	0.6020	0.0152	0.0115	-0.0001
16.0000	-0.0007	0.0008	0.6873	0.0182	0.0130	-0.0008
18.0000	-0.0008	0.0009	0.7733	0.0205	0.0145	-0.0008
20.0000	-0.0008	0.0010	0.8587	0.0233	0.0159	-0.0010
18.0000	-0.0008	0.0009	0.7728	0.0211	0.0145	-0.0005
16.0000	-0.0006	0.0008	0.6868	0.0188	0.0129	-0.0006
14.0000	-0.0006	0.0007	0.6012	0.0163	0.0114	-0.0004
12.0000	-0.0005	0.0006	0.5155	0.0138	0.0098	-0.0004
10.0000	-0.0004	0.0006	0.4299	0.0111	0.0082	-0.0002
8.0000	-0.0003	0.0004	0.3440	0.0088	0.0066	-0.0000
6.0000	-0.0002	0.0003	0.2581	0.0065	0.0050	0.0001
4.0000	-0.0002	0.0002	0.1717	0.0047	0.0033	0.0000
2.0000	-0.0001	0.0001	0.0858	0.0025	0.0016	-0.0000

normalised by load applied

2.00000000	-0.00003836	0.00005553	0.04284016	0.00121774	0.00085660	0.00002577
4.00000000	-0.00004451	0.00004493	0.04296001	0.00110204	0.00084870	-0.00001888
6.00000000	-0.00004456	0.00004950	0.04292813	0.00113884	0.00084123	0.00002400
8.00000000	-0.00004591	0.00005200	0.04294223	0.00113360	0.00083550	-0.00001118
10.00000000	-0.00004810	0.00005213	0.04296322	0.00111757	0.00082990	0.00001695
12.00000000	-0.00004443	0.00005063	0.04299836	0.00108670	0.00082795	-0.00000469
14.00000000	-0.00004283	0.00005474	0.04300190	0.00108606	0.00082071	-0.00000513
16.00000000	-0.00004450	0.00005235	0.04295356	0.00113781	0.00081076	-0.00004881
18.00000000	-0.00004258	0.00005074	0.04296065	0.00113874	0.00080554	-0.00004305
20.00000000	-0.00004051	0.00005068	0.04293662	0.00116512	0.00079660	-0.00005060
18.00000000	-0.00004393	0.00005180	0.04293162	0.00117222	0.00080291	-0.00002915
16.00000000	-0.00004031	0.00005027	0.04292762	0.00117473	0.00080577	-0.00003554
14.00000000	-0.00004037	0.00004981	0.04294068	0.00116504	0.00081269	-0.00003018

12.00000000	-0.00004147	0.00005284	0.04295579	0.00115142	0.00081827	-0.00003358
10.00000000	-0.00004418	0.00005543	0.04299394	0.00111430	0.00082210	-0.00001753
8.00000000	-0.00004006	0.00005285	0.04300166	0.00110608	0.00082533	-0.00000452
6.00000000	-0.00004007	0.00005357	0.04302144	0.00109156	0.00083123	0.00001100
4.00000000	-0.00005039	0.00005897	0.04293469	0.00118191	0.00082735	0.00000978
2.00000000	-0.00004354	0.00004207	0.04287964	0.00124146	0.00079860	-0.00001737

average values

-0.00004319	0.00005162	0.04295115	0.00114331	0.00082199	-0.00001383

TABLE – 10 LOADING : S2 Negative

LOAD(kgf)	EX(v)	N1(v)	N2(v)	S1(v)	S2(v)	A1(v)	L1(v)
0.0000	5.0000	0.1945	-0.3741	-0.1899	0.1145	-0.1658	0.5882
2.0000	5.0000	0.1946	-0.3703	-0.1987	-0.3180	-0.1586	0.5871
4.0000	5.0000	0.1948	-0.3670	-0.2101	-0.7476	-0.1519	0.5863
6.0000	5.0000	0.1950	-0.3633	-0.2223	-1.1765	-0.1451	0.5859
8.0000	5.0000	0.1951	-0.3595	-0.2338	-1.6060	-0.1384	0.5849
10.0000	5.0000	0.1954	-0.3558	-0.2458	-2.0353	-0.1315	0.5833
12.0000	5.0000	0.1954	-0.3521	-0.2580	-2.4646	-0.1247	0.5813
14.0000	5.0000	0.1955	-0.3487	-0.2651	-2.8986	-0.1178	0.5826
16.0000	5.0000	0.1956	-0.3454	-0.2765	-3.3283	-0.1107	0.5806
18.0000	5.0000	0.1958	-0.3418	-0.2868	-3.7594	-0.1041	0.5788
20.0000	5.0000	0.1958	-0.3385	-0.2948	-4.1926	-0.0974	0.5775
18.0000	5.0000	0.1956	-0.3418	-0.2852	-3.7616	-0.1041	0.5813
16.0000	5.0000	0.1953	-0.3452	-0.2744	-3.3315	-0.1112	0.5826
14.0000	5.0000	0.1953	-0.3484	-0.2610	-2.9042	-0.1182	0.5828
12.0000	5.0000	0.1948	-0.3520	-0.2504	-2.4736	-0.1251	0.5829
10.0000	5.0000	0.1948	-0.3554	-0.2400	-2.0431	-0.1320	0.5836
8.0000	5.0000	0.1946	-0.3590	-0.2301	-1.6120	-0.1391	0.5849
6.0000	5.0000	0.1941	-0.3624	-0.2195	-1.1809	-0.1459	0.5862
4.0000	5.0000	0.1941	-0.3663	-0.2087	-0.7508	-0.1528	0.5862
2.0000	5.0000	0.1939	-0.3700	-0.1980	-0.3200	-0.1594	0.5872
0.0000	5.0000	0.1937	-0.3738	-0.1888	0.1128	-0.1662	0.5886

drift corrected data, normalised by excitation voltage

LOAD(kgf)	N1(v)	N2(v)	S1(v)	S2(v)	Ax(v)	L(v)
2.0000	0.0000	0.0008	-0.0018	-0.0865	0.0014	-0.0002
4.0000	0.0001	0.0014	-0.0041	-0.1724	0.0028	-0.0004
6.0000	0.0001	0.0022	-0.0065	-0.2581	0.0042	-0.0005
8.0000	0.0001	0.0029	-0.0088	-0.3440	0.0055	-0.0007
10.0000	0.0002	0.0036	-0.0112	-0.4299	0.0069	-0.0010
12.0000	0.0002	0.0044	-0.0137	-0.5157	0.0082	-0.0014
14.0000	0.0003	0.0051	-0.0151	-0.6025	0.0096	-0.0011
16.0000	0.0003	0.0057	-0.0174	-0.6884	0.0110	-0.0016
18.0000	0.0003	0.0064	-0.0195	-0.7746	0.0124	-0.0019
20.0000	0.0003	0.0071	-0.0211	-0.8613	0.0137	-0.0022
18.0000	0.0003	0.0064	-0.0192	-0.7750	0.0124	-0.0014
16.0000	0.0003	0.0057	-0.0170	-0.6890	0.0110	-0.0012
14.0000	0.0003	0.0051	-0.0144	-0.6035	0.0096	-0.0011
12.0000	0.0002	0.0044	-0.0122	-0.5174	0.0082	-0.0011
10.0000	0.0002	0.0037	-0.0102	-0.4313	0.0068	-0.0010
8.0000	0.0001	0.0030	-0.0082	-0.3450	0.0054	-0.0007
6.0000	0.0001	0.0023	-0.0061	-0.2588	0.0041	-0.0005
4.0000	0.0001	0.0015	-0.0040	-0.1727	0.0027	-0.0005
2.0000	0.0000	0.0008	-0.0018	-0.0866	0.0014	-0.0003

normalised by load applied

2.00000000	0.00001526	0.00037584	-0.00088503	-0.04324323	0.00071596	-0.00010945
4.00000000	0.00001710	0.00035454	-0.00101548	-0.04309558	0.00069681	-0.00009980
6.00000000	0.00001965	0.00035847	-0.00108640	-0.04302296	0.00069183	-0.00007868
8.00000000	0.00001748	0.00036414	-0.00110400	-0.04300433	0.00068724	-0.00008528
10.00000000	0.00002261	0.00036404	-0.00112261	-0.04298641	0.00068844	-0.00010019
12.00000000	0.00001915	0.00036472	-0.00113986	-0.04297648	0.00068696	-0.00011680
14.00000000	0.00001894	0.00036095	-0.00107960	-0.04303494	0.00068730	-0.00008174
16.00000000	0.00001792	0.00035690	-0.00108731	-0.04302573	0.00069062	-0.00009709
18.00000000	0.00001903	0.00035734	-0.00108201	-0.04303431	0.00068807	-0.00010606
20.00000000	0.00001703	0.00035440	-0.00105431	-0.04306253	0.00068595	-0.00010891
18.00000000	0.00001732	0.00035670	-0.00106527	-0.04305714	0.00068752	-0.00007889

16.00000000	0.00001673	0.00035872	-0.00106401	-0.04306246	0.00068596	-0.00007271
14.00000000	0.00001847	0.00036506	-0.00102526	-0.04310891	0.00068413	-0.00008131
12.00000000	0.00001448	0.00036518	-0.00102052	-0.04311464	0.00068252	-0.00009312
10.00000000	0.00001807	0.00037042	-0.00101749	-0.04312575	0.00068304	-0.00009849
8.00000000	0.00001844	0.00037246	-0.00102485	-0.04312764	0.00067687	-0.00009038
6.00000000	0.00001184	0.00038186	-0.00101587	-0.04313087	0.00067657	-0.00007738
4.00000000	0.00001889	0.00037706	-0.00098822	-0.04318572	0.00066769	-0.00011875
2.00000000	0.00002134	0.00038236	-0.00091197	-0.04328487	0.00068314	-0.00013655

average values

0.00001788	0.00036533	-0.00104158	-0.04308866	0.00068666	-0.00009640

TABLE – 11 LOADING : S2 Positive

LOAD(kgf)	EX(v)	N1(v)	N2(v)	S1(v)	S2(v)	A1(v)	L1(v)
0.0000	5.0000	0.1900	-0.4073	0.5511	0.7525	-0.1689	0.5857
2.0000	5.0000	0.1899	-0.4088	0.5593	1.1849	-0.1747	0.5856
4.0000	5.0000	0.1897	-0.4102	0.5667	1.6185	-0.1807	0.5880
6.0000	5.0000	0.1896	-0.4117	0.5831	2.0430	-0.1862	0.5867
8.0000	5.0000	0.1897	-0.4133	0.5899	2.4772	-0.1921	0.5882
10.0000	5.0000	0.1895	-0.4148	0.5929	2.9153	-0.1982	0.5879
12.0000	5.0000	0.1893	-0.4161	0.6040	3.3453	-0.2038	0.5850
14.0000	5.0000	0.1893	-0.4177	0.6101	3.7804	-0.2097	0.5881
16.0000	5.0000	0.1893	-0.4187	0.6215	4.2104	-0.2152	0.5895
18.0000	5.0000	0.1892	-0.4204	0.6290	4.6439	-0.2211	0.5881
20.0000	5.0000	0.1891	-0.4220	0.6411	5.0730	-0.2268	0.5890
18.0000	5.0000	0.1893	-0.4203	0.6315	4.6419	-0.2209	0.5863
16.0000	5.0000	0.1895	-0.4188	0.6207	4.2117	-0.2150	0.5859
14.0000	5.0000	0.1896	-0.4173	0.6122	3.7792	-0.2092	0.5859
12.0000	5.0000	0.1897	-0.4155	0.6032	3.3478	-0.2030	0.5864
10.0000	5.0000	0.1899	-0.4139	0.5940	2.9157	-0.1972	0.5853
8.0000	5.0000	0.1900	-0.4127	0.5846	2.4845	-0.1913	0.5849
6.0000	5.0000	0.1902	-0.4109	0.5766	2.0521	-0.1855	0.5852
4.0000	5.0000	0.1903	-0.4094	0.5686	1.6194	-0.1795	0.5858
2.0000	5.0000	0.1903	-0.4082	0.5602	1.1870	-0.1737	0.5858
0.0000	5.0000	0.1905	-0.4068	0.5519	0.7544	-0.1678	0.5851

drift corrected data, normalised by excitation voltage

LOAD(kgf)	N1(v)	N2(v)	S1(v)	S2(v)	Ax(v)	L(v)
2.0000	-0.0000	-0.0003	0.0016	0.0865	-0.0012	-0.0000
4.0000	-0.0001	-0.0006	0.0031	0.1732	-0.0024	0.0005
6.0000	-0.0001	-0.0009	0.0064	0.2580	-0.0035	0.0002
8.0000	-0.0001	-0.0012	0.0077	0.3449	-0.0047	0.0005
10.0000	-0.0001	-0.0015	0.0083	0.4325	-0.0059	0.0005
12.0000	-0.0002	-0.0018	0.0105	0.5184	-0.0070	-0.0001
14.0000	-0.0002	-0.0021	0.0117	0.6054	-0.0082	0.0005
16.0000	-0.0002	-0.0023	0.0140	0.6914	-0.0094	0.0008
18.0000	-0.0002	-0.0027	0.0155	0.7781	-0.0106	0.0005
20.0000	-0.0002	-0.0030	0.0179	0.8639	-0.0117	0.0007
18.0000	-0.0002	-0.0027	0.0160	0.7777	-0.0105	0.0002
16.0000	-0.0002	-0.0024	0.0138	0.6916	-0.0094	0.0001
14.0000	-0.0002	-0.0021	0.0121	0.6051	-0.0082	0.0001
12.0000	-0.0001	-0.0017	0.0103	0.5188	-0.0070	0.0002
10.0000	-0.0001	-0.0014	0.0085	0.4323	-0.0058	0.0000
8.0000	-0.0001	-0.0012	0.0066	0.3461	-0.0047	-0.0001
6.0000	-0.0000	-0.0008	0.0050	0.2596	-0.0035	-0.0000
4.0000	-0.0000	-0.0005	0.0034	0.1730	-0.0023	0.0001
2.0000	-0.0000	-0.0003	0.0017	0.0865	-0.0012	0.0001

normalised by load applied

2.00000000	-0.00001090	-0.00015372	0.00080941	0.04322626	-0.00058566	-0.00000974
4.00000000	-0.00001666	-0.00014822	0.00077406	0.04328786	-0.00059556	0.00011616
6.00000000	-0.00001504	-0.00014829	0.00106161	0.04300743	-0.00058359	0.00003653
8.00000000	-0.00000871	-0.00015195	0.00096446	0.04310794	-0.00058501	0.00006391
10.00000000	-0.00001144	-0.00015192	0.00083165	0.04324506	-0.00059156	0.00004582
12.00000000	-0.00001369	-0.00015025	0.00087806	0.04320354	-0.00058727	-0.00000840
14.00000000	-0.00001199	-0.00015081	0.00083832	0.04324626	-0.00058824	0.00003632
16.00000000	-0.00001140	-0.00014508	0.00087543	0.04321401	-0.00058483	0.00005078
18.00000000	-0.00001100	-0.00014804	0.00086119	0.04322824	-0.00058612	0.00002892

20.00000000	-0.00001092	-0.00014961	0.00089600	0.04319482	-0.00058433	0.00003612
18.00000000	-0.00001038	-0.00014777	0.00088886	0.04320315	-0.00058462	0.00001049
16.00000000	-0.00001018	-0.00014762	0.00086414	0.04322574	-0.00058471	0.00000687
14.00000000	-0.00001087	-0.00014749	0.00086636	0.04322095	-0.00058623	0.00000782
12.00000000	-0.00001051	-0.00014235	0.00085911	0.04323159	-0.00058125	0.00001835
10.00000000	-0.00000873	-0.00014052	0.00084735	0.04323450	-0.00058252	0.00000084
8.00000000	-0.00001067	-0.00014623	0.00082299	0.04326152	-0.00058352	-0.00000742
6.00000000	-0.00000766	-0.00013555	0.00082922	0.04326564	-0.00058428	-0.00000063
4.00000000	-0.00000625	-0.00013108	0.00083874	0.04325854	-0.00058165	0.00003433
2.00000000	-0.00001229	-0.00013908	0.00083899	0.04326394	-0.00058425	0.00006903

average values

-0.00001102	-0.00014608	0.00086558	0.04321721	-0.00058554	0.00002822

TABLE – 12 LOADING : POSITIVE AXIAL FORCE

LOAD(kgf)	EX(v)	N1(v)	N2(v)	S1(v)	S2(v)	A1(v)	L1(v)
0.0000	5.0000	0.1879	-0.3997	0.1619	0.4144	0.7081	0.5995
2.0000	5.0000	0.1875	-0.4000	0.1565	0.4163	0.9784	0.5995
4.0000	5.0000	0.1900	-0.4011	0.1504	0.4182	1.2479	0.5995
6.0000	5.0000	0.1916	-0.4021	0.1491	0.4184	1.5179	0.5996
8.0000	5.0000	0.1929	-0.4026	0.1435	0.4205	1.7878	0.5995
10.0000	5.0000	0.1957	-0.4035	0.1374	0.4226	2.0575	0.5994
12.0000	5.0000	0.1964	-0.4034	0.1334	0.4239	2.3275	0.5995
14.0000	5.0000	0.1963	-0.4042	0.1335	0.4239	2.5972	0.5993
16.0000	5.0000	0.1971	-0.4045	0.1271	0.4261	2.8671	0.5996
18.0000	5.0000	0.2005	-0.4060	0.1220	0.4278	3.1368	0.5993
20.0000	5.0000	0.2045	-0.4065	0.1155	0.4295	3.4066	0.5996
18.0000	5.0000	0.1986	-0.4051	0.1237	0.4277	3.1364	0.5992
16.0000	5.0000	0.2010	-0.4057	0.1287	0.4263	2.8664	0.5994
14.0000	5.0000	0.2014	-0.4052	0.1291	0.4261	2.5963	0.5993
12.0000	5.0000	0.1985	-0.4046	0.1382	0.4239	2.3266	0.5994
10.0000	5.0000	0.1975	-0.4038	0.1373	0.4243	2.0566	0.5995
8.0000	5.0000	0.1932	-0.4025	0.1417	0.4231	1.7869	0.5995
6.0000	5.0000	0.1946	-0.4027	0.1467	0.4214	1.5172	0.5996
4.0000	5.0000	0.1929	-0.4016	0.1516	0.4198	1.2473	0.5994
2.0000	5.0000	0.1909	-0.4005	0.1563	0.4183	0.9777	0.5996
0.0000	5.0000	0.1897	-0.4000	0.1624	0.4163	0.7081	0.5997

drift corrected data, normalised by excitation voltage

LOAD(kgf)	N1(v)	N2(v)	S1(v)	S2(v)	Ax(v)	L(v)
2.0000	-0.0001	-0.0001	-0.0011	0.0004	0.0541	-0.0000
4.0000	0.0004	-0.0003	-0.0023	0.0007	0.1080	-0.0000
6.0000	0.0007	-0.0005	-0.0026	0.0007	0.1620	-0.0000
8.0000	0.0009	-0.0006	-0.0037	0.0011	0.2159	-0.0000
10.0000	0.0015	-0.0008	-0.0049	0.0015	0.2699	-0.0000
12.0000	0.0016	-0.0007	-0.0057	0.0018	0.3239	-0.0000
14.0000	0.0015	-0.0009	-0.0057	0.0018	0.3778	-0.0001
16.0000	0.0017	-0.0009	-0.0070	0.0022	0.4318	-0.0000
18.0000	0.0024	-0.0012	-0.0080	0.0025	0.4858	-0.0001
20.0000	0.0031	-0.0013	-0.0093	0.0028	0.5397	0.0000
18.0000	0.0019	-0.0010	-0.0077	0.0024	0.4857	-0.0001
16.0000	0.0024	-0.0012	-0.0067	0.0021	0.4317	-0.0001
14.0000	0.0025	-0.0011	-0.0066	0.0021	0.3776	-0.0001
12.0000	0.0019	-0.0009	-0.0048	0.0016	0.3237	-0.0001
10.0000	0.0016	-0.0008	-0.0050	0.0017	0.2697	-0.0000
8.0000	0.0008	-0.0005	-0.0041	0.0014	0.2158	-0.0000
6.0000	0.0010	-0.0005	-0.0031	0.0011	0.1618	-0.0000
4.0000	0.0007	-0.0003	-0.0022	0.0007	0.1079	-0.0001
2.0000	0.0002	-0.0001	-0.0012	0.0004	0.0539	-0.0000

normalised by load applied

2.00000000	-0.00005286	-0.00002521	-0.00054332	0.00017655	0.02703020	-0.00000116
4.00000000	0.00009199	-0.00006936	-0.00057762	0.00018215	0.02699190	-0.00000171
6.00000000	0.00011387	-0.00007874	-0.00042872	0.00012478	0.02699487	-0.00000023
8.00000000	0.00011494	-0.00007228	-0.00046269	0.00014285	0.02699373	-0.00000149
10.00000000	0.00014600	-0.00007509	-0.00049188	0.00015423	0.02698788	-0.00000436
12.00000000	0.00013175	-0.00006066	-0.00047650	0.00014930	0.02699068	-0.00000169
14.00000000	0.00010975	-0.00006265	-0.00040745	0.00012659	0.02698803	-0.00000405

16.00000000	0.00010595	-0.00005907	-0.00043699	0.00013691	0.02698780	-0.00000013
18.00000000	0.00013088	-0.00006863	-0.00044575	0.00013865	0.02698626	-0.00000326
20.00000000	0.00015654	-0.00006640	-0.00046668	0.00014087	0.02698553	0.00000001
18.00000000	0.00010712	-0.00005830	-0.00042706	0.00013544	0.02698089	-0.00000454
16.00000000	0.00014985	-0.00007307	-0.00041851	0.00013431	0.02697884	-0.00000374
14.00000000	0.00017505	-0.00007605	-0.00047231	0.00014961	0.02697454	-0.00000495
12.00000000	0.00015528	-0.00007809	-0.00040130	0.00013613	0.02697613	-0.00000544
10.00000000	0.00016471	-0.00007859	-0.00049870	0.00016903	0.02697132	-0.00000294
8.00000000	0.00009547	-0.00006459	-0.00051350	0.00017875	0.02696973	-0.00000491
6.00000000	0.00017167	-0.00009122	-0.00051981	0.00018038	0.02697100	-0.00000511
4.00000000	0.00016722	-0.00008324	-0.00053763	0.00018360	0.02696260	-0.00001529
2.00000000	0.00012206	-0.00005039	-0.00060528	0.00021055	0.02696510	-0.00000944

average values

0.00012406	-0.00006798	-0.00048062	0.00015530	0.02698353	-0.00000392

TABLE – 13

LOADING : RM Negative

LOAD(kgf)	EX(v)	N1(v)	N2(v)	S1(v)	S2(v)	A1(v)	L1(v)
0.0000	5.0000	-0.9905	-1.3494	0.1313	0.4302	-0.1941	0.5900
20.0000	5.0000	-0.9848	-1.3548	0.1416	0.4085	-0.2020	0.3787
40.0000	5.0000	-0.9822	-1.3563	0.1517	0.3854	-0.2097	0.1608
60.0000	5.0000	-0.9792	-1.3585	0.1615	0.3624	-0.2161	-0.0539
80.0000	5.0000	-0.9753	-1.3617	0.1704	0.3386	-0.2221	-0.2700
100.0000	5.0000	-0.9705	-1.3653	0.1785	0.3141	-0.2272	-0.4857
80.0000	5.0000	-0.9741	-1.3626	0.1684	0.3362	-0.2213	-0.2718
60.0000	5.0000	-0.9777	-1.3596	0.1582	0.3588	-0.2148	-0.0547
40.0000	5.0000	-0.9828	-1.3559	0.1480	0.3815	-0.2084	0.1595
20.0000	5.0000	-0.9872	-1.3523	0.1384	0.4052	-0.2010	0.3764
0.0000	5.0000	-0.9863	-1.3535	0.1301	0.4293	-0.1931	0.5938

drift corrected data, normalised by excitation voltage

LOAD(kgf)	N1(v)	N2(v)	S1(v)	S2(v)	Ax(v)	L(v)
0.0000	0.0000	0.0000	0.0000	0.0000	0.0000	0.0000
20.0000	0.0011	-0.0010	0.0021	-0.0043	-0.0016	-0.0423
40.0000	0.0015	-0.0012	0.0041	-0.0089	-0.0032	-0.0860
60.0000	0.0020	-0.0016	0.0061	-0.0135	-0.0045	-0.1290
80.0000	0.0027	-0.0021	0.0079	-0.0183	-0.0057	-0.1723
100.0000	0.0036	-0.0028	0.0096	-0.0231	-0.0067	-0.2155
80.0000	0.0028	-0.0021	0.0076	-0.0187	-0.0056	-0.1728
60.0000	0.0020	-0.0015	0.0055	-0.0142	-0.0043	-0.1295
40.0000	0.0009	-0.0006	0.0035	-0.0096	-0.0030	-0.0867
20.0000	-0.0001	0.0002	0.0016	-0.0048	-0.0016	-0.0434
0.0000	0.0000	0.0000	0.0000	0.0000	0.0000	0.0000

normalised by load applied

20.00000000	0.00005286	-0.00004936	0.00010406	-0.00021640	-0.00008001	-0.00211612
40.00000000	0.00003703	-0.00003047	0.00010351	-0.00022278	-0.00007898	-0.00214959
60.00000000	0.00003336	-0.00002612	0.00010194	-0.00022506	-0.00007456	-0.00215002
80.00000000	0.00003382	-0.00002657	0.00009897	-0.00022816	-0.00007116	-0.00215377
100.00000000	0.00003572	-0.00002754	0.00009558	-0.00023119	-0.00006718	-0.00215524
80.00000000	0.00003474	-0.00002671	0.00009454	-0.00023351	-0.00006950	-0.00216010
60.00000000	0.00003271	-0.00002443	0.00009237	-0.00023601	-0.00007156	-0.00215782
40.00000000	0.00002145	-0.00001569	0.00008841	-0.00023984	-0.00007557	-0.00216781
20.00000000	-0.00000494	0.00000836	0.00008217	-0.00024201	-0.00007817	-0.00216960

average values

0.00003075	-0.00002428	0.00009573	-0.00023055	-0.00007408	-0.00215334

TABLE – 14

LOADING : RM Positive

LOAD(kgf)	EX(v)	N1(v)	N2(v)	S1(v)	S2(v)	A1(v)	L1(v)
0.0000	5.0000	-0.9833	-1.3564	0.2172	0.5075	-0.1935	0.6193
20.0000	5.0000	-0.9866	-1.3538	0.2068	0.5297	-0.1847	0.8330
40.0000	5.0000	-0.9869	-1.3544	0.1966	0.5525	-0.1754	1.0503
60.0000	5.0000	-0.9920	-1.3497	0.1874	0.5755	-0.1656	1.2653
80.0000	5.0000	-0.9960	-1.3458	0.1798	0.6001	-0.1551	1.4805
100.0000	5.0000	-0.9985	-1.3436	0.1720	0.6237	-0.1442	1.6951
80.0000	5.0000	-0.9947	-1.3471	0.1816	0.6017	-0.1557	1.4817
60.0000	5.0000	-0.9911	-1.3503	0.1904	0.5789	-0.1664	1.2690
40.0000	5.0000	-0.9895	-1.3514	0.2005	0.5561	-0.1763	1.0510
20.0000	5.0000	-0.9857	-1.3549	0.2102	0.5327	-0.1855	0.8357
0.0000	5.0000	-0.9850	-1.3552	0.2181	0.5081	-0.1941	0.6187

drift corrected data, normalised by excitation voltage

LOAD(kgf)	N1(v)	N2(v)	S1(v)	S2(v)	Ax(v)	L(v)
0.0000	0.0000	0.0000	0.0000	0.0000	0.0000	0.0000
20.0000	-0.0006	0.0005	-0.0021	0.0044	0.0018	0.0428
40.0000	-0.0007	0.0004	-0.0042	0.0090	0.0036	0.0862
60.0000	-0.0016	0.0013	-0.0060	0.0136	0.0056	0.1292
80.0000	-0.0024	0.0020	-0.0076	0.0185	0.0077	0.1723
100.0000	-0.0029	0.0024	-0.0091	0.0232	0.0099	0.2152
80.0000	-0.0021	0.0017	-0.0072	0.0188	0.0076	0.1726
60.0000	-0.0013	0.0011	-0.0055	0.0142	0.0055	0.1300
40.0000	-0.0010	0.0008	-0.0035	0.0096	0.0035	0.0864
20.0000	-0.0002	0.0001	-0.0016	0.0049	0.0017	0.0434
0.0000	0.0000	0.0000	0.0000	0.0000	0.0000	0.0000

normalised by load applied

20.00000000	-0.00003142	0.00002482	-0.00010489	0.00022133	0.00008857	0.00213761
40.00000000	-0.00001646	0.00000891	-0.00010411	0.00022428	0.00009098	0.00215578
60.00000000	-0.00002730	0.00002117	-0.00010021	0.00022625	0.00009341	0.00215380
80.00000000	-0.00003018	0.00002536	-0.00009455	0.00023100	0.00009648	0.00215347
100.00000000	-0.00002881	0.00002450	-0.00009131	0.00023183	0.00009904	0.00215216
80.00000000	-0.00002612	0.00002132	-0.00009051	0.00023455	0.00009530	0.00215700
60.00000000	-0.00002213	0.00001758	-0.00009147	0.00023647	0.00009143	0.00216697
40.00000000	-0.00002456	0.00002019	-0.00008720	0.00024054	0.00008830	0.00216082
20.00000000	-0.00000884	0.00000349	-0.00007844	0.00024579	0.00008462	0.00216938

average values

-0.00002398	0.00001859	-0.00009363	0.00023245	0.00009201	0.00215633

TABLE – 15

Elements of Co-efficient Matrix (wt11.cof)

	N1	N2	S1	S2	Axf	RM
***N1**	2.8750395e-02	2.2560500e-04	-1.7676000e-04	-1.4450000e-05	1.2406000e-04	2.7365000e-05
***N2**	1.7784000e-04	2.8813985e-02	5.1980000e-05	-2.5570500e-04	-6.7980000e-05	2.1435000e-05
***S1**	4.6772000e-04	1.2745000e-05	4.3051200e-02	9.5358000e-04	-4.8062000e-04	9.4680000e-05
***S2**	-4.8030000e-05	-4.5847000e-04	1.0690550e-03	4.3152935e-02	1.5530000e-04	2.3150000e-04
***Axf**	-3.2421000e-04	-1.0632000e-04	8.2268500e-04	-6.3610000e-04	2.6983530e-02	8.3045000e-05
****RM**	-1.5895000e-05	-3.8514000e-04	-7.9050000e-06	6.2310000e-05	-3.9200000e-06	2.1548350e-03

*mV/V/kg ** mV/V/kg-cm

TABLE – 16

Elements of the Inverse Co-efficient Matrix (wt11.dat)

	N1	N2	S1	S2	Axf	RM
***N1**	3.4779882e+01	-2.6680151e-01	1.4612786e-01	3.8491678e-03	-1.5792989e-01	4.5642935e-01
***N2**	-2.1275579e-01	3.4705670e+01	-4.9672081e-02	2.0849109e-01	8.6273388e-02	-3.7583912e-01
***S1**	-3.7348412e-01	1.9222625e-04	2.3231453e+01	-5.0883771e-01	4.1858884e-01	1.0545418e+00
***S2**	4.2997240e-02	3.3476573e-01	-5.7379681e-01	2.3189588e+01	-1.4340423e-01	-2.5137919e+00
***Axf**	4.2877935e-01	1.2237132e-01	-7.2054189e-01	5.6499592e-01	3.7041674e+01	-1.5156765e+00
****RM**	2.1669164e-01	6.1916215e+00	9.2705653e-02	-6.3410488e-01	8.7322167e-02	4.6408265e+02

*mV/V/kg ** mV/V/kg-cm

TABLE – 17

Loading : Negative N1

Load applied Kg	load obtained Kg	error percent
-10.0000	-9.9826	0.1740
-20.0000	-19.9682	0.1590
-10.0000	-9.9924	0.0760

Loading : Negative N2

Load applied Kg	load obtained Kg	error percent
-10.0000	-9.9302	0.6980
-20.0000	-19.8787	0.6065
-10.0000	-9.9394	0.6060

Loading : Negative N1+N2

Load applied Kg	load obtained Kg	error percent
-10.0000	9.9650	0.3500
-20.0000	-19.9274	0.3630
-10.0000	-9.9694	0.3060

Loading : Positive N1

Load applied Kg	load obtained Kg	error percent
10.0000	9.9803	0.1970
20.0000	20.0117	0.0585
10.0000	10.0043	0.0430

Loading : Positive N2

Load applied Kg	load obtained Kg	error percent
10.0000	9.9601	0.3990
20.0000	19.9178	0.4110
10.0000	9.9637	0.3630

Loading : Positive N1+N2

Load applied Kg	load obtained Kg	error percent
10.0000	9.9683	0.3170
20.0000	19.9282	0.3590
30.0000	29.8941	0.3530
20.0000	19.9287	0.3565
10.0000	9.9643	0.3570

Loading : Negative S1

Load applied Kg	load obtained Kg	error percent
5.0000	-4.9987	0.0260
10.0000	-9.9929	0.0710
5.0000	-4.9972	0.0560

Loading : Negative S2

Load applied Kg	load obtained Kg	error percent
5.0000	-4.9779	0.4420
10.0000	-9.9593	0.4070
5.0000	-4.9788	0.4240

Loading : Negative S1+S2

Load applied Kg	load obtained Kg	error percent
4.0000	-3.9887	0.2825
10.0000	-9.9839	0.1610
4.0000	-3.9882	0.2950

Loading : Positive S1

Load applied Kg	load obtained Kg	error percent
5.0000	4.9864	0.2720
10.0000	10.0061	0.0610
5.0000	4.9898	0.2040

Loading : Positive S2

Load applied Kg	load obtained Kg	error percent
5.0000	4.9875	0.2500
10.0000	9.9656	0.3440
5.0000	4.9862	0.2760

Loading : Positive S1+S2

Load applied Kg	load obtained Kg	error percent
4.0000	3.9839	0.4025
10.0000	9.9681	0.3190
4.0000	3.9844	0.3900

Loading : Positive Axial Force

Load applied Kg	load obtained Kg	error percent
5.0000	5.0079	0.1580
10.0000	10.0104	0.1040

Loading : +ve and -ve Rolling Moment

Load applied Kg-cm	load obtained Kg-cm	error percent
20.0000	20.0400	0.2000
40.0000	40.1100	0.2750
20.0000	20.0200	0.1000
-20.0000	-19.9700	0.1500
-40.0000	-39.9000	0.2500
-20.0000	-20.0400	0.2000

Loading : +ve Normal Force and -ve Rolling Moment

POSITIVE NORMAL FORCE			NEGATIVE ROLLING MOMENT		
Load applied Kg	load obtained Kg	error percent	Load applied Kg-cm	load obtained Kg-cm	error percent
10.0000	9.9650	0.3500	20.0000	20.0300	0.1500

Figure 1: A view of WT11 Balance with rear adapter

Figure:2 A view of WT11 Balance and calibration body

Figure 3: A view of WT11 Balance and Dummy balance with front adapter

Figure 4: A view of rear adapter

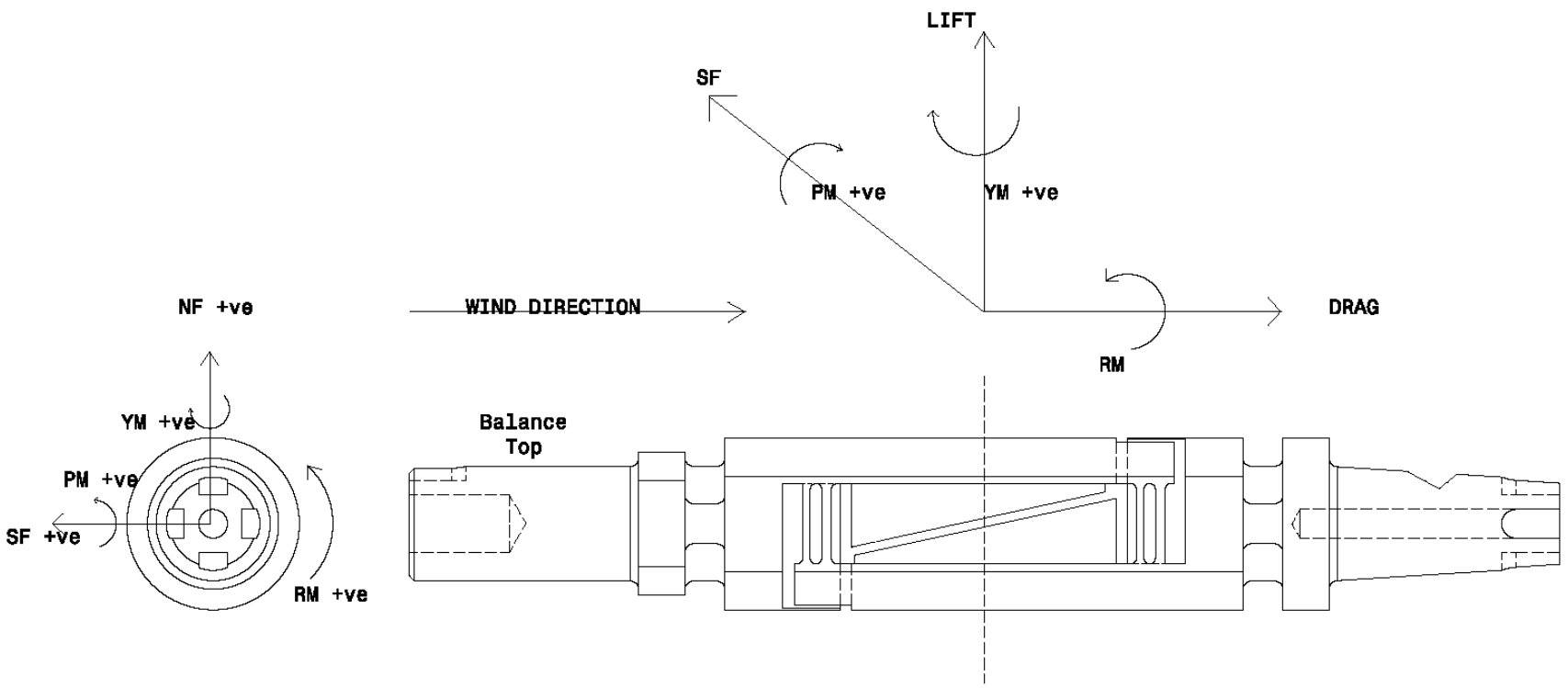

Fig.A Sign Convention

All dimensions are in mm

This drawing is our property. It can't be reproduced or communicated without our written agreement.		OCWT/IISc	
DRAWN BY main data	DATE 10/21/2016	DRAWING TITLE RDR Balance Sign Convention	
CHECKED BY XXX	DATE xxx	SIZE A4	DRAWING NUMBER OCWT/001 REV X
DESIGNED BY XXX	DATE xxx	SCALE 1:1	WEIGHT(kg) 0.00 SHEET 1/1

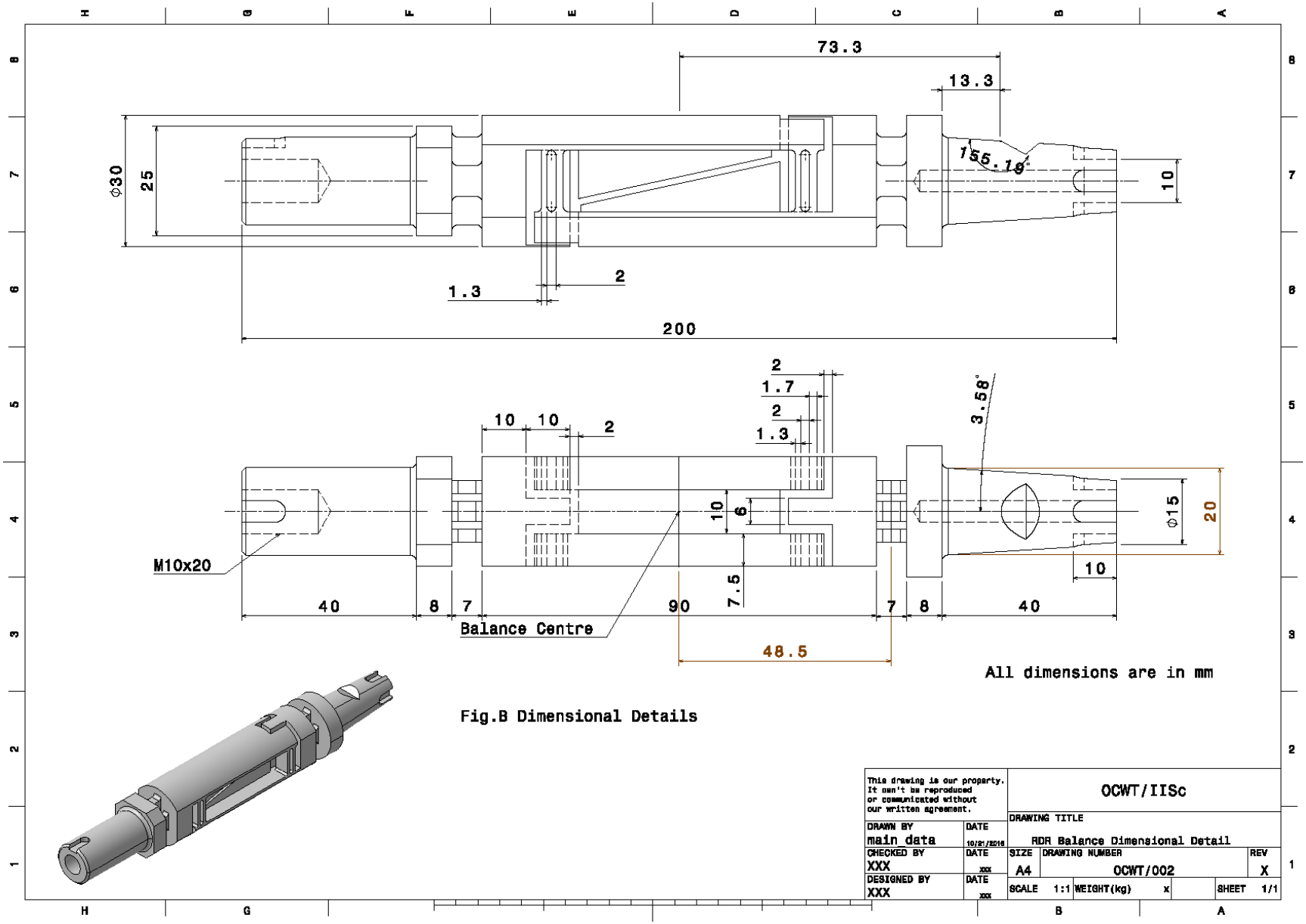

Fig.B Dimensional Details

This drawing is our property. It can't be reproduced or communicated without our written agreement.		OCWT/IISc		
		DRAWING TITLE: RDR Balance Dimensional Detail		
DRAWN BY: main data	DATE: 10/21/2016			
CHECKED BY: XXX	DATE: XXX	SIZE: A4	DRAWING NUMBER: OCWT/002	REV: X
DESIGNED BY: XXX	DATE: XXX	SCALE: 1:1	WEIGHT(kg): x	SHEET: 1/1

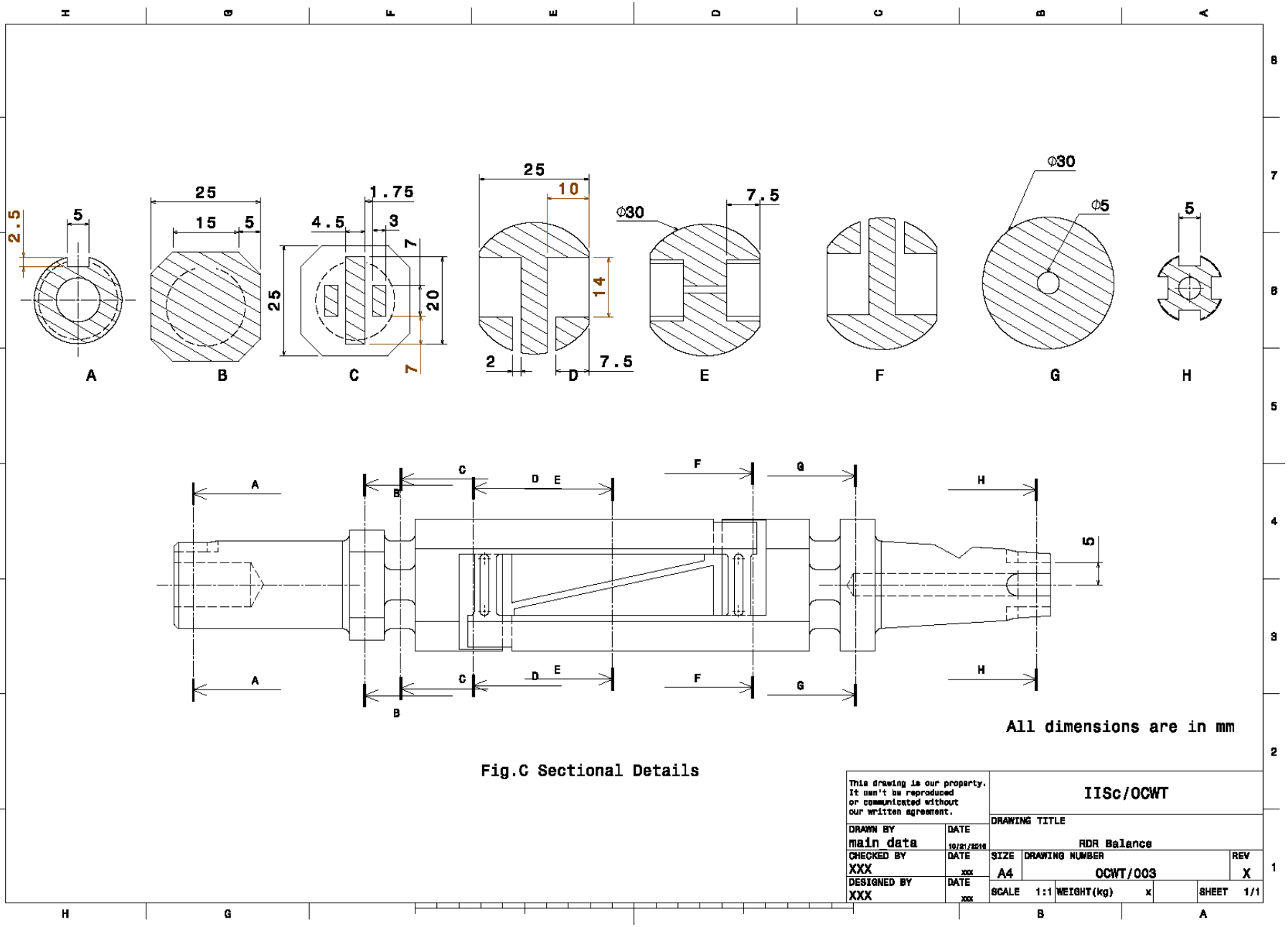

Fig.C Sectional Details

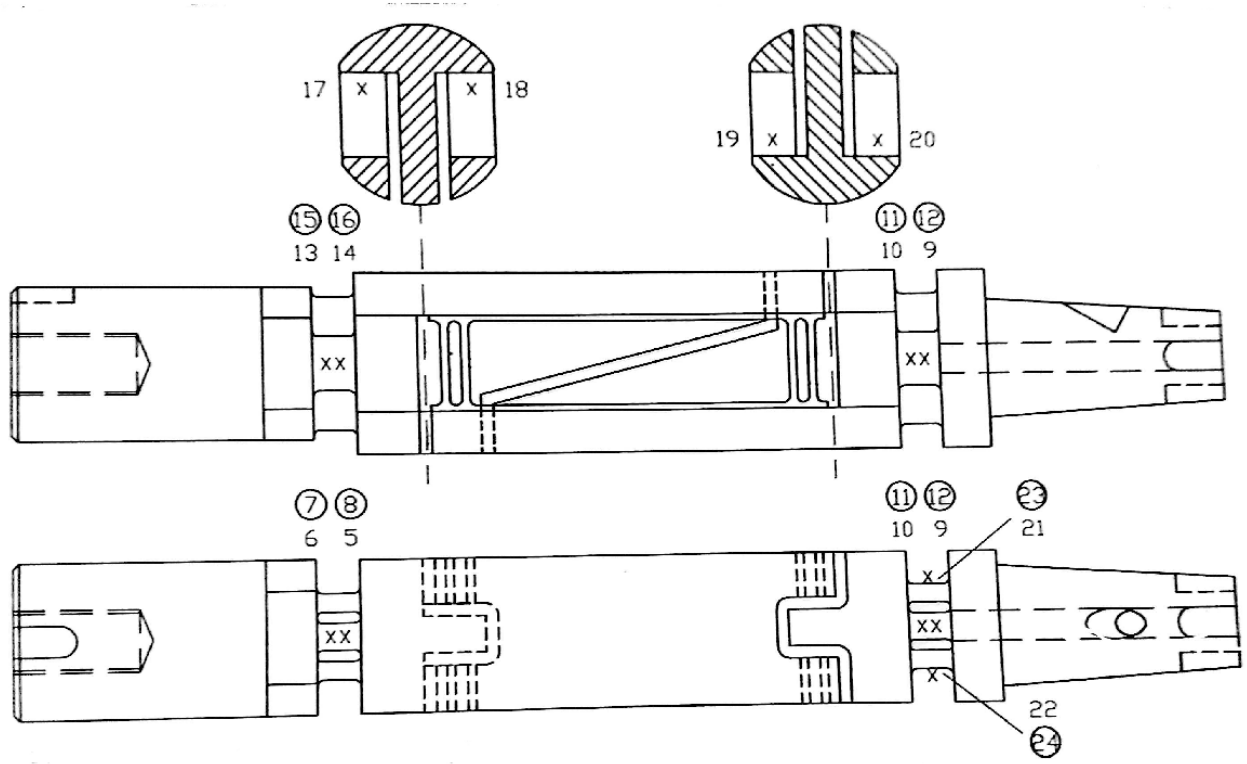

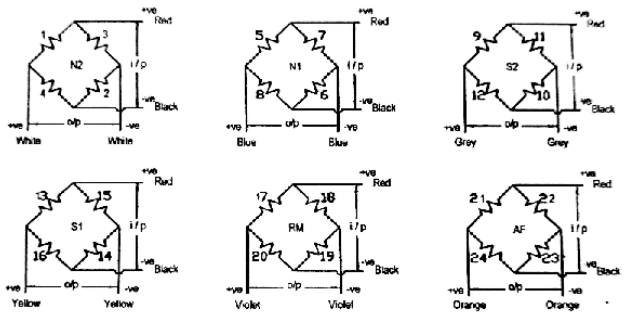

Fig.D Wiring & Gaging Details

This drawing is our property. It can't be reproduced or communicated without our written agreement.		IISc/OCWT	
DRAWN BY: main data	DATE: 10/2/2016	DRAWING TITLE: RDR Balance Wiring & Gaging	
CHECKED BY: XXX	DATE: xxx	SIZE: A2	DRAWING NUMBER: OCWT/004 REV: X
DESIGNED BY: XXX	DATE: xxx	SCALE: 1:1	WEIGHT(kg): x SHEET: 1/1

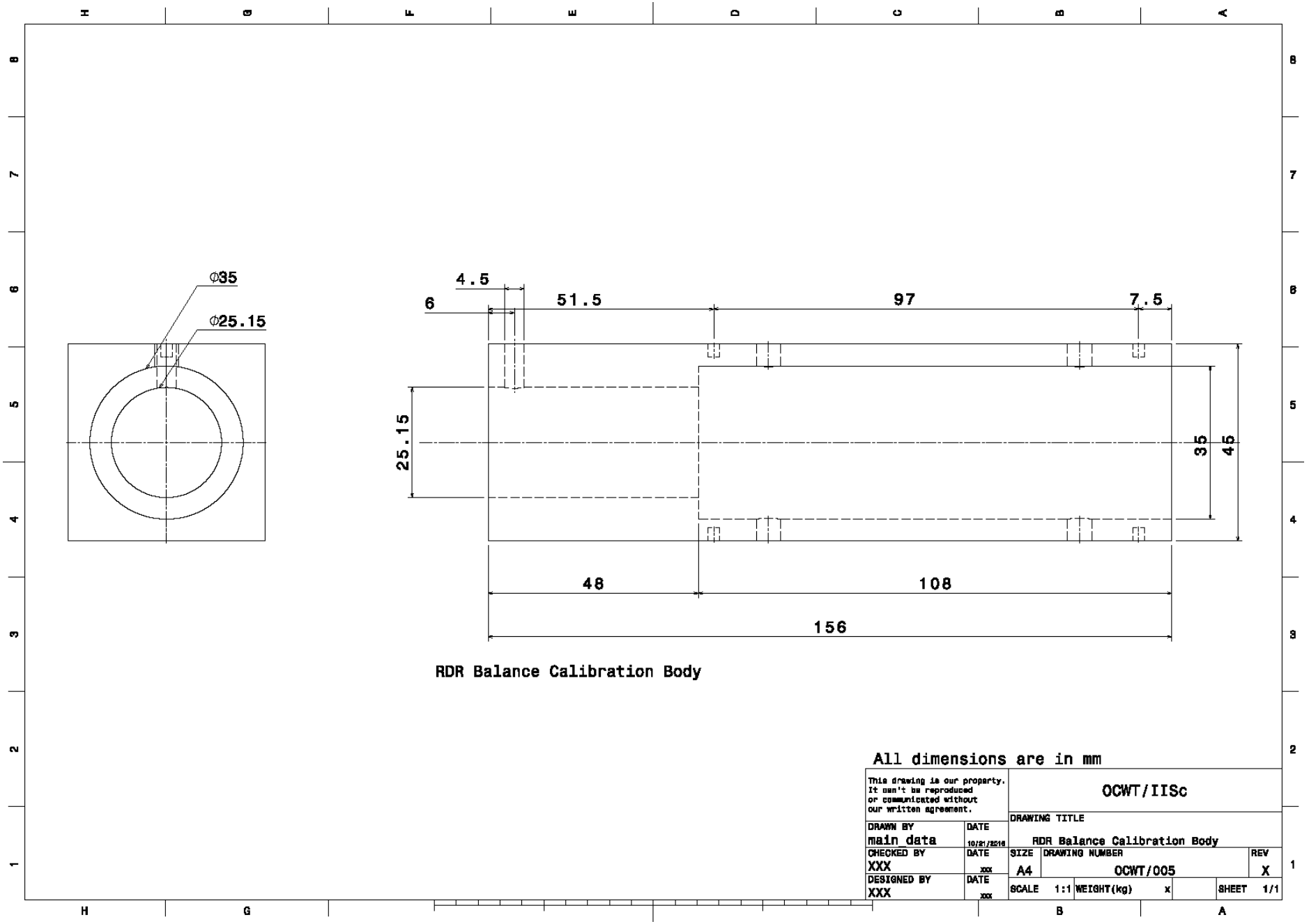
Φ35
Φ25.15
4.5
6
51.5
97
7.5
25.15
35
45
48
108
156
RDR Balance Calibration Body
All dimensions are in mm
This drawing is our property. It can't be reproduced or communicated without our written agreement.
OCWT/IISc
DRAWING TITLE
RDR Balance Calibration Body
DRAWN BY
main data
DATE
10/21/2016
CHECKED BY
XXX
DATE
XXX
DESIGNED BY
XXX
DATE
XXX
SIZE
A4
DRAWING NUMBER
OCWT/005
REV
X
SCALE 1:1
WEIGHT(kg) x
SHEET 1/1

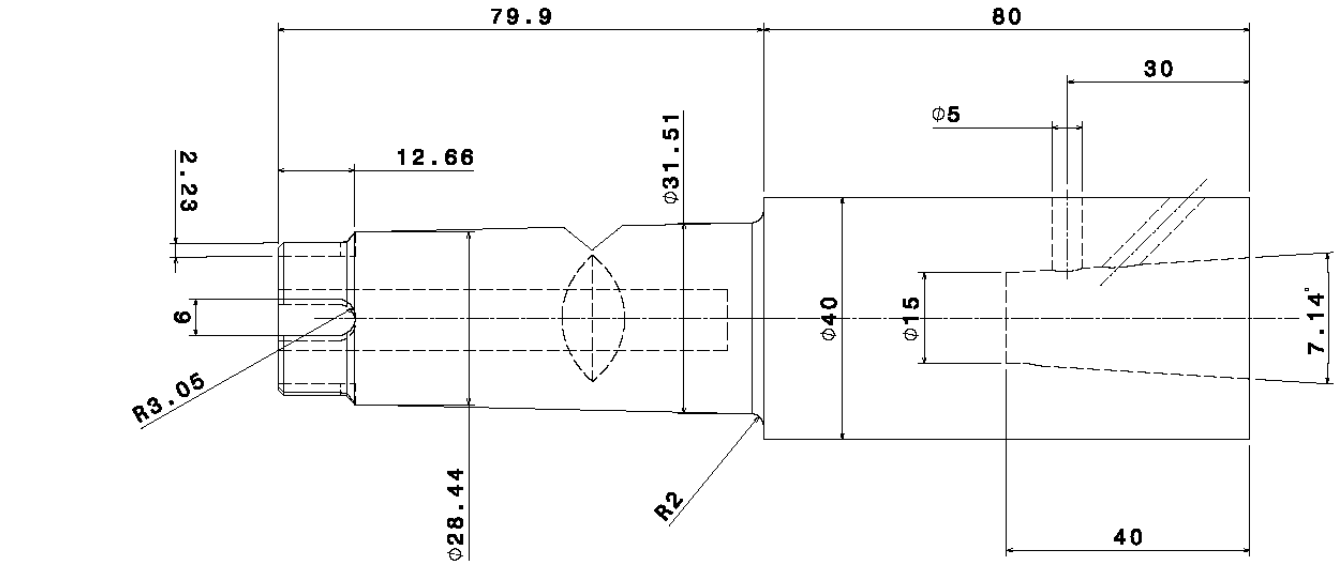

Balance Rear adapter

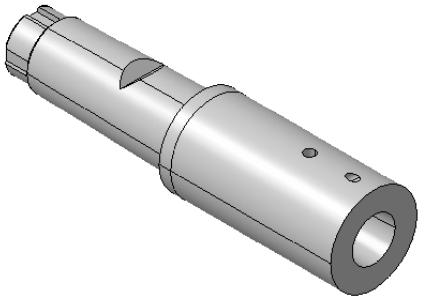

All dimensions are in mm

This drawing is our property. It can't be reproduced or communicated without our written agreement.		IISc/OCWT	
DRAWN BY: main_data	DATE: 11/3/2016	DRAWING TITLE: Balance Rear Adapter	
CHECKED BY: XXX	DATE: XXX	SIZE: A4	DRAWING NUMBER: OCWT/006 — REV: X
DESIGNED BY: XXX	DATE: XXX	SCALE: 1:1	WEIGHT(kg): x — SHEET: 1/1

Positive Normal Force loading			**Positive Side force Loading**		
Load applied (kg)	load obtained (kg)	error percent	Load applied (Kg)	load obtained (Kg)	error percent
10.0000	9.9683	0.3170	4.0000	3.9839	0.4025
20.0000	19.9282	0.3590	10.0000	9.9681	0.3190
30.0000	29.8941	0.3530	4.0000	3.9844	0.3900
20.0000	19.9287	0.3565			
10.0000	9.9643	0.3570			

Negative Normal Force Loading			**Negative Side Force Loading**		
Load applied	load obtained	error percent	Load applied	load obtained	error percent
Kg	Kg		Kg	Kg	
-10.0000	-9.9650	0.3500	- 4.0000	-3.9887	0.2825
-20.0000	-19.9274	0.3630	-10.0000	-9.9839	0.1610
-10.0000	-9.9694	0.3060	-4.0000	-3.9882	0.2950
Positive Axial Force			**Combined Loading Case**		
Load applied	load obtained	error percent	**POSITIVE NORMAL FORCE**		
Kg	Kg		Load applied	load obtained	error percent
5.0000	5.0079	0.1580	Kg	Kg	
10.0000	10.0104	0.1040	10.0000	9.9650	0.3500
Positive and Negative Rolling Moment			**NEGATIVE ROLLING MOMENT**		
Mom. applied	Mom obtained	error percent	Mom. applied	Mom. obtained	error percent
Kg-cm	Kg-cm		Kg-cm	Kg-cm	
20.0000	20.0400	0.2000	20.0000	20.0300	0.1500
40.0000	40.1100	0.2750			
20.0000	20.0200	0.1000			
-20.0000	-19.9700	0.1500			
-40.0000	-39.9000	0.2500			
-20.0000	-20.0400	0.2000			

APPENDIX B

Pressure scanner calibration and operation

The ZOC33 is an electronic pressure scanner which can accept up to 128 pneumatic inputs. Each ZOC33 module incorporates 64 individual piezo-resistive pressure sensors. Each eight pressure sensors are manufactured in housing designed to facilitate field replacement. No special tools are required to access the sensors. The ZOC33 electronic pressure scanning module is specifically designed for use in wind tunnels, flight tests or applications where space is at a premium and pressures will not exceed 50 psi. The modes are selected by applying control pressures in a predetermined and logical order. The ZOC33 pressure sensors are arranged in blocks of 8. In all variations except the valve less model, each block of eight sensors has its own individual calibration valve. This valve had four modes of operations:

- Operate: This connects each Px input to its associated pressure sensor. The ZOC33/64PxX2 module allows the customer to select one of two banks for input.
- Calibrate: This mode connects all the pressure sensors to the calibration input.
- Purge: This mode connects the Px inputs to the pressure sensors and the calibration input. A safe purge pressure can be applied to purge input lines.
- Isolate: This mode isolates the pressure sensors from the Px and calibration lines.

This module contains sixty four pressure sensors in eight sensor packs. Each sensor pack contains:

- Eight sensors
- A calibration valve
- A duplexing valve
- An excitation board
- A high speed multiplexer

- 16 input tubes (Bank A and Bank B with 8 inputs each)

The sensors are arranged in eight groups of eight. Each sensor has two pneumatic inputs: Bank A and Bank B. The inputs are switched pneumatically by enabling the duplexing valve. Even though there are 128 pressure inputs only one Bank of 64 pressure inputs can be measured at one time. Each group of eight sensors may be a different range. The standard output of the module is ±2.5Vdc corresponding to the channel selected by a CMOS level 6 bit binary address.

Pressure scanner calibration

Pressure scanners have to go through 2 processes for calibration. First is Calibration Test and the second one is Check Calibration. Before starting these tests we need to know the connections to be made. Pressure measuring system consists of the following components:

- Pressure Scanner.
- Control Box.
- Data Acquisition System.
- Computer.
- Projection Manometer/ U Tube manometer.
- Nitrogen Cylinder.

Pressure Scanners have following inputs;

- CAL I/P
- REF
- PxA
- PxB
- Cal

Calibration Test

In this process, we need to calculate the slope of the scanner which is a relation between voltage and mm of H2O. The connections to be made are as follows:

- Input from the Projection Manometer/ U Tube Manometer is to be connected to CAL I/P of scanner through a T joint.
- PxA, PxB, Cal of scanner to be connected to A, B, C tubes coming from Control box.
- Ref port of the scanner to be kept open.
- Scanner connector should be connected to Control box connector.
- 65 psi from Nitrogen Cylinder is to be given to Control box.

After all these connections, open the LabVIEW program named 'esp scanner' and keep it in run mode for about 1 hour for warm up. In the Labview program there are 2 modes namely Operation mode and Calibration mode. During Calibration test we use Calibration mode¿pressure scanner operation in this mode is represented in Fig.1.

- After warm up, first take the bias value by clicking on calibration button and then click the start button. All 64 ports of the scanner will start reading the values.
- In case of using Projection manometer (which is rather more accurate and suitable compared to U tube manometer), adjust the level of the manometer to 10 mm with the help of turning knob attached to the projector. Then again click on calibration button and blow 10 mm into one of the port of the T joint which connects Projection manometer/U tube manometer to the scanner. Hold the pressure at that level (with the help of your thumb), click on start button and wait till all 64 ports read the values.
- Repeat the same procedure and blow pressure ranging from 10 mm to 200 mm. (NOTE: Make sure there is no leakage in the Tubes or joints. Else the readings will carry error which in turn reads wrong pressure during experiments).
- After blowing the pressure into the scanner from 10mm to 200 mm, take one more bias.
- Open Matlab and run the calibration.m program which you should copy into the folder which contains all the labview files (.lvm). Running this code gives the

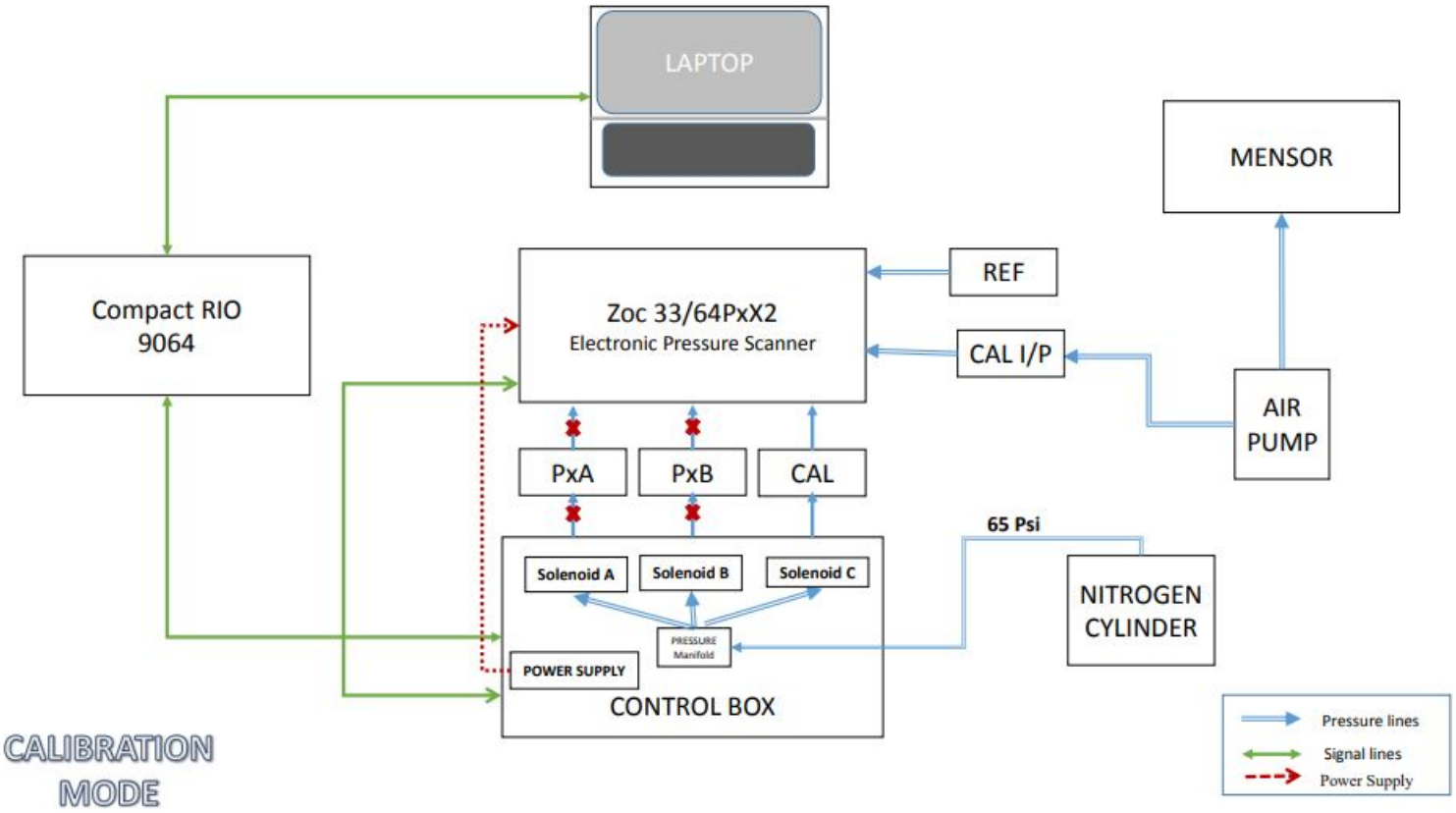

Figure 1: Schematic of calibration process of pressure scanner

relation between the pressure and voltage and the calibration curve is obtained names slope.xls

Check calibration

In order to assess the calibration carried out as above, some known values of pressure should be given and checked for accuracy of the results obtained.

- Create another folder inside the calibration folder and copy the program and slope.xls file created by calibration.m program.
- Mention this folder name in labview and take the bias.
- Next give some arbitrary pressure through the T joint and carry out the experiment similar to Calibration test and in the end again take the bias.
- Run the *check.calibartion.m* program and you will get a graph of pressure in mm of H2O (Y axis) and port number(X axis).
- Check for several values in the same manner with pressure ranging from lower to higher value.

NOTE: The error band should not be more than 0.2 mm of H2O. Check calibration can also be done by giving input to any one of the port instead of CAL I/P. Then only that port will read the value, other ports reading 0.

Operation of scanner in wind Tunnel

During Wind tunnel operation, there will be few functional changes to be done before running the tunnel. The connections from scanner to control box remains the same but in this case we don't use Projection/U tube manometer. Instead, the ports of the scanner should be connected to the body which is of interest. The connections are as mentioned below.

- The ports of the scanner should be connected to the tubes which will be tapped from the body to be experimented.
- The Tunnel Total and Static tubes should be connected to the 2 ports of the scanner. Note that the ports coloured in red colour is read first in the scanner(1 to 64)

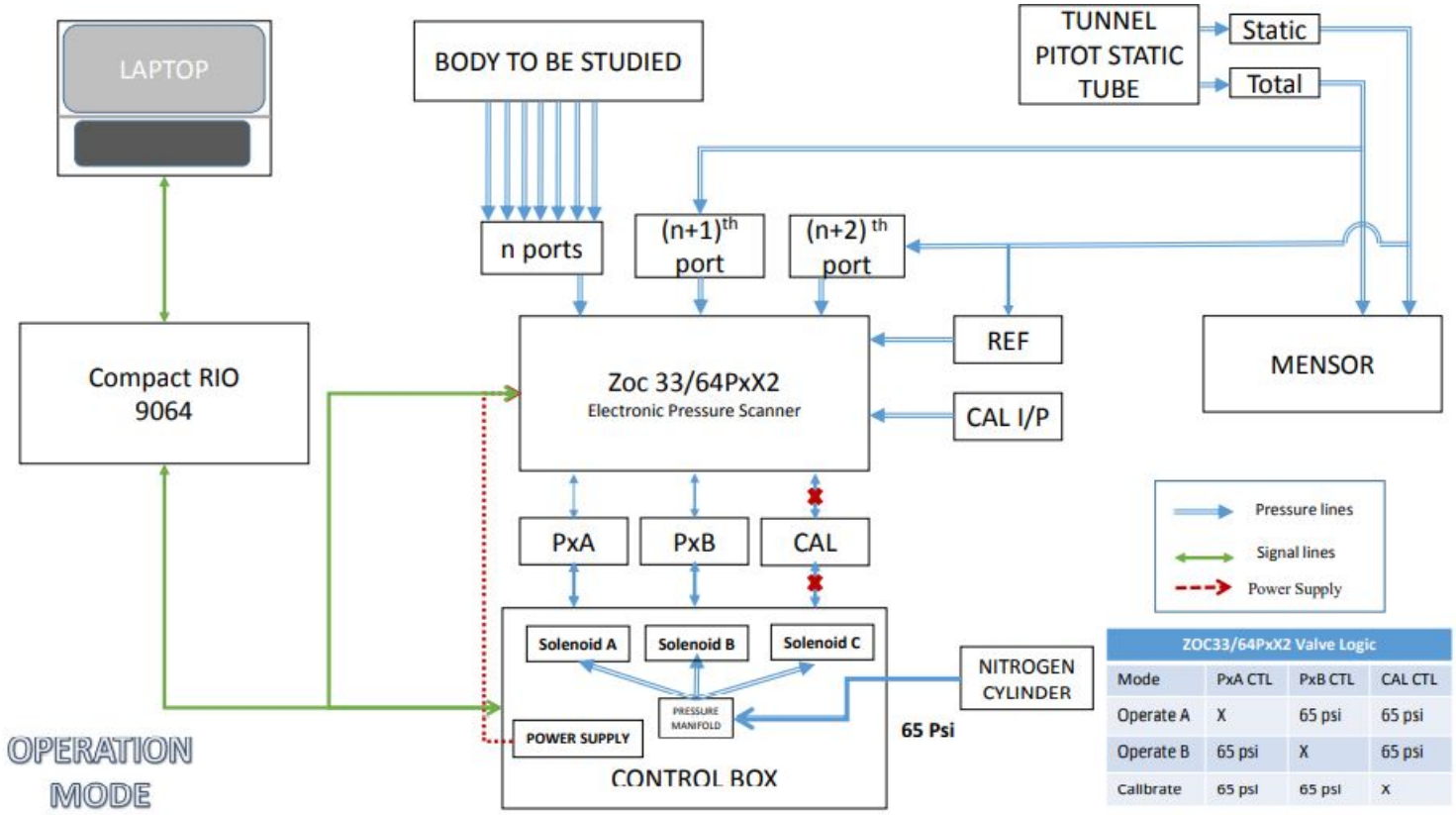

Figure 2: Schematic of operation process of pressure scanner

and the ports coloured black is read second(65 to 128). So if readings to be taken for more than 64 ports then connect Tunnel's Total and Static ports in parallel to both red colour ports and black colour ports.

- The Tunnel's Static port should be connected in parallel with Ref port of the scanner and CAL I/P will be open to atmosphere.
- PxA, PxB, Cal of scanner to be connected to A, B, C of Control box.
- Scanner connector should be connected to Control box connector.
- 65 psi from Nitrogen Cylinder is to be given to Control box.

After all these connections, open the Labview program named 'esp scanner' and keep it in run mode for about 1 hour for warm up. In the Labview program there are 2 modes namely Operation mode and Calibration mode. During Operation we should use Operate mode. The schematic of operation mode of pressure scanner is represented in Fig.2

- After warm up, first take the bias value by clicking on operate button and then start button. All 64(or 128) ports of the scanner will start reading the values.
- Start running the tunnel after taking bias value and wait till the required speed is achieved.
- When the required speed is achieved, click on the start button in Operation mode and take 3 samples one after the other. If the tests are to be done for different speeds then takes 3 samples for each speed and stop the tunnel.
- Take another bias in the end and run the *check.calibartion.m* program to read the pressure values of each port.

NOTE: Do not forget to change the port no in labview as well as matlab program from 64 to 128(or as required) before processing.

Jeena Joseph

Personal Details

13 January,1989

C-79, Shreyas 1, MIT Quarters, Manipal, Karnataka

+91 94814 25602

me16f05.jeena@nitk.edu.in

jeenajoseph@live.in

Indian

Social Network

www.facebook.com/jeen.e.joseph

Languages

- English
- Malayalam
- Hindi
- Tamil
- Kannada

Computer Skills

MS Office

Solid Works

Catia

Latex

ANSYS Fluent

Star CCM+

Research Interests

Biomimetic flow control | Wind Energy | Experimental Aerodynamics | Renewable Energy | VAWT

Working Experience

2015-2016 **Application Engineer** Ark InfoSolutions Pvt.Ltd,Mumbai,India
Training and client support for ANSYS Fluent

2012 – 2013 **Lecturer** Karavali Institute of Technology,Mangalore, India
Fluid Mechanics, Aerodynamics, Aircraft Structures

2011 – 2012 **Lecturer** Jawaharalal College of Engineering,Palakkad,India
Strength of Materials, Manufacturing Technology

Education

2016 – 2022 **Doctoral Fellow** National Institute of Technology Karnataka,India
Effect of Humpback whale-inspired tubercles on Vertical Axis Wind Turbine blade

2013 – 2015 **M.Tech** University of Petroleum and Energy Studies, Dehradun, India
M.Tech in Computational Fluid Dynamics

2007 – 2011 **B.Tech** National Aerospace University, Kharkiv,Ukraine
B. Tech in Aerospace Engineering (Aircraft Design and Manufacture)

Publications

Journals

2023 **An Experimental Study on the Effect of Geometrical Parameters and Shape of Leading Edge Tubercles on Vertical Axis Wind Turbines (VAWTs)**
Jeena Joseph, A.Sathyabhama, Surya Sridhar, Jayakrishnan R.
(Manuscript Communicated)

2022 **Leading edge tubercle on wind turbine blade to mitigate problems of stall, hysteresis, and laminar separation bubble**
Jeena Joseph, A.Sathyabhama
Energy Conversion and Management
https://doi.org/10.1016/j.enconman.2022.115337

2022 **Implementation of tubercles on Vertical Axis Wind Turbines (VAWTs): An Aerodynamic Perspective**
Surya Sridhar, Jeena Joseph, Jayakrishnan Radhakrishnanan
Sustainable Energy Technologies and Assessments
https://doi.org/10.1016/j.seta.2022.102109

2022 **Experimental and numerical analysis of humpback whale inspired tubercles on swept wings**
Jeena Joseph,A.Sathyabhama, Surya Sridhar
Aircraft Engineering and Aerospace Technology
https://doi.org/10.1108/AEAT-04-2021-0114

2021 **Experimental Study on the Effect of Tubercle on Aerodynamic Characteristics of Swept Wings at low Reynolds Number**
Jeena Joseph, A.Sathyabhama
Iranian Journal of Science and Technology, Transactions of Mechanical Engineering
https://doi.org/10.1007/s40997-021-00455-z

Jeena Joseph

Personal Details

About Me

A motivated person aspiring to be a great teacher looking for opportunities to improve research and teaching capabilities .

Life Philosophy

"Bloom where you are planted."

A day in my life

working woman | young researcher | mother of two toddlers

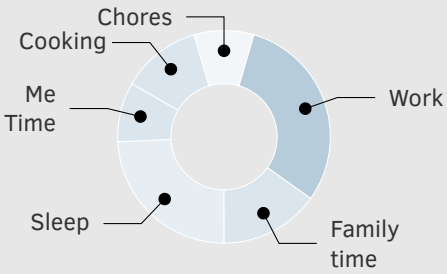

Hobbies

- Riding
- Trekking
- Stock Market
- Cooking
- Gardening

Conference Participation

Jan. 2020 — **2nd International Conference on Numerical Heat Transfer and Fluid Flow- NHTFF 2020** — NIT Warangal, India
Numerical study on the effect of tubercle on symmetrical airfoil at low Reynolds number

Dec. 2019 — **3rd International Heat and Mass Transfer Conference -IHMTC 2019** — IIT Roorkee,India
"Experimental study on the effect of leading-edge tubercle on high swept wing at low Reynolds number

Dec. 2019 — **46th National Conference on Fluid Mechanics and Fluid Power -FMFP 2019** — PSG College,Coimatore,India
A Comparison on the Effect of Leading Edge Tubercle on Straight and Swept Wing at Low Reynolds Number

Internships

Jan–Sep 2015 — **Industrial Research and Consultancy Centre** — IIT-Bombay,India
"CFD modelling of scramjet engine" using ANSYS Fluent
Department of Aerospace Engineering
Indian Institute of Technology-Bombay

Jun –Jul 2014 — **Cyient** — Hyderabad,India
"Modeling heat transfer in exhaust manifold" using STAR CCM+

Mar–May 2010 — **Kharkiv Aviation Factory** — Kharkiv, Ukraine
Familiarizing production and maintenance operations of aircraft

Certificates

ANSYS — Technical professional in Fluids(ANSYS Fluent)
EdX — Hypersonics - from shock waves to scramjets
Wipro Misson 10X — High Impact teaching skills

REFERENCES

- **Dr. A Sathyabhama (PhD Supervisor)**
  Associate Professor, Department of Mechanical Engineering
  National Institute of Technology Karnataka
  Surathkal, Karnataka,India
  Email id: sathyabhama@nitk.edu.in
  Cell:(+91) 94481 34433

- **Dr.Rajesh Yadev**
  Associate Professor, Department of Aerospace Engineering
  University of Petroleum & Energy Studies, Dehradun,India
  Email id: rajeshyadav@ddn.upes.ac.in
  Cell:(+91) 97604 05280

- **Dr.Andrey Chernyavsky**
  Head of Engineering Geometry and Computer Modeling Department
  National Aerospace University, Kharkiv, Ukraine
  Email id: a.cherniavskyi@khai.edu
  Cell:(+38) 06394 71715

December 26, 2022 — Jeena Joseph